COMPUTATIONAL METHODS FOR NON-IDEAL PLASMAS

By

Lucas J. Stanek

A DISSERTATION

Submitted to
Michigan State University
in partial fulfillment of the requirements
for the degree of

Computational Mathematics, Science and Engineering – Doctor of Philosophy

2022

ABSTRACT

Plasmas are many-body systems of interacting charged particles that exist naturally and can be created experimentally. For example, plasmas are found in many astrophysical systems like the corona of the sun, the Earth's ionosphere, and in the interior of white-dwarf stars. In engineering and medicine, plasmas are used during the design process of semi-conductors or for inactivating viruses like COVID-19. Plasmas also occur in nuclear fusion experiments which promise a nearly infinite supply of clean, renewable energy.

Quantifying the behaviors of plasmas experimentally can be challenging due to the short time-scales and small length-scales that interactions between the plasma particles occur. In many cases, computational approaches are used to simulate the dynamics of plasmas to supplement the dearth of experimental data. The accuracy of these computational methods is largely unknown across the entire parameter regimes plasmas occupy limiting their predictive capabilities. This dissertation is composed of four distinct projects all with the common goal of developing numerical methods for rapidly and accurately computing properties of non-ideal plasmas.

First, we focus on the data-driven discovery of pair interaction potentials for molecular dynamics simulations of dense plasmas across a wide range of temperatures and elements. We find that our pair interaction potentials simulate the ionic interactions in a plasma with accuracy comparable to Kohn-Sham molecular dynamics but with orders of magnitude less computation cost. Second, we develop theoretical models that avoid the need for numerical simulations of plasma mixtures altogether. Our theoretical models show reasonable agreement with molecular dynamics data across the both the weak and strong coupling regimes. Third, we use techniques in machine learning to interpolate plasma properties data with multiple sources of data. We find that our machine learning method accurately predicts trends in data even in the absence of high-fidelity calculations. Lastly, we implement a numerical scheme for solving kinetic equations with applications to ultracold neutral plasma mixtures and high-energy-density plasmas. With our simulation results, we suggest plasma conditions for future experiments and we discuss natural extensions of our numerical method that will be the basis of future work.

To my mother, father, and sister.

ACKNOWLEDGEMENTS

There have been numerous individuals that have helped me throughout the pursuit of completing my Ph.D. These individuals exist in the form of mentors, colleagues, friends, and family who have tirelessly supported me in a variety of ways for which I am eternally grateful; without them, I would not be where I am at today. In particular, I have had the pleasure of working with and learning from patient, thoughtful, and talented mentors who have guided me in my academic endeavors and have pushed me to become a better student and researcher.

I would like to thank my research advisor Michael Murillo for guiding me along this journey. You have always extended a helping hand and a critical ear whenever needed. You have mentored me since my first days in CMSE and have made learning about all things plasma physics fun and exciting. Your mentoring spans far beyond physics in that you have made deliberate efforts to ensure that I have the necessary skills in presenting and technical writing. You have instilled in me your affinity for exploring alternative avenues in research and love for data visualization. I think that you'll find the plots in this dissertation are, "just like downtown."

Thank you to Brian O'Shea for his constant support throughout graduate school. Brian, you were an excellent graduate advisor, and have always provided me with guidance. I'd like to also thank Shaunak Bopardikar for introducing me to the field of multi-fidelity modeling and offering a unique and valuable perspective on research. Additionally, I want to thank Chandre Dharma-wardana for his continued involvement in furthering my understanding of physics and technical writing. A big shoutout to my colleagues Jeff Haack and Liam Stanton. Jeff, you have always been insightful and helpful in "everything numerics" and have made yourself available whenever I have needed to phone-a-friend. Liam, you have offered me advice in both life and math. I deeply value our many conversations about and am grateful that you have pushed me to be precise in my understanding of physics. Thank you to Lisa Murillo for her careful editing of many of my manuscripts. Lisa, because of you, I write much more gooder now.

I want to extend my gratitude to John Luginsland and Frank Graziani for being great mentors and crucial members of my professional network. On numerous occasions, both of you have allowed

me access to doors that would otherwise be shut. I'd also like to thank all of my mentors at Sandia National Laboratories for their involvement in my Ph.D. work over the years. In particular, I'd like to thank Kris Beckwith, Ray Clay, Pat Knapp, and Stephanie Hansen for making my internship experience at Sandia exciting and fruitful.

I am indebted to my friends who have cheered me on and supported me for many years. Adam, you have supported me in numerous ways and have always offered me encouragement. Tyler, I value our conversations about life and grad school. Dustin, thank you for your random phone calls to check-in and offering me advice whenever needed.

I would also like to acknowledge my friends in CMSE. Nat, you have been a constant fount of support and I am so grateful for you. I appreciate our video game session, our mutual ridiculousness, and your help throughout this journey. Sarah, I look back fondly on when we'd study together for our qual classes and end up distracting each other by playing battleship. Our friendship has offered a much needed respite from the hectic life of graduate school and I could not have done it without you. Bill, without you, I would have not learned about CMSE. Thank you for being a proponent of me over the years; I am glad we were able to experience grad school together.

Lastly, my family has consistently provided unwavering support. Mom, you have taught me to be compassionate and caring, Dad, you have always offered unbiased advice to me when I've needed it, Mike, you have provided me with endless guidance, and Lindsey, you have been a role model for me since we were kids and have instilled your work ethic and tenacity in me.

TABLE OF CONTENTS

CHAPTER 1

INTRODUCTION

1.1 Background

Plasmas are charged particle systems that can be commonly found in nature. Plasmas respond strongly to electric and magnetic fields – requiring free electrons much like a metal. Free electrons in a system are created by a process called *ionization*. When an element is ionized, bound electrons are removed from an atom by sources of extreme pressure, temperature, and/or radiation. For metals, the free electrons result from pressure ionization due to the density of the metal. In ultracold neutral plasmas (UNPs), ionization occurs due to radiation. In other states of matter, like hot dense matter, ionization can result from combinations of pressure, temperature, and radiation sources.

As shown in Fig. 1.1, plasmas occupy a wide temperature and density range and can be classified as hot, magnetized, non-ideal, ultracold, dusty, non-neutral, etc. Many astrophysical systems like the Sun's corona, the interiors of gas giants, and Earth's ionosphere are considered plasmas. Plasmas have many applications in medicine, technology, and energy production. For example, plasmas can be used for inactivating viruses like COVID-19 [1], during the manufacturing process of semiconductors [2], or in nuclear fusion experiments for generating large amounts of clean, renewable energy.

Nuclear fusion experiments typically require intense lasers or high-energy x-rays that can only be produced at a select number of facilities in the world. Examples of these facilities include the Z Machine at Sandia National Laboratories, The National Ignition Facility at Lawrence Livermore National Laboratory, and the OMEGA laser facility at The Laboratory for Laser Energetics at The University of Rochester. While nuclear fusion is currently not feasible for energy production, data collected during these experiments are used to optimize their set-up to maximize the likelihood of sustained thermonuclear burn. Such data include equations of state, plasma transport coefficients, neutron yield, plasma temperature, and data on collective effects like plasma waves or hydrodynamic

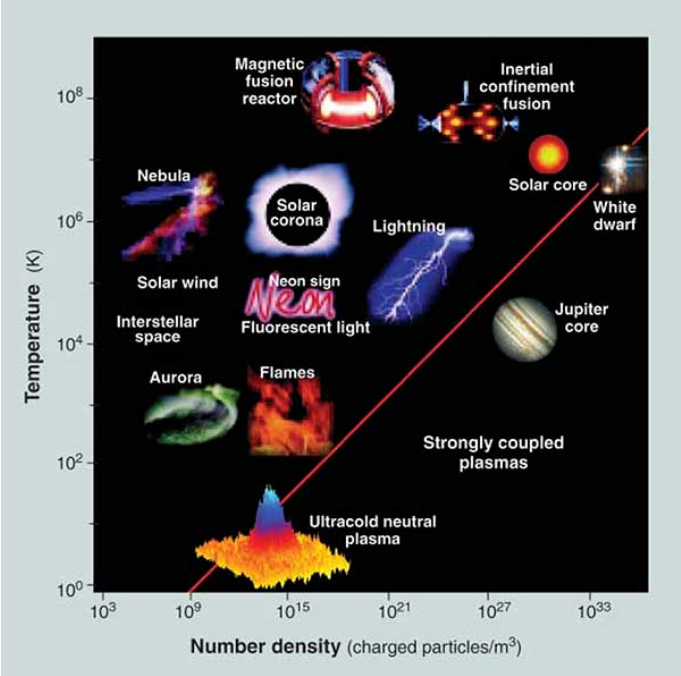

Figure 1.1: Common plasmas at different temperatures and densities. This figure was originally presented in Ref. [3]. The red curve corresponds to $\Gamma = 1$ [see Eq. (1.1)], for mean-ionization state $\langle Z \rangle = 1$. Below the curve, $\Gamma > 1$ and above the curve $\Gamma < 1$.

instabilities. The cost associated with carrying out these experiments prohibits the availability of wide-ranging experimental data which is further limited by the accessible parameter regime of the experiments.

Computational approaches are used to generate large amounts of plasma properties data to support the few high-fidelity experimental calculations. Often, these computational approaches are used in physical regimes absent of experimental data for “extrapolation." By coupling data from experimental platforms to results from numerical simulations, burning plasmas have recently been created in inertial confinement fusion (ICF) experiments at The National Ignition Facility [4–6] resulting in the largest amount of fusion energy output to date. This progress has highlighted the importance of accurate and rapid calculations of plasma properties using computational methods. A major challenge in computational plasma physics is quantifying the accuracy of the numerical methods used for simulating plasmas. The aim of this dissertation is focused on the development of numerical methods for rapidly computing accurate plasma properties of non-ideal plasmas.

1.2 Plasma Preliminaries

Fundamentally, plasmas are many-body systems of interacting charged particles. To estimate the nature of these interactions, dimensionless parameters such as the Coulomb coupling parameter, degeneracy parameter, and Knudsen number are used. These dimensionless parameters estimate the significance of correlations between particles, if quantum statistics are necessary, and if the plasma behaves as a fluid. The *Coulomb coupling parameter* is often described as the ratio of the average potential energy of particles in a plasma to their average kinetic energy and is defined as [7–11]

$$\Gamma = \frac{\langle Z \rangle^2 e^2}{a_i T}, \tag{1.1}$$

where $\langle Z \rangle$ is the effective charge (or mean-ionization state) of an ion [12], e is the elementary charge, $a_i = (4\pi n_i/3)^{-1/3}$ is the Wigner-Seitz radius for the ion number density n_i, and T is the temperature of the plasma in energy units. Equation (1.1) quantifies the importance of many-body interactions to the plasma's properties. A plasma is said to be "weakly coupled" when $\Gamma < 1$ and "strongly coupled" when $\Gamma > 1$. For $\Gamma \ll 1$, the average kinetic energy of the particles in the plasma is far greater than their average potential energy. In this limit, the plasma particles behave like an ideal gas and the plasma is referred to as an "ideal plasma." In the opposite limit, when the $\Gamma \gg 1$, the average potential energy of the particles dominates the average kinetic energy and the particles in the plasma are strongly correlated; a plasma in this state is referred to as a "non-ideal" plasma. Note that there are a variety of plasma conditions that correspond to a $\Gamma > 1$. For example, when a plasma is dense (e.g., white dwarf stars), cold (e.g., ultracold neutral plasmas), or if the mean-ionization state is large which is true for dusty plasmas where the plasma macroparticles (referred to as "dust grains") can have $\langle Z \rangle \sim 1000$ [13, 14]. We stress that multiple types of plasma may share the same value of Γ; this fact allows for connections between disparate plasmas such as high-energy-density (HED) plasmas and UNPs [15]. Note that Eq. (1.1) is for a single, unscreened[1] species. If electron screening is significant which is often the case in strongly coupled plasmas [11],

[1] "Screening" or "shielding" refers the reduction of a plasma particle's force range due to the accumulation of oppositely charged particles.

we can modify Eq. (1.1) to include electron screening with a *screening function*. The resulting coupling parameter is referred to as an "effective coupling parameter" as shown in Refs. [16–18]. Moreover, if we wish to extend Eq. (1.1) to binary plasma mixtures of ion species i and j, (see Chapter 3) we have

$$\Gamma_{ij} = \frac{\langle Z_i \rangle \langle Z_j \rangle e^2}{a_{\text{tot}} T_{ij}}, \tag{1.2}$$

where $a_{\text{tot}} = (4\pi n_{\text{tot}}/3)^{-1/3}$ with $n_{\text{tot}} = n_i + n_j$, and $T_{ij} = (m_i T_j + m_j T_i)/(m_i + m_j)$ [19].

In addition to the coupling of the ions, we must also consider the nature of the electrons. That is, if we can treat the electrons as classical point particles or if we need to include quantum statistics to describe their interactions. If quantum statistics are needed to describe the electrons, the plasma is said to be "degenerate" or "partially degenerate." If we can treat the electrons as classical point particles, the plasma is said to be "non-degenerate." The magnitude of the degeneracy of a plasma is given by the *degeneracy parameter* which we define as [20]

$$\theta = \frac{T_e}{E_F}, \tag{1.3}$$

where $E_F = \hbar^2 (3\pi^2 n_e)^{2/3}/2m_e$ is the Fermi energy for the electron number density n_e, electron mass m_e, and the electron temperature T_e is in energy units. A system is non-degenerate when $\theta > 1$, and degenerate or partially degenerate when $\theta < 1$. For dense or cold plasmas we have that $\theta < 1$ and the wave packet describing the electrons begin to overlap. In this case, it is no longer appropriate to approximate the electrons by classical statistical mechanics and quantum statistics are needed. However, for high temperatures and/or low densities, the overlap of wave packets does not occur and the electrons may be treated as classical point particles.

The final dimensionless quantity we introduce is the *Knudsen number* which helps determine if a system is in a hydrodynamic state i.e., if the plasma may be treated with continuum mechanics instead of statistical mechanics. The Knudsen number is defined as [21]

$$K_n = \frac{\lambda}{L}, \tag{1.4}$$

where λ is the mean-free-path, the average distance that a particle travels before collision, and L is some reference length scale. As highlighted by Fig. 1.2, the magnitude of K_n suggests appropriate

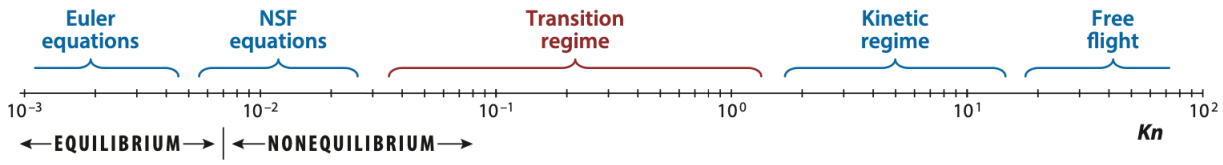

Figure 1.2: Different theoretical regimes for different Knusden numbers. This figure was originally presented in Ref. [21]. As K_n becomes small hydrodynamic approximations such as the Euler or Navier-Stokes-Fourier (NSF) equations are valid. For larger K_n, kinetic theory becomes an accurate description of the system.

plasma type	element	n_i (cm^{-3})	T_i (eV)	T_e (eV)	$\langle Z \rangle$	Γ	θ	K_n
UNP	Ca	1×10^{9}	8.6×10^{-5}	8.6×10^{-3}	1	2.3	2.4×10^{6}	1.1×10^{-3}
CDM	H	2×10^{22}	0.01	0.01	0.34	71	3.7×10^{-3}	6.1×10^{-8}
WDM	H	6×10^{24}	10	10	0.84	3	0.083	5×10^{-6}
HDM	H	6×10^{25}	1000	1000	0.97	0.086	1.8	8.4×10^{-4}

Table 1.1: Comparison of non-dimensional parameters for different plasmas. Here we abbreviate cold-, warm-, and hot-dense matter as CDM, WDM, and HDM, respectively. We have chosen experimentally relevant conditions for each plasma type with a focus on fusion fuel in ICF experiments for the CDM, WDM, and HDM cases. To compute the Knudsen numbers, a reference length-scale of $L_{\text{UNP}} = 1$ mm and $L_{\text{ICF}} = 1$ μm, were used for the UNP and ICF plasmas. A Thomas-Fermi model was used to compute the mean-ionization state $\langle Z \rangle$ for the ICF plasmas; for UNPs, $\langle Z \rangle$ is known exactly and is often unity.

models for the plasma. For example, in the highly collisional limit ($K_n \ll 1$), the plasma is close to equilibrium and Euler hydrodynamics is an applicable model. In contrast, in the transition/kinetic regimes, particles collide and interact but are out of equilibrium so non-equilibrium statistical mechanics (i.e., kinetic theory) must be employed.

In each chapter of this dissertation, we reference each of these three dimensionless parameters to 1) support the choice of models/numerical approaches we implement, and 2) make connections to relevant experimental platforms that benefit from this work. As an example, Table 1.1 displays all three dimensionless parameters for different plasma types at various number densities and temperatures. Note that warm dense matter (WDM) and UNPs share a similar Coulomb coupling parameters suggesting that UNPs can be used as a proxy for WDM.

1.3 Computational Modeling of Plasmas

The numerical techniques used to simulate plasmas are just as diverse as the parameter space they span. These techniques range from various forms of molecular dynamics (MD) [22–38], where explicit interactions between particles are calculated, to coarse-grained methods such as the particle-in-cell technique [39–43], models based on kinetic theory [44–60], and hydrodynamics [61–78]. Usually, the choice of which numerical is appropriate for a given plasma depends on certain limiting physical regimes e.g., high density and low temperatures or low density and high temperatures.

At low densities and temperatures, $\Gamma > 1$ and $\theta < 1$ resulting in a strongly coupled, degenerate plasma. To numerically treat strong coupling and quantum statistics, computational methods such as Kohn-Sham MD [79–87], and orbital-free MD [32, 83, 88–92] are employed. In Kohn-Sham MD [93], the quantum statistics are treated by solving Schrödinger's equation for the one-particle wave function referred to as "Kohn-Sham orbitals" or simply "orbitals." Once the orbitals are obtained, the electron density is constructed and the force acting on the ions due to the electronic structure (i.e., the placement of the electrons) is computed at every simulation time step. Determining the electronic structure in the Kohn-Sham MD formalism is a computationally expensive procedure that scales numerically as $\mathcal{O}(N_e^3)$ where N_e is the number of free electrons in the system. To mitigate the computational cost associated with N_e, *pseudopotentials* are implemented to represent the non-interacting core of an atom which reduces the number of orbitals that need to be numerically obtained reducing computation cost. At higher temperatures ($T \sim 15$ eV), pseudopotentials must be used with caution because an ion may become fully ionized and an "all-electron" calculation may be needed.

Orbital-free MD [94] is the generalized, original formalism of which Kohn-Sham MD is based. In orbital-free MD, the orbitals are not calculated and algorithms such as the fast Fourier transform can be implemented which results in a numerical scaling of $\mathcal{O}(N_e \log N_e)$ [94–96]. Orbital-free MD methods allow for simulations with orders of magnitude more particles and are especially effective at high system temperature. As shown in Ref. [97], orbital-free MD numerically scales as $\sim \mathcal{O}(1)$ with system temperature T in contrast to Kohn-Sham MD which numerically scales as

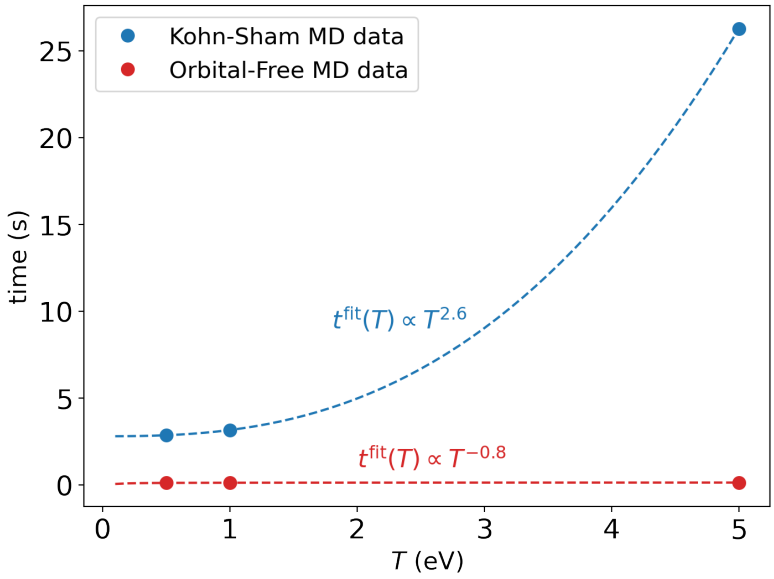

Figure 1.3: Time to update one particle in Kohn-Sham MD and orbital-free MD versus system temperature (see Ref. [97]). The orbital-free MD data does not fit a power-law form unlike the Kohn-Sham MD data which scales with temperature as $\sim O(T^{2.6})$.

$\sim O(T^{2.6})$. Figure 1.3 shows data of simulation time versus temperature using both Kohn-Sham MD and orbital-free MD obtained from Ref. [97]. The points correspond to the time to update one particle using both methods for a given system temperature. A fit has been obtained from the data showing the aforementioned temperature scaling. The best-fit parameters to the orbital-free MD data indicate that a power-law does not describe its numerical scaling in contrast to Kohn-Sham MD. The approximations of orbital-free MD (and thus Kohn-Sham MD) lie in the determination of various functionals that account for the kinetic energy and the exchange and correlation of the system. Figure 1.4 displays data obtained from the literature that showcases simulations carried out using Kohn-Sham MD and orbital-free MD for different systems in a space-time diagram. We see that Kohn-Sham MD is sequestered to physical systems on the length- and time-scales of angstroms (Å) and pico-seconds (ps); this clustering is a direct consequence of the computational complexity associated with Kohn-Sham MD. In contrast, orbital-free MD can access much larger spatial scales, even on the order of micrometers (μm). Importantly, there is a *third axis* of temperature that is not displayed here. We emphasize that orbital-free MD is able to simulate plasmas at temperatures of hundreds of eV making orbital-free MD an ideal method for simulating high-energy-density

plasmas. In contrast, Kohn-Sham MD is more accurate than orbital-free MD at lower temperatures (e.g., on the order of fractions of an eV) making Kohn-Sham MD an ideal candidate for simulating warm-dense-matter, when $\Gamma \approx \theta \approx 1$.

In addition to Kohn-Sham and orbital-free MD, Figure 1.4 also displays data from MD simulations which span a much larger time and space scales. The difference in viable simulation scales is due to the fact that MD makes use of *pre-computed* potentials that can be derived from Kohn-Sham/orbital-free methods or obtained empirically. Some examples of pre-computed potentials include the Coulomb potential, the Yukawa potential, or the Lennard-Jones potential. These potentials eliminate the need for an electronic structure calculation as it is accounted for in the potentials functional form. Molecular dynamics typically scales as $O(N \log N)$ where N is the number of particles in the MD simulation by utilizing fast-neighbor-list algorithms to compute particle interactions. In Chapter 2 we make comparisons of Kohn-Sham MD, orbital-free MD, and MD by carrying out simulations of dense plasmas ranging in temperature, density, and nuclear charge.

The last remaining methods in Figure 1.4 are kinetics and hydrodynamics. Instead of simulating explicit particle interactions, these methods simulate statistical distributions of particles, greatly reducing computation cost and allows these methods to access even larger space and time scales than MD. The computational complexity associated with kinetics and hydrodynamics varies based on the numerical methods implemented, but the key distinction between these methods and MD is that they are often *grid-based methods*, instead of *particle-based methods*. Chapter 5 is dedicated to the development of a grid-based numerical method for solving kinetic equations with applications to UNPs.

In recent years, machine learning has become a widely used tool for both obtaining plasma properties data as well as utilizing and analyzing existing datasets. Commonly used machine learning methods for plasma properties data range from deep neural networks, which are favored as they can learn non-linear relationships between features in a dataset, to dimensionality reduction techniques like principal component analysis. In reference to Fig. 1.4, the influence of machine learning

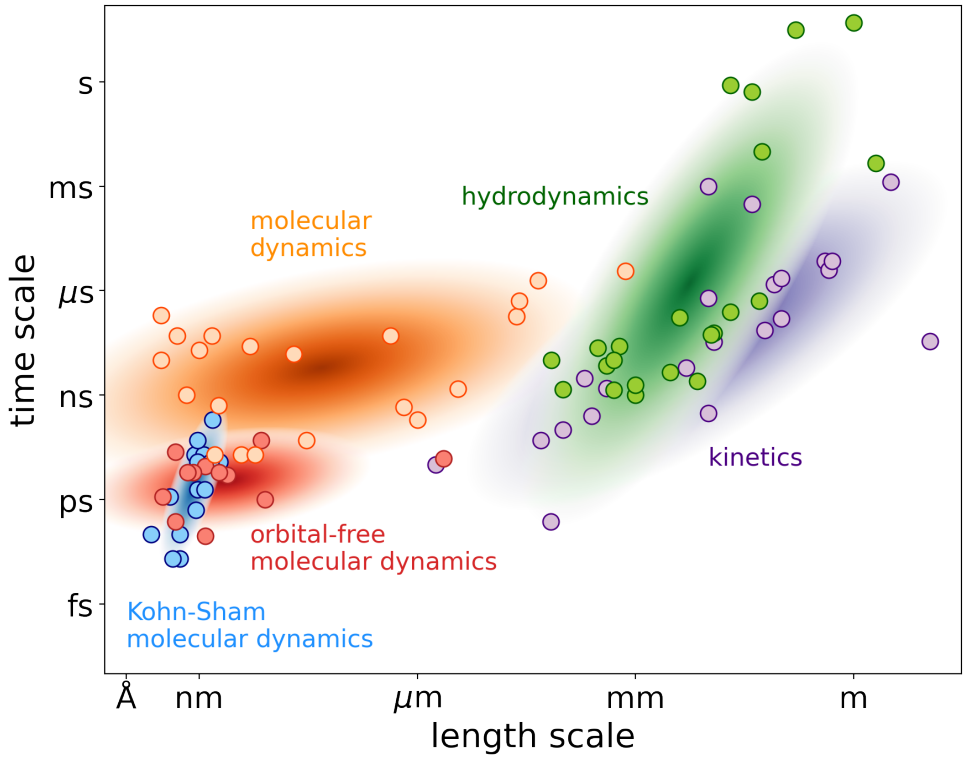

Figure 1.4: Computational methods employed at various time- and length-scales for physical systems. Each data point represents published data from a variety of disciplines starting in the year 2012; ellipses computed based on the principal components of the data are also plotted. Note that Kohn-Sham molecular dynamics [79–87] and orbital-free molecular dynamics [32, 83, 88–92] simulations are typically done at the scale of angstroms and picoseconds; this is a direct result of their computational complexity which limits these methods to small system sizes. Coarse-grained methods such as kinetics [44–60] and hydrodynamics [61–78] are able to access larger spatio-temporal scales because instead of computing interactions between explicit particles as is done in MD [23–38], a statistical average of particles is computed which greatly reduces computation cost.

would be seen across the entire spatio-temporal domain making machine learning the most widely applicable method for determining plasma properties. Some concrete examples of machine learning include its use in Kohn-Sham MD to determine the necessary exchange correlation functional or in hydrodynamics for obtaining the necessary constituent data (i.e., transport coefficients and equations of state). In Chapter 4 we present a machine learning method for regressing multi-modal datasets to rapidly generate accurate predictions of plasma transport data.

1.4 Dissertation Overview

This dissertation consists of multiple objectives which are directed toward the common goal of creating more accurate, computationally efficient, methods for simulating plasmas across disparate temperature and density regimes. The computational methods focused on herein are those of MD, machine learning, and kinetic theory. Each chapter is dedicated to one of these methods which are applied to numerical calculations of non-ideal plasmas.

The focus of Chapter 2 is to elucidate the efficacy of force laws used for MD simulations of dense plasmas. A review of commonly used force laws is presented along with a discussion of the current state-of-the-art models that stem from data-driven machine learning approaches. We present a non-parametric, data-driven approach for obtaining force laws for a wide range of elements at various temperatures and densities allowing for an increase in simulation time by orders of magnitude while also reducing statistical errors.

The scope of the work presented in Chapter 2 was limited to plasmas comprised of a single ionic species. However, in many scenarios (e.g., ICF experiments or UNP mixtures), an understanding of the interactions between particles in plasma mixtures is vital. Chapter 3 addresses the theoretical challenges associated with dense plasma mixtures where we derive analytic models for the thermodynamic factor and interdiffusion transport coefficient. Our analytical formulae agree with molecular dynamics data in certain limiting regimes. Thus, we are able to avoid the need for molecular dynamics simulation, and as a result, eliminates the associated computation cost and reduces statistical error.

While Chapters 2 and 3 focused on *generating* accurate plasma properties data, Chapter 4 focuses on interpolating multi-modal datasets to improve predictions in regions were high-fidelity measurements do not exist. We compare our multi-fidelity machine learning approach to its single-fidelity counterpart and show that by using data from multi-modal datasets, the predictions across regions absent of high-fidelity data are more accurate with reduced uncertainty.

In Chapter 5 we model the interactions of UNP mixtures using kinetic theory to investigate their expansion into a vacuum as well as their entropy production. We begin by providing an overview

of kinetic theory, as well as a derivation of the Vlasov equation in spherical coordinates which is scarce in the literature and appears seemingly nowhere. Using a multi-species kinetic equation in Cartesian coordinates, we simulate UNP mixtures and find that the initial plasma conditions can be chosen such that the dynamics are time-reversible. Additionally we apply our kinetic simulations to HED plasmas where we analyze the dominant drivers of diffusive mixing.

The findings of this dissertation are summarized in Chapter 6 along with a discussion on how the methods presented herein can be improved.

CHAPTER 2

DATA-DRIVEN FORCE LAWS FOR MOLECULAR DYNAMICS SIMULATIONS OF DENSE PLASMAS

2.1 Introduction

ln strongly coupled plasmas, N-body simulations are required to correctly account for collective effects (e.g., plasma waves) or instabilities (e.g., the two-stream or bump-on-tail instability [98]). As discussed in Sec. 1.3, MD[1] is a simulation method that encodes N-body effects by integrating Newton's second law for a system of interacting particles. The critical input of MD is the force-law or interaction potential that quantifies the particle interactions. For example, the Lennard-Jones interaction potential is used for MD simulation of noble gasses, and the Yukawa interaction potential is used to simulate a system of charged particles (i.e., plasmas). As most plasmas are made up of ions and electrons where electron screening is present, the Yukawa potential, which approximates electron screening, is commonly used for MD simulations of plasmas and is favored for its short-range interactions and pre-computed form. However, the range of validity of the Yukawa potential is unknown for different plasma conditions.

While MD "stands alone" as its own simulation method, it may be unable to simulate large time and length scales that may be required for some applications (see Fig. 1.4). In these situations coarse-grained methods based on hydrodynamics or kinetic theory are employed. However, coarse-grained methods still require detailed microscopic information, often from MD simulations, as "closures." The quality of the microscopic information directly influences the results of the coarse-grained methods and therefore quantifying the sensitivity of the choice of interaction potential for MD simulations is crucial for obtaining high-fidelity macroscopic simulations of plasmas. This chapter[2] focuses on the delineation of the accuracy boundary between microscale simulation methods by comparing a variety of force laws for plasma simulation across a wide range of elements,

[1] See Ref. [23] for an overview of MD.

[2] The content described in this chapter has been reproduced from *Lucas J. Stanek, Raymond C. Clay III, M. W. C. Dharma-wardana, Mitchell A. Wood, Kristian R. C. Beckwith, and Michael S. Murillo , "Efficacy of the radial pair potential approximation for molecular dynamics simulations of dense plasmas", Physics of Plasmas 28, 032706 (2021) https://doi.org/10.1063/5.0040062,"* with the permission of AIP Publishing and has been modified to address the requirements of this dissertation; see Ref. [87] for the full published article.

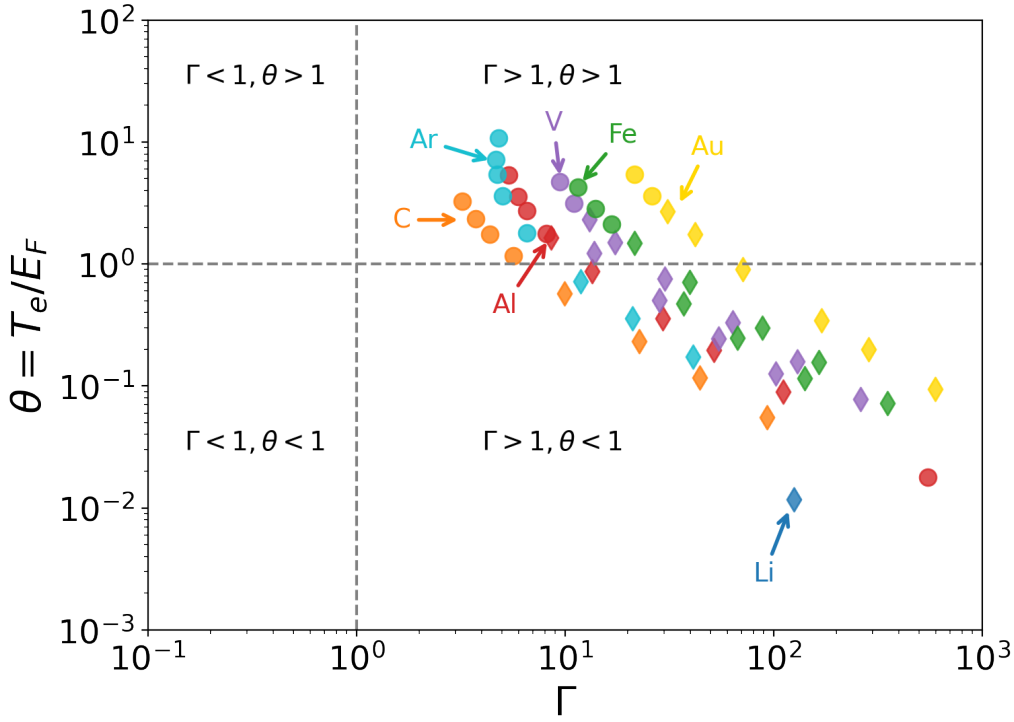

Figure 2.1: Different plasma conditions studied in this chapter; each color corresponds to a different element. The cases studied here are strongly coupled and span the non-degenerate and degenerate regimes. For all cases, the Knudsen number $10^{-6} < Kn < 10^{-2}$ where we have chosen a reference length scale of $L = 5$ Å which is approximately the size of the simulation cell for all cases. The diamonds (♦) denote the MD simulations for which we have both RPP-MD *and* KS-MD data. The circles (•) denote MD simulations for which we only have RPP-MD data.

temperature, and density; these conditions are are shown in Fig. 2.1. As a baseline, we employ Kohn-Sham density functional theory molecular dynamics (KS-MD) and compare results obtained from radial pair potential molecular dynamics (RPP-MD). By extracting the optimal RPP from KS-MD data using force matching, we constrain its functional form and dismiss classes of potentials that assume a constant power law for small interparticle distances. Our results show excellent agreement between RPP-MD and KS-MD for multiple metrics of accuracy at temperatures of only a few electron volts. The use of RPPs offers orders of magnitude decrease in computational cost and indicates that three-body potentials are not required beyond temperatures of a few eV. Due to its efficiency, the validated RPP-MD provides an avenue for reducing errors due to finite-size effects that can be on the order of $\sim 20\%$.

A wide variety of RPPs have been developed for modeling dense plasmas. In some cases the

accuracy of the model can be inferred from its theoretical underpinnings; in other cases, comparison to higher-fidelity approaches or experiments is needed. Limitations of the RPP approximation are generally unknown unless compared to an N-body potential simulation result such as KS-MD. Both KS-MD simulations and this comparison are time-consuming processes that are limited to the temperature regime in which the pseudopotentials necessary for KS-MD are valid [99, 100]. Moreover, comparisons between RPP-MD and KS-MD are limited in the literature, have not been carried out for a range of elements and temperatures, and are often validated with integrated quantities where individual particle dynamics have been averaged and results are subject to cancellation of errors.

We carry out KS-MD simulations for a range of elements, temperatures, and densities, allowing for a systematic comparison of three RPP models. While multiple RPP models can be selected [101–105], we choose to compare the widely used Yukawa potential, which accounts for screening by linearly perturbing around a uniform density in the long-wavelength (Thomas-Fermi) limit, a potential constructed from a neutral pseudo-atom (NPA) approach [106–109], and the optimal force-matched RPP that is constructed directly from KS-MD simulation data.

Each of the models we chose impacts our physics understanding and has clear computational consequences. For example, success of the Yukawa model reveals the insensitivity to choices in the pseudopotential and screening function and allows for the largest-scale simulations. Large improvements are expected from the NPA model, which makes many fewer assumptions with a modest cost of pre-computing and tabulating forces. The force-matched RPP requires KS-MD data, and is therefore the most expensive to produce, but it reveals the limitations of RPPs themselves, since they are by definition the optimal RPP.

Using multiple metrics of comparison between RPP-MD and KS-MD including the relative force error, ion-ion equilibrium radial distribution function $g(r)$, Einstein frequency, power spectrum, and the self-diffusion transport coefficient, the accuracy of each RPP model is analyzed. By simulating disparate elements, namely an alkali metal, multiple transition metals, a halogen, a non-metal, and a noble gas, we see that force-matched RPPs are valid for simulating dense plasmas at temperatures

above fractions of an eV and beyond. We find that for all cases except for low temperature carbon, force-matched RPPs accurately describe the results obtained from KS-MD to within a few percent. By contrast, the Yukawa model appears to systematically fail at describing results from KS-MD at low temperatures for the conditions studied here validating the need for alternate models such as force-matching and NPA approaches at these conditions.

In Sec. 2.2 we discuss how RPPs arise from second order perturbation theory and how their representation influences the shape of $g(r)$ due to particle crowding and/or attraction. Comparisons between RPPs and KS-MD are done in Sec. 2.3, where we begin by comparing interparticle forces illustrating how an increase in temperature indicates an increase in accuracy. In addition, the microfield distribution of forces, Einstein frequency, power spectrum, self-diffusion coefficient, and $g(r)$ are compared, highlighting how an approximately accurate $g(r)$ does not ensure similar accuracy in time correlation functions and transport coefficients. A description of how we accurately compute the self-diffusion coefficient and its uncertainty when finite-size errors are non-negligible is given in Sec. 2.3.3. This further emphasizes the need for RPPs, as we minimize finite-size errors in KS-MD simulations by making the necessary corrections as shown in Sec. 2.3.5. We conclude by comparing fully converged (in particle number and simulation time) self-diffusion coefficients to an analytic transport theory; benchmarking its accuracy and providing an effective interaction correction to extend the range of applicability.

2.2 Models for the Interaction Potential

The theoretical foundations of the models we will compare are described in this section; their connections are shown in Fig. 2.2. We compare three classes of interactions that are based on the ionic N-body energy, shown in the top box, pair interactions that are pre-computed and are analytic or tabulated, shown in the lower-left box, and optimal pair interactions extracted from the N-body results, shown in the lower-right box. By comparing these three approaches we aim to answer several specific questions. First, given the nuclear charge Z, ionic number density n_i, and temperature T, what ranges in $\{Z, n_i, T\}$ space are the fast, pre-computed interactions valid and therefore allow for large-scale heterogeneous simulations? Second, how accurate is the “optimal"

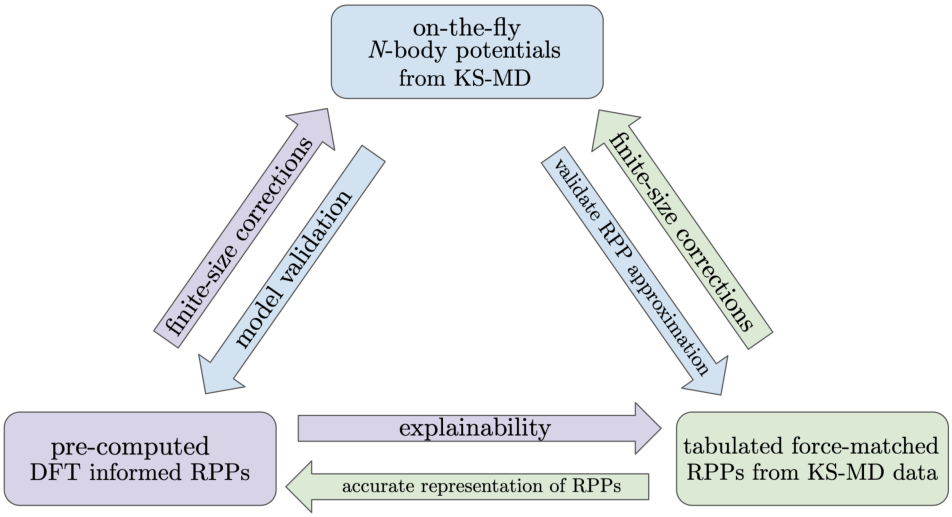

Figure 2.2: Connections between different portions of this work. N-body potentials, shown in the top box, are used to validate pair potential models (lower left) and produce optimal tabulated potentials (lower right). Both pre-computed RPPs and tabulated force-matched RPPs provide finite-size corrections to KS-MD data; assuming they accurately reproduce the Kohn-Sham potential energy surface. The tabulated force-matched RPPs highlight the appropriate RRP representation (e.g., oscillations). The pre-computed RPPs give physical intuition to the representation determined by the KS-MD data.

pair interaction, and what do its limitations reveal about the need for three-body interactions (and perhaps beyond)? Can these interactions be used to test and correct for finite-size errors? Third, can the optimal interactions guide the development of pre-computed interactions? To simplify the discussion we will consider single species matter with a range of Z, each species at its normal solid ionic mass density ρ_i, or in some cases half of that, and in thermodynamic equilibrium at temperature T. While we do not consider mixtures in here, the framework is general and can be straightforwardly applied to them.

Assuming the Born-Oppenheimer approximation holds, we define a potential energy surface for the ions as

$$U_{tot} = U_N(\mathbf{r}_1, \mathbf{r}_2, \ldots, \mathbf{r}_N). \tag{2.1}$$

Physically, the ionic potential energy surface is determined by the electronic charge distribution arising from ions at a particular set of coordinates; in general, Eq. (2.1) does not simplify into sums over pairwise terms. There are two major approaches to obtaining Eq. (2.1) in practice. The

approach represented by the top box in Fig. 2.2 computes the electronic charge distribution for each ionic distribution. This is achieved computationally in Kohn-Sham approaches by reducing the electron many-body problem to a single-electron problem in which the Kohn-Sham electron moves in the external field of N-ionic centers. The dominant computational cost comes from solving an $N_o \times N_o$ set of eigenvalue equations, where N_o is the number of single-particle orbitals. Even though the electron many-body problem has been simplified to a one-body problem, matrix diagonalization incurs a cost of $O(N_o^3)$, and at high temperatures the smearing of the Fermi-Dirac distribution requires an increasing number of orbitals leading to significant increases in computational cost. The complexity of the electron charge distribution also demands the use of an advanced "Jacob's ladder" of exchange-correlation functions to address the electron many body problem.

This approach yields an intrinsically ionic N-body potential energy surface; the electronic density is computed using a description appropriate to the choice of $\{Z, n_i, T\}$. The second approach to calculating the potential energy surface is to use a cluster-type expansion, which takes the form

$$U_{tot} = \sum_{i}^{N} U_1(\mathbf{r}_i) + \sum_{i,j}^{N} U_2(\mathbf{r}_i, \mathbf{r}_j) + \sum_{i,j,k}^{N} U_3(\mathbf{r}_i, \mathbf{r}_j, \mathbf{r}_k) + \cdots . \tag{2.2}$$

When this expansion can be truncated with only a few terms, interactions can be pre-computed, and fast neighbor algorithms allow for a very rapid evaluation of forces, typically many orders of magnitude faster than through use of Eq. (2.1). This allows, for example, for simulations with trillions of particles [110–112]. However, the disadvantages are that the computational cost increases rapidly as more terms are included, and the accuracy of a specific truncation and choice of functional forms with that truncation are not usually known; part of our goal is to assess how accurate the potential energy surface in Eq. (2.1) can be represented by the first two terms of Eq. (2.2).

2.2.1 N-body Interaction Potentials

The most accurate forces are obtained from the gradient of the total energy in Eq. (2.1), which requires the entire ionic configuration. Although machine learning approaches are enabling the ability to pre-learn that relationship [113–115], it remains more common to compute the forces for each ionic configuration during the simulation ("on-the-fly"). We obtain the electronic number density for each ionic configuration in the Kohn-Sham-Mermin formulation of the density

$$n_e(\mathbf{r}) = \sum_i f_i(T)|\phi_i(\mathbf{r})|^2, \tag{2.3}$$

where T is the temperature of the system in energy units, the Fermi occupations are given by $f_i(T) = \left[1 + e^{\beta(E_i-\mu)}\right]^{-1}$, and the Kohn-Sham-Mermin orbitals $\phi_i(\mathbf{r})$ satisfy

$$\left[-\frac{1}{2}\nabla^2 + v_{eff}(\mathbf{r})\right]\phi_i(\mathbf{r}) = \epsilon_i\phi_i(\mathbf{r}), \tag{2.4}$$

where

$$v_{eff}(\mathbf{r}) = V_{ext}(\mathbf{r}) + \int d\mathbf{r}' \left[\frac{n_e(\mathbf{r}')}{|\mathbf{r}-\mathbf{r}'|} + \frac{\delta E_{xc}[n_e]}{\delta n_e(\mathbf{r})}\right], \tag{2.5}$$

is a sum of the external (N ion-electron), Hartree, and exchange-correlation energies. Our KS-MD simulations were done using the Vienna Ab-initio Simulation Package (VASP) [116–119]. The finite temperature electronic structure was treated with the Mermin free-energy functional, and we used the Perdew–Burke-Ernzerhof functional for the exchange correlation energy [120]. To improve computational efficiency, we eliminated the chemically inactive core electrons with the projector augmented-wave [121] pseudopotential. Due to the anticipated high temperatures and small interionic separations, we used the smallest core "GW" pseudopotentials available in VASP. Here, "GW" denotes that the "GW approximation" has been made; the details of the approximation can be found in Ref. [122]. Sixty-four atoms ($N = 64$) were used in these simulations, with an energy cutoff of 800 eV and at the Baldereschi mean-value k-point [123] for all temperatures ranging from $T = 0.5$ to 15 eV. A simulation time step of 0.1 fs was used, and the total simulation lengths for each case vary and are on the order of a few picoseconds. All KS-MD simulations were first equilibrated in the NVT ensemble and then carried out in the NVE ensemble where data was collected.

2.2.2 Force Matching

After the Kohn-Sham potential energy surface has been computed, we aim to construct a compact representation of Eq. (2.1) with Eq. (2.2). By assuming a parameterized functional form for Eq. (2.2), the force-matching procedure [124–129] was used to generate the optimal RPP model based on the KS-MD force data. From each KS-MD simulation, a dataset of $K \equiv 3NM$ forces (3 force components, N atoms, and M atomic configurations) is obtained. Atomic simulation data at nearby time points is highly correlated; thus, a stride between atomic configurations was used to generate 100-200 independent configurations.

With each KS-MD dataset, we determine the optimal RPP for that system by minimizing the loss function

$$L(\zeta) = \sum_{k=1}^{K} w_k [F_k(\zeta) - F_k^0]^2. \tag{2.6}$$

Here, ζ is a set of optimizable parameters, $F_k(\zeta)$ is the k-th force for the parameterized model with parameters ζ, F_k^0 is the k-th force from KS-MD reference dataset, and w_k is a weight factor. The weight factor $w_k = 1/(F_k^0 + \varepsilon)^2$ ensures that both large, and small forces contribute equally to Eq. (2.6). The parameter ε should be varied for each temperature and element but in most cases here, $\varepsilon \approx 1$.

The choice of parameterization can either have a pre-computed functional form, such as Eq. (2.8), or be determined completely from the data as is the case for a tabulated potential [130] with spline interpolation – the choice here. For each system, we begin by sampling a Thomas-Fermi Yukawa (see Sec. 2.2.3) RPP at 15 locations in r and use that as the initial condition for the force-matching procedure. The Thomas-Fermi Yukawa RPP is sampled such that $r_{min} < r < 8$ Å where r_{min} is the minimum ionic separation in the KS-MD dataset. To ensure that the core repulsion and/or attractive oscillation regions are sampled sufficiently, 10 points are placed in the region where $r_{min} < r < 4$ Å, leaving the 5 remaining points to be placed where $r > 4$ Å. To test for convergence of the optimal force-matched RPP, two optimization methods were used (specifically simulated annealing, and differential evolution.) By choosing a tabulated potential form for the RPP, the explicit form of the model is entirely determined from the KS-MD force data and not

limited to a fixed functional form.

While the force-matched RPP yields the best RPP to reproduce the KS-MD force data, it could be the case 3-body and higher interactions are non-negligible. To check this, we selectively employ the Spectral Neighborhood Analysis Potential (SNAP) which constructs a potential energy surface from a set of 4-body descriptors (bispectrum components),where each descriptor is independently weighted, and these weights are determined by regressing against KS-MD data of energies and forces. A descriptor captures the strength of density correlations between neighboring atoms and the central atom within a given cutoff distance, details can be found in Refs. [131, 132]. The parameterization of the SNAP uses descriptors of the local atomic environment capturing up to 4-body interactions when represented in the form of Eq. (2.2), so lower errors associated with SNAP compared to an optimal RPP are entirely due to 3- and 4-body interactions. While higher bodied inter-atomic potentials exist in the literature [133], it can be expected there are diminishing accuracy returns with higher interaction moments, thus SNAP offers a leading order check on the RPP compared here.

SNAP potentials utilizing 56 bispectrum component descriptors were trained on 10% of the KS-MD dataset, and additionally tested against an additional 10% to ensure regression errors were properly minimized and avoided over-fitting of the KS-MD data.

2.2.3 Radial Pair Potentials

As the computational cost of using on-the-fly N-body interactions is often prohibitive, the least expensive approach utilizes pre-computed RPPs ignoring most of the terms in Eq. (2.2). Many functional forms for the RPP have been proposed for application to warm dense matter often using the second-order perturbation-theory interaction energy

$$u(k) = \langle Z \rangle^2 u_C(k) + |u_{ei}(k)|^2 \, \chi(k), \tag{2.7}$$

which is the standard Fourier-space result [134] written in terms of the mean ionization state $\langle Z \rangle$, the bare Coulomb potential $u_C(k) = 4\pi e^2/k^2$, the electron-ion pseudopotential $u_{ei}(k)$ and the susceptibility $\chi(k)$.

In practice, pair interactions are constructed using nearly the same steps as for the N-body interactions, with the primary difference being that each ion is replaced with a single "average atom" (AA), which is an all-electron, non-linear, finite-temperature density functional theory calculation [12]; such calculations can also be relativistic [135,136]. From the AA, a pseudopotential $u_{ei}(k)$ and an accurate free/valence electron response function $\chi(k)$ are constructed and Eq. (2.7) is formed. This approach has three strengths: (1) typical AA models are not limited to low temperatures, (2) the interaction Eq. (2.7) can be pre-computed for use in MD, and (3) pair interactions with a fast nearest neighbor algorithm are very computationally efficient. As we alluded to above, the accuracy loss attendant to these strengths is what we wish to determine. The AA itself is aware of the ionic number density n_i, which sets the ion-sphere radius $a_i = (3/4\pi n_i)^{1/3}$, and includes the fact that there is only one ion in the ion sphere, which implies a $g(r)$; this indirect inclusion of higher-order terms in Eq. (2.2) is true for all AA-based interactions.

Among the simplest variants of Eq. (2.7), one approximates the pseudopotential as $u_{ei}(k) \approx -4\pi\langle Z\rangle e^2/k^2$, where the mean ionization state $\langle Z\rangle$ results from a AA calculation [12], and $\chi(k)$ in its long-wavelength (Thomas-Fermi) limit $\chi_{TF}(k)$; this is known as the "Yukawa" interaction [104, 137]. Here, we employ a Yukawa interaction with inputs from a Thomas-Fermi AA [88], which we will refer to as "TFY." This procedure yields an analytic potential in real space of the form

$$u^{TFY}(r) = \frac{\langle Z\rangle^2 e^2}{r}\exp\left(-r/\lambda_{TF}\right), \tag{2.8}$$

where the electron screening is approximated by the Thomas-Fermi screening length

$$\lambda_{TF}^{-2} = \frac{\sqrt{8T}}{\pi}\mathcal{F}_{-1/2}(\beta\mu_e), \tag{2.9}$$

where $\mathcal{F}_{-1/2}$ is the Fermi-Dirac integral of order $-1/2$, $\beta = 1/T$, and μ_e is the electron chemical potential. Padé fits of Fermi-Dirac integrals and their inverses are carried out in [138, 139]. An approximation to these fits [140] yields

$$\lambda_{TF}^{-2} \approx \frac{4\pi n_e e^2}{\sqrt{T^2 + (\frac{2}{3}E_F)^2}}, \tag{2.10}$$

where the Fermi energy $E_F = \hbar^2(3\pi^2 n_e)^{2/3}/2m_e$. Note that the TFY interaction is monotonically decreasing (purely repulsive). Computationally, the TFY model is highly desirable because of its radial, pair, analytic form with an exponentially-damped short range. Its weaknesses are the relatively approximate treatments of $u_{ei}(k)$ and $\chi(k)$. The TFY model can be extended by including the gradient corrections to $\chi_{TF}(k)$, but otherwise retaining the other approximations. This improvement yields the Stanton-Murillo potential [104]; the gradient correction to $\chi_{TF}(k)$ introduces oscillations in the potential in some plasma regimes that are absent in the monotonic TFY model. Moreover, gradient corrections add improvements to the cusp at the origin and the large-r asymptotic behavior. Here, however, we will only employ the simpler TFY model.

A great deal of accuracy can be gained by abandoning analytic inputs to Eq. (2.7). In this case, self-consistent numerical calculations of each of the terms can be carried out, still allowing for pre-computed interactions; there is essentially no computational overhead for tabulated interactions [130]. Here, we employ a NPA model that yields both the mean ionization state and its pseudopotential using a Kohn-Sham-Mermin approach, as described above, but with a finite-temperature exchange-correlation potential; the susceptibility is determined by the Lindhard function with local field corrections [107]. Note that the electron-ion pseudopotential $u_{ei}(k)$ introduces additional oscillations on length scales different from $\chi(k)$, although the Friedel oscillations in $\chi(k)$ contribute much more to the pair interaction. Note that the name “NPA" has been used by many authors to several different average-atom models, and many of them involve approximations that limit those models to higher temperatures, e.g., $T > E_F$; however, here we use the one-center density functional theory model developed by Dharma-wardana and Perrot as this model has been tested at high temperatures as well as at very low temperatures, and found to agree closely with more detailed N-center density functional theory simulations and path-integral quantum calculations where available.

It is worth comparing predictions based on Eq. (2.7) with other forms suggested previously. A popular RPP for warm dense matter studies is the short-range repulsion interaction, which adds a long-range, power-law correction to the TFY model of the form A/r^4 [32, 103, 141–145]; for $A > 0$,

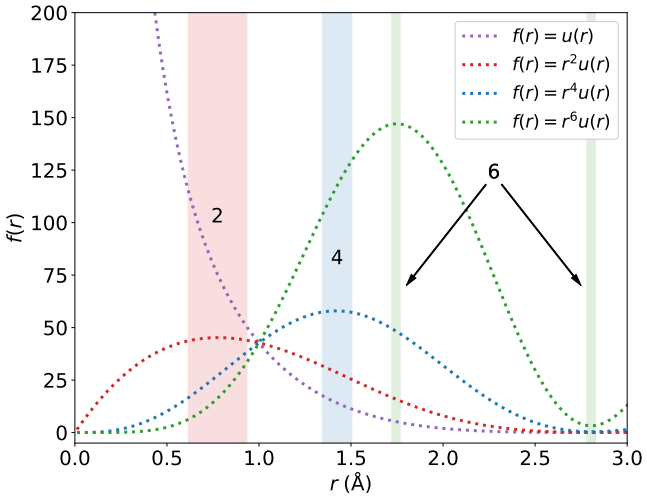

Figure 2.3: NPA RPP for Al at 2.7 g/cm^3 and $T = 1$ eV. Various power laws are valid at different values of r. The appropriate power law for a given range of r is shaded and denoted with a "2," "4," or "6."

this is also a monotonic interaction, with the goal of increasing the strength of the TFY model, which underestimates the peak height of $g(r)$. In Fig. 2.3, we examine this ansatz by computing a NPA interaction for Al at solid density and $T = 1$ eV. To find the "best" power law, we multiply the NPA interaction by various powers r^a to find regions where the interaction is flat; a flat region with $a = 4$ would recover the short-range repulsion interaction. It is clear that the A/r^4 is only valid over a very small range of r values; importantly, the NPA interaction shows that the exponent a increases as r becomes large, which is a true short-ranged interaction - the empirical correction the short-range repulsion model adds greatly overestimates the strength of the interaction at large interparticle separations [106]. Worse, the short-range repulsion model potentially gets an accurate answer for the wrong reason, as we explore in Fig. 2.4.

Because the form of Eq. (2.7) generally has oscillations, the enhanced peak height of $g(r)$ from the NPA model over the TFY model occurs for two, independent reasons. Attractive regions of the interaction, as shown in the top panel of Fig. 2.4, can produce very strong peaks in $g(r)$. Conversely, stronger overall repulsion at intermediate r can lead to a similar $g(r)$ behavior, as shown in the bottom panel of Fig. 2.4, but with rapid decay of the interaction at larger r. The functional form of Eq. (2.7) naturally contains both the "crowding" and "attraction" behaviors as special cases. Fig. 2.5

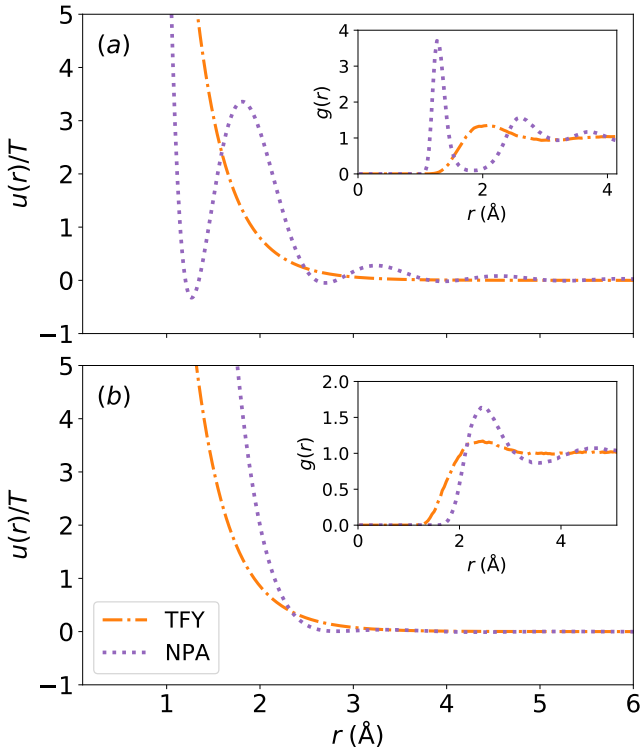

Figure 2.4: Comparison of TFY and NPA RPPs for C and Al with corresponding $g(r)$ computed from MD simulation: (a) C at 2.267 g/cm^3 and $T = 0.5$ eV. The increase in magnitude of the first $g(r)$ peak results, in this case, from particle attraction. (b) Al at 2.7 g/cm^3 and $T = 1$ eV. In this case, it is particle crowding increases the magnitude of the first $g(r)$ peak.

shows a comparison of the RPPs for C, Al, V, and Au at $T = 0.5$ and 5 eV. The TFY model is purely monotonic whereas the force-matched and NPA RPPs have attractive and repulsive regions in their oscillations. Below, we will explore the consequences of these features of the interaction on ionic transport.

Once the RPPs have been constructed, MD simulations were carried out using in the Large-scale Atomic/Molecular Massively Parallel Simulator (LAMMPS) [146]. For the tabulated RPPs (force-matched and NPA) a linear interpolation was needed to determine the force value between tabulation points. To make a direct comparison between the RPP-MD and KS-MD results, all simulations were carried out in a 3 dimensional periodic box with 64 atoms and a time step of 0.1 fs. The length of each simulation is identical to the corresponding simulation performed with KS-MD. Keeping these conditions identical avoids the unintentional reduction in statistical errors

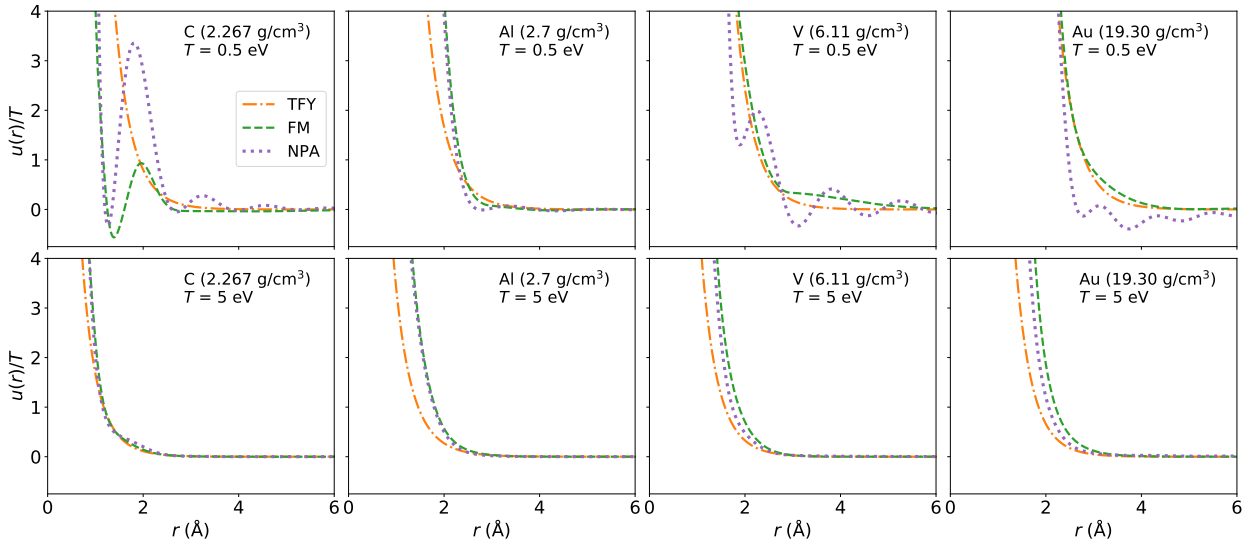

Figure 2.5: The RPP models normalized by temperature versus distance for C, Al, V, and Au. Top row, $T = 0.5$ eV: the representation of the RPP is element dependent with strong agreement for aluminum. Bottom row, $T = 5$ eV: The agreement between models improves significantly. The differences in the representation can be connected back to Eq. (2.7) where the treatment of the mean ionization, electron-ion pseudopotential, and susceptibility define the RPP.

between KS-MD and RPP-MD. All simulations were first equilibrated in the NVT ensemble so that the average temperature for each simulation during the data collection phase is within 1% of the reported temperature in Table 2.1. The data collection phase was carried out in the NVE ensemble. In Sec. 2.3.5, a finite-size effect study was done for the cases of C at 2.267 g/cm^3 and V at 6.11 g/cm^3 where the total simulation length was increased by 10 times and the number of atoms N increases from 64 to 256, 3375, and 8000.

2.3 Numerical Results

2.3.1 Force Error Analysis

One metric for establishing the accuracy of approximations to the Kohn-Sham potential energy surface is to compute relative force errors between Kohn-Sham force data and a parameterized model (RPP or many-body potential) for M particle coordinate configurations. For this, we compute the mean-absolute force error

$$MAE = \frac{1}{3MN} \sum_{\alpha,i,m} |F^{(PAR)}_{\alpha,i,m} - F^{(KS-MD)}_{\alpha,i,m}|, \tag{2.11}$$

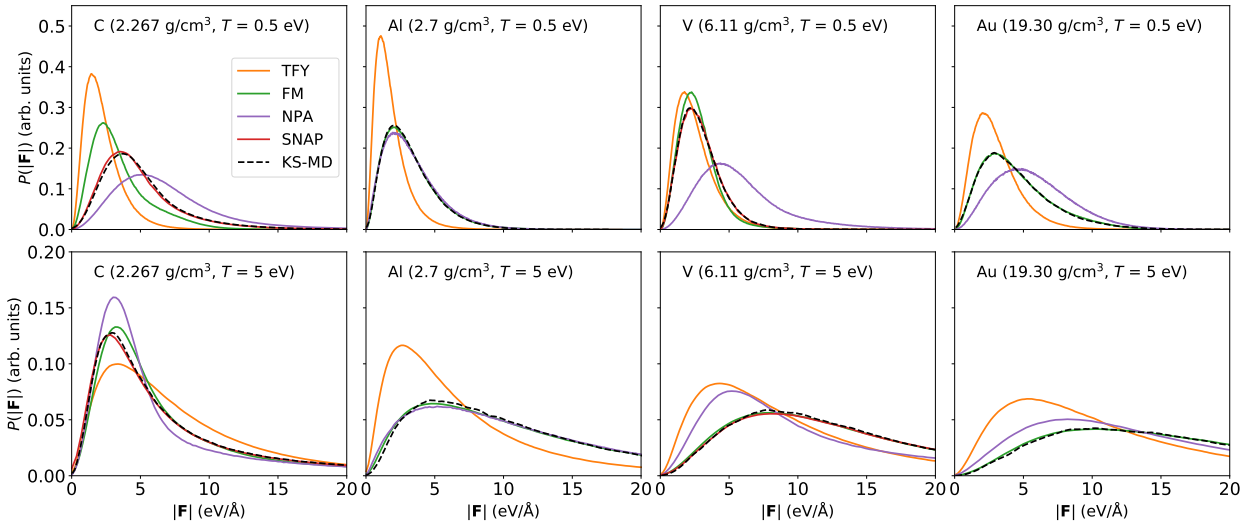

Figure 2.6: Microfield distributions for C, Al, V, and Au. The observed trends of the microfields agree with the trends of the self-diffusion coefficients in Table 2.1. In general, when the microfields are similar to that of KS-MD, the agreement between the self-diffusion coefficient increases. To assess the importance of 3-body or higher interactions, SNAP results are reported for C and V at both $T = 0.5$ and 5 eV.

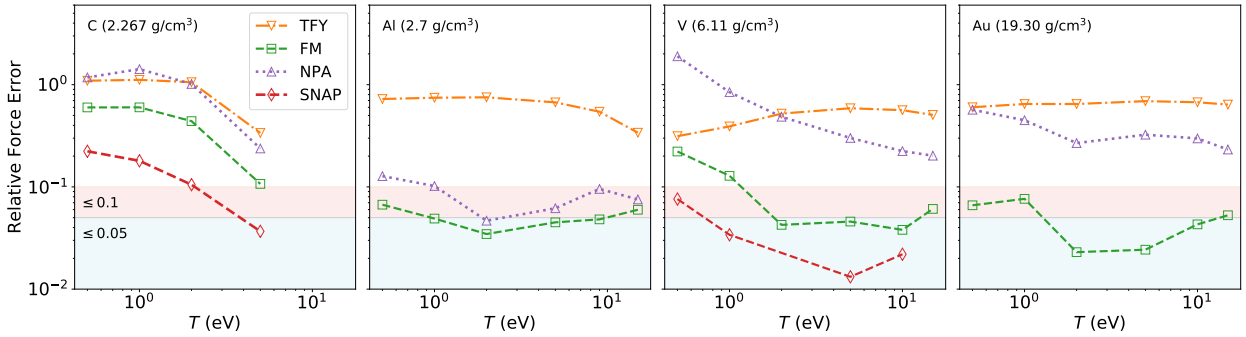

Figure 2.7: Relative force error versus temperature computed from Eq. (2.13) for C, Al, V, and Au. The red shaded region indicates force accuracy of ≤ 0.1 and the blue shaded region indicates force accuracy of ≤ 0.05. SNAP and force-matched RPP yields the lowest relative force error and decreases or remains constant as temperature increases. This indicates an increases in accuracy of the RPP models as temperature increases.

where $F^{(PAR)}_{\alpha,i,m}$ and $F^{(KS-MD)}_{\alpha,i,m}$ are the α-th force components (x, y, or z) on the i-th atom in particle coordinate configuration number m for the parameterized model and the KS-MD force data respectively.

Note that a direct comparison of the mean absolute error between different elements, temperatures, and densities cannot be done as the distributions of forces associated with systems of different elements at different thermodynamic conditions are in general quite different. This can be observed in Fig. 2.6 where a microfield distribution of the force magnitudes is shown. In all cases but C at 2.267 g/cm^3 and $T = 5$ eV, the TFY model peaks at a smaller field value than KS-MD. In contrast, for C, V, and Au at $T = 0.5$ eV the NPA RPP peaks at a higher field value than KS-MD. These trends can be connected back to Eq. (2.7) where the choice of $\langle Z \rangle$, $u_{ei}(k)$, and $\chi(k)$ all contribute to the construction of a RPP model and hence the force magnitudes. More work needs to be done to determine how each term influences the RPP model, the predicted forces, and observables.

As the microfield force distributions vary for different elements and temperatures, the mean absolute error will also vary. To this end, we seek a scale factor for Eq. (2.11) to normalize the results across the different elements, temperatures, and densities studied here. Such a scale factor is the “mean absolute force" defined as

$$MAF = \frac{1}{3MN} \sum_{\alpha,i,m} |F^{(KS-MD)}_{\alpha,i,m}|. \tag{2.12}$$

Using Eq. (2.11) and Eq. (2.12), we define the relative force error as

$$RFE = \frac{\sum_{i,\alpha,m} |F^{(PAR)}_{\alpha,i,m} - F^{(KS-MD)}_{\alpha,i,m}|}{\sum_{\alpha,i,m} |F^{(KS-MD)}_{\alpha,i,m}|}. \tag{2.13}$$

The metric, Eq. (2.13), has the following desirable property: if the mean absolute error changes with density or temperature in the same way as the underlying force distribution, the relative force error will maintain roughly the same value. Therefore, as we change the thermodynamic conditions for a given element, Eq. (2.13) provides a temperature independent metric as measured with respect to a KS-MD force data “baseline." Intuitively, when Eq. (2.13) evaluates to 1, the mean absolute

error is the same order of magnitude as the mean absolute force and when Eq. (2.13) is zero, the parameterized model is exactly reproducing the per-component KS-MD force data.

Fig. 2.7 displays Eq. (2.13) as a function of temperature for C, Al, V, and Au where general trends can be observed. One trend is that for most RPPs, the relative force error decrease towards higher temperatures, which confirms an intuition long held for the validity of the NPA and TFY models. However, for all systems pictured except C, force matching drastically reduces the relative force error compared to the NPA and TFY results. Specifically, the force-matched RPPs routinely achieve a relative force error of roughly 0.05 above $T = 5$ eV. Except for the case of the NPA RPP for Al, the NPA and TFY RPPs maintain an error of around 0.2 across the entire the temperature range.

The second major observation from Fig. 2.7 is that while force-matched RPPs drastically lower the observed relative force errors across temperatures compared against other RPPs, we immediately see where a RPP approximation is likely invalid. For example, the relative force error for C using the force-matched RPP is uncharacteristically high (roughly 0.6) until $T = 5$ eV. A similar situation appears for the case of V at $T = 0.5$ eV where the relative force error for the force-matched RPP is roughly 0.25. We can demonstrate explicitly that these discrepancies come from the neglect of 3-body and higher interactions by showing relative force errors using a SNAP model. For C, the relative force error drops from roughly 0.6 using a force-matched RPP to 0.2 using a SNAP model at $T = 0.5$ eV. Likewise for V, the relative force error drops from roughly 0.25 using a force-matched RPP to 0.07 using a SNAP model at the same temperature.

Ultimately, it is not the component-wise force or the interaction potential we care about generating, but rather observables such as $g(r)$ and the self-diffusion coefficient. To address this connection, we examine correlations between the force error and the self-diffusion coefficient error, as shown in Fig. 2.8. While there is a general trend with increasing errors in both quantities (shown with a linear fit), there are also some clear outliers. For the case of C at 2.267 g/cm^3 and $T = 0.5$ eV, we find that the NPA and TFY RPPs produce a self-diffusion coefficient that differs from the KS-MD result by many factors. However, C under these conditions exists in several charge states

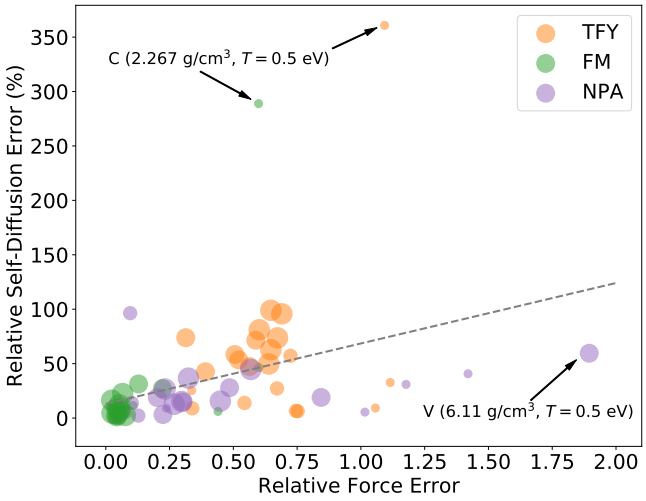

Figure 2.8: Relative (to KS-MD) self-diffusion error versus the relative force error for C, Al, V, and Au. The size of each point corresponds to the atomic number. The grey dashed line is a linear fit to the points showing a positive correlation between self-diffusion error and force error.

with transient bonding; only the NPA accounts for this. This case is marked with arrows in Fig. 2.8. Conversely, for V at $T = 1$ eV, the relative self-diffusion percent error is low, yet the relative force error is high. The imperfect mapping of relative self-diffusion error versus relative force error suggests that physics beyond a RPP is needed, possibly at least a three-body angular dependence, but further work is needed.

2.3.2 Radial Distribution Function and The Einstein Frequency

The radial distribution function [125] is a measure of spatial correlations normalized by the ideal gas. It has been shown that in general, there always exists a RPP that can reproduce $g(r)$ from a N-body simulation [147], and the force-matching procedure provides an avenue for obtaining this RPP. Fig. 2.9 compares $g(r)$ computed from MD simulations for all RPP models for C, Al, V, and Au. Each row corresponds to a different temperature, and clear trends can be observed, such as the improvement in agreement between models as the temperature increases. We note that the force-matched RPP always obtains the correct $g(r)$, and the NPA model generally predicts the location of the first peak but sometimes over-predicts the magnitude or misses the location of the first peak altogether as observed in the case of V at 6.11 g/cm^3 for $T = 0.5$ eV. The TFY model always underestimates the magnitude of the first peak height, and the location is usually shifted.

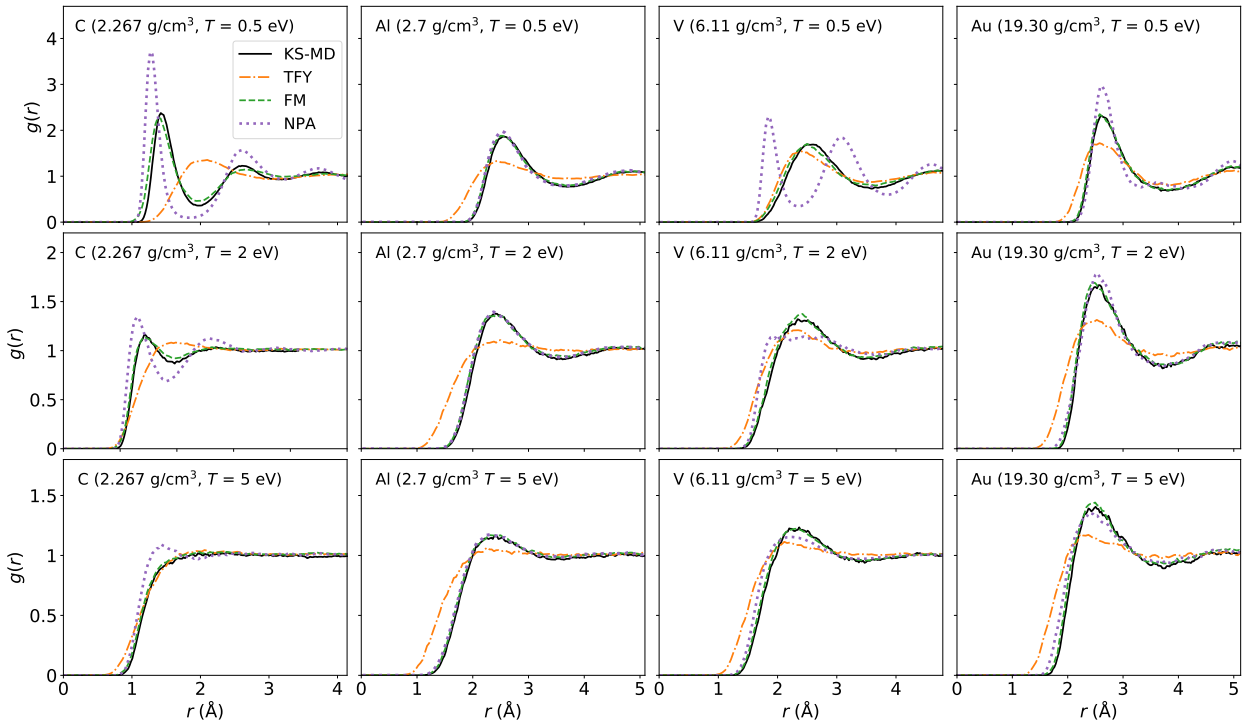

Figure 2.9: The radial distribution functions for C, Al, V, and Au are shown. The top row corresponds to $T = 0.5$ eV, the middle row $T = 2$ eV, and the bottom row $T = 5$ eV. The force-matched RPP always reproduces the $g(r)$ obtained from KS-MD.

Insight into the connection between the $g(r)$ peak height and the the self-diffusion coefficient can be obtained from the normalized velocity autocorrelation function [148]

$$Z(t) = \frac{\langle \mathbf{v}(t) \cdot \mathbf{v}(0) \rangle}{\langle \mathbf{v}(0) \cdot \mathbf{v}(0) \rangle}, \tag{2.14}$$

where $\mathbf{v}(t)$ is the velocity of a particle at time t and $\langle \cdot \rangle$ is an ensemble average over particles *and* time. A short time expansion of Eq. (2.14) yields

$$Z(t) = 1 - \Omega_0^2 \frac{t^2}{2!} + \cdots, \tag{2.15}$$

where Ω_0 is the Einstein frequency

$$\Omega_0^2 = \frac{4\pi\rho_i}{3m_i} \int_0^\infty dr\, r^2 g(r) \nabla^2 u(r), \tag{2.16}$$

where m_i is the ion mass in grams. The Einstein frequency gives insight into the relationship between $u(r)$ and $g(r)$, highlighting how different regions are weighted more or less depending

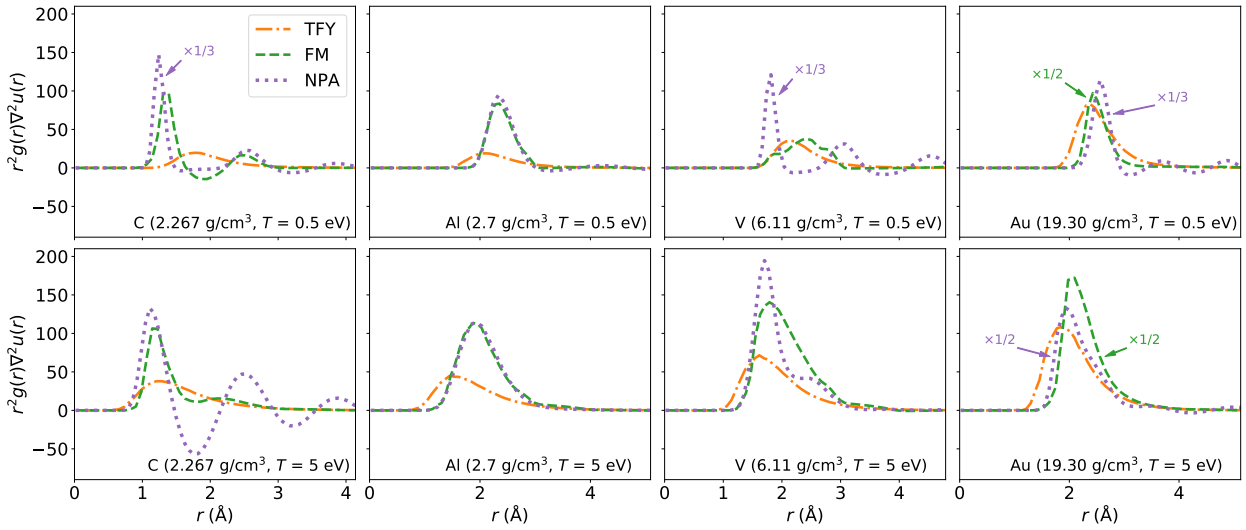

Figure 2.10: The integrand of the Einstein frequency Eq. (2.16). All integrands are consistent with values reported in Table 2.1 as the self-diffusion coefficient decrease as the integral of the Einstein frequency increases. This allows for a "by eye" comparison of the self-diffusion coefficient from different RPP models.

on the curvature of $u(r)$. In Fig. 2.10, the integrand of Eq. (2.16) is shown. For the TFY model, the integrand is always smaller than those predicted by force-matched and NPA RPPs. The area under each curve in Fig. 2.10 can be directly connected to the self-diffusion coefficient through the Green-Kubo relation (in 3 dimensions)

$$D = \frac{T}{m} \int_0^\infty dt\, Z(t), \tag{2.17}$$

by substituting, Eq. (2.15) into Eq. (2.17). Doing so shows that the TFY model will always predict a larger self-diffusion coefficient than the force-matched or NPA model as the area under these curves is larger. This is confirmed later when the self-diffusion coefficients are explicitly calculated as discussed in Sec. 2.3.3.

2.3.3 Self Diffusion

Another approach to compute the self-diffusion coefficient is via the the slope of the mean-squared displacement from the Einstein relation

$$D = \lim_{t\to\infty} \frac{\langle |\mathbf{r}(t) - \mathbf{r}(0)|^2 \rangle}{6t}. \tag{2.18}$$

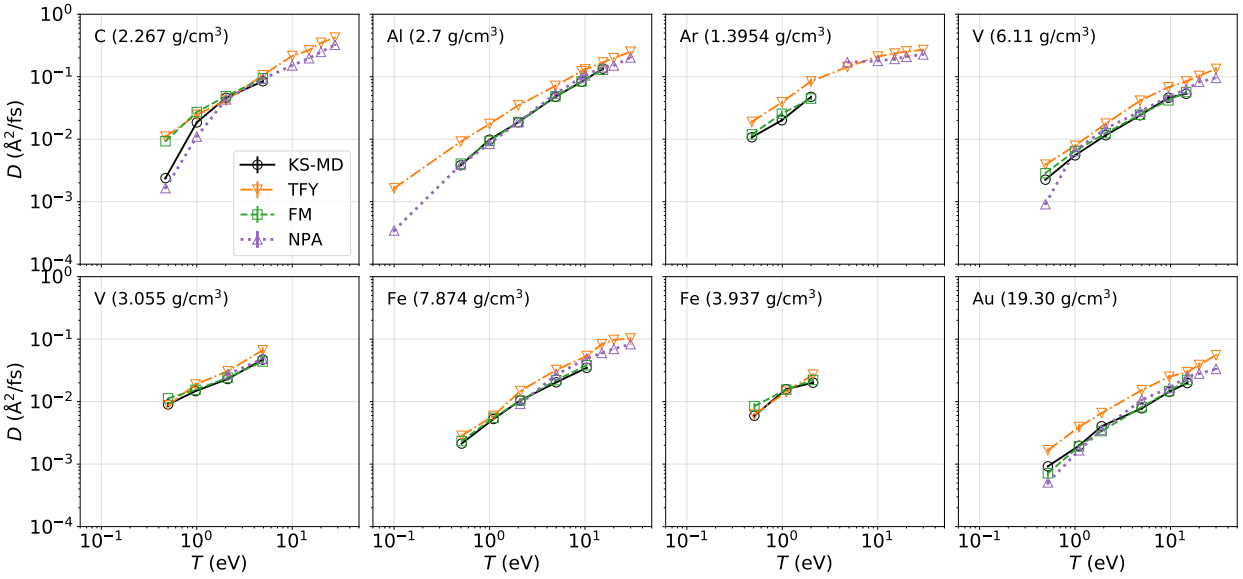

Figure 2.11: Self-diffusion coefficients for different elements and densities versus temperature. The numerical values are reported in Table 2.1. For all cases all models predict values that have roughly the same order of magnitude. The only case where the force-matched RPP fails to reproduce the KS-MD self-diffusion coefficient is for C at 2.267 g/cm^3 and $T = 0.5$ eV. The TFY RPP model generally predicts larger self-diffusion coefficients, which is consistent with the Einstein frequency in Fig. 2.10. Note that the NPA RPP model, in contrast, agrees with results obtained from the force-matched RPP and KS-MD models very well.

Both Eqs. (2.17) and (2.18) can be used to compute the self-diffusion coefficient and have been shown to be equivalent [149]. Here, the self-diffusion coefficient has been calculated from a linear fit to the mean-squared displacement, $\langle|\mathbf{r}(t) - \mathbf{r}(0)|^2\rangle$.

Due to finite-size effects, two problems arise when computing the slope and uncertainty of the linear fit. First, we must ensure that the linear fit is carried out in the late-time linear regime of the mean-squared displacement. Second, we dismiss statistically unconverged late-time behavior of the mean-squared displacement where the ensemble average contains sparse amounts of data. To remedy both of these concerns, we uniformly randomly sub-sample the mean-squared displacement 100 times with 10 points along each sub-sample. Next, a linear fit is determined for each sub-sample, and the standard deviation of the sub-sample slopes is computed. Once the standard deviation is known, a cutoff time is calculated by determining the point in time that the standard deviation of the sub-sample fits is less than half of the standard deviation computed from *sub-sample* fits to the

entire mean-squared displacement. The simulation data for the mean-squared displacement after the cutoff time is discarded, and the fitting procedure described above is repeated. The average, and standard deviation of the fits to the reduced dataset yield self-diffusion coefficient and the uncertainty in the fit respectively and are reported in Table 2.1.

Given the values for the self-diffusion coefficient reported in Table 2.1, we can answer the following question: at what temperature are computationally inexpensive models adequate? To do this, we compute the relative self-diffusion coefficients D_{NPA}/D_{KS-MD} and D_{TFY}/D_{NPA}. For example, the top panel in Fig. 2.12 suggests that NPA models may be accurate from $T = 1$ eV and above if the target error tolerance is 50% of the self-diffusion coefficient computed from KS-MD. Similarly in the bottom figure, the TFY model is generally accurate to within 50% of the NPA model from $T = 5$ eV and beyond.

Two important observations can be made from the trends in Fig. 2.12. The top panel illustrates temperatures at which an N-body potential is needed and when NPA is adequate. The bottom panel shows a comparison with TFY, which has the simplest $u_{ei}(k)$ and $\chi(k)$, and we see temperatures at which TFY becomes comparable to NPA, suggesting when we can exploit simpler approximations for those inputs.

2.3.4 Power Spectrum

The self-diffusion coefficient is useful for comparing and quantifying the accuracy of RPP models and transport theories, but in order to assess how accurately the particle dynamics are reproduced, we look at the power spectrum of the velocity autocorrelation function $Z(t)$

$$\tilde{Z}(\nu) = \int_0^\infty dt \cos(2\pi\nu t)\, Z(t). \tag{2.19}$$

In Fig. 2.13, we compare $\tilde{Z}(\nu)$ calculated using TFY, force-matched, and NPA RPPs against results obtained from KS-MD. We find that with the exception of low temperature C and V, force-matched RPPs agree with the KS-MD results across the entire frequency range. This, combined with the low relative force errors and accurate reproduction of static properties discussed previously, indicates that the the force-matched RPPs accurately approximate the Kohn-Sham potential energy surface.

Element	ρ_i (g/cm^3)	T (eV)	D_{KS-MD}	D_{FM}	D_{TFY}	D_{NPA}
Li	0.513	0.054	1.4 ± 0.13	1.27 ± 0.054	5.6 ± 0.39	1.26 ± 0.077
C	2.267	0.47	2.4 ± 0.12	9.3 ± 0.20	11.0 ± 0.60	1.69 ± 0.060
		1.0	18.6 ± 0.7	27.2 ± 0.77	25 ± 1.64	11.0 ± 0.45
		2.0	46 ± 1.68	49 ± 1.0	42 ± 3.70	43 ± 3.86
		4.9	85 ± 5	94 ± 5.82	106 ± 5.37	92 ± 3.45
		10.0	–	–	215 ± 4.49	151 ± 4.63
		15	–	–	266 ± 3.46	198 ± 5.10
		20	–	–	349 ± 7.60	249 ± 2.35
		28	–	–	423 ± 13.28	324 ± 12.17
Al	2.7	0.1	–	–	1.6 ± 0.14	0.35 ± 0.0217
		0.50	3.8 ± 0.16	4.1 ± 0.13	9.17 ± 0.099	3.9 ± 0.11
		1.1	9.8 ± 0.30	9.4 ± 0.11	17.5 ± 0.70	8.5 ± 0.44
		2.0	18.7 ± 0.50	18.8 ± 0.68	34.8 ± 0.52	18.8 ± 0.40
		4.9	48 ± 3.56	49 ± 3.17	72 ± 3.03	54 ± 2.7
		9.2	83 ± 1.63	84 ± 5.67	122 ± 5.83	94 ± 8.80
		10.0	–	–	131 ± 6.77	105 ± 13.53
		15.4	134 ± 3.68	129 ± 3.37	169 ± 5.26	142 ± 6.17
		20.0	–	–	197 ± 5.21	151 ± 2.55
		30.0	–	–	252 ± 4.74	203 ± 6.44
Ar	1.395	0.48	10.7 ± 0.43	12 ± 1.03	19 ± 1.10	–
		1.0	20.1 ± 0.89	26 ± 3.0	39 ± 2.22	–
		2.0	48 ± 1.75	45 ± 2.84	85 ± 8.75	–
		5	–	–	143 ± 6.55	171 ± 4.09
		10.0	–	–	210 ± 14.53	179 ± 6.21
		15.0	–	–	235 ± 13.34	193 ± 11.95
		20.0	–	–	255 ± 6.73	209 ± 8.91
		30.0	–	–	268 ± 2.73	228 ± 8.26
V	6.11	0.49	2.25 ± 0.050	2.86 ± 0.079	3.9 ± 0.18	0.91 ± 0.027
		1.0	5.5 ± 0.21	6.5 ± 0.16	7.9 ± 0.36	6.6 ± 0.15
		2.1	11.6 ± 0.78	12.5 ± 0.68	17.8 ± 0.74	14.8 ± 0.50
		4.8	24.2 ± 0.63	24.7 ± 0.88	41 ± 2.76	27.7 ± 0.90
		9.5	46 ± 3.41	42 ± 2.65	68 ± 2.10	47.6 ± 0.93
		14.6	53 ± 1.81	57 ± 3.25	84 ± 4.83	63 ± 1.19
		20.0	–	–	103 ± 6.10	82.7 ± 0.78
		30.0	–	–	134 ± 8.57	96 ± 1.86

Table 2.1: The self-diffusion coefficient for all systems. For each RPP model, the number of particles, time step, and simulation length were kept identical for each element, density, and temperature. Finite-size corrections are carried out in Sec. 2.3.5.

Table 2.1 (cont'd)

Element	ρ_i (g/cm^3)	T (eV)	D_{KS-MD}	D_{FM}	D_{TFY}	D_{NPA}
V	3.055	0.5	9.0 ± 0.81	11.3 ± 0.29	8.7 ± 0.23	–
		0.97	14.7 ± 0.47	15.4 ± 0.43	19 ± 1.39	–
		2.0	23 ± 1.13	24 ± 1.84	31 ± 1.26	27 ± 1.84
		4.9	47 ± 4.38	44 ± 2.52	66 ± 7.30	48 ± 2.02
Fe	7.874	0.51	2.13 ± 0.047	2.34 ± 0.042	2.84 ± 0.030	–
		1.1	5.27 ± 0.098	5.5 ± 0.16	5.9± 0.39	–
		2.1	10.4 ± 0.72	10.4 ± 0.73	14.8 ± 0.46	9.2 ± 0.47
		5.0	20.4 ± 0.61	22.0 ± 0.97	32 ± 1.41	27.1 ± 0.19
		10.4	35 ± 1.14	38 ± 1.40	54 ± 1.25	49 ± 2.90
		15.0	–	–	83 ± 5.18	60 ± 2.60
		20.0	–	–	97 ± 2.93	70 ± 1.04
		30.0	–	–	103 ± 4.69	83.0 ± 0.94
Fe	3.937	0.51	6.0 ± 0.39	8.5 ± 0.94	6.2 ± 0.21	–
		1.1	15.8 ± 0.70	15.6 ± 0.67	14.4 ± 0.33	–
		2.1	20 ± 1.18	22 ± 2.07	27 ± 1.28	–
Au	19.30	0.52	0.92 ± 0.028	0.71 ± 0.084	1.67 ± 0.12	0.51 ± 0.042
		1.1	2.0 ± 0.11	1.92 ± 0.088	3.9 ± 0.42	1.66 ± 0.069
		1.9	4.0 ± 0.14	3.4 ± 0.15	6.6 ± 0.16	3.52 ± 0.05
		5.0	7.8 ± 0.40	8.2 ± 0.21	15.3 ± 0.63	10.7 ± 0.50
		9.7	14.4 ± 0.64	15 ± 1.19	25 ± 1.94	16.6 ± 0.86
		15.0	19.82 ± 0.80	22 ± 2.56	30 ± 1.95	25 ± 2.79
		20.0	–	–	39 ± 3.49	28.0 ± 0.97
		30.0	–	–	56 ± 2.23	33 ± 1.26

For higher temperatures, the NPA RPP is very similar to the force-matched RPP for low and high frequencies for all elements. For $T = 0.5$ eV, the dynamics predicted from the NPA model are noticeably less similar to those from KS-MD where NPA underestimates the prevalence of low-frequency modes in Au and both low and high-frequency modes in V. Interestingly, the NPA RPP captures the single-particle dynamics of low temperature C very well, but Figs. 2.5 and 2.9 indicate that this agreement comes at the expense of sacrificing the accuracy of static properties. Lastly, the TFY RPP exhibits roughly the same trends across all elements and temperatures– overestimation of the low frequency modes and underestimation of the high-frequency modes except for the case of C at 2.267 g/cm^3 and $T = 5$ eV where excellent agreement with KS-MD is observed.

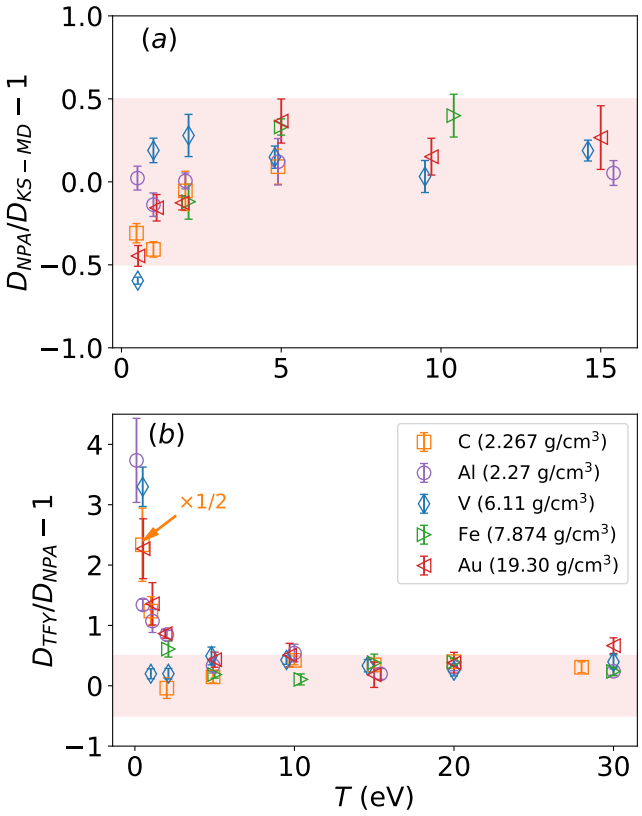

Figure 2.12: Relative self-diffusion coefficients. The shaded region brackets the range of −0.5 and 0.5. (*a*) For all cases except V at $T = 0.5$ eV, the points fall within the bounds of the bracketed region. The NPA RPP fails to reproduce the KS-MD results at $T = 0.5$ eV, revealing a temperature boundary below which KS-DFT is needed. In (*b*) the points are within 50% of the NPA value from $T = 5$ eV and above for most cases. The orange point marked with an arrow has been reduced by a factor of $1/2$ to improve clarity of the banded region.

2.3.5 Finite-Size Corrections

Generally, thousands or even millions of atoms are needed to approximate the thermodynamic limit [88, 110]. While the KS-MD framework provides an accurate description of the electronic structure and the N-body potential is determined on-the-fly, corrections for finite-size effects must be considered. When the shear viscosity η of the system is known, finite-size corrections can be determined from [150]

$$D_\infty = D_N + \frac{\xi T}{6\pi\eta L}, \tag{2.20}$$

where D_∞ is the self-diffusion coefficient in the thermodynamic limit, D_N is the self-diffusion coefficient computed from a system of finite number of particles N, and $\xi = 2.837297$ for cubic

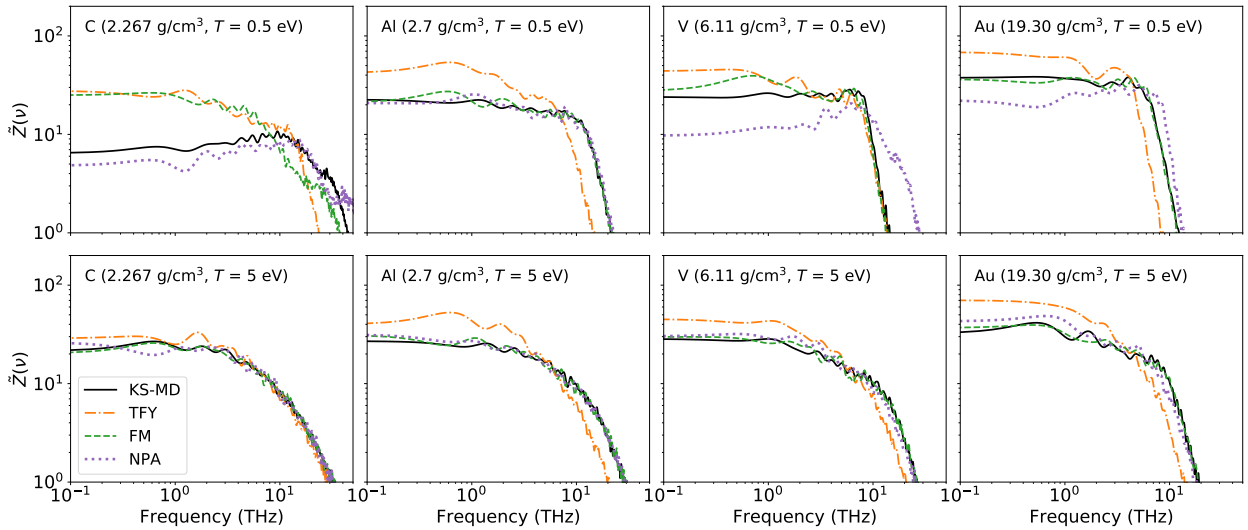

Figure 2.13: The normalized power spectrum for C, Al, V, and Au. For C at $T = 0.5$ eV, the single particle dynamics are poorly described by the TFY and force-matched models but more accurately described with the NPA model. As the temperature increases from $T = 0.5$ to 5 eV, all models more accurately reproduce small and high frequency dynamics with the most notable improvement for C.

simulation boxes with periodic boundary conditions. When η is unknown, multiple simulations of increasing particle number are carried out, and a linear fit is used to determine D_∞. Results from this procedure are shown in Fig. 2.14 where D_∞ is determined via linear extrapolation to $1/L = 0$.

By finding the percent difference in D_∞ and D_N, we approximate the errors from finite-size effects in the KS-MD self-diffusion coefficient at these conditions. The approximate error in KS-MD for the case shown in Fig. 2.14, is $\sim 20\%$. While the error will vary with $\{Z, n, T\}$, the impact of finite-size effects is significant. From this study, the most promising approach is to fully converge the NPA MD results, using force-matched RPPs when necessary (for low temperatures $T \lesssim 1$ eV).

Finite-size corrections allow for a direct comparison to analytic transport theories, namely the Stanton-Murillo model [151]. The Stanton-Murillo model, provides a closed form solution for ionic self diffusion by using an effective interaction potential in a Boltzmann kinetic theory framework. The major benefit of this model is that the computation of ionic transport is nearly instantaneous. However, its applicability in the cold dense matter and warm dense matter regimes is unknown.

The results in Table 2.2 show that the effective interaction approach of the Stanton-Murillo

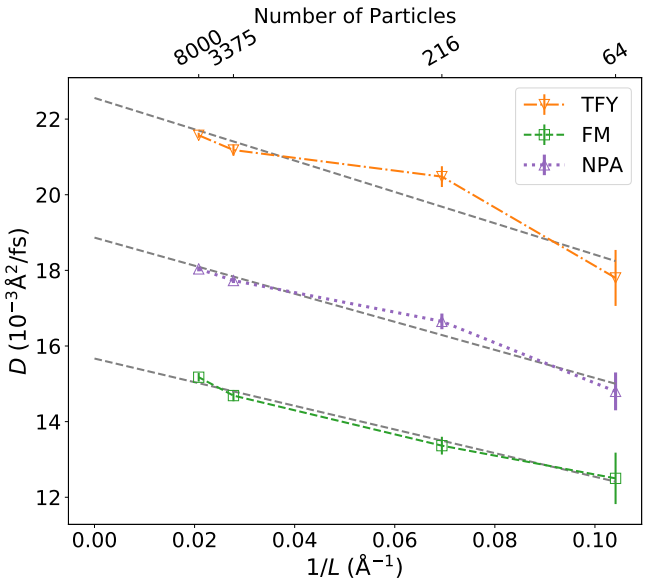

Figure 2.14: Finite-size effect study for V at 6.11 g/cm^3 and $T = 2$ eV. Identical MD simulations were carried out with increasing particle number. Extrapolating with a linear fit (grey dashed line) to $1/L = 0$ approximates the thermodynamic limit, correcting the values in Table 2.1.

model captures much of the many-body physics included in the TFY RPP results. The main weakness of the model, and also TFY, is therefore the functional form of the interaction they employ, as the differences with the force-matched and NPA columns reveal. Because self diffusion is a relatively simple transport coefficient [151], more work is needed to quantify these trends for other transport properties.

With the converged self-diffusion data, we generate an effective interaction correction to the Stanton-Murillo model. The effective interaction corrected Stanton-Murillo model is

$$D_{CSM} = \alpha(Z,T) D_{SM}, \tag{2.21}$$

where $\alpha(Z,T)$ is determined by fitting the ratio of the self-diffusion coefficient from the best performing RPP model and the self-diffusion coefficient computed from the Stanton-Murillo model D_{SM} to the functional form

$$\alpha(Z,T) = \frac{a\mathrm{erf}(bT)}{bT} + 1, \tag{2.22}$$

which asymptotes to D_{SM} as T increases. Here the “best performing RPP model" refers to the RPP model that most accurately reproduced the self-diffusion coefficient computed from 64 particle

Element	T (eV)	D_{FM}	D_{NPA}	D_{TFY}	D_{SM}	D_{CSM}
C	0.47	10.55	2.14	12.66	13.08	2.14
	1.0	32.44	14.21	25.57	26.11	13.87
	2.0	56.70	43.12	51.14	50.53	39.23
	4.9	99.51	109.55	117.88	118.34	106.76
	10.0	–	169.91	210.76	217.34	206.71
	15.0	–	219.99	296.21	293.54	284.10
	20.0	–	256.33	342.15	356.41	348.04
	28.0	–	327.32	470.10	439.44	432.07
V	0.49	4.14	1.01	5.42	6.76	4.39
	1.0	8.54	8.53	11.53	12.26	7.96
	2.1	15.67	18.87	22.56	23.14	15.03
	4.8	28.72	31.34	42.42	46.25	30.18
	9.5	49.49	54.90	73.76	77.10	51.16
	14.6	66.98	74.44	99.82	99.78	67.97
	20.0	–	87.90	118.24	117.89	83.15
	30.0	–	105.60	143.63	141.66	106.94
	50.0	–	131.84	175.35	171.07	143.02
	75.0	–	178.34	202.93	194.31	172.91
	100.0	–	209.50	207.20	211.86	194.36

Table 2.2: Self-diffusion coefficient in the thermodynamic limit. Both elements are at solid density (2.267 g/cm^3 for C, and 6.11 g/cm^3 for V).

KS-MD simulations. The parameters a and b are reported in Table 2.3 for C at 2.267 g/cm^3 and V at 6.11 g/cm^3, and their values vary considerably between both cases emphasizing the need for a comprehensive finite size effect study to produce correction factors for additional elements and conditions. This correction factor allows for the use of the Stanton-Murillo model in regions of previously unknown accuracy. The finite-size corrections along with the corrected Stanton-Murillo model results are shown Fig. 2.15 with the numerical values given in Table 2.2. Note that for low temperature C at 2.267 g/cm^3, the best performing RPP model was NPA (as reported in Fig. 2.11 and Table 2.1) explaining why the corrected Stanton-Murillo model tends towards the NPA RPP at low temperatures. For V at 6.11 g/cm^3, the best performing RPP model was the force-matched RPP again explaining the low temperature trend.

In an attempt to summarize our work in a single figure, Fig. 2.16 shows our suggested use cases for all RPPs studied here for two relative self-diffusion accuracies computed from Table 2.1.

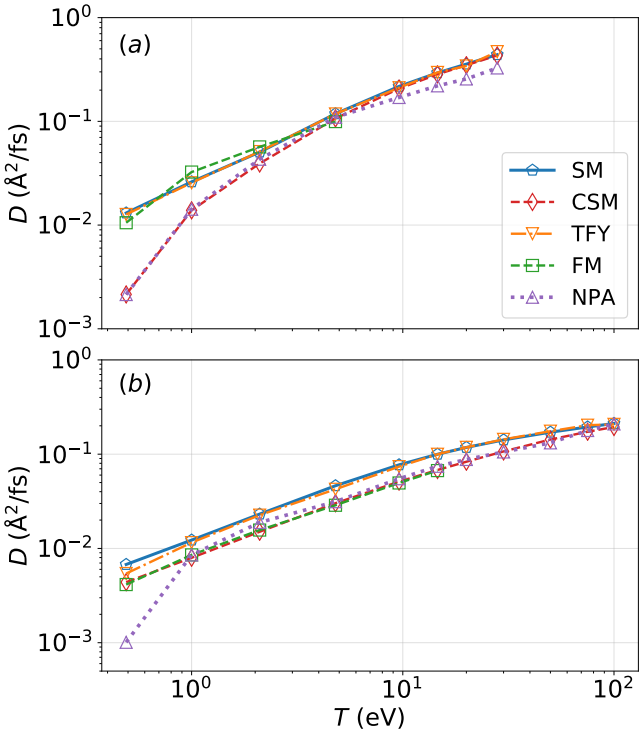

Figure 2.15: Self-diffusion coefficient versus temperature in the thermodynamic limit. The points displayed here are taken from Table 2.2. (*a*) Self-diffusion coefficient for C at 2.267 g/cm^3. (*b*) Self-diffusion coefficient for V at 6.11 g/cm^3. The Stanton-Murillo model (denoted SM) fails for low temperature C. For V, the Stanton-Murillo model shows excellent agreement with the force-matched RPP even at low temperatures. The validity of the Stanton-Murillo model is extended to low temperatures with an effective interaction correction (denoted CSM).

Element	a	b
C (2.267 g/cm^3)	2.198	-1.032
V (6.11 g/cm^3)	0.03767	-0.3112

Table 2.3: Coefficients a, and b for the effective interaction correction Eq. (2.22). Note that the values of a and b vary considerably for each element.

When points (the average value or its uncertainty) for a given model are within the appropriate tolerance (30% for the top panel and 15% for the bottom panel), we consider the model as being accurate for that temperature and element and is denoted with a colored bar or arrow. We rank the computational expense from lowest to highest as: TFY, NPA, force matching, and KS-MD. When a computationally cheaper model is accurate, it replaces the more computationally expensive model in Fig. 2.16. Based on trends observed in Figs. 2.7, 2.12, and 2.15, we assume that the models remain accurate for higher temperatures and illustrate this by upward pointing colored arrows. For example, consider the case of Fe in the top panel of Fig. 2.16. The force-matched RPP is accurate to within 30% of the KS-MD result from T = 0.5 eV and up. The NPA model, which is computationally cheaper than the force-matched RPP, becomes accurate (within 30% of KS-MD) at $T = 2$ eV and up, hence the transition between the force-matched and NPA models. For Al, the NPA RPP is within 15% of KS-MD at all temperatures. However, at $T = 15$ eV the TFY model becomes accurate therefore replacing the NPA RPP.

2.4 Conclusions and Outlook

A systematic study of various RPPs for molecular dynamics simulations of dense plasmas was performed for a wide range of elements versus temperature for solid and half-solid density cases. Of the RPPs studied here, RPPs constructed from a NPA approach come closest to accurately reproducing the transport and structural properties predicted by KS-MD. The failures of NPA for metals near $T = 0.5$ eV are expected: V is a polyvalent metal and s-d hybridization occurs in Au, which is not treated at all in our variant of the NPA model. Thus, it is unclear if inaccuracies in NPA reveal the need for N-body interactions or an improved NPA treatment. Moreover, finite-size corrections to KS-MD are seen to be significant; prior work on Si suggests that at least 108 particles are needed to accurately treat elements like C at low temperatures [152]. Studies on C and Si where there are transient covalent bonding at low temperatures have raised the inadequacy of the PBE XC-functional that has been used here. In [152], the SCAN functional was used showing remarkable agreement between VASP calculations and NPA results for super-cooled high-density Si. This implies that VASP calculations for systems in the low temperature warm dense matter

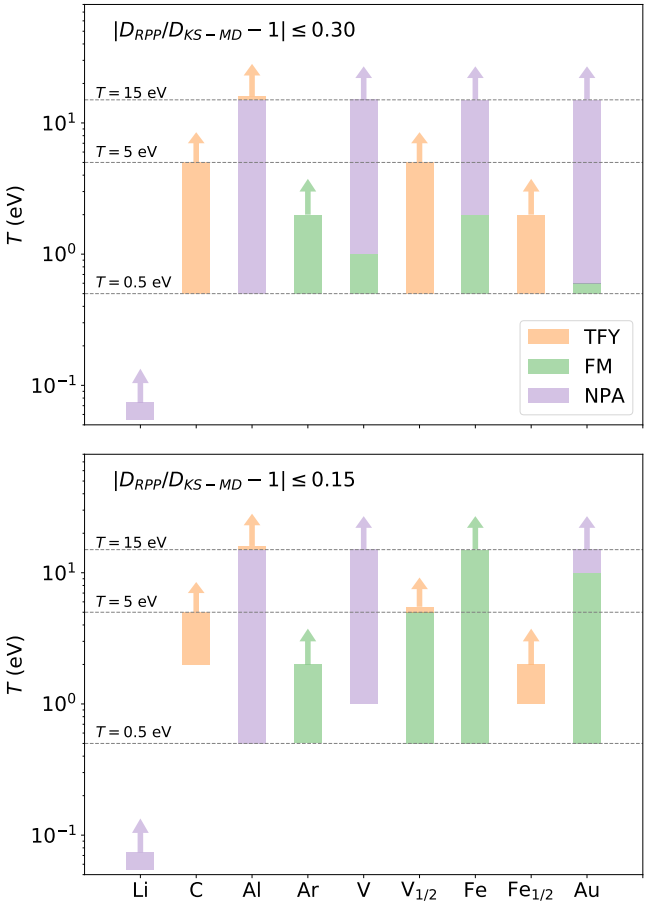

Figure 2.16: Suggested use cases for RPPs based on the relative self-diffusion coefficient error (between RPP-MD and KS-MD) and cheapest computation cost. The top and bottom panels correspond to a 30% and 15% relative error respectively. The elements denoted with a subscript of "1/2" corresponds to half solid density (V at 3.055 g/cm^3 and Fe at 3.937 g/cm^3). The colored bars indicate the computationally cheapest RPP that generates a self-diffusion coefficient to within the specified error tolerance available for that system based on Table 2.1. The empty space under each bar indicates regions where no KS-MD data was collected so no assessment on a RPPs accuracy can be made.

regime become sensitive to the choice of the XC-functional. Similarly, the XC-functionals for transition metals like V, Fe, etc., are known to need Hubbard-type corrections that are not included in our studies. Although this work does not fully resolve these issues, the trends seen for the lowest temperature for C, V and Au should be examined in detail in future work. Additionally, the NPA model is exceptionally accurate for Al. As Al is a free electron metal, its electronic structure is well described as a Fermi-Liquid, the precise physical model in which NPA performs well. In the cases where the electronic structure of the system is not well described as a Fermi-liquid, the performance of the NPA model decreases at low temperature, further emphasizing the need for a comprehensive study over a range of elements and conditions.

As in previous works [89,103], the TFY model predicts the least structured $g(r)$. Notionally, the accuracy of the TFY model appears to follow the machine learning trend of $\langle Z\rangle/Z > 0.35$ [153], although it was not possible to use all models here at high enough temperatures to be quantitative. In contrast, the NPA model with its improved Kohn-Sham treatment and use of a pseudopotential in Eq. (2.7) eliminates most of these errors except for C and V at $T = 0.5$ eV, elements for which we would recommend NPA for $T > 2$ eV. Because we examined seven diverse elements over the warm dense matter regime, the accuracy of NPA (and for moderate temperature, even TFY) suggests that no additional "short-range repulsion" [32, 103, 141–145] is needed beyond Eq. (2.7); as Eq. (2.7) does not contain core-core repulsion, the structure of the interaction is more likely to be effective core-valence repulsion captured by $u_{ei}(k)$, as well as structure in $\chi(k)$ beyond $\chi_{TF}(k)$. However, we note, that in treating weakly ionized systems like warm-dense Ar with a mean ionization of $\langle Z\rangle = 0.3$, some 70% of the Ar atoms are neutral, while about 30% of the atoms are singly ionized. Thus, the neutrals interact via a core-core interaction screened by the free electrons. In such cases the use of Eq. (2.7) alone is inadequate. The NPA model treats such a two-component mixture using three pair potentials. In general, core-core interactions are important for weakly-ionized atoms with a large core. These core-core interactions can be readily calculated using the core-electron density obtained from the NPA Kohn-Sham calculation. As expected, the force-matched RPP reproduced the $g(r)$ computed from KS-MD for all cases. In only one case, again C at 2.267

g/cm^3 and $T = 0.5$ eV, the force-matched RPP overestimated the self-diffusion coefficient; this suggests that the spherical pair interaction isn't applicable, and non-spherical corrections, which could include three-body contributions, are needed as suggested by the near-perfect agreement of the SNAP and KS-MD microfield of force magnitudes in Fig. 2.6. However, for all cases considered with $T > 1$ eV, the $g(r)$ and self-diffusion coefficient are adequately described by a RPP. With the force-matched-validated NPA interaction, pre-computing the interaction allows for much larger pair-potential simulations.

As fast analytic expressions for transport coefficients are needed for hydrodynamic modeling, we compared our self-diffusion results from all models to the Stanton-Murillo model for both C and V. In both cases, the Stanton-Murillo model was consistent with the TFY model (on which it is based) and both have agreement with force-matched-based results. The error between the Stanton-Murillo model and the force-matched results is $< 65\%$ below $T = 10$ eV for V and $< 25\%$ below $T = 5$ eV for C, adding confidence to the use of this model in hydrodynamics models above that temperature. For experiments that are rapidly heated above a few eV, little time is spent where the errors are large; because the transport coefficients are numerically very small during this transient heating, negligible transport can occur during that time. For example, note that the V diffusion coefficient varies by a factor of about 30 in the range $T = 0.5$ to 100 eV. Conversely, for experiments that dwell at lower temperatures, we provide a RPP-based correction factor to the Stanton-Murillo model with an error of less than 1% for C at $T = 0.5$ eV and 6% for V at $T = 0.5$ eV.

Our results suggest several new avenues of investigation. From a data science perspective, larger collections of systematically-obtained simulation results would aid in better defining accuracy boundaries. In particular, more elements that produce more material types should be studied. For mixtures, N-body potentials could be explored; here, we cast all of the pair potentials as heteronuclear. Additionally, our conclusions are based on studies of the microfield distribution of forces, Einstein frequency, power spectrum, self-diffusion coefficient, and $g(r)$, which could be extended to include other properties such as viscosities and interdiffusion in mixtures, electrical conductivity, thermal conductivity, and ion-dynamical properties like the speed of sound [109].

While we focused primarily on force matching, effective interaction potentials can be obtained through “structure matching" [125, 154, 155]. Finally, as very large scale simulations become more common, spatially heterogeneous plasmas can be modeled; much less is known about potentials in such environments, although recent work has explored non-spherical potentials [88].

CHAPTER 3

ANALYTIC MODELS FOR INTERDIFFUSION IN DENSE PLASMA MIXTURES

3.1 Introduction

The contents of Chapter 2 were focused on assessing the validity of force laws for MD simulations of plasmas of a single ion species. In this chapter[1], we extend our study to binary plasma mixtures where we focus on formulating analytic models for the interdiffusion coefficient.

Interdiffusion, which is atomic-scale mixing driven by density gradients, occurs in extremely disparate physical systems. Early experimental work in alloys addressed interdiffusion at interfaces between solids [157–159]. The interpretation of these experiments led to the development of early theories in an attempt to quantify observed effects [160]. Interdiffusion remains important for industrial applications and has been studied in the context of neutral liquids [161, 162] and liquid metals [163–165]. In stellar environments, interdiffusion controls the distribution of elements throughout the star, impacting its evolution [166–168]. Additionally, diffusive mixing of thermonuclear fuel in inertial confinement fusion experiments [169] can spoil the burn conditions through radiative losses [170–174]. Recent large-scale MD simulations [88] of heated plasma interfaces have exposed many complex issues: multiple ionic temperatures, jetting of light particles across the interface, uncoupled velocity fields, and intense electric fields. Experimental data for these processes is minimal, but has motivated several current experiments [175–179].

Despite progress in the theory of interdiffusion and charged particle transport [180], several gaps remain. In contrast with its one-particle counterpart, self diffusion, interdiffusion, a collective property, is investigated relatively rarely. In most computational studies of interdiffusion, the thermodynamic factor is set to unity [102, 148, 181, 182]. While this may be accurate in some cases [161], a complete exploration across physical regimes for a wide range of mixtures is lacking. This has been addressed only recently in work that employed MD to create a data set of thermodynamic factors [183]. Computation of the relevant autocorrelation function, and the thermodynamic

[1]The content of this chapter has been reproduced from *Lucas J. Stanek and Michael S. Murillo , "Analytic models for interdiffusion in dense plasma mixtures", Physics of Plasmas 28, 072302 (2021) https://doi.org/10.1063/5.0047961"* with the permission of AIP Publishing; see Ref. [156] for the full published article.

factor, is subject to finite-size effects [184]. These effects are particularly important when computational models are very expensive, as is the case with on-the-fly potentials [87]. Because of these computational issues, there is a lack of interdiffusion data within the dense-plasma community. Seen from a data-science perspective, binary interdiffusion is at least seven dimensional: one must specify, among other choices of variables, the mean density, stoichiometry, temperature, charge, and mass of each species. If the interparticle potentials have other dependencies, then additional parameters must be used. Machine learning has been applied to this setting and has shown promising results [183]. In practice, it is preferable to employ validated theoretical models that are very rapid to compute [151, 185, 186]; more work is needed to validate such models in this seven-dimensional space.

We begin Sec. 3.2 by stating the definitions used here to define a binary mixture, and we show how the interdiffusion coefficient arises from hydrodynamic equations of motion. In Sec. 3.3, we derive analytic forms for the thermodynamic factor that cover a wide range of plasma conditions; these forms employ both the radial distribution function and the structure factor. Lastly, in Sec. 3.4, we derive a rapidly computable analytic expression for the interdiffusion coefficient in a binary ionic mixture (BIM). We compare this result to MD data, revealing excellent agreement in moderately and strongly coupled regimes.

3.2 Interdiffusion

The description of interdiffusion, and the values of the interdiffusion coefficients, are not unique. In this section, we review various formulations of interdiffusion and establish the conventions and notations we will use. For simplicity, we examine only binary plasmas; we consider a binary plasma that contains N_i ions of each species "i," with charge $Z_i e$ and mass M_i. Note that in contrast to Chapter 2, here we denote the mean ionization of species i as Z_i instead of $\langle Z_i \rangle$. The total number of ions in the system is $N = N_1 + N_2$. We assume that the ionic species are in thermodynamic equilibrium at inverse temperature $\beta = 1/T$ and that the electrons are at inverse temperature $\beta_e = 1/T_e$. The average number and mass densities are n_i and $\rho_i = M_i n_i$, respectively, with corresponding total densities $n = n_1 + n_2$ and $\rho = \rho_1 + \rho_2$. Additionally, we define the number

and mass concentrations as $x_i = n_i/n$ and $c_i = \rho_i/\rho$, respectively.

The mean ionization and mass of the binary mixture are given as

$$\langle Z^\alpha \rangle \equiv x_1 Z_1^\alpha + x_2 Z_2^\alpha, \tag{3.1}$$

$$\langle M \rangle \equiv x_1 M_1 + x_2 M_2, \tag{3.2}$$

where $\alpha \in \mathbb{R}$. From Eqs. (3.1) and (3.2), we define $z_i = Z_i/\langle Z \rangle$ and $m_i = M_i/\langle M \rangle$. Lastly, we define the Coulomb coupling parameter of the ions as

$$\Gamma_0 = \frac{e^2}{aT}, \tag{3.3}$$

where

$$a = \left(\frac{4\pi n}{3}\right)^{-1/3} \tag{3.4}$$

is the total ion-sphere radius. Note that Eq. (3.3) does not depend on the mean ionization of the ions. To include the mean ionization of the ions, we define

$$\Gamma_{ii'} = \frac{Z_i Z_{i'} e^2}{aT} = Z_i Z_{i'} \Gamma_0. \tag{3.5}$$

We now begin our discussion of interdiffusion by defining the microscopic density and velocity fields as

$$n_i(\mathbf{r}, t) = \sum_{j=1}^{N_i} \delta[\mathbf{r} - \mathbf{r}_{i,j}(t)], \tag{3.6}$$

$$\mathbf{u}_i(\mathbf{r}, t) = \sum_{j=1}^{N_i} \mathbf{v}_{i,j}(t) \delta[\mathbf{r} - \mathbf{r}_{i,j}(t)]. \tag{3.7}$$

In Eqs. (3.6) and (3.7), the index j refers to the jth particle of species i. The time evolution of the density Eq. (3.6), using Eq. (3.7), yields the continuity equation

$$\frac{\partial n_i(\mathbf{r}, t)}{\partial t} = -\nabla \cdot \left[n_i(\mathbf{r}, t) \mathbf{u}_i(\mathbf{r}, t) \right]. \tag{3.8}$$

Equation (3.8) is not closed until we specify the evolution of the velocity field $\mathbf{u}_i(\mathbf{r}, t)$; it is such closures that yield diffusion equations. However, in many physical systems, including plasmas, the

flow fields can be complex and the velocity field must also be evolved as part of a hydrodynamic description. As the fluid density evolves in time, both advection and diffusion occur. To isolate diffusion from advection, we define the diffusive flux $\mathbf{j}_i(\mathbf{r}, t)$ relative to a reference frame as

$$\mathbf{j}_i(\mathbf{r}, t) = n_i(\mathbf{r}, t)\left[\mathbf{u}_i(\mathbf{r}, t) - \mathbf{u}_{\text{ref}}(\mathbf{r}, t)\right], \tag{3.9}$$

where $\mathbf{u}_{\text{ref}}(\mathbf{r}, t)$ is a reference velocity. The choice of the reference velocity $\mathbf{u}_{\text{ref}}(\mathbf{r}, t)$ is problem dependent and some common choices are listed in Table 3.1. Written in terms of the reference velocity, the continuity equation becomes

$$\frac{\partial n_i(\mathbf{r}, t)}{\partial t} + \nabla \cdot [n_i(\mathbf{r}, t)\mathbf{u}_{\text{ref}}(\mathbf{r}, t)] = -\nabla \cdot \mathbf{j}_i(\mathbf{r}, t). \tag{3.10}$$

The diffusion model and the values of the diffusion coefficients depend on the choice of reference velocity. While the reference-velocity field is assumed to be evolved by a separate equation, the closures for the diffusive flux are usually in the form of a slowly varying ansatz.

Most hydrodynamic models employ mass densities rather than number densities. In this scenario, natural choices for the reference velocity and fluxes are the center-of-mass velocity (see Table 3.1) and

$$\mathbf{j}_i(\mathbf{r}, t) = \rho_i(\mathbf{r}, t)\left[\mathbf{u}_i(\mathbf{r}, t) - \mathbf{u}_{\text{com}}(\mathbf{r}, t)\right], \tag{3.11}$$

respectively. With Eq. (3.11) as the choice for the diffusive flux, we can propose a closure of the form

$$\mathbf{j}_i(\mathbf{r}, t) = -D_{\mathbf{x}}\nabla\mathbf{x}, \tag{3.12}$$

where the mass density flux is driven by forces caused by $\mathbf{x}$ with proportionality $D_{\mathbf{x}}$; again, there is considerable leeway in how these quantities are chosen. Different choices for the diffusive flux will yield different proportionality coefficients that have different physical meanings. Two of the most common choices for $\mathbf{x}$ are the chemical potential and the number density; these choices yield the diffusive fluxes [148, 187–189]

$$\mathbf{j}_i(\mathbf{r}, t) = -\frac{1}{T}D_\mu\nabla\mu_i(\mathbf{r}, t), \tag{3.13}$$

and

$$\mathbf{j}_i(\mathbf{r}, t) = -D_n \nabla n_i(\mathbf{r}, t), \tag{3.14}$$

respectively. For the specific choices of $\mathbf{x}$ in Eq. (3.13) and (3.14), the relationship between D_μ and D_n is given by the thermodynamic factor [187, 190], which is addressed in Sec. 3.3. In a plasma hydrodynamics context, it is reasonable to choose to write the diffusive flux as [191]

$$\mathbf{j}_i(\mathbf{r}, t) = -\rho(\mathbf{r}, t) D \nabla c_i(\mathbf{r}, t), \tag{3.15}$$

where D is the interdiffusion coefficient. Note that Eq. (3.15) assumes that particle fluxes are not driven by other gradients (e.g., temperature, pressure, electrostatic potential, etc.) or that other gradients are present but are collectively in equilibrium. Although we presume a separate time-evolution equation for $\mathbf{u}_{\text{ref}}(\mathbf{r}, t)$ in Eq. (3.10), the slowly varying form of Eq. (3.15) is assumed for $\mathbf{j}_i(\mathbf{r}, t)$.

It is worth summarizing the steps taken so far. To arrive at Eqs. (3.10) and (3.15), many non-unique choices were made. Perhaps more importantly, the form of Eq. (3.15) is an ansatz that may or may not be accurate for a given plasma scenario. The use of a chemical-potential gradient is associated with a special state referred to as "mechanical equilibrium," [189] in which the pressure and temperature gradients have already relaxed; thus, the flux is not driven by gradients in those quantities. A generalized form for Eq. (3.15) may be needed to account for baro- and thermo-diffusion processes [70, 192, 193], for example. Nevertheless, in this work, we will proceed under the assumptions that the diffusive flux is given by Eq. (3.15).

One can obtain a Green-Kubo relation consistent with these choices [188]. The interdiffusion coefficient is calculated as [181]

$$D = \frac{\mathcal{J}}{3N x_1 x_2} \int_0^\infty dt \langle \mathbf{j}(t) \cdot \mathbf{j}(0) \rangle, \tag{3.16}$$

where $\mathbf{j}(t)$ is the interdiffusion current defined as

$$\mathbf{j}(t) = x_2 \sum_{j=1}^{N_1} \mathbf{v}_{1,j}(t) - x_1 \sum_{j=1}^{N_2} \mathbf{v}_{2,j}(t). \tag{3.17}$$

Name	Reference Velocity
barycentric (center of mass)	$\mathbf{u}_{\text{com}} = \sum_{i=1} \frac{\rho_i}{\rho} \mathbf{u}_i$
mean molar velocity	$\mathbf{u}_{\text{mmv}} = \sum_{i=1} \frac{n_i}{n} \mathbf{u}_i$
mean volume velocity	$\mathbf{u}_{\text{mvv}} = \sum_{i=1} \rho_i v_i \mathbf{u}_i$

Table 3.1: Possible choices for the reference velocity. Here, v_i is the partial molar volume of species i.

In reduced form, the interdiffusion coefficient is given by

$$D^* = D/\omega_p a^2, \tag{3.18}$$

$$\omega_p^2 = \frac{4\pi n \langle Z \rangle^2 e^2}{\langle M \rangle}, \tag{3.19}$$

where ω_p is the "hydrodynamic" plasma frequency [181]. The evolution of the interdiffusion current is assumed to be stationary and to include all interparticle interactions. The brackets $\langle \cdots \rangle$ represent an ensemble average over initial conditions (time *and* position) of the interacting plasma mixture. The prefactor $\mathcal{J}$ is the thermodynamic factor [191]

$$\mathcal{J} = \frac{x_1 x_2}{S_{cc}(k=0)}, \tag{3.20}$$

where $S_{cc}(k)$ is the concentration-concentration structure factor that can be decomposed into partial structure factors as

$$S_{cc}(k) = x_1 x_2 [x_2 S_{11}(k) + x_1 S_{22}(k) - 2\sqrt{x_1 x_2} S_{12}(k)]. \tag{3.21}$$

Models for the partial structure factors are discussed in Sec. 3.3.

Many researchers [186, 194–198] have explored a simplified form of Eq. (3.16) known as the Darken relation [160]. We revisit the derivation of this relation to assess its utility for modeling dense plasma mixtures. Key to obtaining the Darken relation is isolating the intraparticle contributions

from the interparticle contributions, as in

$$\begin{aligned} D &= \frac{\mathcal{J}}{3Nx_1x_2}\int_0^\infty dt\langle \mathbf{j}(t)\cdot\mathbf{j}(0)\rangle \\ &= \frac{\mathcal{J}x_2}{3Nx_1}\int_0^\infty dt\left\langle \sum_{j=1}^{N_1}\mathbf{v}_{1,j}(t)\cdot\sum_{j'=1}^{N_1}\mathbf{v}_{1,j'}(0)\right\rangle \\ &\quad + \frac{\mathcal{J}x_1}{3Nx_2}\int_0^\infty dt\left\langle \sum_{j=1}^{N_2}\mathbf{v}_{2,j}(t)\cdot\sum_{j'=1}^{N_2}\mathbf{v}_{2,j'}(0)\right\rangle \\ &\quad - \frac{2\mathcal{J}}{3N}\int_0^\infty dt\left\langle \sum_{j=1}^{N_1}\mathbf{v}_{1,j}(t)\cdot\sum_{j'=1}^{N_2}\mathbf{v}_{2,j'}(0)\right\rangle. \end{aligned} \tag{3.22}$$

Although all particles are interacting and the ensemble average $\langle\ldots\rangle$ is taken over initial conditions of the interacting system, we can *d*efine a type of self-diffusion coefficient in analogy with the single-species case as

$$\begin{aligned} D_i &= \frac{1}{3N_i}\int_0^\infty dt\left\langle \sum_{j=1}^{N_i}\mathbf{v}_{i,j}(t)\cdot\mathbf{v}_{i,j}(0)\right\rangle \\ &= \frac{1}{3}\int_0^\infty dt\left\langle \mathbf{v}_{i,j}(t)\cdot\mathbf{v}_{i,j}(0)\right\rangle \quad (j=1,2,\cdots,N_i). \end{aligned} \tag{3.23}$$

Note that self diffusion refers to only intraparticle correlations (independent of species), whereas interparticle correlations (of any species) are described by the terms [188, 199]

$$f_{ii} = \frac{1}{3N}\int_0^\infty dt\left\langle \sum_{j=1}^{N_i}\sum_{j'\neq j}^{N_i}\mathbf{v}_{i,j}(t)\cdot\mathbf{v}_{i,j'}(0)\right\rangle, \tag{3.24}$$

$$f_{12} = \frac{1}{3N}\int_0^\infty dt\left\langle \sum_{j=1}^{N_1}\sum_{j'=1}^{N_2}\mathbf{v}_{1,j}(t)\cdot\mathbf{v}_{2,j'}(0)\right\rangle. \tag{3.25}$$

Note that f_{ii} and f_{12} are intraspecies and interspecies contributions, respectively. Finally, we arrive at the form

$$D = \mathcal{J}\left[x_2D_1 + x_1D_2 + x_1x_2\left(\frac{f_{11}}{x_1^2} + \frac{f_{22}}{x_2^2} - 2\frac{f_{12}}{x_1x_2}\right)\right]. \tag{3.26}$$

The Darken relation is obtained by assuming that the third term vanishes, yielding

$$D \approx \mathcal{J}(x_2D_1 + x_1D_2). \tag{3.27}$$

The Darken relation has direct application to systems for which experimental measurements yield D_1 and/or D_2 [198]; in a computational setting, no such limitation exists.

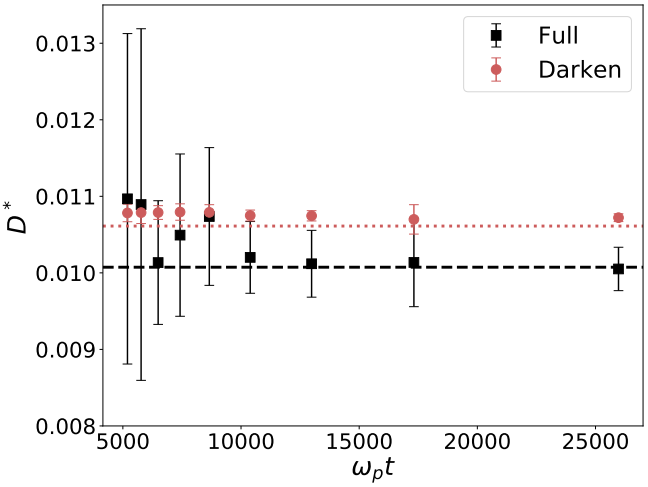

Figure 3.1: The interdiffusion coefficient, Eq. (3.16), and the Darken relation, Eq. (3.27) versus time. An MD simulation was carried out for a H^+-He^{2+} BIM where $N = 2000$ particles, $x_1 = 0.5$, $n_i = 1.62 \times 10^{28}$ cm^{-3}, and $T = 14.7$ eV. Each point is calculated from a subset of the total simulation length ($\omega_p t = 51946$). The value of D^* for the total simulation time is shown as a dotted (using Darken) or dashed [using Eq. (3.16)] line. The Darken relation has smaller statistical uncertainty but converges to the incorrect value.

Note that use of the Darken relation does not impact MD simulations needed to create trajectory information; the Darken relation reduces the post analysis to two autocorrelation functions rather than five. Thus, the Darken relation potentially produces a less accurate result for a small improvement in computational cost. However, it is possible that the terms that the Darken relation retains have smaller statistical fluctuations, thereby allowing for a smaller MD trajectory calculation (as well as the faster post-MD analysis). We explore this hypothesis in Fig. 3.1 by performing MD with increasingly longer trajectories to identify when the statistical errors in the full autocorrelation, Eq. (3.26), are comparable to the Darken relation, Eq. (3.27). We find that, indeed, the full form of Eq. (3.26) has larger statistical errors and Eq. (3.27) converges more quickly. However, the mean value of the full autocorrelation is either consistent with the mean value from the Darken relation or better. Thus, suggesting that there is no penalty for using the full form even for small simulations. Moreover, converged full results are easily obtained with a modestly longer simulation. Here, we will always use the full result.

3.3 Thermodynamic Factor

Once the values of Eqs. (3.23), (3.24), and (3.25) have been converged in particle number and simulation length, it remains to compute the prefactor $\mathcal{J}$ in Eq. (3.26). Typically, $\mathcal{J}$ is taken to be unity [102, 148, 181, 182, 200], often in analogy with neutral (Lennard-Jones) systems [161, 201, 202]. Other non-unity forms have been suggested [191, 194] but have been explored very little. Comprehensive MD results have been obtained recently [183] in the context of the Darken relation.

The thermodynamic factor can be obtained from integral equation theory, which gives the radial distribution functions [148] as

$$g_{ii'}(r) = \exp\left[-\beta u_{ii'}(r) + h_{ii'}(r) - c_{ii'}(r) + B_{ii'}(r)\right], \tag{3.28}$$

where $u_{ii'}(r)$ is a pair potential [87], $h_{ii'}(r) = g_{ii'}(r) - 1$ are the pair correlation functions, $c_{ii'}(r)$ are the direct correlation functions (DCFs), and $B_{ii'}(r)$ are the bridge functions [203]. While many choices for $u_{ii'}(r)$ are possible, a BIM assumes the form of

$$u_{ii'}^{\mathrm{BIM}}(r) = \frac{Z_i Z_{i'} e^2}{r}. \tag{3.29}$$

The binary Yukawa model (BYM) includes effects from electron screening (e.g., Thomas-Fermi screening) and has the form

$$u_{ii'}^{\mathrm{BYM}}(r) = \frac{Z_i Z_{i'} e^2}{r} e^{-r/\lambda_{TF}}, \tag{3.30}$$

$$\lambda_{TF}^{-2} \approx \frac{4\pi n_e e^2}{\sqrt{T_e^2 + \left(\frac{2}{3}E_F\right)^2}}, \tag{3.31}$$

where $E_F = \hbar^2(3\pi^2 n_e)^{2/3}/2m_e$ for electron number density n_e and mass m_e. Note that in contrast to Chapter 2, the Thomas-Fermi screening length, Eq. (3.31), now depends on the *electron temperature*; here, the ions and electrons are assumed to have different temperatures.

Equation (3.28) is a closure to the Ornstein-Zernicke equations (OZEs) that are given by

$$h_{ii'}(r) = c_{ii'}(r) + \sum_k n_k \int d^3r'\, c_{ik}(|\mathbf{r} - \mathbf{r}|')h_{ki'}(r'). \tag{3.32}$$

For weakly to moderately coupled plasmas, we can employ the hypernetted chain approximation by setting $B_{ii'}(r) = 0$ which allows us to find $g_{ii'}(r)$ given $u_{ii'}(r)$.

After Fourier transformation, the pair correlation functions can be defined in terms of partial static structure factors [148] given by

$$S_{ii'}(k) = \delta_{ii'} + \sqrt{x_i x_{i'}} n h_{ii'}(k). \tag{3.33}$$

For a two-component mixture, we can write $h_{ii'}(k)$ in terms of the DCFs as

$$\begin{bmatrix} h_{11} \\ h_{12} \\ h_{22} \end{bmatrix} = \begin{bmatrix} 1 - n_1 c_{11} & -n_2 c_{12} & 0 \\ 0 & 1 - n_1 c_{11} & -n_2 c_{12} \\ 0 & -n_1 c_{21} & 1 - n_2 c_{22} \end{bmatrix}^{-1} \begin{bmatrix} c_{11} \\ c_{12} \\ c_{22} \end{bmatrix}. \tag{3.34}$$

We can write the partial structure factors $S_{ii'}(k)$ $(i, i' \in \{1, 2\})$ in terms of the direct correlation functions (DCFs) $c_{ii'}(k)$ as [148, 204, 205]

$$S_{12}(k) = \frac{\sqrt{x_1 x_2} n c_{12}(k)}{\Delta(k)}, \tag{3.35}$$

$$S_{11}(k) = \frac{1 - x_2 n c_{22}(k)}{\Delta(k)}, \tag{3.36}$$

$$S_{22}(k) = \frac{1 - x_1 n c_{11}(k)}{\Delta(k)}, \tag{3.37}$$

where

$$\Delta(k) = [1 - x_1 n c_{11}(k)] [1 - x_2 n c_{22}(k)] - x_1 x_2 n^2 c_{12}^2(k). \tag{3.38}$$

Various approximations for the DCFs yield corresponding approximations for $\mathcal{J}$. We give examples of such approximations in Secs. 3.3.1, 3.3.2, and 3.3.4 where we derive the thermodynamic factor from approximations of the DCFs for the following cases: classical weakly coupled plasmas, two-temperature electron-ion plasmas, partially degenerate dense plasmas, and strongly coupled plasmas. In Sec. 3.3.3, we derive the thermodynamic factor from estimates of the radial distribution functions (RDFs) $g_{ii'}(r)$, showing equivalence to the DCF approach.

When the system is at high temperature, transport coefficients will have the largest numerical value; thus, the thermodynamic factor in that limit is an important special case. Therefore, we

expand the exponential in Eq. (3.28) to obtain

$$c_{ii'}(r) = -\beta u_{ii'}(r), \tag{3.39}$$

which is referred to as the mean-field limit. Substituting Eq. (3.39) into Eq. (3.34) allows us to compute $h_{ii'}(k)$ directly; using $h_{ii'}(k)$, $\mathcal{J}$ can easily be found in k-space from Eq. (3.33). Using Eq. (3.39) and setting $B_{ii'}(r) = 0$ in the nonlinear form, Eq. (3.28), we arrive at an approximation for the RDFs in r-space

$$g_{ii'}(r) \approx \exp[h_{ii}(r)]. \tag{3.40}$$

Now, given an interaction potential $u_{ii'}(r)$, the pair correlation function $h_{ii'}(r)$ in Eq. (3.40) can be obtained by solving Eq. (3.34) for $h_{ii'}(k)$ and applying an inverse Fourier transform. Specifically, when $u_{ii'}(r) = u_{ii'}^{\mathrm{BYM}}(r)$, we have a non-linear (NL) model for the RDFs

$$g_{ii'}(r) \approx \exp\left(-\frac{\Gamma_{ii'}}{r} e^{-r\tilde{k}_t}\right), \tag{3.41}$$

where $\tilde{k}_t = \sqrt{\kappa^2 + 3x_1\Gamma_{11} + 3x_2\Gamma_{22}}$ is the dimensionless total screening wavevector, and $\kappa = a/\lambda_{TF}$. Notice the effective potential in Eq. (3.41) depends on the total screening length from all species, which arose from solving the mixture OZE in Eq. (3.34). Effective potentials with wider applicability beyond Eqs. (3.39) and (3.34) will be discussed in Sec. 3.3.4.

3.3.1 Classical Mean-Field Approximation

As mentioned in Sec. 3.3, hot plasmas that are classical and weakly coupled have the largest interdiffusion coefficients; mixing processes are rapid in such plasmas. Apart from some astrophysical plasmas, most laboratory plasmas have separate electron and ion temperatures; we allow for an independent electron temperature dependence through the effective ionic pair interaction. For two-temperature hot plasmas, we assume a standard Debye-Hückel model, which is expressed in terms of the mean-field DCF form, Eq. (3.39).

For plasma mixtures, the DCF can be written in Fourier space as

$$c_{ii'}(k) \approx -\frac{4\pi Z_i Z_{i'} e^2 \beta}{k^2 + k_e^2}. \tag{3.42}$$

Electronic screening of the ionic Coulomb interaction enters through the wavevector

$$k_e^2 = 4\pi e^2 \beta_e n_e. \tag{3.43}$$

Using Eq. (3.42), the partial structure factors are

$$S_{12}(k) = -\frac{\sqrt{x_1 x_2} Z_1 Z_2 k_r^2}{k^2 + k_e^2 + k_1^2 + k_2^2}, \tag{3.44}$$

$$S_{11}(k) = \frac{k^2 + k_e^2 + k_2^2}{k^2 + k_e^2 + k_1^2 + k_2^2}, \tag{3.45}$$

$$S_{22}(k) = \frac{k^2 + k_e^2 + k_1^2}{k^2 + k_e^2 + k_1^2 + k_2^2}, \tag{3.46}$$

in terms of reference and ionic species wavevectors

$$k_r^2 = 4\pi e^2 \beta n, \tag{3.47}$$

$$k_i^2 = 4\pi Z_i^2 e^2 \beta n_i, \tag{3.48}$$

respectively. Note the general trends that $S_{12}(k) < 0$ and $0 < S_{ii}(k) < 1$. Moreover, in the long-wavelength limit, there is no dependence on e^2, and when $\beta_e = \beta$, there is no temperature dependence, except possibly through the Z_i.

Using the intermediate results, Eqs. (3.44) - (3.46), in Eq. (3.21), the concentration-concentration structure factor is then

$$S_{cc}(k) = \frac{x_1 x_2 (k^2 + k_e^2 + k_r^2 \langle Z \rangle^2)}{k^2 + k_e^2 + k_r^2 \langle Z^2 \rangle}. \tag{3.49}$$

Taking the long-wavelength limit ($k \to 0$) of Eq. (3.49) and using Eq. (3.20), we have

$$\mathcal{J}^{\mathrm{DH}} = \frac{\beta_e \langle Z \rangle + \beta \langle Z^2 \rangle}{\beta_e \langle Z \rangle + \beta \langle Z \rangle^2}. \tag{3.50}$$

Equation (3.50) is the main result of this subsection and will be derived below in Eq. (3.69) using the RDFs to show the equivalence of the two approaches. The first terms in both the numerator and denominator arise from electronic screening; while Eq. (3.43) implies that the screening is given by classical electrons, the electronic wavevector could instead be chosen to include electron degeneracy via Thomas-Fermi screening, Eq. (3.31).

Note that Eq. (3.50) generalizes a prior result for a one-temperature plasma [194, 206],

$$\mathcal{J}^{\text{1T-DH}} = \frac{\langle Z \rangle + \langle Z^2 \rangle}{\langle Z \rangle + \langle Z \rangle^2}, \tag{3.51}$$

to two temperatures. Note that with this generalization we can examine the limit $\beta_e \to 0$ for fixed β (i.e., the limit in which the electrons have a much higher effective temperature than the ions); in that limit, Eq. (3.51) reduces to the known BIM limit [191],

$$\mathcal{J}^{\text{BIM}} = \frac{\langle Z^2 \rangle}{\langle Z \rangle^2}. \tag{3.52}$$

Unless otherwise noted, we use a Thomas-Fermi ionization model to determine the mean ionization state of each species in the mixture [151].

To assess the importance of electron screening in computing the thermodynamic factor, we compare calculations from Eqs. (3.51) and (3.52) as shown in column (a) of Fig. 3.2. At high temperatures, where ionization increases, the value of $\mathcal{J}$ increases. Additionally, when the number concentration differs (top and bottom rows), we find that the asymptotic value of $\mathcal{J}$ also differs. Column (b) shows the dependence of the value of $\mathcal{J}$ on ionization by using Eq. (3.51) for different combinations of fully ionized plasmas of species with charges Z_1 and Z_2. We see that as the difference in charge between the ion species increases, $\mathcal{J}$ also increases and is maximized in the most extreme case (e.g., H-Og mixtures). Column (c) shows the value of $\mathcal{J}$ in the two-temperature setting via Eq. (3.50); a strong dependence of $\mathcal{J}$ on the electron temperature is evident. The red diagonal line indicates where $T = T_e$, which is equivalent to using Eq. (3.51). The region above the red line ($T < T_e$) corresponds to plasmas produced using lasers in laboratory experiments. The region below the red line ($T > T_e$) shows common scenarios of plasmas produced by shocks.

It is worth commenting on the ideal-gas limit of $\mathcal{J}$; the results in Fig. 3.2 reveal that $\mathcal{J} \neq 1$. For neutral systems, such as Lennard-Jones systems, $\mathcal{J}$ is typically of order unity [161] and is strictly unity in the ideal-gas limit. The ideal-gas limit can be recovered by choosing $c_{ii'}(r) = 0$, which yields $S_{cc}(k) = 1$. However, the plasma case is qualitatively different from neutral systems [191]. Note that Eq. (3.51), which we expect to be accurate in hot plasmas, has no temperature dependence above temperatures at which a plasma is fully ionized. At very high temperatures, $\mathcal{J}$ has a constant,

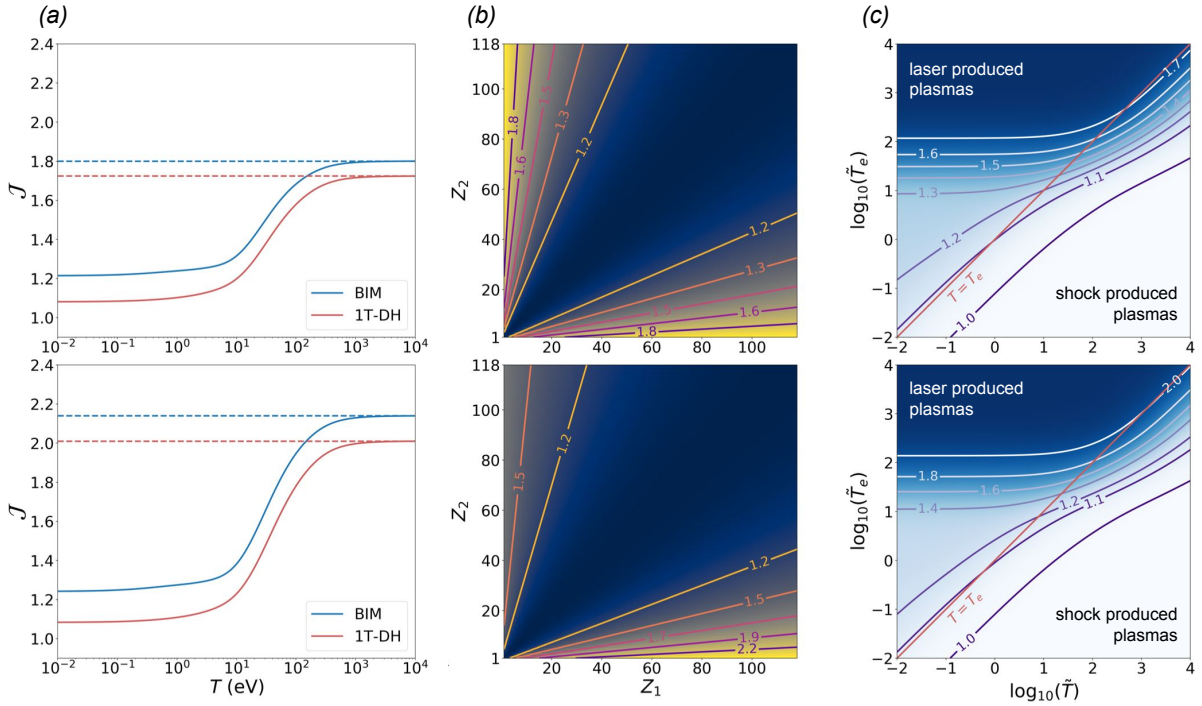

Figure 3.2: (a) Comparison of the thermodynamic factor $\mathcal{J}$ for a H-Ar binary mixture at $n = 10^{22}$ cm^{-3}. The subscript "1" denotes H, and "2" denotes Ar. In the top row, $x_1 = 0.5$; in the bottom row, $x_1 = 0.6$. Curves for $\mathcal{J}$ computed from Eqs. (3.51) and (3.52) are shown with their corresponding high temperature limiting values as dashed lines. (b) Contour lines show the thermodynamic factor for fully ionized mixtures (ranging from H to Og), calculated using Eq. (3.51). The contours show that $\mathcal{J}$ increases with the difference in charge between the species. The value of $\mathcal{J}$ is lowest for mixtures where $Z_1 \approx Z_2$. When $x_1 > x_2$, $\mathcal{J}$ increases more quickly with Z_1 than with Z_2. (c) Contours show $\mathcal{J}$ for the H-Ar mixture of (a) computed from the DH model Eq. (3.50), where $\tilde{T} = T/\text{eV}$ and $\tilde{T}_e = T_e/\text{eV}$. Note that $\mathcal{J}$ tends to unity as the ion temperature increases which is equivalent to setting $\beta = 0$ in Eq. (3.50). The red line along the diagonal shows where $T = T_e$, the situation described by Eq. (3.51). The region above the red line shows a typical scenario for a laser produced plasma. The region below the red line shows typical scenarios for shock produced plasmas.

non-unity value unless $\langle Z^2 \rangle = \langle Z \rangle^2$. The lack of an ideal-gas limit can be traced to the fact that screening decreases with increasing temperature because the interaction strength increases with temperature; unlike Lennard-Jones systems, plasmas have explicit temperature-dependent interactions that strengthen both as ionization increases and as screening decreases, yielding a $\mathcal{J}$ that tends to a constant, non-unity value at high temperatures. Mathematically, this can be seen by the fact that at very high temperatures $\mathcal{J}$ depends on charge ratios that are inherent to the plasma composition. The exception to this rule is the two-temperature plasma case in which there are very cold electrons ($\beta_e \to \infty$) and very hot ions ($\beta \to 0$), which yields $S_{cc}(0) \to 1$. (The inverse of this limit, $\beta_e \to \infty$, is the BIM case.) Cold electrons and hot ions could occur in a plasma shock wave; however, degeneracy plays a role in that low electron-temperature limit and predictions based on the models discussed so far are inadequate. Thus, we now turn to treating electronic degeneracy and exchange.

3.3.2 Yukawa Screening

We generalize the classical result, Eq. (3.50), to dense plasmas in which the electrons can be partially degenerate. We retain the functional form of Eq. (3.42) but allow for a more general form of the electron screening length k_e^{-1}; we will refer to such a model generically as a "Yukawa" model. As in the previous subsection, we allow for separate electron and ion temperatures.

The electronic wavevector in our Yukawa model is given by

$$k_{e-TF}^2 = \frac{1}{\lambda_{TF}^2}, \tag{3.53}$$

The electronic screening contribution now has a degeneracy correction through the Thomas-Fermi screening length λ_{TF}, Eq. (3.31), which generalizes Eq. (3.50) to

$$\mathcal{J}^{\mathrm{TF}} = \frac{\beta_e^{\mathrm{TF}} \langle Z \rangle + \beta \langle Z^2 \rangle}{\beta_e^{\mathrm{TF}} \langle Z \rangle + \beta \langle Z \rangle^2}, \tag{3.54}$$

where

$$\beta_e^{\mathrm{TF}} = \frac{1}{\sqrt{T_e^2 + \left(\frac{2}{3} E_F\right)^2}}. \tag{3.55}$$

Importantly, β_e^{TF} is finite for $T_e \to 0$ ($\beta_e \to \infty$). We can add a finite-temperature exchange-correlation (XC) contribution [12, 104, 207] to obtain the modified Yukawa electronic wavevector

$$k_{e-XC}^2 = \frac{1}{\lambda_{TF}^2 - \gamma_0}, \tag{3.56}$$

where γ_0 is defined as

$$\gamma_0 \approx \frac{\hbar^2 \beta_e \theta}{8 m_e}[h(\theta) - 2\theta h'(\theta)], \tag{3.57}$$

and we employ the form

$$h(\theta) = \frac{\mathcal{N}(\theta)}{\mathcal{D}(\theta)} \tanh(\theta^{-1}), \tag{3.58}$$

$$\mathcal{N}(\theta) = 1 + 2.8343\theta^2 - 0.2151\theta^3 + 5.2759\theta^4, \tag{3.59}$$

$$\mathcal{D}(\theta) = 1 + 3.9431\theta^2 + 7.9138\theta^4, \tag{3.60}$$

where $\theta = T_e / E_F$. These steps yield the thermodynamic factor

$$\mathcal{T}^{\mathrm{XC}} = \frac{\beta_e^{\mathrm{XC}} \langle Z \rangle + \beta \langle Z^2 \rangle}{\beta_e^{\mathrm{XC}} \langle Z \rangle + \beta \langle Z \rangle^2}, \tag{3.61}$$

where our final effective inverse electron temperature is

$$\beta_e^{\mathrm{XC}} = \frac{1}{\sqrt{T_e^2 + \left(\frac{2}{3} E_F\right)^2} - 4\pi n_e e^2 \gamma_0}. \tag{3.62}$$

The XC correction has the effect of lowering the effective temperature relative to its over-estimated Thomas-Fermi value.

3.3.3 Kirkwood-Buff Approach

All of the above derivations were preformed in k-space. However, approximate forms for the partial structure factors, and therefore $\mathcal{T}$, can be obtained through standard approximate forms for the RDFs. The partial structure factors are related to the RDFs by

$$S_{ii'}(k) = \delta_{ii'} + \sqrt{n_i n_{i'}} \int d^3 r \; [g_{ii'}(r) - 1] \, e^{i\mathbf{k}\cdot\mathbf{r}}. \tag{3.63}$$

In the long-wavelength limit, Eq. (3.63), reduces to

$$S_{ii'}(0) = \delta_{ii'} + \sqrt{n_i n_{i'}} \int_0^\infty dr \; 4\pi r^2 \; [g_{ii'}(r) - 1], \tag{3.64}$$

where $\delta_{ii'}$ is the Kronecker delta. The integral that appears here is related to the well-known Kirkwood-Buff integrals [183, 208, 209]

$$G_{ii'} = \int_0^\infty dr\, 4\pi r^2 \left[g_{ii'}(r) - 1\right], \tag{3.65}$$

which, using Eq. (3.21), yield

$$\mathcal{J} = \frac{1}{1 + x_2 n_1 \left(G_{11} + G_{22} - 2G_{12}\right)}. \tag{3.66}$$

With approximate forms for the RDFs, we can construct predictions for $\mathcal{J}$.

Approximate RDFs can be constructed in different limits. Because transport coefficients tend to be largest in hot plasmas,We first consider $\mathcal{J}$ in the high temperature limit. For example, hot plasmas are well described by Debye-Hückel theory, which, for a BYM, yields the RDFs and Kirkwood-Buff integrals

$$g_{ii'}(r) \approx 1 - \beta \frac{Z_i Z_{i'} e^2}{r} e^{-k_t r}, \tag{3.67}$$

$$G_{ii'} = -4\pi\beta Z_i Z_{i'} e^2 k_t^{-2}, \tag{3.68}$$

resulting in

$$\mathcal{J}^{\mathrm{DH}} = \frac{\beta_e \langle Z \rangle + \beta \langle Z^2 \rangle}{\beta_e \langle Z \rangle + \beta \langle Z \rangle^2}. \tag{3.69}$$

Note that Eq. (3.69) is identical to Eq. (3.50) but has been derived in r-space. Here, $k_t = \sqrt{k_e^2 + k_1^2 + k_2^2}$ is the total screening wavevector and k_e is given by Eq. (3.43). Note that by using alternative forms of k_e [e.g., Eqs. (3.53) or (3.56)] as inputs to k_t, we would arrive at Eqs. (3.54) and (3.61) respectively.

All results for analytic expressions of the thermodynamic factor, namely Eqs. (3.50), (3.54), and (3.61), have relied on the mean-field approximation, Eq. (3.39). While these results are applicable for hot plasmas, we wish to quantify conditions for which these analytic expression may fail. We begin by comparing estimates of the RDFs via Eq. (3.41) to results from MD simulation. Molecular dynamics simulations of a H-He BYM were carried out for a range of Γ_0 with $N = 10000$ particles and $x_1 = 0.5$, using standard techniques. Figure 3.3 shows the RDFs for MD simulations

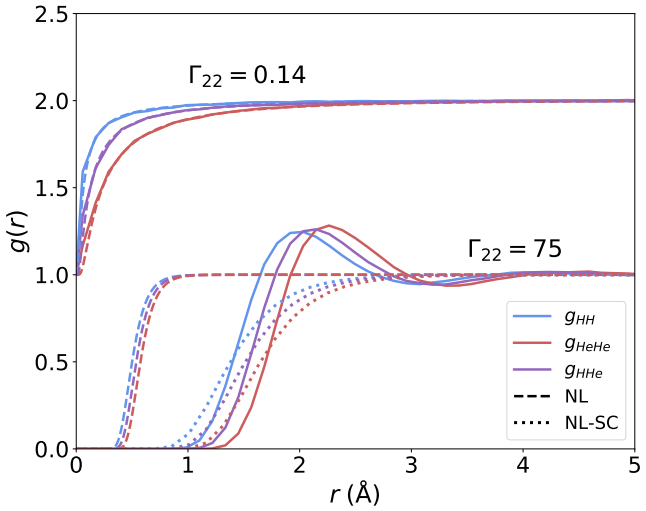

Figure 3.3: Hydrogen-helium RDFs generated from a MD simulation (solid lines) for a H-He BYM with $N = 10000$ particles and $n = 10^{23}\text{cm}^{-3}$ using standard techniques. Note that Γ_{22} denotes the Coulomb coupling between the He ions. For the weakly coupled case ($\Gamma_{22} = 0.14$), the RDFs have been vertically displaced by unity for clarity. The NL model accurately reproduces the RDFs for $\Gamma_{22} = 0.14$, but fails at strong coupling ($\Gamma_{22} = 75$) whereas the NL-SC model shows reasonable agreement.

corresponding to two values of Γ_{22}: a weakly coupled case ($\Gamma_{22} = 0.14$), and a strongly coupled case ($\Gamma_{22} = 75$). At $\Gamma_{22} = 0.14$, the NL approximation Eq. (3.41), shown with dashed lines, agrees with the MD results, differing most notably at small r. For the case of strong coupling ($\Gamma_{22} = 75$), the NL approximation fails and a strong-coupling correction is needed. Following [151], such a correction is introduced in the dimensionless total screening wavevector

$$\tilde{k}_t^{\text{SC}} = \sqrt{\kappa^2 + \sum_i \frac{3x_i\Gamma_{ii}}{1 + 3\left(\langle Z\rangle/Z_i\right)^{1/3}\Gamma_{ii}}}. \tag{3.70}$$

Together, Eqs. (3.70) and (3.41) result in a NL model with a strong-coupling correction (NL-SC) for the RDFs. We observe that the RDFs from the NL-SC model, shown with dotted lines for $\Gamma_{22} = 75$, show reasonable agreement with the MD results, revealing that the substantial improvement that Eq. (3.70) provides. The most notable improvement is observed in the “Coulomb hole" region.

For MD simulations, finite-size corrections to Eq. (3.65) must be considered [210] yielding

$$G_{ii'}^{FS} = \int_0^\infty dr\, 4\pi r^2 [g_{ii'}(r) - 1]\left(1 - \frac{3x^2}{2} + \frac{x^3}{2}\right), \tag{3.71}$$

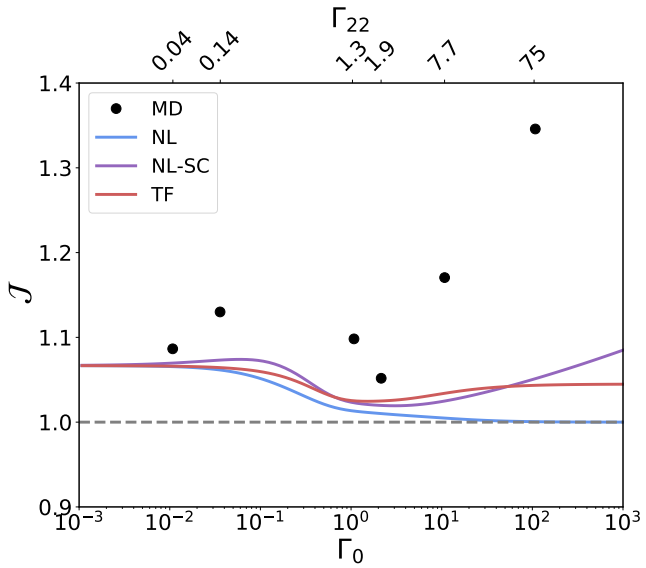

Figure 3.4: Thermodynamic factor for a H-He BYM. Note that Γ_{22} denotes the Coulomb coupling between the He ions in the mixture. The details of the MD are the same as in Fig. 3.3. The thermodynamic factor was computed from MD using Eq. (3.71). The grey dashed line denotes $\mathcal{J} = 1$. We note that the mean-field approximation for $\mathcal{J}$, Eq. (3.54), denoted as TF, begins to fails for $\Gamma_{22} > 2$.

where $x = r/L$ and L is the cutoff distance. Here, we chose L to be half the side length of the cubic simulation cell. Calculations of $\mathcal{J}$ via Eq. (3.71) are displayed in Fig. 3.4. We find that Eqs. (3.54), and (3.41), show excellent agreement with MD at weak coupling with less than a 2% error at $\Gamma_0 = 0.01$. The models remain accurate until roughly $\Gamma_0 = 11$ where the error increases to 12% for Eq. (3.54) and 14% for Eq. (3.41). Thus, based on results from Figs. 3.3 and 3.4, we conclude that the mean-field approximation, Eq. (3.39) and corresponding thermodynamic factors, Eqs. (3.50) - (3.52), (3.54), and (3.61), should only be used when $\Gamma_{22} < 2$; for $\Gamma_{22} > 2$, an alternate approach to treating strong coupling, which results in an analytic form for $\mathcal{J}$, is explored in the next section.

3.3.4 Strongly Coupled Plasmas

In Secs. 3.3.1 and 3.3.2 we obtain results that include ion and electron screening, electron degeneracy, finite temperature exchange, separate electron and ion temperatures, and strong coupling through the electronic wavevector Eq. (3.70). However, the absence of oscillatory behavior limits

their applicability to moderate coupling. In this subsection, based on numerical results from the hypernetted chain approximation for a BYM, we formulate a DCF to capture oscillations in $S_{ii'}(k)$ and $g_{ii'}(r)$. Our DCF model for strongly coupled plasmas is given in real space by an "empty-core" form

$$c_{ii'}(r) = \begin{cases} -\beta u_{ii'}(r^c_{ii'}), & r < r^c_{ii'}, \\ -\beta u_{ii'}(r), & r > r^c_{ii'}, \end{cases} \tag{3.72}$$

$$u_{ii'}(r) = \frac{Z_i Z_{i'} e^2}{r} e^{-k_e r}, \tag{3.73}$$

$$r^c_{ii'} = \frac{\Gamma_{ii'} d_{ii'}}{1 + \Gamma_{ii'}}. \tag{3.74}$$

where $d_{ii'}$ is the distance of closest approach. To determine $d_{ii'}$, one can measure the "Coulomb hole" portion of the RDFs (see Fig. 3.3). However, in order to produce an analytic expression for $\mathcal{J}$ that does not rely on computing the RDFs, we approximate $d_{ii'} \approx a_{ii'}$, where $a_{ii'} = (4\pi n_{ii'}/3)^{-1/3}$ and

$$n_{ii'} = \begin{cases} (n_i + n_{i'})/2, & i = i', \\ n, & i \neq i'. \end{cases} \tag{3.75}$$

Note that the DCF above could use any of the electronic wavevectors defined up to this point; therefore, we denote the electronic wavevector generically as k_e. Note that Eq. (3.72) reduces to the mean-field form, Eq. (3.39), in the limit $\Gamma_{ii'} \to 0$. In Fourier space, we find that

$$c_{ii'}(k) = -\frac{4\pi Z_i Z_{i'} e^2 \beta}{k^2 + k_e^2} \Lambda_{ii'}(k), \tag{3.76}$$

where

$$\Lambda_{ii'}(k) = \frac{k^2 + k_e^2}{k r^c_{ii'}} e^{-k_e r^c_{ii'}} \left[\frac{\sin(k r^c_{ii'}) - k r^c_{ii'} \cos(k r^c_{ii'})}{k^2} + \frac{k_e r^c_{ii'} \sin(k r^c_{ii'}) + k r^c_{ii'} \cos(k r^c_{ii'})}{k^2 + k_e^2} \right]. \tag{3.77}$$

The factor $\Lambda_{ii'}(k)$ is the strong-coupling correction factor, which has the long-wavelength limit

$$\Lambda_{ii'}(0) = \left(1 + k_e r^c_{ii'} + \frac{k_e^2 {r^c_{ii'}}^2}{3} \right) e^{-k_e r^c_{ii'}}. \tag{3.78}$$

The partial structure factors are then

$$S_{12}(k) = -\frac{\sqrt{x_1 x_2} Z_1 Z_2 k_r^2}{k^2 + k_e^2 + \Lambda_{11}(k) k_1^2 + \Lambda_{22}(k) k_2^2} \Lambda_{12}(k), \tag{3.79}$$

$$S_{11}(k) = \frac{k^2 + k_e^2 + \Lambda_{22}(k) k_2^2}{k^2 + k_e^2 + \Lambda_{11}(k) k_1^2 + \Lambda_{22}(k) k_2^2}, \tag{3.80}$$

$$S_{22}(k) = \frac{k^2 + k_e^2 + \Lambda_{11}(k) k_1^2}{k^2 + k_e^2 + \Lambda_{11}(k) k_1^2 + \Lambda_{22}(k) k_2^2}, \tag{3.81}$$

from which the concentration-concentration structure factor can be obtained.

Our final form for the thermodynamic factor that allows for two temperatures, degeneracy and strong coupling is then

$$\mathcal{J}^{\text{TF-SC}} = \frac{\beta_e^{\text{TF}} \langle Z \rangle + \beta \mathcal{T}(0)}{\beta_e^{\text{TF}} \langle Z \rangle + \beta \mathcal{B}(0)}, \tag{3.82}$$

$$\mathcal{T}(0) = x_1 Z_1^2 \Lambda_{11}(0) + x_2 Z_2^2 \Lambda_{22}(0), \tag{3.83}$$

$$\mathcal{B}(0) = x_1^2 Z_1^2 \Lambda_{11}(0) + x_2^2 Z_2^2 \Lambda_{22}(0) + 2 x_1 x_2 Z_1 Z_2 \Lambda_{12}(0), \tag{3.84}$$

where we have used the electronic wavevector Eq. (3.31).

We compare the impact of each screening model on $\mathcal{J}$ in Fig. 3.5 for a H-Ar mixture at density $n = 10^{22}\text{cm}^{-3}$ for $x_1 = 0.5$. In panel (a), screening is approximated via a Debye-Hückel formulation, Eq. (3.50). In (b), the addition of degeneracy with Eq. (3.54) changes the low-temperature behavior of $\mathcal{J}$. In (c), the XC correction Eq. (3.61) once again changes the low-temperature behavior of $\mathcal{J}$. The regions where $\beta_e^{\text{XC}} < 0$ or $\theta < 0.1$ have been omitted as the XC correction either fails (in the case of negative screening) or may be inaccurate (when $\theta < 0.1$ [207]). Additionally, the accuracy of the XC correction is unknown for $\theta > 12$; as a result, we set $\gamma_0 = 0$ and recover Eq. (3.31). Panel (d) shows the impact of strong coupling; the value of $\mathcal{J}$ is lower at lower ion temperatures in this case than in the cases shown in panels (a) and (b).

To assess the validity of the analytic expressions for $\mathcal{J}$ we have derived, Table 3.2 shows a comparison of different forms of $\mathcal{J}$ and results from MD simulation or the hypernetted chain approximation. For the strongly coupled H^+-C^{4+} BYM, the strong-coupling correction, Eq. (3.82), is accurate to the hypernetted chain results to within 6%. For the moderately coupled H^+-Al^{6+} BYM, Eq. (3.61) is within 5% of the MD data.

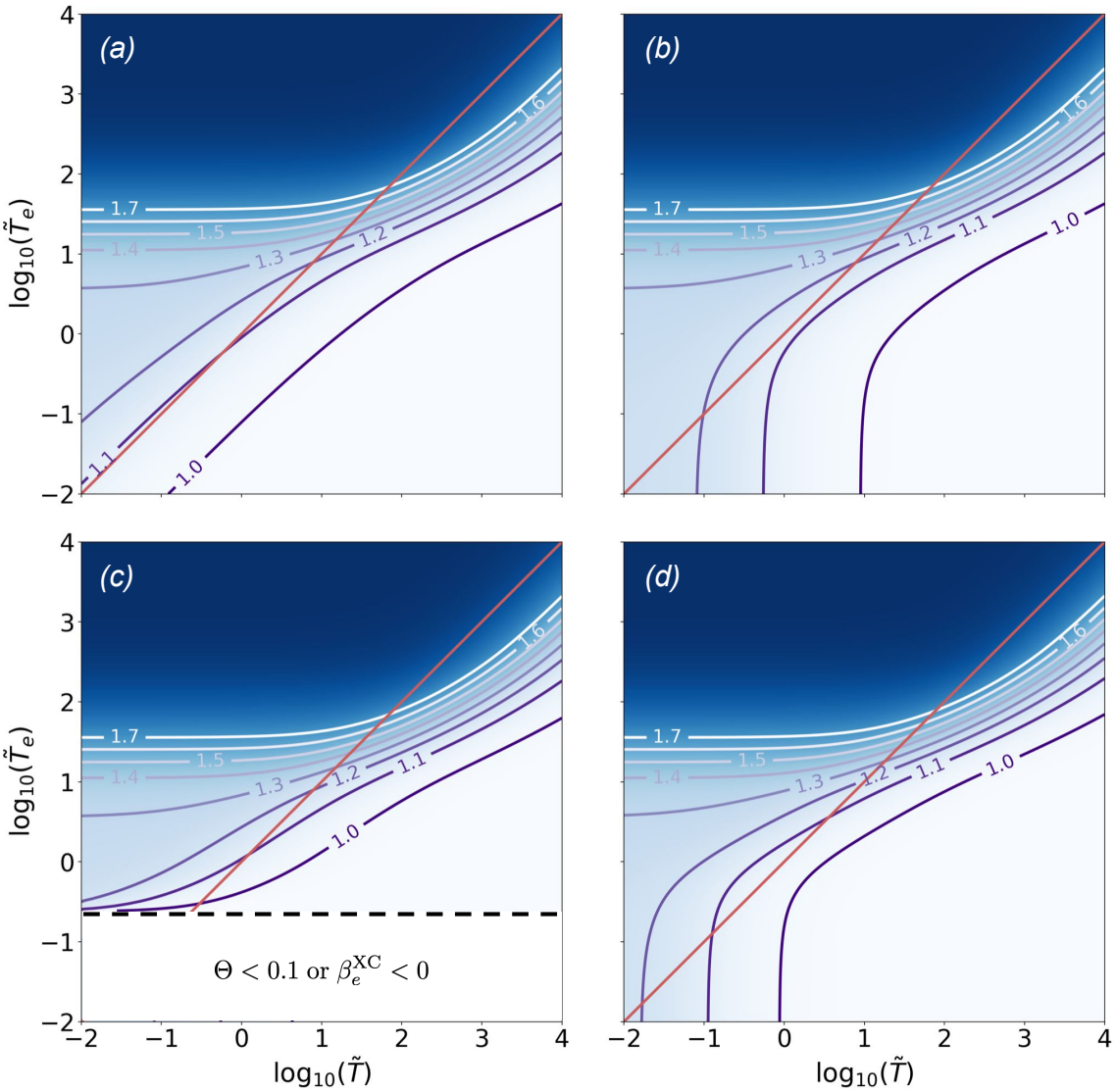

Figure 3.5: Comparison of $\mathcal{J}$ for a H-Ar plasma at $n = 10^{22}\mathrm{cm}^{-3}$ for $x_1 = 0.5$. As in Fig. 3.2, $\tilde{T} = T/\mathrm{eV}$ and $\tilde{T}_e = T_e/\mathrm{eV}$. (*a*) The electrons are treated classically with Debye-Hückel screening, Eq. (3.50). (*b*) Degeneracy is included with Thomas-Fermi screening, Eq. (3.54). (*c*) An XC correction is added, Eq. (3.61), which fails in the region below the dashed horizontal line. The failure occurs because either $\theta < 0.1$ (as described in Ref. [207]) or $\beta_e^{\mathrm{XC}} < 0$. (*d*) Strong coupling is included, Eq. (3.82). The red line shows the case in which $T = T_e$; this case is equivalent to Eq. (3.51).

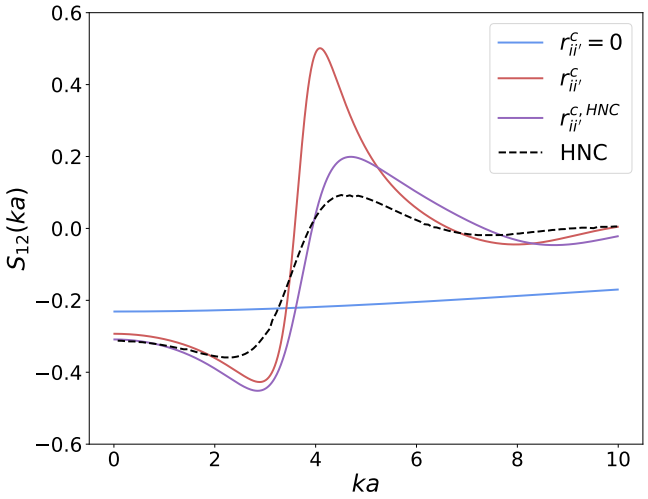

Figure 3.6: The mixture partial structure factor $S_{12}(k)$, Eq. (3.79), of a H^+-C^{4+} BYM at $n = 5 \times 10^{23}$ cm^{-3}, where $x_1 = 0.5$ and $T = 1.7$ eV. The hypernetted chain results, denoted as HNC, were obtained from Ref. [211]. The strong-coupling correction, Eq. (3.79), with distance of closest approach estimated from the RDFs of the HNC results is denoted as $r^{c,HNC}_{ii'}$. The strong-coupling correction using Eq. (3.75), is denoted as $r^c_{ii'}$. When $r^c_{ii'} = 0$, we obtain the mean-field result, Eq. (3.44). Note that the strong-coupling correction accurately approximates $k = 0$ and predicts oscillations.

Additionally, we compare the results of the $S_{12}(k)$ with a hypernetted chain calculation [211]. In Fig. 3.6, we evaluate Eqs. (3.44) and (3.79) using Eq. (3.31). The distances of closest approach $d_{ii'}$ are approximated from the corresponding RDFs in Ref. [211]. Specifically, their values are $d_{11} = 0.5$, $d_{12} = 0.9$, and $d_{22} = 1.25$. The prediction for Eq. (3.79) using these values of $d_{ii'}$ is denoted as $r^{c,HNC}_{ii'}$ in Fig. 3.6. For the entire domain of k, Eq. (3.79) shows reasonable agreement with the hypernetted chain calculations, and excellent agreement is achieved as $k \to 0$. Predictions of the partial structure factor are also computed by using Eq. (3.79) with the distance of closest approach from Eq. (3.75), are denoted as $r^c_{ii'}$. The predictions show reasonable agreement as $k \to 0$. The agreement in this limit increases our confidence in the resulting thermodynamic factor from Eq. (3.79).

3.4 Interdiffusion Models

The previous sections have focused on approximations to DCFs and the resulting thermodynamic factors. We now turn our focus to two analytic models for the interdiffusion coefficient, including

an analytic expression for the BIM autocorrelation function. The models are then compared with MD data for a H^+-He^{2+} BIM.

3.4.1 BIM Gaussian Autocorrelation Function

We begin by deriving an analytic expression for the interdiffusion coefficient of a BIM. To do this, we rewrite the Green-Kubo result of Eq. (3.16) in terms of a normalized autocorrelation function $J(t)$ as

$$J(t) = \frac{\langle \mathbf{j}(t) \cdot \mathbf{j}(0) \rangle}{\langle \mathbf{j}(0) \cdot \mathbf{j}(0) \rangle}, \tag{3.85}$$

$$D = \frac{\mathcal{J}}{\beta \langle M \rangle m_1 m_2} \int_0^\infty dt J(t). \tag{3.86}$$

Given the known behaviors of autocorrelation functions at short and long times [148, 212], we propose a Gaussian ansatz [213] for $J(t)$ of the form

$$J(t) = \exp\left(-\Omega^2 t^2/2\right), \tag{3.87}$$

which satisfies $d^2J(0)/dt^2 = -\Omega^2$. Here, Ω is the Einstein frequency associated with interdiffusion; Hansen *e*t al. [181] compute this quantity for a BIM and obtain

$$\Omega = \frac{\omega_p}{\sqrt{3}} \sqrt{\frac{x_1 m_1^2 z_2 + x_2 m_2^2 z_1}{m_1 m_2}}, \tag{3.88}$$

which is the familiar relation between the hydrodynamic plasma frequency Eq. (3.19) and the Einstein frequency generalized to a BIM [181]. Statistical mechanics reveals that autocorrelation functions are even in time [148] and decay to zero; these requirements are approximately satisfied with a Gaussian ansatz. For a normalized autocorrelation function, this is a single-parameter model that can be computed analytically for the case of a BIM [181]. Such an ansatz is reasonably accurate for strong coupling, although in principle, a richer ansatz could be used [212] if more parameters could be determined (e.g., fit to MD data).

The reduced interdiffusion coefficient in this Gaussian approximation is then

$$D^*_{GAF} = \frac{\mathcal{J}\sqrt{6\pi}}{3\langle Z \rangle^2 \Gamma_0 \sqrt{x_1 m_1^3 m_2 z_2 + x_2 m_1 m_2^3 z_1}}. \tag{3.89}$$

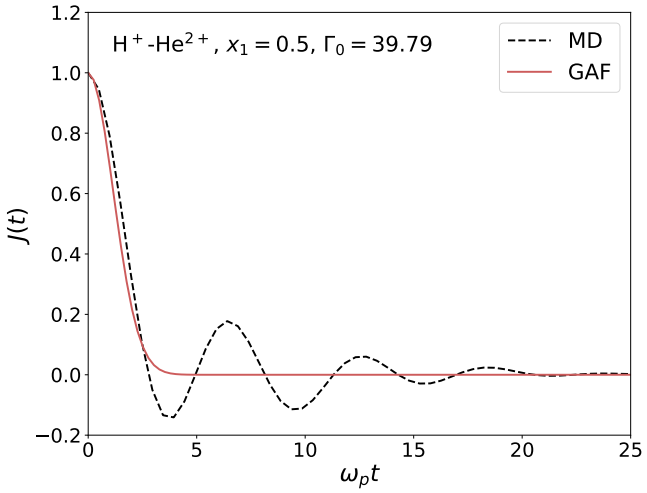

Figure 3.7: Autocorrelation function for a H^+-He^{2+} BIM versus time. The system conditions are the same as described in Table 3.2, and we compute $\Omega/\omega_p = 0.87$. The GAF approximates the early-time decay of the autocorrelation function calculated from MD data.

We will refer to the above model as the Gaussian autocorrelation function (GAF) model. Taking the GAF model together with the thermodynamic factors from Sec. 3.3, we have a complete, albeit approximate, analytical model of interdiffusion. We compare an autocorrelation function calculated using the Gaussian ansatz, Eq. (3.87), to one computed from MD simulation data of H^+-He^{2+} BIM in Fig. 3.7. We see that the early-time decay of $J(t)$ computed using the GAF is comparable to that found with a direct computation from MD data. The GAF model, Eq. (3.89), is most accurate when the decay is roughly exponential, as is the case for strongly coupled plasmas. The GAF model relies on the cancellation of oscillations in the integral of the autocorrelation function to generate an accurate value for the interdiffusion coefficient.

Such a simple result arises only for a BIM. Below, we will explore the accuracy of the GAF model compared with a transport theory that has been derived from an effective interaction potential in a Boltzmann kinetic theory framework [151].

3.4.2 Stanton-Murillo Transport Model

The analytic model, Eq. (3.89), by definition, includes no screening effects. The Stanton-Murillo transport (SMT) model, however, includes screening effects in the effective interaction potential that is used to compute the collision integrals numerically. From the SMT model [151],

mixture	x_1	Γ_0	θ	$\mathcal{J}^{\text{BIM}}$	$\mathcal{J}^{\text{DH}}$	$\mathcal{J}^{\text{TF}}$	$\mathcal{J}^{\text{XC}}$	$\mathcal{J}^{\text{DH-SC}}$	$\mathcal{J}^{\text{TF-SC}}$	$\mathcal{J}$
H^+-He^{2+} (BIM)	0.5	40	0.5	1.11						1.03^a
H^+-C^{4+} (BYM)	0.5	11	0.1		1.26	1.35		0.99	1.23	1.16^b
H^+-Al^{6+} (BYM)	0.3	1.5	0.3		1.21	1.24	1.25	1.15	1.21	1.31^a

Table 3.2: Comparison of the thermodynamic factor $\mathcal{J}$ from different models with those from MD (denoted with superscript "a") and the hypernetted chain approximation (denoted with superscript "b") [211] results. To compute $\mathcal{J}$ for cases a and b, Eq. (3.20) was employed. The MD simulations were carried out for $N = 2000$ particle using standard techniques. After computing the partial structure factors, an extrapolation to $k = 0$ was implemented. $\mathcal{J}^{\text{DH-SC}}$ corresponds to the strong-coupling correction, Eq. (3.82) using (3.43).

we have the following expression for the interdiffusion in a BYM:

$$D_{SMT} = \frac{3T^{5/2}}{16\sqrt{2\pi\mu_{12}}nZ_1^2Z_2^2e^4\mathcal{K}_{11}(g)}, \tag{3.90}$$

where $\mu_{12} = M_1M_2/(M_1+M_2)$, and $K_{nm}(g)$ is a fit to the collision integral for the effective coupling g. The expression for $K_{nm}(g)$ is given in Appendix C of [151]. For a BIM, the effective coupling g is

$$g = \Gamma_{12}\left[\sum_{i=1}^{2}\frac{3x_i\Gamma_{ii}}{1+3(x_i/Z_in_i)^{1/3}\Gamma_{ii}}\right]^{1/2}. \tag{3.91}$$

We note that in Ref. [151], the numerator of the summation term was written as $3x_i^{-1}\Gamma_{ii}$, when it should be $3x_i\Gamma_{ii}$ as written here. In Ref. [181], the interdiffusion coefficient was computed for H^+-He^{2+} mixtures for three cross-species coupling parameters $\Gamma_{12} = 0.8, 8, 80$. We compare the interdiffusion coefficient calculated from this data with those computed using the GAF and SMT models, and the results are shown in Fig. 3.8. We see that the simple form of the GAF model estimates the interdiffusion coefficient for moderate and strong coupling reasonably well, with errors similar to those of the SMT model. However, for weak coupling, the GAF model begins to fail, while the SMT model remains accurate.

3.5 Conclusions and Outlook

In summary, we have explored interdiffusion in plasmas with a focus on the Darken relation that thermodynamic factor. The Darken relation simplifies the autocorrelation function necessary for computing interdiffusion by neglecting cross-species current correlations. By comparing the

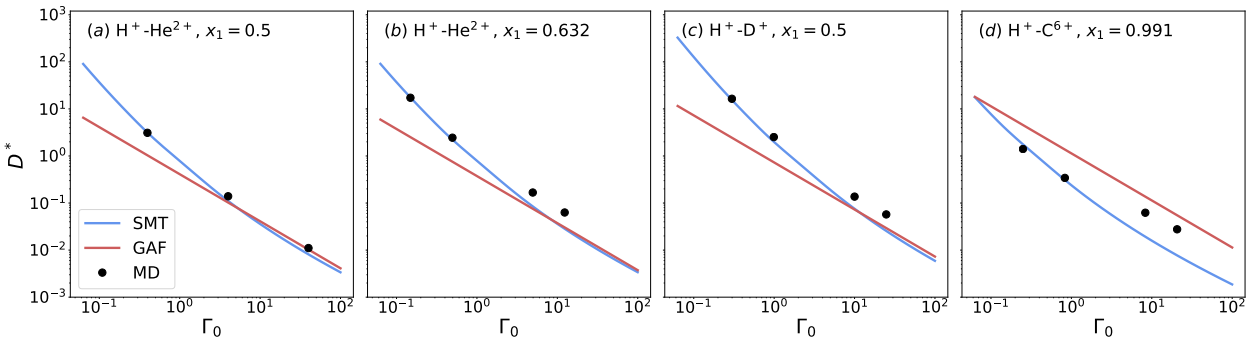

Figure 3.8: Normalized interdiffusion coefficient D^* of various BIMs. The MD data in (a)–(d) was collected from Refs. [181, 214]. The GAF model accurately reproduces the MD data at moderate and strong coupling but fails at weak coupling.

Darken approximation to the full result, we found that the Darken relation results in smaller statistical errors, but does not converge to the full result. To explore the possible advantages of the Darken relation, we set up a series of MD simulations of varying lengths. For short simulations, the full result had larger uncertainty but a mean value that was comparable to the Darken approximation; thus, showing that the Darken relation was not advantageous. At increasingly longer simulations, we identify where the uncertainty bands no longer overlapped, highlighting where the Darken relation fails. Further studies for a wider range of systems is warranted.

Next, we turned to the development of rapidly computable analytic expressions for the thermodynamic factor to model plasmas in disparate regimes. We provide the derivation of Eqs. (3.52) and (3.51) revealing the physical regime in which they apply. Furthermore, we have generalized Eq. (3.51) to allow for separate electron and ion temperatures, allowing for a description of laser or shock produced plasmas. We account for electron degeneracy with Thomas-Fermi screening and finite temperature exchange. We extended these results to strong coupling in two ways: by including a modified screening length and through an empty-core DCF. Comparisons to MD and hypernetted chain calculations give confidence of their use but a more comprehensive study should be performed.

We formulated a complete model for the interdiffusion of a BIM using a GAF, which is based on the short-time expansion of the interdiffusion current correlation function. A comparison of the GAF model with MD data shows reasonable accuracy in the intermediate to strong coupling

regime. However, at weak coupling, the GAF model begins to fail and but the SMT model remains accurate. Combining the GAF and SMT models, gives a reasonable prediction for interdiffusion across the entire coupling regime.

There are many opportunities to extend the results presented here. First, the inputs to the analytic expressions derived here could be improved upon with a more robust finite-temperature exchange-correlation potential. Furthermore, numerical calculations of the hypernetted chain equations allows one to calculate quantities of interest (e.g., $g_{ii'}(r), S_{ii'}(k)$, $\mathcal{J}$, etc.) for strongly coupled systems. Such calculations have a slightly increased computational cost relative to the results here but much less than MD.Additionally, we assumed that the pair-interaction potentials were Coulombic. That assumption may not apply to warm dense matter and a pair-interaction potential with gradient corrections [104] or one constructed from N-body MD simulations with force matching [87] may be needed.

CHAPTER 4

MULTI-FIDELITY REGRESSION FOR PLASMA PROPERTIES DATA

4.1 Introduction

The types of plasmas that were studied in Chapters 2 and 3 were strongly coupled plasmas that spanned both the non-degenerate and degenerate regimes. In this chapter[1], we expand the scope of our study and parameter regime to include weakly coupled plasmas. Our aim is to make accurate predictions of ionic transport property data across two disparate physical regimes: the strongly coupled and weakly coupled regimes. Having accurate predictions of transport coefficients and equations of state across these regimes is necessary for closures of macroscopic simulations of plasmas at large time and length scales. Due to the computational cost associated with generating microscopic data, closure data is typically precomputed and cast in the form of "look-up" tables which are used as inputs to macroscopic simulations. Because it is impossible to generate a look-up table with infinitely small resolution, interpolation between values is needed. These interpolation methods should be robust by providing uncertainty associated with the interpolation as well as numerically efficient for high-dimensional data. As mentioned in Chapter 2, the fidelity of numerical results rely directly on these look-up tables and therefore it is of interest to 1) quantify uncertainty associated with using models to generate them, and 2) create tables that are wide-ranging that agree with known results in limiting regimes (e.g., the ideal-gas law).

The plasma conditions we study here are displayed in Figure 4.1 which include four elements pertinent to HED experiments across a wide temperature regime. Because out dataset is multi-modal and uses a low fidelity model that is rapidly computable anywhere in this range of conditions, we have continuous lines throughout the $\Gamma - \theta$ plane in Figure 4.1(a). We also note that Figure 4.1(b) highlights that our study spans well into the highly-collisional and free-flight regimes.

The low-fidelity (LF) models used in this work provide a computationally efficient, wide-

[1]The content described in this chapter was reproduced from *Lucas J. Stanek, Shaunak D. Bopardikar, and Michael S. Murillo, "Multifidelity regression of sparse plasma transport data available in disparate physical regimes", Physical Review E 104, 065303 (2021) https://doi.org/10.1103/PhysRevE.104.065303*. This article was published by the American Physical Society under the terms of the Creative Commons Attribution 4.0 International license and has been modified to address the requirements of this dissertation; see Ref. [215] for the full published article.

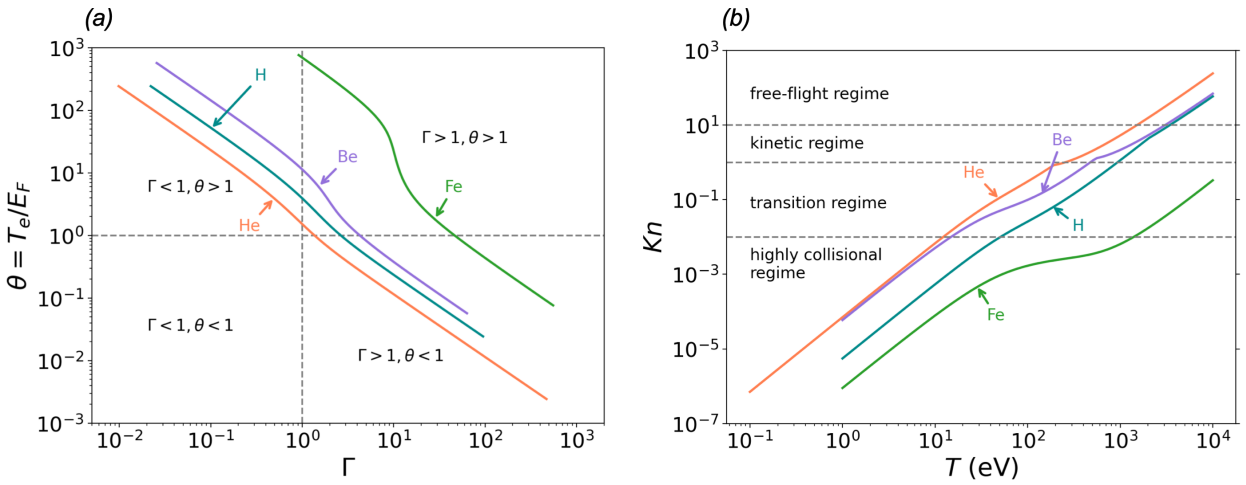

Figure 4.1: (a) electron degeneracy parameter versus coulomb coupling parameter and (b) Knudsen number versus temperature for all plasma conditions of this chapter. Note that the Knudsen number ranges from the highly collisional regime to the free-flight regime. A goal of this chapter is to use high-fidelity data that is local to the highly-collisional regime and free-flight regime to make predictions across the transition and kinetic regimes.

ranging prediction of transport coefficients that span disparate regimes. However the LF models lacks accuracy in certain regimes where high-fidelity (HF) data are needed. The generation HF data requires substantial resources that limit the volume of data that can be generated. Moreover, the size and scope of datasets are constrained by the experimental accessibility of physical regimes and by the applicability and efficiency of computational models. These limitations can be addressed by combining data from several sources to form a dataset that contains multiple, separated point clouds that can be "interpolated." For example, the equation of state can be measured in one regime with a laser-heated diamond anvil cell [216] and computed in another regime with accurate electronic-structure methods [217]. Or, one may combine experimental data obtained along a shock Hugoniot with computational data available only at very low temperatures. Computational models for equations of state, atomic properties, and charged-particle transport [12, 87, 180, 218] can also be combined to create a larger dataset.

Combining data sources in this way creates two challenges. First, predictions will be based on data in potentially very different physical regimes. Second, while it is natural to consider adding LF data, which can be generated cheaply, to datasets to cover a parameter space more uniformly, it

is not clear how to exploit such LF data in making predictions.

Machine-learning (ML) methods offer promising alternative frameworks for interpolating physical data [115, 219, 220]. ML treats the interpolation problem as regression in a high-dimensional space using non-traditional techniques such as neural networks. Gaussian-process regression [221] (GPR) is a nonparametric ML technique that interpolates data in multiple dimensions; importantly, GPR provides an uncertainty estimate that can be used to suggest where new data points should be acquired.

Here, we will explore GPR as an approach for interpolating physical data. In particular, we will examine the situation in which there are islands of HF data in parameter space, possibly from different sources, and we will fill the space between these islands with easier-to-compute LF data. Such an approach utilizes multi-fidelity (MF) extensions [222] of GPR. Here, we use GPR to refer to the methodology described in [221], and MF-GPR to refer to its MF extensions [222–225].

The generality of MF-GPR methods enables their use in many disciplines and applications [226–233]. The original MF-GPR framework has been improved to reduce the risk of overfitting during the training procedure [225], to include nonlinear relationships between LF and HF models [223, 224], and to address concerns that arise with diverse data structures and dataset selection [234, 235].

This chapter is organized as follows. As described in the following section, we will illustrate our ML ideas using the example of ionic transport coefficients. The methods we used to generate our dataset of ionic transport coefficients are discussed in Sec. 4.2.1. In Sec. 4.2.2, we compare single-fidelity regression methods and highlight the benefit of GPR over simple cubic spline regression. We then transition to MF regression and discuss the formulation of MF-GPR, as introduced by Kennedy and O'Hagan [222], in Sec. 4.2.3. Using toy examples, we show when MF-GPR adds value over single-fidelity GPR; we also show where improvements to this formulation are needed. We conclude Sec. 4.2.3 by reporting a table of computation times and regression errors for MF-GPR and single-fidelity GPR to assess the cost-benefit trade-off for these methods.

Sec. 4.3 illustrates an approach for choosing an LF model that is the most appropriate for an

MF-GPR setting and examines how this choice impacts the resulting MF-GPR fit. A natural choice for LF and HF models are those with the same output quantity (e.g., both predict the viscosity of a system). However, the outputs of both models need not be the same quantities. We explore the use of models in MF-GPR that have different output quantities, as well as different levels of computational complexity.

In Sec. 4.4.1, we compare regression errors resulting from single-fidelity GPR and MF-GPR analyses of sparse, disparate plasma transport-coefficient datasets. We find that while MF-GPR may result in modestly smaller errors compared to single-fidelity GPR, the uncertainty of the MF-GPR prediction is consistently much smaller. Finally, in Sec. 4.4.2, we compare three approaches for sampling HF data to reduce the MF-GPR regression error. For a fixed number of HF data points, a simple approach we explored outperforms sampling from a uniform grid. We offer conclusions and discuss potential areas for future work in Sec. 4.5.

4.2 Dataset and Regression Methods

In this section, we discuss our dataset and review the ML approaches we will employ in Secs. 4.3 and 4.4. We begin in Sec. 4.2.1 by describing plasma transport-coefficient data and the fidelities of several commonly used models based on the approximations they employ. In Secs. 4.2.2 and 4.2.3, we describe the GPR methodology, including standard, single-fidelity GPR and its MF generalization. Our goals in Secs. 4.2.2 and 4.2.3 are to answer the following questions: what value does GPR add compared to simpler regression methods? And, how does including data from multiple levels of fidelity impact a prediction?

4.2.1 Ionic Transport-Coefficient Dataset

For our study, we chose to explore MF-GPR in the context of plasma ionic transport coefficients because plasmas span many orders of magnitude in density, temperature and nuclear charge. Plasmas can include many species, which makes it difficult to use a single (computational or experimental) method to make accurate predictions. Computational methods that are typically used can be divided into LF and HF methods by examining the underlying assumptions of the

models. Moreover, we can usually identify a limited parameter regime in which each model is HF. These delineations occur because the theoretical models that underpin the computational methods are known to have high accuracy only in certain limits (e.g., asymptotically at high temperature); methods that are not asymptotically accurate in a parameter regime are designated as LF there. The limiting regimes typically depend on multiple dimensionless parameters (e.g., the Coulomb coupling parameter and the degeneracy parameter) that rely on some combination of nuclear charge, density, and temperature of the system. We will use just the temperature of the system to specify the limiting regimes since models developed at extremes of temperature tend to have very different assumptions.

Data in the low-temperature regime, loosely defined here as $T < O(10^1)$ eV, and in a high-temperature regime, defined here as $T > O(10^3)$ eV, will be generated using appropriate LF and HF models. For the self-diffusion transport coefficient D, we will use the following HF models to generate data. At low temperatures, the HF data are obtained from density functional theory molecular dynamics (DFT-MD) simulations [83, 236–238], which accurately calculate the electronic structure on-the-fly. At high temperatures, the Stanton-Murillo transport (SMT) model [151], which uses numerically computed cross-sections and an effective interaction potential, is employed. The LF model used across the entire temperature range is given by Hansen, McDonald, and Pollock (HMP) for a one-component plasma (OCP) [239].

Similarly, for viscosity η, we use one HF model at low temperatures and a different HF model at high temperatures. Once again, the HF data at low temperatures are obtained from DFT-MD simulations. We employ the Yukawa viscosity model (YVM) [140], which is based on a quasi-universal form fit to MD data, as our HF model at high temperatures. Our LF model is derived from a correspondence between an OCP system and a Yukawa system. The correspondence is obtained from the Gibbs-Bogolyubov inequality [137]; this model will be referred to as the YGBI model.

The HF and LF models for the self-diffusion and viscosity coefficients in each temperature range are summarized in Table 4.1. These models are used in analyses presented in Sec. 4.4.1.

Coeff.	T (eV)	HF	LF
D	$T < O(10^1)$	DFT-MD [83, 236–238]	HMP [239]
	$O(10^1) < T < O(10^3)$	–	HMP [239]
	$T > O(10^3)$	SMT [151]	HMP [239]
η	$T < O(10^1)$	DFT-MD [83, 236–238]	YGBI [137]
	$O(10^1) < T < O(10^3)$	–	YGBI [137]
	$T > O(10^3)$	YVM [140]	YGBI [137]

Table 4.1: HF and LF models for the self-diffusion and viscosity transport coefficients in each temperature regime. Each LF model is used across the entire temperature range.

4.2.2 Single-Fidelity Regression

To provide a baseline to which results of MF-GPR can be compared in later sections, we first consider approaches that require only one level of data fidelity, i.e., single-fidelity approaches. We consider cubic-spline regression and GPR. Cubic-spline regression is a parametric regression method that aims to determine the optimal *parameters* that define a cubic-spline fit to data. In contrast, GPR is a nonparametric regression approach that determines the optimal *function* that is fit to data. We begin with a brief overview of GPR that will provide a framework for understanding its MF generalization.

We introduce GPR with a discussion of prior and posterior distributions. Before observing the data, we have some prior beliefs about functions that are suitable. These functions are drawn from a *prior distribution*: a distribution of random functions that are consistent with our prior beliefs about the data. An example of a prior distribution is one in which the distribution of functions have zero mean at each input point and vary smoothly over the entire input space. For plasma transport data, we could impose constraints on our prior distribution of functions to enforce nonnegativity and such that the functions reflect the known behaviors of different transport coefficients (e.g., increasing with temperature). After constructing a prior distribution, a *posterior distribution* is created by using available data to constrain the random functions by ensuring that they pass through the observed data points. As we will see, the mean and the covariance matrix of a posterior distribution are the prediction and uncertainty estimates of GPR.

Defining the prior and posterior distributions for GPR requires a kernel function that defines a measure of similarity among the input variables of a dataset. The kernel function determines the representation of the functions from the prior and posterior distributions (e.g., smoothness, periodicity, etc.). A common choice of kernel function, that we will use here, is the squared-exponential kernel

$$k(x_i, x_j; \sigma^2, \ell) = \sigma^2 \exp\left(-\frac{1}{2\ell^2}\|x_i - x_j\|^2\right), \tag{4.1}$$

where for d-dimensional data, we have m points $x_i \in \mathbb{R}^d$ and n points $x_j \in \mathbb{R}^d$. Evaluating the kernel $k(x_i, x_j; \sigma^2, \ell)$ gives the ijth entry of the kernel matrix (or covariance matrix) $K \in \mathbb{R}^{m\times n}$. The hyperparameters of Eq. (4.1) are the variance σ^2 and the length scale ℓ; they will be compactly denoted as the set $\theta \in \{\sigma^2, \ell\}$. These hyperparameters reveal the strength and extent of correlations in the data. As we will see, the values of the hyperparameters are particularly useful for quantifying the quality of MF-GPR methods.

A single-fidelity GPR problem is posed as follows: *given a set of n training points in d dimensions, represented by the columns of a matrix* $X_{SF} \in \mathbb{R}^{d\times n}$ *and the corresponding (scalar) output values* $y \in \mathbb{R}^n$ *of the unknown function at each training point, predict the value of the unknown function at a set of m test points* $X_* \in \mathbb{R}^{d\times m}$. As shown in Ref. [221], the posterior distribution of the unknown function using GPR at the new set of data points X_* is a multivariate Gaussian with mean $\boldsymbol{\mu}_*$ and covariance Σ_* given by

$$\boldsymbol{\mu}_*(X_*) = K(X_*, X_{SF}; \theta)K(X_{SF}, X_{SF}; \theta)^{-1} y, \tag{4.2}$$

$$\Sigma_*(X_*) = K(X_*, X_*; \theta) - K(X_*, X_{SF}; \theta)K(X_{SF}, X_{SF}; \theta)^{-1}K(X_{SF}, X_*; \theta), \tag{4.3}$$

where the hyperparameters θ of the kernel function are determined by optimizing the log-likelihood function $\mathcal{L}(y, X_{SF}, \theta)$, as discussed in Ref. [221]. The function $\mathcal{L}$ measures the likelihood that the observations are given by the values y at training locations X_{SF} for a given value of θ.

We now examine a simple example of GPR and compare with a cubic spline interpolation. Viscosity data were generated using the YVM for the element C at $n_i = 5.01 \times 10^{22}$ cm^{-3}, and fits to these data using GPR [240] and cubic-spline regression [241] are shown in Fig. 4.2. The

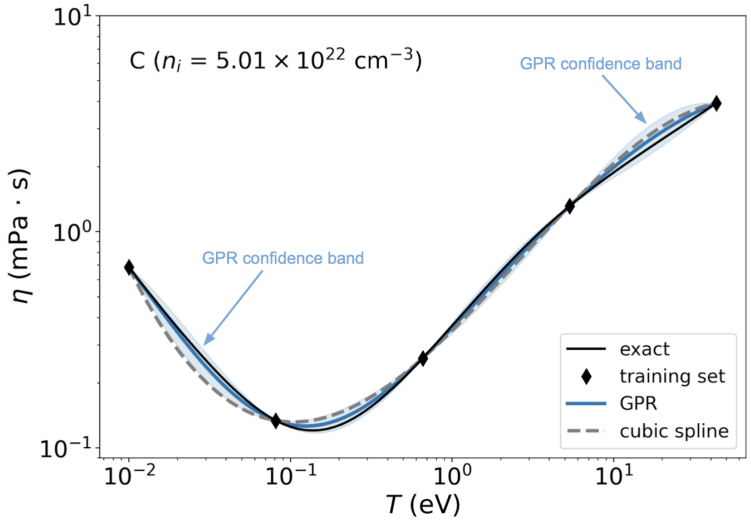

Figure 4.2: Comparison of GPR and cubic-spline regression for a single-fidelity viscosity dataset using the YVM for the element C at $n_i = 5.01 \times 10^{22}$ cm^{-3}. The training points (black diamonds) were fit using both GPR (blue line) and a cubic spline (grey dashed line). The shaded bands show a 95% confidence interval around the GPR fit. Locations of future HF training points are suggested by the confidence band.

GPR fit, denoted as “GPR," corresponds to $\boldsymbol{\mu}_*(X_*)$ from Eq. (4.2); the shaded bands around $\boldsymbol{\mu}_*(X_*)$ correspond to a 95% confidence interval and are computed from Eq. (4.3). The fit generated using cubic-spline regression on the same dataset is denoted as “cubic spline." For all GPR fits, the data were first scaled to unit variance and zero mean. The hyperparameter optimization routine was carried out using the limited-memory quasi-Newton algorithm [242] with 15 random restarts, and a measurement noise with a variance of 10^{-6} was added to ensure that the kernel matrix $K(X_{SF}, X_{SF}; \theta)$ for computing the posterior distribution would be guaranteed to be positive-definite (and therefore, invertible) during fitting. Both the cubic-spline regression and GPR methods produced accurate fits, as shown by comparison to the underlying true solution, which is denoted with a black line in Fig. 4.2 and labeled “exact." A key difference between cubic splines and GPR is that the GPR method provides a confidence interval (shaded bands) around the GPR prediction – suggesting where additional data are needed to improve the prediction.

4.2.3 Multi-Fidelity Gaussian-Process Regression

We now turn to the case where there are two sources of data, one LF and one HF. The outputs of the LF model are denoted as $y_{LF} \in \mathbb{R}^{N_{LF}}$ and are evaluated at $X_{LF} \in \mathbb{R}^{d \times N_{LF}}$. Similarly, the outputs from the HF model are denoted as $y_{HF} \in \mathbb{R}^{N_{HF}}$ and are evaluated at $X_{HF} \in \mathbb{R}^{d \times N_{HF}}$. Here, the numbers of LF and HF data points are denoted as N_{LF} and N_{HF}, respectively.

To understand how the LF data can be used in HF predictions with an MF method, consider this simple procedure with three steps. First, in step (a), we combine the LF and HF data into a single dataset with greater coverage than the HF data alone offer. In step (b), we use LF data to influence HF predictions by quantifying correlations between the LF and HF datasets with a correlation hyperparameter, ρ. Finally, step (c) of the procedure imposes a constraint that a prediction at a HF data point ignores the LF data.

Each part of the above procedure is addressed by the original MF-GPR formulation proposed by Kennedy and O'Hagan [222], which begins by assuming that there is a linear mapping between fidelities that is described by the autoregressive model

$$f_{HF}(x) = \rho f_{LF}(x) + \delta_{HF}(x). \tag{4.4}$$

The function $\delta_{HF}(x)$ is to be viewed as the error or *bias* between the HF data and a scaled value of the LF data, where the correlation hyperparameter ρ is the scaling term. Notice that if the LF and HF data are uncorrelated, i.e., $\rho = 0$, then $\delta_{HF} = f_{HF}$. The key idea in this approach is to use the LF and HF data to learn the parameters governing the unknown functions f_{LF} and δ_{HF} and the hyperparameter ρ to be able to predict the value of f_{HF} at a test point x. The functions f_{LF} and δ_{HF} are typically assumed to be realizations of independent Gaussian processes with zero mean and a kernel matrix K. This means that on a test set X_*, $f_{LF}(X_*)$, and $\delta_{HF}(X_*)$ are independent Gaussian random variables that are normally distributed as per

$$f_{LF}(X_*) \sim \mathcal{N}[\mathbf{0}, K(X_*, X_*; \theta_{LF})], \tag{4.5}$$

$$\delta_{HF}(X_*) \sim \mathcal{N}[\mathbf{0}, K(X_*, X_*; \theta_{HF})], \tag{4.6}$$

where θ_{LF} and θ_{HF} denote the hyperparameters for the LF and HF models, respectively. The notation $\mathcal{N}(\mathbf{0}, \Sigma)$ denotes a multivariate Gaussian random variable with mean $\mathbf{0}$ and covariance Σ. Because f_{LF} and δ_{HF} are independent, it follows that [2]

$$f_{HF}(X_*) \sim \mathcal{N}[\mathbf{0}, \rho^2 K(X_*, X_*; \theta_{LF}) + K(X_*, X_*; \theta_{HF})]. \tag{4.7}$$

For brevity, we denote

$$K_{11}(X, X') \equiv K(X, X'; \theta_{LF}), \tag{4.8}$$

$$K_{12}(X, X') \equiv \rho K(X, X'; \theta_{LF}), \tag{4.9}$$

$$K_{21}(X, X') \equiv K_{12}(X, X'), \tag{4.10}$$

$$K_{22}(X, X') \equiv \rho^2 K(X, X'; \theta_{LF}) + K(X, X'; \theta_{HF}). \tag{4.11}$$

Equations (4.5), (4.6), and (4.7) can be jointly written as [222, 223]

$$\begin{bmatrix} f_{LF}(X_{LF}) \\ f_{HF}(X_{HF}) \\ f_{HF}(X_*) \end{bmatrix} \sim \mathcal{N}\left\{ \begin{bmatrix} \mathbf{0} \\ \mathbf{0} \\ \mathbf{0} \end{bmatrix}, \begin{bmatrix} K_{11}(X_{LF}, X_{LF}) & K_{12}(X_{LF}, X_{HF}) & K_{12}(X_{LF}, X_*) \\ K_{21}(X_{HF}, X_{LF}) & K_{22}(X_{HF}, X_{HF}) & K_{22}(X_{HF}, X_*) \\ K_{21}(X_*, X_{LF}) & K_{22}(X_*, X_{HF}) & K_{22}(X_*, X_*) \end{bmatrix} \right\}. \tag{4.12}$$

The form of Eq. (4.12) reveals how the LF and HF data are combined (i.e., through K_{12} and K_{21}), completing step (a). Note that when the hyperparameter ρ, which couples the LF and HF models, is equal to zero, Eq. (4.12) reduces to two decoupled Gaussian processes. This means that when the LF and HF models are uncorrelated, the LF data will not influence the HF regression, resulting in one single-fidelity GPR at each fidelity level.

Following the procedure for determining optimal hyperparameters θ for a kernel function, the hyperparameter ρ is also determined by optimizing a log-likelihood function, as discussed in Sec. 2.4 of Ref. [222]. As a result of this optimization procedure, if ρ turns out to have a large value, then there is substantial correlation between the LF and HF models. Otherwise, the LF and HF models are uncorrelated. Thus, the correlation hyperparameter ρ determined from the MF dataset

[2] Recall that for two independent normally distributed random variables $A \sim \mathcal{N}(\boldsymbol{\mu_A}, \sigma_A^2)$ and $B \sim \mathcal{N}(\boldsymbol{\mu_B}, \sigma_B^2)$, then $C = A + B \sim \mathcal{N}(\mu_A + \mu_A, \sigma_A^2 + \sigma_B^2)$. Also, for some constant α, a random variable $D \sim \alpha\mathcal{N}(\boldsymbol{\mu}_D, \sigma_D^2) = \mathcal{N}(\boldsymbol{\mu}_D, \alpha^2\sigma_D^2)$

directly quantifies the influence of the LF data on the HF fit, completing part (b) of the procedure mentioned above.

We have shown how data from LF and HF models can be combined into a single MF dataset and how the degree of influence of LF data on fits to HF data can be quantified using the correlation hyperparameter ρ. However, we still need to show how to produce a fit to HF data using Eq. (4.12), while also completing step (c) of the procedure mentioned above. By conditioning the joint Gaussian prior distribution, Eq. (4.12), the predictive mean and the covariance matrix are obtained from the Gaussian posterior distribution

$$f_{*,HF}|X_*, X_{LF}, X_{HF}, \mathbf{y} \sim \mathcal{N}[K_*\mathbf{K}^{-1}\mathbf{y}, K_{22}(X_*, X_*) - K_*\mathbf{K}^{-1}K_*^T], \tag{4.13}$$

where $f_{*,HF}$ denotes the posterior distribution of the HF data, and

$$\mathbf{y} \equiv \begin{bmatrix} y_{LF} \\ y_{HF} \end{bmatrix}, \tag{4.14}$$

$$K_* \equiv \begin{bmatrix} K_{21}(X_*, X_{LF}) & K_{22}(X_*, X_{HF}) \end{bmatrix}, \tag{4.15}$$

$$\mathbf{K} \equiv \begin{bmatrix} K_{11}(X_{LF}, X_{LF}) & K_{12}(X_{LF}, X_{HF}) \\ K_{21}(X_{HF}, X_{LF}) & K_{22}(X_{HF}, X_{HF}) \end{bmatrix}. \tag{4.16}$$

We note that the hyperparameters θ_{LF} and θ_{HF} of the kernels and ρ are all determined *simultaneously*by optimizing the log-likelihood function, as discussed in Refs. [222–224]. From Eq. (4.13), the MF predictive mean and covariance for the HF data are

$$\boldsymbol{\mu}_{*,HF}(X_*) = K_*\mathbf{K}^{-1}\mathbf{y}, \tag{4.17}$$

$$\Sigma_{*,HF}(X_*) = K_{22}(X_*, X_*) - K_*\mathbf{K}^{-1}K_*^T. \tag{4.18}$$

Note that when $X_* = X_{HF}$, we have $\boldsymbol{\mu}_{*,HF}(X_{HF}) = y_{HF}$ [3], which guarantees that the regression will pass through the HF data. This satisfies the constraint imposed in step (c) of the procedure and is due to the independence assumption of f_{LF} and δ_{HF}, as discussed in Ref. [243].

[3]This can be most easily seen by using a single test point $x_* = x_{HF}$ and single training points x_{LF} and x_{HF}

To highlight how the MF-GPR approach given by Eq. (4.4), which we denote as "linear MF-GPR," may add value over single-fidelity GPR, we consider the pedagogical case where the LF and HF models have the form

$$y_{LF}(x) = \sin(2\pi x), \tag{4.19}$$

$$y_{HF}(x) = \frac{1}{3}\sin(2\pi x), \tag{4.20}$$

for $x \in [0, 4]$. Note that the LF and HF models are linearly related by the factor of 1/3 in Eq. (4.20). Predictions from single-fidelity GPR and linear MF-GPR are shown in Fig. 4.3, with $N_{HF} = 6$ and $N_{LF} = 22$. For all MF-GPR and GPR fits, the data were first scaled to unit variance and mean zero. The hyperparameter optimization routine was carried out using the limited-memory quasi-Newton algorithm for 15 random restarts, and a measurement noise with a variance of 10^{-6} was added to each kernel matrix to ensure a positive-definite matrix during fitting (see Ref. [244] for more information on the numerical implementation used here).

In Fig. 4.3, the linear MF-GPR fit, denoted by a purple solid line, corresponds to $\boldsymbol{\mu}_{*,HF}(X_*)$ from Eq. (4.17); the confidence bands around $\boldsymbol{\mu}_{*,HF}(X_*)$ were computed from Eq. (4.18) and are approximately the width of the thickness of the purple line. The GPR fit, denoted by a blue solid line, corresponds to $\boldsymbol{\mu}_*(X_*)$ from Eq. (4.2), and the shaded confidence bands around $\boldsymbol{\mu}_*(X_*)$ are computed from Eq. (4.3). We see that inclusion of the LF data leads to a more accurate prediction, as linear MF-GPR recovers the exact HF solution. The GPR result, which is fit to only the HF data, is unable to recover the HF true solution. In addition, the 95% uncertainty band reported in Fig. 4.3 around the fit is much narrower with linear MF-GPR than with GPR, and the agreement of the linear MF-GPR fit with the HF true solution persists even beyond the last HF data point. It is important to note that all regression methods based on GPR will generate a fit that will regress to the mean of the data when the distance between a new test point and an HF training point is greater than the length-scale of the kernel(s).

This particular example can also be viewed through an information-theoretic lens. Observe that the LF and HF models have the same period of 1 s and therefore, according to the Nyquist-Shannon sampling theorem [245, 246], the sampling period must be less than 0.5 s to reconstruct

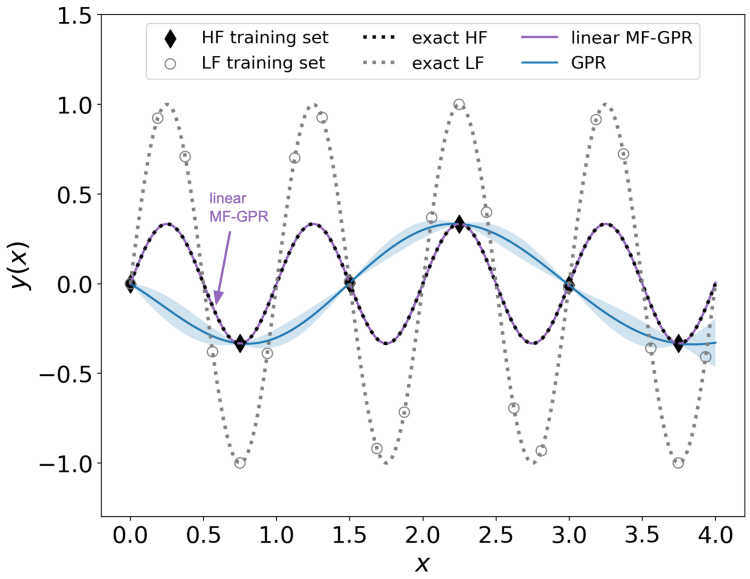

Figure 4.3: Comparison of linear MF-GPR and single-fidelity GPR for a linear mapping between fidelities. The shaded bands represent a 95% confidence interval around a fit. The single-fidelity GPR result is shown as a blue line; single-fidelity GPR is used to fit only the HF data and does not recover the exact HF solution. The linear MF-GPR result is shown in purple; linear MF-GPR accurately predicts the exact HF solution by using the LF data in addition to the HF data, and this result overlaps the exact HF solution. The confidence interval for the linear MF-GPR fit is approximately the width of the thickness of the purple line.

the HF model with sufficient accuracy. Note that the HF data by themselves do not satisfy the Nyquist-Shannon sampling rate. Thus, a GPR fit to the given HF data will be unable to recover the exact HF solution. If the LF model *is* sampled sufficiently to satisfy the Nyquist-Shannon sampling theorem, then it allows the linear MF-GPR model to recover the exact HF solution. If the LF model is not sampled sufficiently or if the LF model has a different frequency than the HF model, then the LF model is uncorrelated with the HF and, therefore, does not add any new information to the MF-GPR.

Lastly, we note that the LF model introduces bias in the resulting MF regression, and the MF-GPR fit is dependent on the choice of LF model; we compare various choices of LF models and their impact on MF-GPR in Sec. 4.3.

Fig. 4.3 illustrates how the autoregressive model, Eq. (4.4), results in more accurate fits to HF data when the LF and HF models are related linearly. However, in many cases, the LF and HF

models may be related nonlinearly, and schemes beyond the original MF-GPR approach [222] are needed. In recent years, there have been many improvements to the original MF-GPR approach that explore more efficient numerical schemes [247], transform input data to more accurately predict discontinuities in HF data [223], have the ability to learn a nonlinear mapping between LF and HF models [224], and more accurately propagate uncertainty between fidelity levels [225]. The approach proposed in [224] goes beyond the linear autoregressive scheme, Eq. (4.4), by allowing for a spatially dependent nonlinear mapping between fidelities; we denote this mapping as $z(\cdot)$.

Following [224], the modified autoregressive equation that includes this mapping is

$$f_{HF}(x) = z[x, f_{LF}(x)] + \delta_{HF}(x), \tag{4.21}$$

where $z(\cdot)$ is sampled from of a Gaussian process. Note that $z[x, f_{LF}(x)]$ is now a Gaussian process of a Gaussian process and is referred to as a "deep GP" [248, 249]. While the form of Eq. (4.21) has been shown to provide improvements over simpler models [248], computing the mean and covariance of the posterior distribution corresponding to Eq. (4.21) is often computationally intractable [249]. To address this intractability, the Gaussian-process prior $f_{LF}(x)$ is often replaced with the corresponding posterior distribution $f_{*,LF}(x)$ [247], resulting in a recursive multi-fidelity model (i.e., performing GPR at each fidelity level separately and then propagating the results to each successive level of fidelity).

Replacing $f_{LF}(x)$ with $f_{*,LF}(x)$ in Eq. (4.21) and using the independence assumption of $z[f_{LF}(x), x]$ and $\delta_{HF}(x)$ results in a compact recursive multi-fidelity formulation [224]

$$f_{HF}(x) = g[x, f_{*,LF}(x)], \tag{4.22}$$

where the prior distribution g includes dependencies of both x and $f_{*,LF}(x)$. It is shown in Ref. [224] that this recursive multi-fidelity model Eq. (4.22) can be modeled by using a kernel of the form

$$k_g(x_i, x_j) = k_\rho(x_i, x_j; \theta_\rho) \cdot k_f[f_{*,LF}(x_i), f_{*,LF}(x_j); \theta_f] + k_\delta(x_i, x_j; \theta_\delta). \tag{4.23}$$

In contrast with the linear autoregressive model Eq. (4.4), the kernel k_ρ is now a spatially-dependent scaling factor responsible for measuring the correlations between the LF and HF models, k_f

measures the correlations of the *outputs* of the GPR performed on the LF data, and k_δ accounts for the bias between the LF and HF data; in this work, each term in Eq. (4.23) is represented by a kernel of the form in Eq. (4.1).

The set of hyperparameters (variance and length scale) for each kernel is denoted by θ_ρ, θ_f, and θ_δ, respectively. Importantly, unlike the linear autoregressive formulation Eq. (4.4) where all hyperparameters at all fidelity levels are trained simultaneously, the hyperparameters at each fidelity level using the recursive formulation Eq. (4.22) are trained separately. This aspect greatly reduces computation costs associated with hyperparameter estimation. When the correlations between the LF and HF data are small, the product $k_\rho k_f$ will be close to zero, and the MF-GPR fit approximately recovers the GPR fit to the HF data. Recall that this was also the case for the correlation hyperparameter ρ in Eq. (4.4). The product $k_\rho k_f$ in Eq. (4.23) is plotted in Sec. 4.3 to reveal the effectiveness of different choices of LF models.

Next, we turn to the three steps for making an MF prediction using Eq. (4.22) with kernel Eq. (4.23). These are discussed in detail in Ref. [224]; for completeness, we summarize them here. Step 1 involves performing GPR on the lowest-fidelity data. This includes optimizing the kernel hyperparameters using the LF data. Step 2 takes as input the trained GPR model from Step 1, together with the HF data, to construct the posterior distribution according to the kernel in Eq. (4.23) (see Eq. (2.14) of Ref. [224]). The last step, Step 3, calculates the predictive mean and covariance by sampling the posterior distribution using numerical integration techniques (e.g., Monte Carlo [224, 225]). Numerical integration is necessary because unlike the prior distributions of single-fidelity GPR and linear MF-GPR, the prior distribution in Eq. (4.22) ,ay not be Gaussian. As a result, we will be unable to express its posterior distribution as a Gaussian. More details of the MF-GPR approach used in this work and its numerical implementation can be found in Refs. [224, 225, 244].

Recall that the LF and HF models given by Eqs. (4.19) and (4.20) are linearly related, with the quantity in Eq. (4.20) equal to the quantity in Eq. (4.19) multiplied by a coefficient of $1/3$. To highlight the limitations of the linear MF-GPR approach given by Eq. (4.4), we now consider LF

and HF models of the form

$$y_{LF}(x) = \sin(8\pi x), \tag{4.24}$$

$$y_{HF}(x) = x \sin(8\pi x), \tag{4.25}$$

for $x \in [0, 1]$. Note that the coefficient by which Eq. (4.24) is multiplied to get Eq. (4.25) has been changed from $1/3$ to x. As a result of this mapping, we expect that predictions made using Eq. (4.17) will be of poor quality. This expectation is verified in Fig. 4.4, which shows a comparison between predictions from Eqs. (4.4) and (4.22), with $N_{HF} = 8$ and $N_{LF} = 30$. We find that MF-GPR not only exhibits excellent agreement with the exact HF solution but also has far smaller confidence bands than those obtained with the linear MF-GPR model. Fig. 4.4 illustrates the ability of MF-GPR to produce accurate results with limited HF data by incorporating additional data from an LF model that is not linearly related to the HF model.

It would be undesirable to restrict MF-GPR approaches to plasma transport-coefficient data to linear relationships alone, as such data are known or derived to be accurate in certain physical regimes that need not be related linearly. The plasma transport coefficients we are considering illustrate this point; they are obtained using a variety of methods (recall Sec. 4.2.1) that have no simple, prescribed relationship to each other. Thus, we will use the nonlinear formulation of MF-GPR, Eq. (4.22), throughout the reminder of this work, referring to it simply as "MF-GPR."

4.2.4 Error Calculations and Computation Cost

We have shown the benefit of MF regression over single-fidelity techniques by considering toy examples. However, the computational cost of MF-GPR over single-fidelity GPR can not be disregarded. Thus, we would like to determine the cost-benefit trade-off for using MF-GPR over single-fidelity GPR. To begin, we define an error metric to measure the regression error between the HF test set and MF-GPR/GPR predictions. The metric we use is the root-mean-square error (*RMSE*)

$$RMSE = \sqrt{\frac{1}{N_{test}} \sum_{i=1}^{N_{test}} \|y_{i,true} - y_{i,pred}\|^2}, \tag{4.26}$$

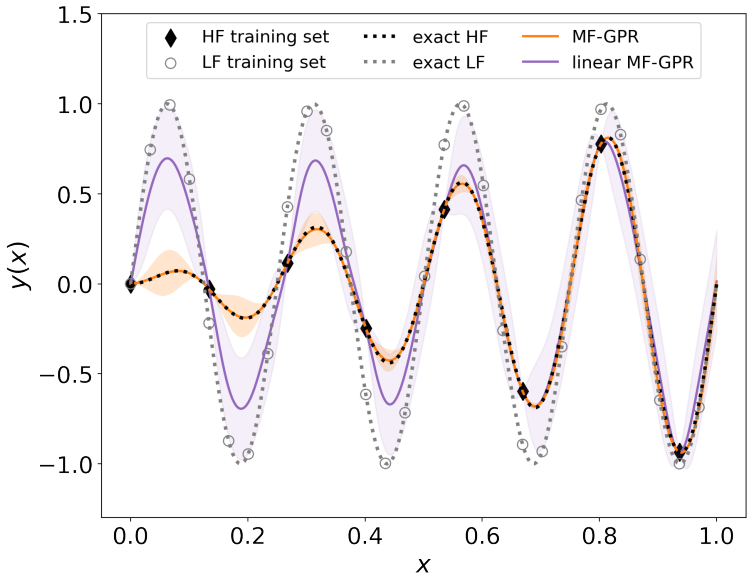

Figure 4.4: Comparison of two MF-GPR approaches. One MF-GPR approach assumes a linear relationship between the fidelity levels [see Ref. [222] and Eq. (4.4)] and is denoted as "linear MF-GPR." The other approach assumes a nonlinear mapping between fidelity levels [see Ref. [224] and Eq. (4.21)] and is denoted as "MF-GPR"; the shaded bands represent a 95% confidence interval around the fit. The MF-GPR approach that assumes a nonlinear mapping between fidelities (orange solid line) is able to recover the underlying exact HF solution, in contrast to the MF-GPR approach that assumes a linear mapping between fidelity levels (purple solid line).

where i denotes the location of a test point, N_{test} is the total number of test points, $y_{i,true}$ is the true solution at location i, and $y_{i,pred}$ is the value of the fit (MF-GPR or GPR) at location i. Table 4.2 compares the computational costs, which includes the costs of both hyperparameter training and predictions, and regression errors for the GPR and MF-GPR methods using the LF and HF models Eqs. (4.24) and (4.25). We find that while MF-GPR is roughly six to ten times more expensive than single-fidelity GPR, the MF-GPR method results in regression errors that are often a couple orders of magnitude lower than those obtained with single-fidelity GPR.

4.3 Multi-fidelity Regression of Plasma Transport-Coefficient Data

In Secs. 4.2.2 and 4.2.3, we have demonstrated the effectiveness and limitations of single-fidelity GPR and different MF-GPR approaches using toy examples. Additionally, in Sec. 4.2.4, we assessed the cost-benefit trade-off between GPR and MF-GPR approaches. We illustrated the fact that relative to single-fidelity GPR, MF-GPR increases computation cost but decreases prediction

N_{LF}	N_{HF}	T^*_{GPR}	$T_{\text{MF-GPR}}/T_{\text{GPR}}$	$RMSE_{\text{GPR}}$	$RMSE_{\text{MF-GPR}}$
30	8	1	6 ± 1	3.2[−1]	8.7[−3]
34	9	1.0 ± 0.1	6 ± 1	3.5[−1]	1.5[−2]
38	10	1.0 ± 0.1	5 ± 1	3.8[−1]	9.4[−4]
43	11	1.3 ± 0.7	6 ± 3	3.5[−1]	1.1[−3]
50	13	1.1 ± 0.1	6 ± 1	3.6[−1]	2.0[−3]
60	15	1.1 ± 0.2	8 ± 2	1.1[−1]	1.9[−4]
75	19	1.4 ± 0.2	7 ± 2	9.0[−3]	1.5[−4]
100	25	1.2 ± 0.2	8 ± 2	5.4[−3]	9.9[−5]
150	38	1.7 ± 0.3	7 ± 2	3.1[−4]	7.7[−5]
300	75	2.1 ± 0.3	10 ± 2	2.1[−4]	6.5[−5]

Table 4.2: Average computation time and regression errors for single-fidelity GPR and MF-GPR, Eq. (4.22) fits using the LF and HF models Eqs. (4.24) and (4.25). Each entry is an average over ten fits, and the hyperparameters for each fit were trained using the limited-memory quasi-Newton algorithm with 15 random restarts. For the *RMSE* values, the numbers in brackets denote the power of ten that the value in front of the brackets is multiplied by (e.g., 3.2[−1] = 0.32). The column labeled T^*_{GPR} shows the computation time for single-fidelity GPR normalized by the computation time when $N_{HF} = 8$. The computational cost of single-fidelity GPR increases by a factor of two when the number of HF training points increases by roughly ten. We note that when $N_{LF} = 50$ and $N_{HF} = 13$, MF-GPR is six times more expensive than single-fidelity GPR but reduces the regression error by more than two orders of magnitude.

error. While these toy examples were useful for building intuition and providing a baseline for computation-cost and error estimates, we will now consider real data generated for ionic plasma transport coefficients; we will begin by analyzing what role the choice of LF model plays in MF-GPR. The LF and HF models will be chosen from those listed in Table 4.1.

We first consider two choices for the LF model for predicting the viscosity for the element C at $n_i = 5.01 \times 10^{22}$ cm^{-3}, as shown in Fig. 4.5. MF-GPR fits produced using the LF SMT model are shown in panel (a) of the figure, and fits produced using the LF YGBI model are shown in panel (b). The HF training data were computed from the YVM. The inserts in Fig. 4.5 show the kernel matrix corresponding to $k_\rho k_f$ in Eq. (4.23).

In panel (a) of Fig. 4.5, with the SMT model used as the LF model, we see that the only nonzero values of the kernel matrix occupy the diagonal and quickly decay to zero a short distance from the diagonal, corresponding to a small length scale for the kernel. Because the entries of the kernel matrix have nearly zero magnitudes, the MF-GPR fit is nearly equivalent to the fit obtained by

performing GPR on the HF data alone; this equivalence explains the overlap of the fits produced by GPR and MF-GPR.

In panel (b) of Fig. 4.5, with the YGBI model used as the LF model, two findings are of note. The first is that there are regions where the MF-GPR and GPR fits do not overlap; this is most clearly seen around $T = 0.2$ eV. Second, the entries of the kernel matrix are nonzero away from the diagonal, implying substantial correlations between the LF and HF data. However, the values are nearly constant throughout the matrix, differing from each other by at most by 1%. Thus, in contrast with the MF-GPR fit shown in panel (a), the MF-GPR fit shown in panel (b) includes information from the LF data and suggests correctly that the LF and HF data differ by an approximately constant shift.

A comparison of the sizes of the confidence bands for the MF-GPR results in panels (a) and (b) in Fig. 4.5 shows that the MF-GPR fit in panel (b) is superior to that in panel (a). The choice of the YGBI model as the LF model for MF-GPR in panel (b) results in a superior fit because the YGBI model provides additional information that is used to improve the fit. This additional information can be seen in the kernel matrix computed from $k_\rho k_f$; an LF model for which kernel entries off the diagonal are non-zero improved the MF-GPR fit over the GPR fit more than an LF model for which the kernel entries are close to zero. Thus, we have found that the kernel matrix computed from $k_\rho k_f$ is a natural indicator of when an LF model is insufficient for MF-GPR and that a different, or more precise, LF model is needed to impact the MF-GPR fit. When kernel matrix entries decay rapidly to zero off the diagonal, it would be best to consider alternative LF models.

In Fig. 4.5, we considered LF and HF models that both predict the same quantity. ML models have been developed in which the LF and HF models do not predict the same quantity; for example, the prediction of rainfall using an elevation model has been examined [250, 251]. As discussed in [250, 251], a large amount of elevation data are available, but only a minimal amount of rainfall data are available; together, these data have been used to construct MF rainfall models. Similarly, a large amount of self-diffusion coefficient data and a minimal amount of viscosity data are available, and MF models of plasma transport coefficients could be constructed using both data sources.

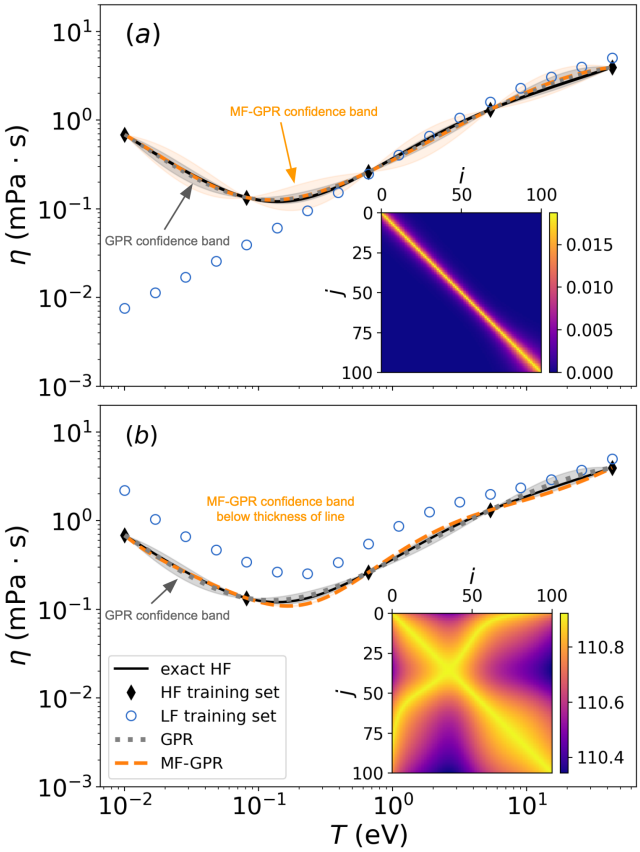

Figure 4.5: MF-GPR prediction of the viscosity of the element C at $n_i = 5.01 \times 10^{22}$ cm^{-3} versus temperature. In both (a) and (b), GPR was performed using the HF training data computed from the YVM, and the GPR results are compared with those of an MF-GPR model constructed using data from both an HF model and an LF model. (a) The LF model is given by the SMT model. (b) The LF model is given by the YGBI model. The inserts in (a) and (b) display the kernel matrix from $k_\rho k_f$ with optimized hyperparameters. In (a), little correlation is found between the HF and LF models, as the only non-zero entries of the kernel matrix are on, or close to, the diagonal; in (b), however, the correlation is substantial, as demonstrated by the extent of the non-zero values off the diagonal of the kernel matrix, as shown in the insert.

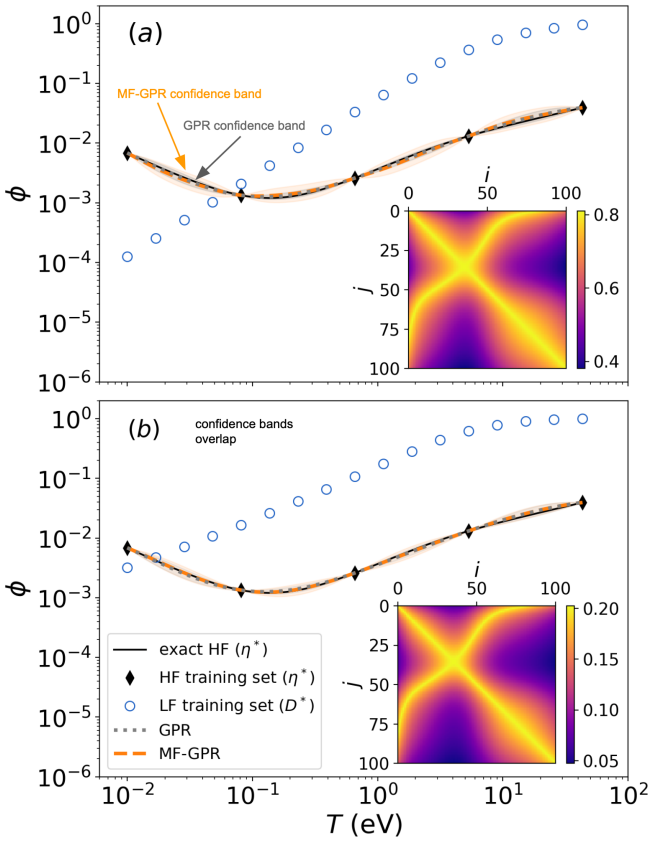

Figure 4.6: Using self diffusion as the LF model to predict viscosity. The reduced transport coefficients $\phi \in \{D^*, \eta^*\}$ are shown for the element C at $n_i = 5.01 \times 10^{22}$ cm^{-3} versus temperature. In both (a) and (b), GPR was performed using the HF training data computed from the YVM, and the GPR results are compared with those of an MF-GPR model constructed using data from both an HF model and an LF model. (a) The LF model is the reduced self-diffusion coefficient D^* from the HMP model. (b) The LF model is D^* computed from the SMT model. The inserts display the kernel matrix from $k_\rho k_f$ with optimized hyperparameters.

Thus, we also consider LF and HF models that do not predict the same quantity. In particular, we assess the validity of using the self-diffusion coefficient (LF model) as a predictor for the viscosity (HF model).

MF-GPR fits for viscosity of the element C at $n_i = 5.01 \times 10^{22}$ cm^{-3} using self-diffusion data for the LF model and viscosity data for the HF model are shown in Fig. 4.6; two different LF models for predicting the self-diffusion coefficient are considered. In both panels (a) and (b), HF data were calculated from the YVM model. In panel (a), the LF data were computed using the HMP model, and in panel (b), the LF data were computed from the SMT model. The transport coefficients have

been reduced such that $D^* = D/\omega_p a_i^2$ and $\eta^* = \eta/m_i n_i \omega_p a_i^2$. Here, $\omega_p = (4\pi n_i Z^2 e^2/m_i)^{1/2}$ is the ion plasma frequency, and $a_i = (4\pi n_i/3)^{-1/3}$ is the ion-sphere radius, where n_i is the ion number density, Z is the mean ionization state, e is the elementary charge, and m_i is the ion mass. The inserts once again show the kernel matrix $k_\rho k_f$.

Fig. 4.6 demonstrates that using self-diffusion coefficient data as our LF model and viscosity as our HF model substantially improves the MF-GPR model of the viscosity compared to using viscosity data for both models. What we mean by this is that the LF data used in both panels of Fig. 4.6 are more strongly correlated with the HF data than the LF data used in panel (a) of Fig. 4.5 are. A comparison between the kernel matrices shown in the insert of panel (a) of Fig. 4.5 and in the insert of both panels of Fig. 4.6 demonstrates this point; in contrast to panel (a) of Fig. 4.5, the kernel matrices shown in both panels of Fig. 4.6 have a non-zero value away from the diagonal. This means that the LF data used in both panels of Fig. 4.6 have a larger contribution to the MF-GPR model than the LF data used in panel (a) of Fig. 4.5 does.

Also note that the entries of the kernel matrix in both panels of Fig. 4.6 are not a constant value, in contrast with the entries in the kernel matrix shown in the insert in panel (b) of Fig. 4.5. Therefore, the LF and HF data used in both panels of Fig. 4.6 are not related by a shift but rather by a nonlinear relationship. Comparisons of the kernel matrix $k_\rho k_f$ provide valuable insight into the effectiveness of an LF model in an MF-GPR framework by quantifying the spatial extent of correlations and type of relationship between the low- and high-fidelity models e.g., linear or nonlinear. In particular, these comparisons revealed the effectiveness of using self-diffusion LF data to predict viscosity HF data. As self-diffusion data are more readily available and are cheaper to compute than viscosity data, Fig. 4.6 illustrates how MF-GPR provides improved estimates of viscosity at low computational cost where it has not been measured.

In addition to selecting a sufficient LF model for MF-GPR, it is imperative to include data in the LF and HF datasets that capture essential special features of a physical system. For example, it is possible that neither the LF data nor the HF data include information about features such as sudden changes (i.e., a jump discontinuity). For plasma transport coefficient data, sudden changes

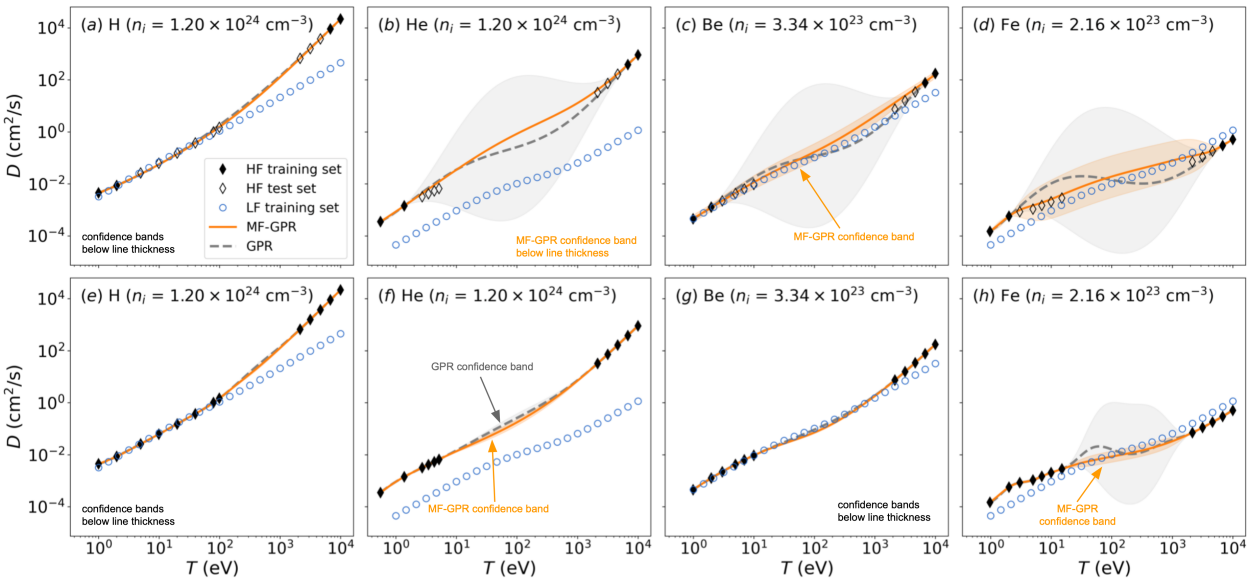

Figure 4.7: MF-GPR and GPR fits, with 95% confidence intervals (shaded bands), of the self-diffusion coefficient versus temperature for multiple elements. The models used to generate this data are given in Table 4.1. Panels (a) through (d) show MF-GPR and GPR fits obtained using a portion (filled diamonds) of the HF data (all diamonds). Panels (e) through (h) compare MF-GPR and GPR fits obtained using all of the available data; GPR is fit to only HF data, whereas MF-GPR uses both the LF and HF data. In general, the MF-GPR fit is less prone to spurious oscillations than the GPR fit, and the size of the uncertainty band is much smaller with MF-GPR than with GPR.

in quantities such as the electrical conductivity may result from a phase transition. In the absence of such data, MF-GPR is incapable of predicting a discontinuity. If this behavior is known in advance, then the LF and HF models should be sampled accordingly to ensure that the MF-GPR framework has sufficient training data near the discontinuity; then, an MF-GPR approach capable of handling a discontinuity, such as that described in Ref. [223], can be used.

4.4 Regression of Sparse Disparate Data

In this section, we will use MF-GPR to predict transport coefficients when HF data are available in disparate physical regimes. We will consider a transport-coefficient dataset, which has “gap" regions, i.e., temperature ranges in which no HF data are available, as shown in Table 4.1.

This section is organized as follows. First, we use MF-GPR to fit gapped transport-coefficient data as a function of temperature. Then, we consider a higher-dimensional feature space of ion number density and temperature. We conclude by varying the approach used to sample the HF

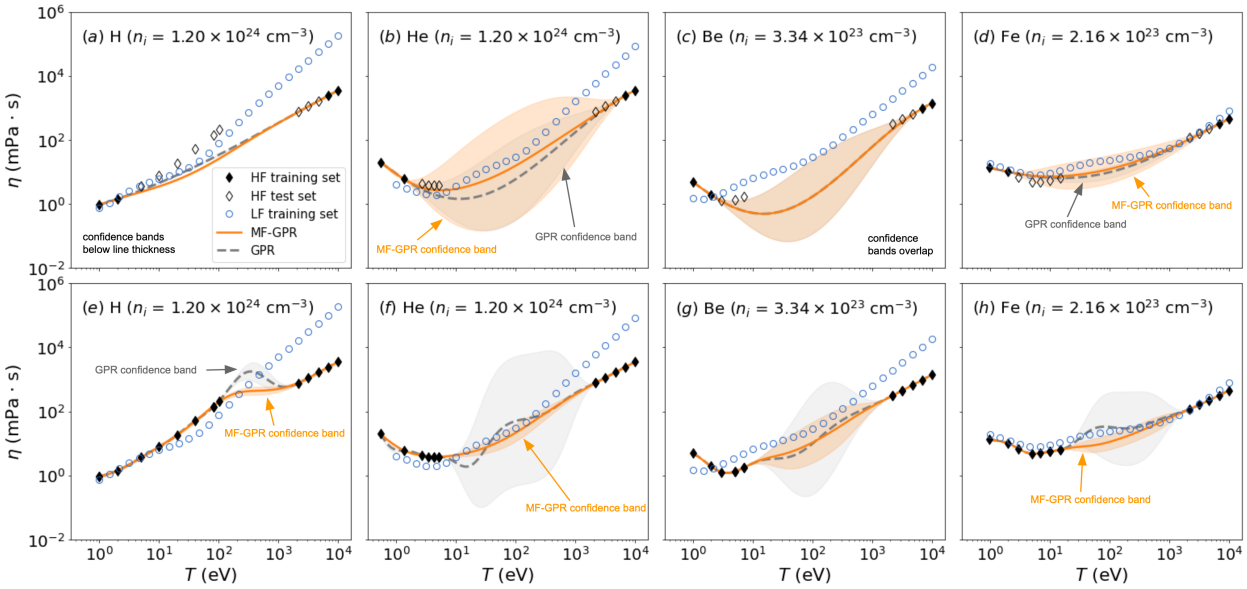

Figure 4.8: MF-GPR and GPR fits, with 95% confidence intervals (shaded bands), of the viscosity coefficient versus temperature for multiple elements. The models used to generate this data are given in Table 4.1. Panels (*a*) through (*d*) show MF-GPR/GPR fits obtained using a portion (filled diamonds) of the HF data (all diamonds). Panels (*e*) through (*h*) show MF-GPR fits obtained using all of the data. In general, the MF-GPR fit is less prone to oscillations than is the GPR fit which uses only HF data.

dataset. We find that using a low-discrepancy sequence [4] to select data-sampling locations yields smaller regression errors than does sampling data on a uniform grid.

4.4.1 Self-diffusion and Viscosity Predictions versus Temperature

We apply MF-GPR to gapped transport-coefficient data for the elements H, He, Be, and Fe. We first consider an HF training set that consists of only four data points – two points at both high and low temperatures – and thus features a large gap between the patches of HF data. Then, this gap is reduced in size by including all HF points in the training set.

This approach is illustrated in Fig. 4.7, which shows MF-GPR and GPR fits for the self-diffusion coefficient. In the top row, we note that multiple inflection points in the GPR predictions for He, Be, and Fe can be seen, while the MF-GPR fits are monotonically increasing. For Fe, a large oscillatory pattern is seen in the GPR fit. These oscillations are not physical and are likely due

[4] A sequence of points is said to be *low-discrepancy* if the proportion of points in the sequence falling into an arbitrary set is (on average) near-proportional to the measure of that set.

to the hyperparameters responsible for specifying the length scale of the kernel Eq. (4.1). With MF-GPR, oscillations do not appear, as the three terms in Eq. (4.23) do not restrict the form of the fit to a single length scale. Similar patterns are observed for the viscosity in Fig. 4.8.

4.4.2 Viscosity Predictions versus Temperature and Number Density

Because only a small amount of HF data were used in the work described in Sec. 4.4.1, a well-defined error metric could not be reported. Therefore, we constructed an HF dataset in the $n_i - T$ plane containing 900 points sampled on a grid. The data were generated using the YVM for H and Fe, and these data will act as a test set for the results described in this section. The dataset spans a temperature range of $T = 10^1 - 10^4$ eV and an ion number density of $n_i = 10^{18} - 10^{26}$ cm^{-3}.

Next, we constructed an MF training dataset. When this MF training dataset is used together with the HF test set described above, we will be able to compute regression errors for GPR and MF-GPR using Eq. (4.26), now in $n_i - T$ space. With the view of mimicking the scenario of datasets containing “gaps," as discussed in Sec. 4.4.1, an MF training dataset was constructed to contain a region lacking HF data. We chose the YGBI model as our LF model and assumed that this LF model can be evaluated everywhere in the domain.

Fig. 4.9 illustrates the concept of physical regimes that include an area or “gap" in which no HF data exist. The figure shows three regions, labeled as “1," “2," and “3." In regions 1 and 3, both the HF (YVM) and LF (YGBI) models can be evaluated. The area between the red dashed lines, denoted with a 2 and labeled as “no HF data," shows the region where no HF data are available. We refer to this region as the “gap region." A summary of the choices of LF and HF models for all of the regions shown in the figure are given in Table 4.3.

Having defined the models used to generate the test and training datasets, we will describe, below in Sec. 4.4.2.1, the three HF sampling approaches we used to create the MF training dataset.

4.4.2.1 Sampling Methods for HF Data

We used three approaches to sample the HF gapped dataset initially: an evenly spaced grid, a low-discrepancy sequence, namely a Halton-23 sequence [252], and a hybrid method that used

Region	HF	LF
1	YVM [140]	YGBI [137]
2	–	YGBI [137]
3	YVM [140]	YGBI [137]

Table 4.3: HF and LF models for the viscosity used in the temperature/number-density regions shown in Fig. 4.9. The same LF model is employed across all regions.

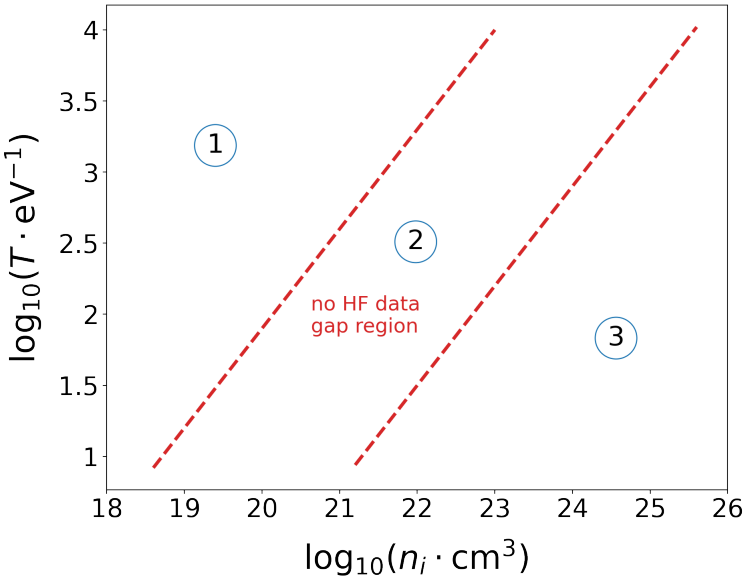

Figure 4.9: The regions of the temperature/number-density space where HF and LF models were used to generate viscosity data for the MF training dataset. The red dashed lines indicate the divisions between the regions. In the regions labeled as “1" and “3," both HF and LF data are available. In the region labeled as “2," only LF data are available. The models used for each region are listed in Table 4.3.

both approaches. For the LF data, we restricted the sampling approach to an evenly spaced grid. The details of each sampling approach are discussed below and summarized in Table 4.4.

To place data on an evenly spaced grid, we first specify the total number of HF data points (e.g., $N_{HF} = 100$). Then, the grid spacing is computed by

$$\Delta x = \frac{x_u - x_\ell}{\sqrt{N_{HF}}}, \tag{4.27}$$

where $x \in \{n_i, T\}$, and the subscripts “u” and “ℓ” denote the upper and lower bounds of x, respectively. Using Eq. (4.27) to determine the spacing between HF points is straightforward; however, we note that in order to refine the grid spacing by a factor of two, four times as many

HF data points are needed. As a result, the evenly spaced grid approach becomes increasingly computationally expensive as the dimension of the input space increases.

Instead of restricting the locations of HF data to points on an evenly spaced grid, their locations may be determined randomly. However, two HF points chosen in this way could be extremely close together, and in such a circumstance, calculations would be repeated at roughly the same location in parameter space. By enforcing a constraint on the minimum distance between two points, calculating HF data at close locations can be avoided. An alternative to enforcing a constraint on the distance between data sampling locations is to use a low-discrepancy sequence to determine sampling locations; this is the second of our sampling methods. Low-discrepancy sequences consist of "quasi-random" numbers that are generated deterministically, and points constructed using these numbers as coordinates cover a domain more quickly and evenly than do points constructed with random numbers as coordinates. Here, we use a Halton-23 low-discrepancy sequence [252]. In the name "Halton-23," "23" denotes the bases 2 for dimension n_i) and 3 (for dimension T); the bases 2 and 3 were chosen as they are mutually prime, which results in a uniform, limiting density of the points in the sequence [252].

While use of only a low-discrepancy sequence to determine HF sampling locations reduces the chance of performing repeated calculations, the edges of the domain may not be included in an HF dataset constructed in this way. If a specific domain is desired, it is necessary to augment the low-discrepancy sequence locations with data along the domain boundary. To ensure coverage in a fixed domain, we used a hybrid sampling method. In this hybrid method, the four extreme corners of the domain of the HF dataset are sampled first. Then, the remainder of the allocated HF data points are sampled using a low-discrepancy sequence.

The three sampling approaches we used are summarized in Table 4.4. In Fig. 4.10, we compare the MF-GPR prediction of the viscosity using each of these sampling methods, for $N_{LF} = 100$ and $N_{HF} = 12$. In the top row, we show the locations in the $n_i - T$ plane where the HF data, indicated by filled black diamonds, and the LF data, indicated by open blue circles, were sampled using each method. The bottom row shows heat maps of the absolute error between the prediction and the

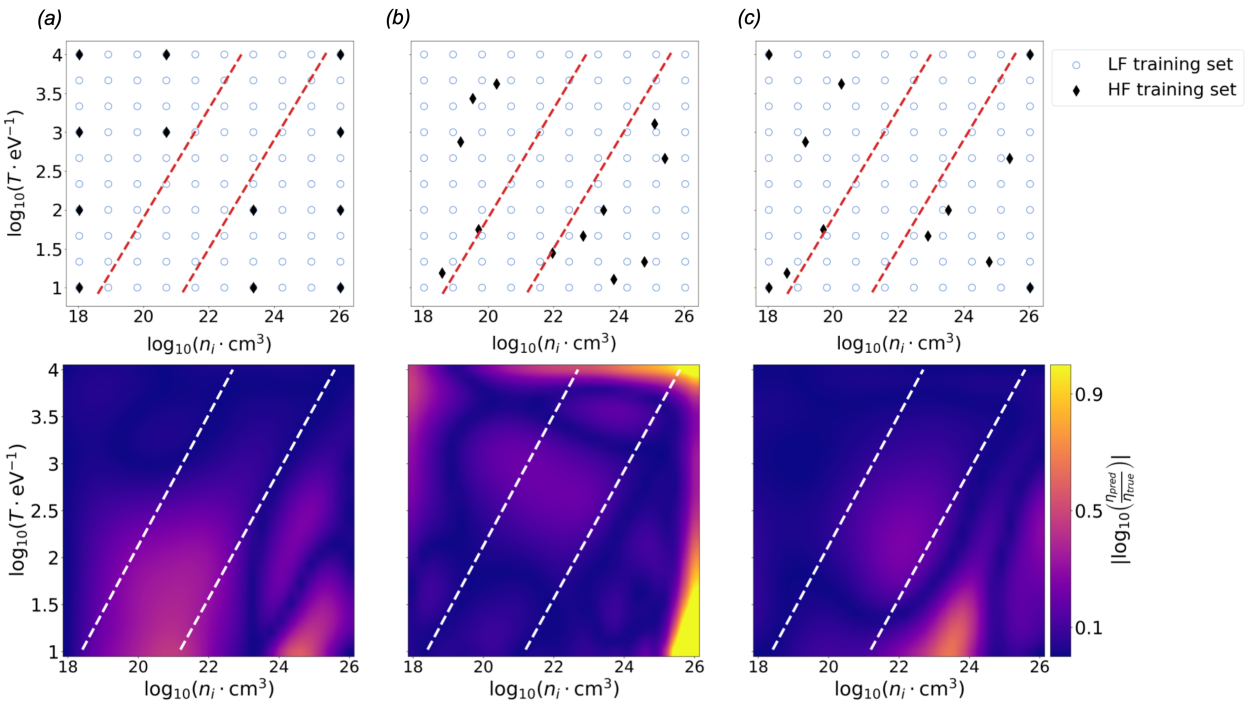

Figure 4.10: MF-GPR prediction of the viscosity of the element Fe using $N_{LF} = 100$ and $N_{HF} = 12$. The HF data were sampled (a) on a uniformly spaced grid, (b) using a Halton-23 sequence, and (c) using a hybrid method. Top row: The locations of the HF training data (filled black diamonds) and LF training data (open blue circles) used to construct the MF training dataset are shown. The red dashed lines denote the boundaries between the regions shown in Fig. 4.9. Bottom row: The absolute differences between the predicted viscosities η_{pred} and the true viscosities η_{true} are shown. The hybrid sampling approach improves the prediction in the gap region between the dashed white lines. Note that the failure of the Halton-23 sampling approach to include the boundaries of the HF data in the training set results in large errors at the boundaries.

true solution, for each sampling method; differences between the sampling methods are apparent. In particular, the regression error in the gap region is substantially smaller with the hybrid method than with the grid method.

4.4.2.2 Regression Error

Fits produced using GPR and MF-GPR are shown in Fig. 4.11, with the HF sampling approach varied as described in Table 4.4. Each point in the figure shows an average of 10 fits, with error bars indicating one standard deviation from the average. For MF-GPR, the LF data were sampled from a grid, and the cases $N_{LF} = 25$ and 400 are shown. The GPR fits were carried out using only the HF data from the MF dataset. We see that *the RMSE decreases as* N_{HF} *increases* for all

HF Sampling	LF Sampling	Description
Grid	Grid	HF and LF data were sampled on an evenly spaced grid in n_i and T.
Halton-23 [252]	Grid	HF data were sampled using a Halton-23 sequence. LF data were sampled on an evenly spaced grid in n_i and T.
Hybrid	Grid	The HF dataset includes the four extreme corners of the domain and data sampled using a Halton-23 sequence. The LF data were sampled on an evenly spaced grid in n_i and T.

Table 4.4: Sampling approaches used to sample the MF training dataset. The LF data were always evaluated on a grid; sampling methods for the HF data varied.

methods, and that *the MF-GPR fit yields smaller RMSE values than does GPR*. In almost all cases, MF-GPR performs at least as well as GPR.

We next computed the *RMSE* of fits to HF viscosity data for different combinations of N_{HF} and N_{LF} for H and Fe. The results for H are displayed in Fig. 4.12, and for Fe, in Fig. 4.13; each column in the figure corresponds to a different HF sampling method. We note that the *RMSE* values for $N_{HF} = N_{LF} = 4$ should be the same in columns (a) and (c), because the hybrid method first samples the four corners from the grid and then adds points sampled using the Halton-23 sequence. The average value of the *RMSE* for $N_{HF} = N_{LF} = 4$ in column (a) is within one standard deviation of the average value of the *RMSE* for the same case in column (c), and vice versa. Therefore, we do not consider these differences to be statistically significant. As shown in Figs. 4.12 and 4.13, fits generated using the hybrid sampling approach result in smaller *RMSE* values overall than do those generated using a simple grid approach. It is also worth noting that the pure Halton-23 method often produced higher *RMSE* values than did the grid method; this is because the boundaries of the domain were not sufficiently sampled in the HF training set. As a result, the MF-GPR fit tends to the mean of the HF data, and the largest errors are incurred near the boundaries, as shown in Fig. 4.10.

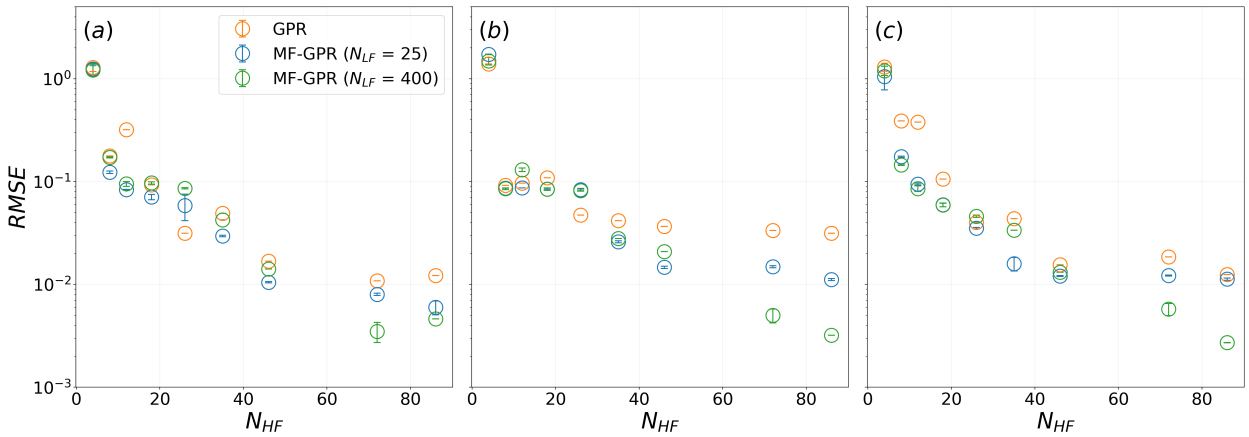

Figure 4.11: The *RMSE* of $\log_{10}(\eta)$ for GPR and MF-GPR fits for the element H using different HF sampling methods. We sampled N_{HF} and N_{LF} points from the gapped dataset shown in Fig. 4.9. The models used to generate the data are specified in Table 4.3. Each *RMSE* value was determined from an average of ten fits, and standard deviations for the values are shown as error bars. The HF data were sampled (a) on an evenly spaced grid, (b) using a Halton-23 sequence, and (c) using a hybrid method. We note that in most cases, MF-GPR outperformed GPR.

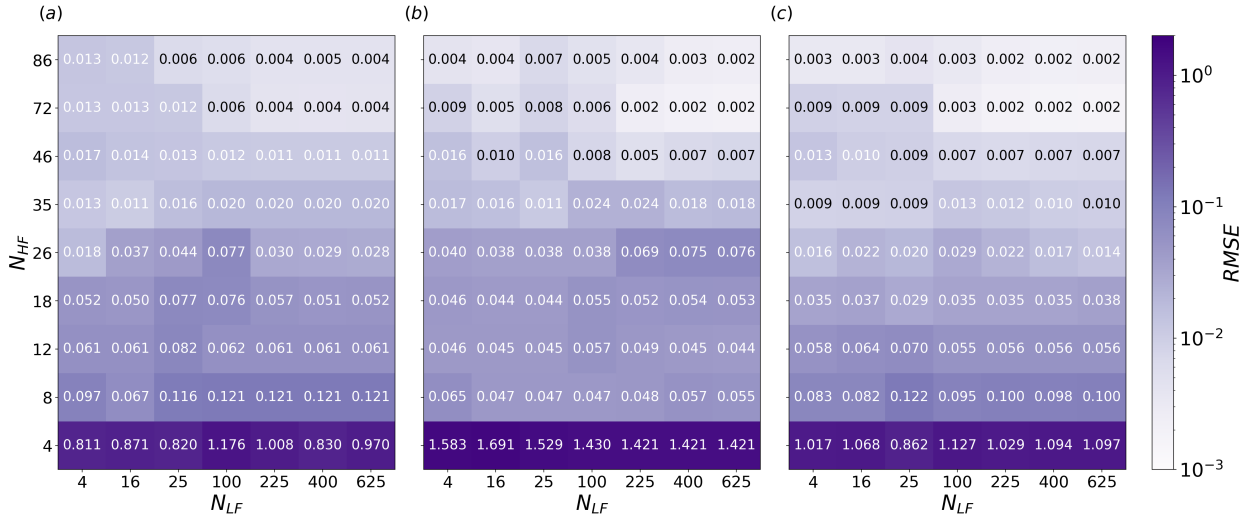

Figure 4.12: The *RMSE* of $\log_{10}(\eta)$ for the element H using MF-GPR with different MF training sets constructed using various HF sampling approaches. (a) The HF data were sampled on a grid. (b) The HF data were sampled using a Halton-23 sequence. (c) The HF data were sampled using our hybrid approach.

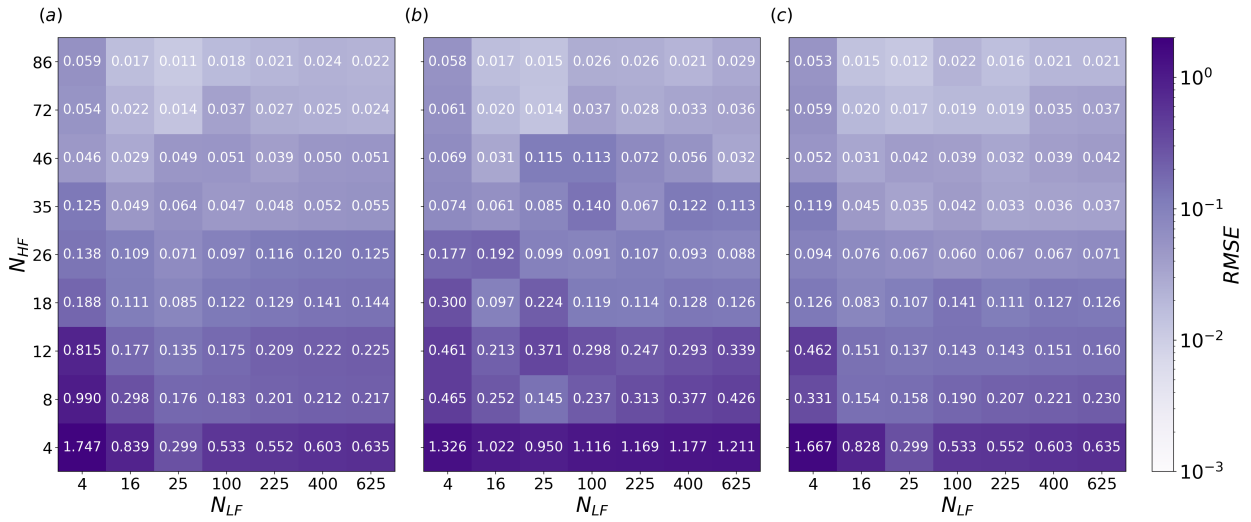

Figure 4.13: The *RMSE* of $\log_{10}(\eta)$ for the element Fe using MF-GPR with different MF training sets constructed using various HF sampling approaches. (a) The HF data were sampled on a grid. (b) The HF data were sampled using a Halton-23 sequence. (c) The HF data were sampled using our hybrid approach.

4.5 Conclusions and Outlook

We have investigated the use of MF-GPR to interpolate plasma transport data over a wide parameter space in which HF data are available in localized patches. We have examined the improvements in both the predicted mean and the predicted uncertainty that MF-GPR provides over GPR. We have seen that in most cases, MF-GPR results in a lower uncertainty than does single-fidelity GPR, sometimes by an order of magnitude. Examining the hyperparameters governing the structure of the $k_\rho k_f$ kernel reveals the improvement in the mean and uncertainty, or lack thereof, given by the LF data.

As a “black-box" regression method, MF-GPR provides increased reliability over single-fidelity methods, as trends from LF models are used during regression where HF data are sparse; the use of such LF trends enables MF-GPR to reduce the occurrence of nonphysical oscillations or inflection points that occur with single-fidelity GPR. In addition, confidence bands generated by MF-GPR and GPR suggest where additional HF data are needed once a fit has been produced; simpler regression methods do not offer this benefit.

From an experimental-design perspective, HF data are often sampled on a grid that is refined

uniformly when finer resolution is needed [253]. We found that when performing MF-GPR, sampling HF data on a uniformly spaced grid can bias length-scale hyperparameters and results in larger regression errors. Therefore, we developed a simple hybrid approach for initially sampling HF data that combines sampling both on a grid and using a low-discrepancy sequence, resulting in smaller regression errors.

The results here can be expanded upon in multiple ways. For example, the MF-GPR framework could be extended to include physically motivated constraints, such as enforcing non-negativity [254]. Additionally, we restricted the work here to the self-diffusion and viscosity transport coefficients, but other transport coefficients, such as the thermal conductivity, the resistivity, and the interdiffusion coefficient in plasma mixtures, can also be investigated. The sampling methods described here can also be improved upon greatly and optimized for higher-dimensional feature spaces to avoid the curse of dimensionality. However, our approaches offer a starting point that highlights the importance of avoiding regressing beyond the bounds of available data in a GPR/MF-GPR setting.

Through the confidence intervals it provides, the GPR approach suggests where it would be most useful to generate additional data; the confidence of a fit would be improved most by obtaining additional HF data points in regions with the greatest uncertainties. Comparing GPR and MF-GPR results show the utility of generating LF data in parallel with HF datasets. In addition, it could be possible to improve the ML approach itself by developing customized kernels for this application [255–257].

CHAPTER 5

KINETIC MODELING OF STRONGLY COUPLED PLASMA MIXTURES

5.1 Introduction

In Chapter 4, we highlighted how machine learning can be used for interpolating multi-modal plasma transport data in disparate physical regimes. Much of the data in Chapter 4 were obtained for *dense plasmas* using methods like MD or analytic models that have known accuracy in certain limits. We change focus in this chapter to applications of ultracold neutral plasmas (UNPs) which have many orders of magnitude lower number density and ion temperature than dense plasmas; this property of UNPs is illustrated in Table 1.1 and Table 5.1. From these tables, we see that UNPs have strongly coupled ions and are non-degenerate. Moreover, UNPs are highly-collisional and close to equilibrium. The method that we develop and employ in this chapter stems from kinetic theory and aims to characterize all of the aforementioned details.

The organization of this chapter is as follows. First, In Sec. 5.2, we provide a brief review kinetic theory where we present the governing equations and specific choices surrounding the collision operator. Then, we derive expressions for the entropy generation in a system from the viewpoint of kinetic theory which will be used to assess the time-reversibility of multi-species

element	n_i (cm^{-3})	T_i (K)	T_e (K)	Γ	θ	K_n	Ref.
Ca	1.8×10^{10}	1	96	7.1	3.4×10^{3}	6.3×10^{-5}	[15]
Yb	2×10^{9}	1	96	3.4	1.5×10^{4}	1.5×10^{-3}	[15]
Sr	5×10^{9}	1.4	70	3.3	5.7×10^{5}	4.5×10^{-4}	[258]
Sr	1×10^{9}	1	100	2.7	2.4×10^{6}	1.1×10^{-3}	[259]
Ca	3.4×10^{9}	1.8	96	2.3	1.9×10^{4}	1.1×10^{-3}	[260]
Yb	1.9×10^{9}	1	96	3.3	1.5×10^{4}	6.0×10^{-4}	[260]
Xe	2×10^{10}	1	500	7.3	3.2×10^{3}	5.7×10^{-4}	[261]

Table 5.1: Comparison of non-dimensional parameters for UNPs. To compute the Knudsen numbers, a reference length-scale of $L = 1$ mm was used. While the ion species in UNPs are typically laser-cooled to temperatures on the order of micro-Kelvin (μK), disorder-induced heating increases the ion temperature to the order of Kelvin (K). Based on the magnitude of the non-dimensional parameters, we classify UNPs as strongly coupled, non-degenerate, highly-collisional systems.

UNPs. Next, we derive the Vlasov equation in the Cartesian, cylindrical [262], and spherical coordinate system showing that additional acceleration terms appear as a result of the coordinate transformation. We present the conservative form of the 1D-1V Vlasov equation that can be used to model plasma with certain symmetries, like the radial symmetry found in Gaussian UNPs. In Sec. 5.6, we detail the numerical methods used to solve the equations derived in Sec. 5.2. The basis of our numerical scheme consists of a fourth-order finite-volume method [262]. We show numerical results for single- and multi-species UNPs as well as multi-species high-energy-density (HED) plasmas. We find that the amount of entropy generated in multi-species UNPs is largely controlled by the initial conditions of the plasma. Additionally, we use our numerical method to simulate the interfacial mixing in multi-species HED plasmas. We interrogate our numerical results to find that the dominant drivers of diffusion across the interface is dominated by the self-consistent electric field. We conclude by summarizing the results and discuss future work in Sec. 5.7.

5.2 Kinetic Theory

Non-equilibrium statistical mechanics or kinetic theory [263, 264] is a vast field of physics that has many applications. The theoretical basis for kinetic theory stems from the Liouville equation which describes the phase-space evolution of the N-particle distribution function. Through statistical averaging, we obtain the so-called "BBGKY" hierarchy which is the starting point for "kinetic equations." Kinetic equations are defined as a closed equation of motion for f_1, the one-particle distribution function. In this work, we will omit the subscript "1" and simply use f_i to denote the one-particle distribution function of species i. A generic set of kinetic equation for N species has the form

$$\frac{\partial f_i}{\partial t} + \mathbf{v} \cdot \nabla_{\mathbf{r}} f_i + \mathbf{a}_i \cdot \nabla_{\mathbf{v}} f_i = \sum_{j=1}^{N} Q(f_i, f_j), \qquad i = 1, 2, \cdots, N, \tag{5.1}$$

where, in a Cartesian coordinate system, the phase-space distribution for species i is $f_i = f_i(\mathbf{r}, \mathbf{v}, t)$, for $\mathbf{r} = (x, y, x)$, $\mathbf{v} = (v_x, v_y, v_z)$, and the acceleration (or force) acting on species i is $\mathbf{a}_i = (a_{i,x}, a_{i,y}, a_{i,z})$. The term $Q(f_i, f_j)$ is the collision operator between species i and j which introduces microscopic information by way of particle collisions. There are many treatments for $Q(f_i, f_j)$

which all stem from the Boltzmann equation. Some examples include the so-called Fokker-Planck, Lenard-Balescu, Lenard-Bernstein, and Bhatnagar-Gross-Krook collision operators; we explore three versions of the collision operator in this work and they are described in Sec. 5.2.1.

A benefit of kinetic equations for modeling plasmas is that they have fewer degrees of freedom than MD, which has $6N$ degrees of freedom, but more degrees of freedom than hydrodynamic models, which have 3 degrees of freedom. The saying that "a distribution function is worth a thousand macroscopic variables" [263] encapsulates this relation of kinetics and hydrodynamics. In essence, you can derive hydrodynamic equations and macroscopic variables by taking specific moments of the distribution function f. Specifically, the first three moments yield the number density, bulk velocity, and temperature of species i

$$n_i(\mathbf{r}, t) = \int f_i(\mathbf{r}, \mathbf{v}, t)\ d\mathbf{v}, \tag{5.2}$$

$$n_i(\mathbf{r}, t)\mathbf{u}_i(\mathbf{r}, t) = \int \mathbf{v} f_i(\mathbf{r}, \mathbf{v}, t)\ d\mathbf{v}, \tag{5.3}$$

$$\frac{3}{2} n_i(\mathbf{r}, t) T_i(\mathbf{r}, t) = \frac{m_i}{2} \int [\mathbf{v} - \mathbf{u}_i(\mathbf{r}, t)]^2 f_i(\mathbf{r}, \mathbf{v}, t)\ d\mathbf{v}. \tag{5.4}$$

In Sec. 5.2.1 we present three distinct collision operators that we will employ in this chapter. We note that all collision operators stem from approximations to the Boltzmann equation. In particular an assumption of two of the collision operators we discuss is that the system is near equilibrium.

5.2.1 Collision Operators

The simplest choice for the collision operator consists of settting $Q(f_i, f_j) = 0$ and replacing the acceleration term $\mathbf{a}_i$ in Eq. (5.1) with a force computed from the self-consistent electric field (the mean-field approximation) obtained from Poisson's equation. These choices result in the "Vlasov-Poisson" equation, or simply the "Vlasov" equation

$$\frac{\partial f_i}{\partial t} + \mathbf{v} \cdot \nabla_{\mathbf{r}} f_i + \frac{Z_i e \mathbf{E}}{m_i} \cdot \nabla_{\mathbf{v}} f_i = 0, \tag{5.5}$$

$$\mathbf{E} = -\nabla \varphi, \tag{5.6}$$

$$-\frac{1}{4\pi} \nabla^2 \varphi = \sum_{i=1}^{N} Z_i e \int f_i(\mathbf{r}, \mathbf{v}, t)\ d\mathbf{v}. \tag{5.7}$$

It is important to note that here, we have assumed that the system is electrostatic and thus no magnetic fields are generated from electric currents. More generally we would replace $\mathbf{a}_i = Z_i e(\mathbf{E}+\mathbf{v}\times\mathbf{B})/m_i$ which is the Lorentz force with the magnetic field $\mathbf{B}$; in this case, obtaining $\mathbf{E}$ and $\mathbf{B}$ would require solving Maxwell's equations. We note that while the Vlasov equation is often referred to as "collisionless" the particles still interact via the self-consistent electric field. For our study of UNPs using kinetic equations, we will require the use of a collision operator as UNPs are highly collisional (see Table 5.1).

One choice of non-zero collision operator that applies to systems near equilibrium is the Bhatnagar, Gross, and Krook (BGK) [265] collision operator. We begin our discussion of collision operators for a single species kinetic equation (dropping all subscripts so that $f_i = f$). For a single species, the BGK collision operator is

$$Q^{\mathrm{BGK}}(f) = \nu\left[\mathcal{M}(\mathbf{v}; n, \mathbf{u}, T) - f\right], \tag{5.8}$$

where ν is the ion collision frequency and $\mathcal{M}(\mathbf{v}; n, \mathbf{u}, T)$ is a Maxwellian distribution that is parameterized by moments of f [see Eqs. (5.2) - (5.4)].

$$\mathcal{M}(\mathbf{v}; n, \mathbf{u}, T) = n(\mathbf{r}, t)\left[\frac{m}{2\pi T(\mathbf{r}, t)}\right]^{3/2} \exp\left\{-\frac{m\left[\mathbf{v} - \mathbf{u}(\mathbf{r}, t)\right]^2}{2T(\mathbf{r}, t)}\right\}. \tag{5.9}$$

The choice of $\mathcal{M}(\mathbf{v}; n, \mathbf{u}, T)$ depending on the moments of f ensures the conservation of mass, momentum, and energy. We stress that the BGK collision operator is not to be confused with a strikingly similar collision operator proposed by Krook which replaces $\mathcal{M}(\mathbf{v}; n, \mathbf{u}, T)$, with some arbitrary equilibrium distribution f_0 independent of the moments of f so that

$$Q^{\mathrm{Krook}}(f) = \nu(f_0 - f). \tag{5.10}$$

Since f_0 in Eq. (5.10) does not rely on moments of f conservation of mass, momentum, and energy is not guaranteed.

The BGK model has the effect of relaxing the distribution function to equilibrium in phase-space at a time scale determined by ν. We note that the BGK collision operator is computationally simple: it consists of a subtraction and a multiplication. However, because of the underlying assumptions

resulting its simplistic nature, it may fail to accurately model certain plasmas. Another option for the collision operator is one proposed by Lenard and Bernstein (LB) [266]. The LB collision operator is derived from a linearization of the Fokker-Planck equation, which is obtained in the "small-angle" or "weak-scattering" approximation of the Boltzmann equation. The LB equation includes information about gradients in velocity space *viz.*

$$Q^{\mathrm{LB}}(f) = \nu \nabla_{\mathbf{v}} \cdot \left[(\mathbf{v} - \mathbf{u}_0) f + v_{0,th}^2 \nabla_{\mathbf{v}} f \right], \tag{5.11}$$

where $\mathbf{u}_0$ is the *initial* bulk/drift velocity and $v_{0,\mathrm{th}} = \sqrt{3T_0/m}$ is the *initial* root-mean-square speed of the ions. Much like the Krook version of the BGK operator, Eq. (5.11) is non-conservative. To remedy this, conservation is imposed by the form

$$Q^{\mathrm{LBD}}(f) = \nu \nabla_{\mathbf{v}} \cdot \left\{ [\mathbf{v} - \mathbf{u}(\mathbf{r}, t)]\, f + v_{th}^2 \nabla_{\mathbf{v}} f \right\}, \tag{5.12}$$

where u_0 had been replaced with the first moment of f and $v_{\mathrm{th}} = \sqrt{3T(\mathbf{r}, t)/m}$ is the root-mean-square speed that now depends on the second central moment of f. To extend the collision operator to N-species, we need to make modifications to the expressions given in Sec. 5.2.1. For example, the multi-species BGK operator between species i and j is

$$Q^{\mathrm{BGK}}(f_i, f_j) = \nu_{ij} \left[\mathcal{M}_{ij}(\mathbf{v}; n_i, \mathbf{u}_{ij}, T_{ij}) - f_i \right]. \tag{5.13}$$

Equation (5.13) now depends on a Maxwellian distribution that is parametrized by the *mixture quantities* $\mathbf{u}_{ij}$ and T_{ij}. There are non-unique choices for these quantities and the versions we implement in this chapter are derived in Ref. [267] and ensure that the multi-species BGK model is conservative and entropic. The mixture bulk velocity is

$$\mathbf{u}_{ij} = \frac{\rho_i \nu_{ij} \mathbf{u}_i + \rho_j \nu_{ji} \mathbf{u}_j}{\rho_i \nu_{ij} + \rho_j \nu_{ji}}, \tag{5.14}$$

and the mixture temperature is

$$T_{ij} = \frac{n_i \nu_{ij} T_i + n_j \nu_{ji} T_j}{n_i \nu_{ij} + n_j \nu_{ji}} + \frac{\rho_i \nu_{ij} (v_i^2 - v_{ij}^2) + \rho_j \nu_{ji} (v_j^2 - v_{ij}^2)}{3(n_i \nu_{ij} + n_j \nu_{ji})}. \tag{5.15}$$

Note that both the BGK and LBD operators depend on the same input: the collision frequency ν_{ij}. There are many choices for obtaining the collision frequency, and the specific choices used in

this chapter are described in Secs. 5.2.2 and 5.2.3. Since we are interested in simulating UNPs, we chose a collision rate model that is accurate for strongly coupled plasmas. We note that most collision rate models are typically accurate for weakly coupled plasmas.

5.2.2 Ion-Ion Collision Rate

As shown in Table 5.1, UNPs are moderately-coupled systems; therefore, the collision rate ν_{ij} must be accurate in these regimes. There are many collision rate models that exist [268, 269] that often make approximations to circumvent issues associated with computing the necessary collision integrals. These approximations introduce the so-called “Coulomb logarithm" which is known to fail at strong coupling. Here, we employ a collision rate model derived in Ref. [267] which is valid for moderately-coupled systems and does not rely on a Coulomb logarithm. The specific collision rate we use in this chapter is the the rate derived from temperature relaxation rate denoted as “ET" in Ref. [267]. The collision rate between species i and j is given by

$$\nu_{ij} = \frac{1}{n_i} \frac{256\pi^2 n_i n_j (m_i m_j)^{1/2} (Z_i Z_j e^2)^2}{3(2\pi)^{3/2} (m_i T_j + m_j T_i)^{3/2}} \mathcal{K}_{11}(g_{ij}), \tag{5.16}$$

$$g_{ij} = \frac{Z_i Z_j e^2 (m_i + m_j)}{\lambda_{\text{eff}} (m_i T_j + m_j T_i)}. \tag{5.17}$$

Where $\mathcal{K}_{11}$ is a fit to the collision integrals with an effective interaction potential

$$\mathcal{K}_{11}(g) = \begin{cases} -\frac{1}{4} \ln\left(\sum_{k=1}^{5} a_k g^k\right), & g < 1 \\ \dfrac{b_0 + b_1 \ln(g) + b_2 \ln^2(g)}{1 + b_3 g + b_4 g^2} & g \geq 1, \end{cases} \tag{5.18}$$

where the a coefficients are $a_1 = 1.4660$, $a_2 = -1.7836$, $a_3 = 1.4313$, $a_4 = -0.55833$, and $a_5 = 0.061162$ and the b coefficients are $b_0 = 0.081033$, $b_1 = -0.091336$, $b_2 = 0.051760$, $b_3 = -0.50026$, and $b_4 = 0.17044$; these coefficients are provided in Appendix C of Ref. [151]. Here, the plasma parameter g_{ij} appears in Eq. (67) of Ref. [151] but with a modified temperature to account for multiple ion temperatures. The *effective* screening length is given by both the ions and electron species as

$$\lambda_{\text{eff}} = \left[\frac{1}{\lambda_{\text{e}}} + \sum_{i=1}^{N} \frac{1}{\lambda_i} \left(\frac{1}{1 + 3\Gamma_i^{\text{IS}}} \right) \right]^{-1/2}, \tag{5.19}$$

where the electron and ion screening lengths are

$$\lambda_{\mathrm{e}}^2 = \frac{\sqrt{T_e^2 + \left(\frac{2}{3}E_F\right)^2}}{4\pi e^2 n_e}, \tag{5.20}$$

$$\lambda_i^2 = \frac{T_i}{4\pi Z_i^2 e^2 n_i}, \tag{5.21}$$

and the modified Coulomb coupling parameter is given by

$$\Gamma_i^{\mathrm{IS}} = \frac{(Z_i e)^2}{a_i^{\mathrm{IS}} T_i}, \tag{5.22}$$

$$a_i^{\mathrm{IS}} = \left(\frac{3Z_i e}{4\pi\rho_{\mathrm{tot}}}\right)^{1/3}, \tag{5.23}$$

$$\rho_{\mathrm{tot}} = \sum_{i=1}^{N} Z_i e n_i. \tag{5.24}$$

We will use Eq. (5.16) in all kinetic simulations where ion-ion interactions are present. Ion-ion kinetic simulations are carried out for HED plasmas in Secs. 5.6.1.1 and 5.6.2.3 and for UNPs in Secs. 5.6.1.2 and 5.6.2. If we are interested in simulating electron-electron collisions, modifications to the collision rate need to be made. We describe eight collision rate models for electron-electron interactions in Sec. 5.2.3.

5.2.3 Electron-Electron Collision Rate

To compute the electron-electron collision rate, we implement eight collision rate models, seven of which require the use of a Coulomb logarithm. The seven models that require a Coulomb logarithm are the Landau-Spitzer (LS) model [270], which assumes a straight-line trajectory and binary interactions, and six models proposed by Gericke, Murillo, and Schlanges (GMS) [269], three of which make modifications to the LS straight-line trajectory assumption and three additional models that introduce the concept of hyperbolic trajectories and binary collisions. The electron-electron collision rate ν_{ee} can be obtained from [151, 271]

$$\nu_{ee} = \frac{8\sqrt{\pi} n_e e^4 \ln\Lambda}{3\sqrt{m_e} T_e^{3/2}}, \tag{5.25}$$

Where $\ln\Lambda$ is the Coulomb logarithm. Expression for the Coulomb logarithm can be found in Refs. [270] and [269]. The final model used for obtaining collision rates does not depend on

a Coulomb logarithm as proposed by Haack, Hauck, and Murillo (HHM) [44, 267]. The HHM collision rate includes effects of particle correlations beyond a binary scattering viewpoint by numerically evaluating the collision integral with an effective interaction potential [151]. The HHM collision rate is given by

$$\nu_{ee}^{\text{HHM}} = \frac{32\sqrt{\pi}n_e e^4}{3\sqrt{m_e}T_e^{3/2}}\mathcal{K}_{11}(\gamma_{ee}), \tag{5.26}$$

$$\gamma_{ee} = \frac{e^2}{T_e\lambda_{\text{TF}}}, \tag{5.27}$$

$$\lambda_{\text{TF}}^2 = \frac{4\pi e^2 n_e}{T_e^2 + (\frac{2}{3}E_F)^2}, \tag{5.28}$$

where $E_F = \hbar^2(3\pi^2 n_e)^{2/3}/2m_e$ is the Fermi energy.

Table 5.2 shows a comparison of the eight collision rate models described here applied to an electron UNP. In Sec. 5.6.1.3 we will use these electron-electron collision rates to simulate the tail-filling in an electron UNP. Tail filling is the process by which "depleted" high-energy tails of a velocity distribution for a system of particles equilibrates. That is, the plasma equilibrates to equilibrium on some time-scale determined by the collision rate – “replenishing" the tails. In general, a system that is in equilibrium does not generate entropy. In Sec. 5.2.4, we mathematically define the process of entropy generation starting from a kinetic theory viewpoint.

5.2.4 Entropy Generation and Time-Reversibility

Ultimately, the role of a collision operator is to drive a system to equilibrium. To quantify when a system has equilibrated, we consider the amount of entropy being generated in a system. When entropy is no longer being generated, the system has reached thermodynamic equilibrium. Later in this chapter, we will show that the initial conditions of a plasma mixture dictate the amount of entropy that is generated. We begin with an equation for the entropy density of an N-species system [189]

$$\rho s = -k_B \sum_{i=1}^{N} \int f_i(\ln f_i - 1)d\mathbf{v}. \tag{5.29}$$

Taking the time derivative of Eq. (5.29) we get

$$\begin{aligned}\frac{\partial \rho s}{\partial t} &= -k_B \sum_{i=1}^{N} \int \ln f_i \frac{\partial f_i}{\partial t} d\mathbf{v} \\ &= k_B \sum_{i=1}^{N} \int \ln f_i \left[\mathbf{v} \cdot \nabla_{\mathbf{r}} f_i + \frac{Z_i e \mathbf{E}}{m_i} \cdot \nabla_{\mathbf{v}} f_i - \sum_{j=1}^{N} Q(f_i, f_j) \right] d\mathbf{v} \\ &= k_B \nabla_{\mathbf{r}} \cdot \sum_{i=1}^{N} \int \mathbf{v} [f_i (\ln f_i - 1)] d\mathbf{v} + k_B \sum_{i=1}^{N} \int \frac{Z_i e \mathbf{E}}{m_i} \cdot \ln f_i \nabla_{\mathbf{v}} f_i d\mathbf{v} \\ &- k_B \sum_{i,j=1}^{N} \int Q(f_i, f_j) \ln f_i d\mathbf{v}, \end{aligned} \tag{5.30}$$

where we have used the relation that $\ln f_i \nabla_{\mathbf{r}} f_i = \nabla_{\mathbf{r}} [f_i (\ln f_i - 1)]$. Integration by parts on the second term in Eq. (5.30) yields zero and holds for any arbitrary non-velocity dependent force. Therefore we have

$$\frac{\partial \rho s}{\partial t} = k_B \nabla_{\mathbf{r}} \cdot \sum_{i=1}^{N} \int \mathbf{v} [f_i (\ln f_i - 1)] d\mathbf{v} - k_B \sum_{i,j=1}^{N} \int Q(f_i, f_j) \ln f_i d\mathbf{v}. \tag{5.31}$$

Adding and subtracting the barycentric velocity defined as

$$\mathbf{u} = \frac{1}{\rho} \sum_{i=1}^{N} \rho_i \mathbf{u}_i, \tag{5.32}$$

$$\rho = \sum_{i=1}^{N} m_i n_i, \tag{5.33}$$

we obtain

$$\frac{\partial \rho s}{\partial t} = k_B \nabla_{\mathbf{r}} \cdot \sum_{i=1}^{N} \int (\mathbf{v} - \mathbf{u} + \mathbf{u}) [f_i (\ln f_i - 1)] d\mathbf{v} - k_B \sum_{i,j=1}^{N} \int Q(f_i, f_j) \ln f_i d\mathbf{v}. \tag{5.34}$$

Rearranging the first term we have

$$\begin{aligned}\frac{\partial \rho s}{\partial t} = k_B \nabla_{\mathbf{r}} \cdot \mathbf{u} \sum_{i=1}^{N} \int f_i (\ln f_i - 1) d\mathbf{v} + k_B \nabla_{\mathbf{r}} \cdot \sum_{i=1}^{N} \int (\mathbf{v} - \mathbf{u}) [f_i (\ln f_i - 1)] d\mathbf{v} \\ - k_B \sum_{i,j=1}^{N} \int Q(f_i, f_j) \ln f_i d\mathbf{v}. \end{aligned} \tag{5.35}$$

Using Eq. (5.29) and defining the entropy *flux* and entropy *source term* as

$$J_s = -k_B \nabla_{\mathbf{r}} \cdot \sum_{i=1}^{N} \int (\mathbf{v} - \mathbf{u})[f_i(\ln f_i - 1)] d\mathbf{v}, \tag{5.36}$$

$$\sigma = -k_B \sum_{i,j=1}^{N} \int Q(f_i, f_j) \ln f_i d\mathbf{v}, \tag{5.37}$$

respectively, Eq (5.35) becomes

$$\frac{\partial \rho s}{\partial t} = -\nabla_{\mathbf{r}} \cdot (\rho s \mathbf{u} + J_s) + \sigma. \tag{5.38}$$

Equation (5.38) is simply an advection equation plus a source term for the entropy density or in other words, a time- and space-dependent equation for the second law of thermodynamics. We stress that the entropy source term σ is characterized purely by the collision operator. In the case of Vlasov, no entropy will be generated in the system implying that the system is not evolving to equilibrium. In fact, solutions of the Vlasov equation, as well as MD, are completely deterministic and *time-reversible*. The fact that MD is also time-reversible should be alarming since fundamentally, our universe is made up of atoms with interactions that could be described by Newton's second law. The time-reversibility of Newton's second law implies that our universe is time-reversible and that after some amount of time, we would expect to return to our "initial condition." While mathematically true, the Poincaré recurrence theorem suggests that the time that would need to pass in order for that to happen would be nearly infinite as there are essentially infinite number of particles in our universe.

5.2.5 Entropy Density in Thermodynamic Equilibrium

Consider the case where of thermodynamic equilibrium where the distribution function has the form of a Maxwellian

$$f_i^{\text{eq}} = n_i \left(\frac{m_i}{2\pi T}\right)^{3/2} \exp\left[-\frac{m_i(\mathbf{v} - \mathbf{u})^2}{2T}\right]. \tag{5.39}$$

We can re-write the above expression by substituting in the thermodynamic potential for an ideal gas mixture

$$\mu_i = \frac{T}{m_i}\left(\ln n_i - \frac{3}{2} \ln \frac{2\pi T}{m_i}\right), \tag{5.40}$$

we get that

$$\exp\left(\frac{m_i\mu_i}{T}\right) = n_i\left(\frac{m_i}{2\pi T}\right)^{3/2}, \tag{5.41}$$

which we can substitute into Eq. (5.39) to obtain

$$\begin{aligned} f_i^{\text{eq}} &= \exp\left(\frac{m_i\mu_i}{T}\right)\exp\left[-\frac{m_i(\mathbf{v}-\mathbf{u})^2}{2T}\right] \\ &= \exp\left[m_i\frac{\mu_i - \frac{1}{2}(\mathbf{v}-\mathbf{u})^2}{2T}\right]. \end{aligned} \tag{5.42}$$

Using Eq. (5.42) into Eq. (5.29) gives

$$\rho s = -k_B\sum_{i=1}^{N}\int f_i^{\text{eq}}\left[m_i\frac{\mu_i - \frac{1}{2}(\mathbf{v}-\mathbf{u})^2}{2T} - 1\right]d\mathbf{v}, \tag{5.43}$$

which reduces to

$$\rho s = -\frac{k_B}{T}\left(\sum_{i=1}^{N}\rho_i\mu_i - \rho u - p\right). \tag{5.44}$$

Equation(5.44) shows that the kinetic theory opinion of the entropy density in equilibrium is consistent with the thermodynamic expression. Using the Gibbs relation, we arrive at an expression for the entropy source term in terms of the diffusion flux, heat flux, and pressure tensor. Decomposing the entropy source term this way allows for an analysis of the dominant terms that generate entropy. That is, we can connect quantities like interdiffusion, thermal conductivity, and viscosity to the amount of entropy production in a plasma.

5.3 The Vlasov Equation in Conservative Form

Before beginning our discussion on the numerical methods we employ to solve our kinetic equation, we wish to represent our kinetic equation in conservative form. Doing so will allow us to utilize numerical methods for conservation laws, in particular, finite-volume methods. Returning to the single-species Vlasov equation, which will be the left-hand-side for all of our spatially dependent kinetic equations in this chapter, we expand Eq. (5.5) as

$$\frac{\partial f}{\partial t} + v_x\frac{\partial}{\partial x}f + v_y\frac{\partial}{\partial y}f + v_z\frac{\partial}{\partial z}f + a_x\frac{\partial}{\partial v_x}f + a_y\frac{\partial}{\partial v_y}f + a_z\frac{\partial}{\partial v_z}f = 0. \tag{5.45}$$

Note that if the a_x, a_y, and a_z are determined from the self-consistent electric field [see Eq. (5.6)], then both the velocity and acceleration components commute with the partial derivatives and

Eq. (5.45) becomes

$$\frac{\partial f}{\partial t} + \frac{\partial}{\partial x}(v_x f) + \frac{\partial}{\partial y}(v_y f) + \frac{\partial}{\partial z}(v_z f) + \frac{\partial}{\partial v_x}(a_x f) + \frac{\partial}{\partial v_y}(a_y f) + \frac{\partial}{\partial v_z}(a_z f) = 0. \tag{5.46}$$

Equation (5.46) can be written in a compact notation as

$$\frac{\partial f}{\partial t} + \nabla_{\mathbf{X}} \cdot (\dot{\mathbf{X}} f) = 0, \tag{5.47}$$

where

$$\mathbf{X} = [x, y, z, v_x, v_y, v_z]^T, \qquad \dot{\mathbf{X}} = [v_x, v_y, v_z, a_x, a_y, a_z]^T. \tag{5.48}$$

We note that Eq. (5.47) is written in *conservative form*, i.e., the time derivative of the distribution function changes due to the divergence of fluxes $\dot{\mathbf{X}} f$.

Representing Eq. (5.5) in conservative form was a trivial task in Cartesian coordinates. The triviality was a direct consequence of the fact that the velocity and acceleration components do not depend on the partial derivatives, allowing them to commute. In Secs. 5.3.1 and 5.3.2, we derive the conservative form of the Vlasov equation in both cylindrical and spherical coordinate systems. The cylindrical form was discussed in detail in Ref. [262] and we follow the same derivation procedure for spherical coordinates. For completeness, we repeat the derivation for cylindrical coordinates carried out in Ref. [262] here. Our ultimate goal is to numerically implement our kinetic model in spherical coordinates. The reason the spherical coordinate system is desirable is due to the fact that UNPs are often initialized as spherically symmetric clouds which then expand radially outward into the surrounding vacuum. Additionally, many diagnostics used in UNP experiments report the radial expansion of the plasma and we wish to compare our work against available experimental data.

5.3.1 Cylindrical Coordinates

In cylindrical coordinates, a vector $\mathbf{r}$ is defined by (ρ, ϕ, z) where

$$\mathbf{r} = \rho \hat{\mathbf{e}}_\rho + \phi \hat{\mathbf{e}}_\phi + z \hat{\mathbf{e}}_z, \tag{5.49}$$

where $\hat{\mathbf{e}}_\xi$ denote unit vectors point along the coordinate ξ. The relation of unit vectors in cylindrical coordinates to the unit vectors in Cartesian coordinates by

$$\hat{\mathbf{e}}_\rho = \cos\phi\hat{\mathbf{e}}_x + \sin\phi\hat{\mathbf{e}}_y, \tag{5.50}$$

$$\hat{\mathbf{e}}_\phi = -\sin\phi\hat{\mathbf{e}}_x + y\cos\phi\hat{\mathbf{e}}_y, \tag{5.51}$$

$$\hat{\mathbf{e}}_z = z\hat{\mathbf{e}}_z. \tag{5.52}$$

The relation of a vector in cylindrical coordinates to Cartesian coordinates is given by

$$\mathbf{r}_{\text{cyl}} \equiv \begin{bmatrix} r_\rho \\ r_\phi \\ r_z \end{bmatrix} = \begin{bmatrix} \rho \\ \phi \\ z \end{bmatrix} = \begin{bmatrix} (x^2+y^2)^{1/2} \\ \arctan\left(\frac{y}{x}\right) \\ z \end{bmatrix}. \tag{5.53}$$

The velocity in cylindrical coordinates is found via

$$\begin{aligned} \mathbf{v}_{\text{cyl}} = \frac{d}{dt}\left(\rho\hat{\mathbf{e}}_\rho + z\hat{\mathbf{e}}_z\right) &= \rho\dot{\hat{\mathbf{e}}}_\rho + \dot{\rho}\hat{\mathbf{e}}_\rho + z\dot{\hat{\mathbf{e}}}_z + \dot{z}\hat{\mathbf{e}}_z \\ &= \dot{\rho}\hat{\mathbf{e}}_\rho + \rho\dot{\phi}\hat{\mathbf{e}}_\phi + \dot{z}\hat{\mathbf{e}}_z. \end{aligned}$$

The velocity vector in cylindrical coordinates is now related to Cartesian coordinates by

$$\mathbf{v}_{\text{cyl}} \equiv \begin{bmatrix} v_\rho \\ v_\phi \\ v_z \end{bmatrix} = \begin{bmatrix} \dot{\rho} \\ \rho\dot{\phi} \\ \dot{z} \end{bmatrix} = \begin{bmatrix} \dfrac{xv_x + yv_y}{(x^2+y^2)^{1/2}} \\ (x^2+y^2)^{1/2}\dfrac{xv_y - yv_x}{x^2+y^2} \\ v_z \end{bmatrix} = \begin{bmatrix} \dfrac{xv_x + yv_y}{(x^2+y^2)^{1/2}} \\ \dfrac{xv_y - yv_x}{(x^2+y^2)^{1/2}} \\ v_z \end{bmatrix}. \tag{5.54}$$

Now define $\bar{\mathbf{F}} \equiv \dot{\mathbf{X}}f$. The goal is to convert the divergence of the fluxes $\bar{\mathbf{F}}$ into a new coordinate system which can be done by using the following relation:

$$\nabla_{\mathbf{X}} \cdot \bar{\mathbf{F}} = J\nabla_{\boldsymbol{\xi}} \cdot \left(\frac{1}{J}\mathbf{J}\bar{\mathbf{F}}\right). \tag{5.55}$$

Where $\mathbf{J}$ denotes the Jacobian matrix with determinant J. The Jacobian matrix is

$$\mathbf{J} = \begin{bmatrix} \dfrac{\partial \mathbf{r}_{\text{cyl}}}{\partial \mathbf{r}_{\text{car}}} & \dfrac{\partial \mathbf{r}_{\text{cyl}}}{\partial \mathbf{v}_{\text{car}}} \\ \dfrac{\partial \mathbf{v}_{\text{cyl}}}{\partial \mathbf{r}_{\text{car}}} & \dfrac{\partial \mathbf{v}_{\text{cyl}}}{\partial \mathbf{v}_{\text{car}}} \end{bmatrix}, \tag{5.56}$$

where

$$\frac{\partial \mathbf{r}_{\text{cyl}}}{\partial \mathbf{r}_{\text{car}}} = \begin{bmatrix} \frac{\partial r_\rho}{\partial x} & \frac{\partial r_\rho}{\partial y} & \frac{\partial r_\rho}{\partial z} \\ \frac{\partial r_\phi}{\partial x} & \frac{\partial r_\phi}{\partial y} & \frac{\partial r_\phi}{\partial z} \\ \frac{\partial r_z}{\partial x} & \frac{\partial r_z}{\partial y} & \frac{\partial r_z}{\partial z} \end{bmatrix} = \begin{bmatrix} \frac{x}{\rho} & \frac{y}{\rho} & 0 \\ \frac{-y}{x^2+y^2} & \frac{x}{x^2+y^2} & 0 \\ 0 & 0 & 1 \end{bmatrix}, \tag{5.57}$$

$$\frac{\partial \mathbf{r}_{\text{cyl}}}{\partial \mathbf{v}_{\text{car}}} = \begin{bmatrix} \frac{\partial r_\rho}{\partial v_x} & \frac{\partial r_\rho}{\partial v_y} & \frac{\partial r_\rho}{\partial v_z} \\ \frac{\partial r_\phi}{\partial v_x} & \frac{\partial r_\phi}{\partial v_y} & \frac{\partial r_\phi}{\partial v_z} \\ \frac{\partial r_z}{\partial v_x} & \frac{\partial r_z}{\partial v_y} & \frac{\partial r_z}{\partial v_z} \end{bmatrix} = \mathbf{0}, \tag{5.58}$$

$$\frac{\partial \mathbf{v}_{\text{cyl}}}{\partial \mathbf{r}_{\text{car}}} = \begin{bmatrix} \frac{\partial v_\rho}{\partial x} & \frac{\partial v_\rho}{\partial y} & \frac{\partial v_\rho}{\partial z} \\ \frac{\partial v_\phi}{\partial x} & \frac{\partial v_\phi}{\partial y} & \frac{\partial v_\phi}{\partial z} \\ \frac{\partial v_z}{\partial x} & \frac{\partial v_z}{\partial y} & \frac{\partial v_z}{\partial z} \end{bmatrix} = \begin{bmatrix} \frac{y(yv_x - xv_y)}{\rho^3} & \frac{x(xv_y - yv_x)}{\rho^3} & 0 \\ \frac{y(xv_x + yv_y)}{\rho^3} & -\frac{x(xv_x + yv_y)}{\rho^3} & 0 \\ 0 & 0 & 0 \end{bmatrix}, \tag{5.59}$$

$$\frac{\partial \mathbf{v}_{\text{cyl}}}{\partial \mathbf{v}_{\text{car}}} = \begin{bmatrix} \frac{\partial v_\rho}{\partial v_x} & \frac{\partial v_\rho}{\partial v_y} & \frac{\partial v_\rho}{\partial v_z} \\ \frac{\partial v_\phi}{\partial v_x} & \frac{\partial v_\phi}{\partial v_y} & \frac{\partial v_\phi}{\partial v_z} \\ \frac{\partial v_z}{\partial v_x} & \frac{\partial v_z}{\partial v_y} & \frac{\partial v_z}{\partial v_z} \end{bmatrix} = \begin{bmatrix} \frac{x}{\rho} & \frac{y}{\rho} & 0 \\ \frac{-y}{\rho} & \frac{x}{\rho} & 0 \\ 0 & 0 & 1 \end{bmatrix}. \tag{5.60}$$

The Jacobian transformation matrix from Cartesian to cylindrical coordinates is

$$\mathbf{J} = \begin{bmatrix} \frac{x}{\rho} & \frac{y}{\rho} & 0 & 0 & 0 & 0 \\ \frac{-y}{\rho^2} & \frac{x}{\rho^2} & 0 & 0 & 0 & 0 \\ 0 & 0 & 1 & 0 & 0 & 0 \\ \frac{y(yv_x - xv_y)}{\rho^3} & \frac{x(xv_y - yv_x)}{\rho^3} & 0 & \frac{x}{\rho} & \frac{y}{\rho} & 0 \\ \frac{y(xv_x + yv_y)}{\rho^3} & -\frac{x(xv_x + yv_y)}{\rho^3} & 0 & \frac{-y}{\rho} & \frac{x}{\rho} & 0 \\ 0 & 0 & 0 & 0 & 0 & 1 \end{bmatrix}. \tag{5.61}$$

We note that the determinant of $\mathbf{J}$ is $J = 1/\rho$. Computing the matrix-vector product defined in Eq. (5.55), we have

$$\nabla_{\mathbf{X}} \cdot \bar{\mathbf{F}} = \frac{1}{\rho} \begin{bmatrix} \frac{\partial}{\partial \rho} \\ \frac{\partial}{\partial \phi} \\ \frac{\partial}{\partial z} \\ \frac{\partial}{\partial v_\rho} \\ \frac{\partial}{\partial v_\phi} \\ \frac{\partial}{\partial v_z} \end{bmatrix} \cdot \left\{ \rho \begin{bmatrix} \frac{x}{\rho} & \frac{y}{\rho} & 0 & 0 & 0 & 0 \\ \frac{-y}{\rho^2} & \frac{x}{\rho^2} & 0 & 0 & 0 & 0 \\ 0 & 0 & 1 & 0 & 0 & 0 \\ \frac{y(yv_x - xv_y)}{\rho^3} & \frac{x(xv_y - yv_x)}{\rho^3} & 0 & \frac{x}{\rho} & \frac{y}{\rho} & 0 \\ \frac{y(xv_x + yv_y)}{\rho^3} & -\frac{x(xv_x + yv_y)}{\rho^3} & 0 & \frac{-y}{\rho} & \frac{x}{\rho} & 0 \\ 0 & 0 & 0 & 0 & 0 & 1 \end{bmatrix} \begin{bmatrix} v_x f \\ v_y f \\ v_z f \\ a_x f \\ a_y f \\ a_z f \end{bmatrix} \right\}, \tag{5.62}$$

which simplifies to

$$\nabla_{\mathbf{X}} \cdot \bar{\mathbf{F}} = \frac{1}{\rho} \begin{bmatrix} \frac{\partial}{\partial \rho} \\ \frac{\partial}{\partial \phi} \\ \frac{\partial}{\partial z} \\ \frac{\partial}{\partial v_\rho} \\ \frac{\partial}{\partial v_\phi} \\ \frac{\partial}{\partial v_z} \end{bmatrix} \cdot \begin{bmatrix} \rho v_\rho f \\ v_\phi f \\ \rho v_z f \\ \left(\rho a_r + v_\phi^2\right) f \\ \left(\rho a_\phi - v_\rho v_\phi\right) f \\ \rho a_z f \end{bmatrix}. \tag{5.63}$$

Where we have made the definitions that

$$a_\rho \equiv \frac{x a_x + y a_y}{\rho}, \tag{5.64}$$

$$a_\phi \equiv \frac{x a_y - y a_x}{\rho}. \tag{5.65}$$

Now that we have an expression for the divergence of the fluxes in the cylindrical coordinate system, we use Eq. (5.47) to obtain the Vlasov equations in cylindrical coordinates

$$\begin{aligned} \frac{\partial f}{\partial t} + \frac{1}{\rho}\frac{\partial}{\partial \rho}(\rho v_\rho f) + \frac{1}{\rho}\frac{\partial}{\partial \phi}(v_\phi f) \\ + \frac{1}{\rho}\frac{\partial}{\partial z}(\rho v_z f) \\ + \frac{1}{\rho}\frac{\partial}{\partial v_\rho}\left[(\rho a_\rho + v_\phi^2) f\right] + \frac{1}{\rho}\frac{\partial}{\partial v_\phi}\left[(\rho a_\phi - v_\rho v_\phi) f\right] + \frac{1}{\rho}\frac{\partial}{\partial v_z}(\rho a_z f) = 0, \end{aligned} \tag{5.66}$$

which is the same result obtained in Refs. [262, 272]. We can further simplify Eq. (5.66) by canceling the pre-factor of ρ to yield

$$\begin{aligned} \frac{\partial f}{\partial t} + \frac{1}{\rho}\frac{\partial}{\partial \rho}(\rho v_\rho f) + \frac{1}{\rho}\frac{\partial}{\partial \phi}(v_\phi f) + \frac{\partial}{\partial z}(v_z f) + \frac{\partial}{\partial v_\rho}\left[\left(a_\rho + \frac{v_\phi^2}{\rho}\right) f\right] \\ + \frac{\partial}{\partial v_\phi}\left[\left(a_\phi - \frac{v_\rho v_\phi}{\rho}\right) f\right] + \frac{\partial}{\partial v_z}(a_z f) = 0. \end{aligned} \tag{5.67}$$

We note that in contrast to the conservative form in the Cartesian coordinate system, additional acceleration terms in Eq. (5.67) appear. Specifically, these additional acceleration terms correspond

to the acceleration from the Coriolis force $-v_r v_\theta / r$ and the centripetal force v_ϕ^2 / r. We will repeat this procedure for the spherical coordinate system in Sec. 5.3.2 and show that these additional acceleration terms also appear.

5.3.2 Spherical Coordinates

A vector in spherical coordinates is described at a point (r, θ, ϕ) so that

$$\mathbf{r} = r\hat{\mathbf{e}}_r + \theta\hat{\mathbf{e}}_\theta + \phi\hat{\mathbf{e}}_\phi, \tag{5.68}$$

where the unit vectors in spherical coordinates are related to the unit vectors in Cartesian coordinates by

$$\hat{\mathbf{e}}_r = \sin\theta\cos\phi\hat{\mathbf{e}}_x + \sin\theta\sin\phi\hat{\mathbf{e}}_y + \cos\theta\hat{\mathbf{e}}_z, \tag{5.69}$$

$$\hat{\mathbf{e}}_\theta = \cos\theta\cos\phi\hat{\mathbf{e}}_x + \cos\theta\sin\phi\hat{\mathbf{e}}_y - \sin\theta\hat{\mathbf{e}}_z, \tag{5.70}$$

$$\hat{\mathbf{e}}_\phi = -\sin\phi\hat{\mathbf{e}}_x + \cos\phi\hat{\mathbf{e}}_y. \tag{5.71}$$

The relation of a vector in spherical coordinates to Cartesian coordinates is given by

$$\mathbf{r}_{\text{sph}} \equiv \begin{bmatrix} r_r \\ r_\theta \\ r_\phi \end{bmatrix} = \begin{bmatrix} r \\ \theta \\ \phi \end{bmatrix} = \begin{bmatrix} (x^2+y^2+z^2)^{1/2} \\ \arccos\left[\dfrac{z}{(x^2+y^2+z^2)^{1/2}}\right] \\ \arctan\left(\dfrac{y}{x}\right) \end{bmatrix}. \tag{5.72}$$

The velocity of a point in spherical coordinates is computed by taking a time derivative

$$\begin{aligned} \mathbf{v}_{\text{sph}} \equiv \frac{d}{dt}\mathbf{r}\hat{\mathbf{e}}_r &= r\dot{\hat{\mathbf{e}}}_r + \dot{r}\hat{\mathbf{e}}_r \\ &= \dot{r}\hat{\mathbf{e}}_r + r\dot{\theta}\hat{\mathbf{e}}_\theta + r\dot{\phi}\sin\theta\hat{\mathbf{e}}_\phi. \end{aligned}$$

The velocity vector is related to Cartesian coordinates by

$$\mathbf{v}_{\text{sph}} \equiv \begin{bmatrix} v_r \\ v_\theta \\ v_\phi \end{bmatrix} = \begin{bmatrix} \dot{r} \\ r\dot{\theta} \\ r\sin\theta\dot{\phi} \end{bmatrix} = \begin{bmatrix} \dfrac{xv_x + yv_y + zv_z}{(x^2+y^2+z^2)^{1/2}} \\ (x^2+y^2+z^2)^{1/2}\dfrac{xzv_x + yzv_y - (x^2+y^2)v_z}{(x^2+y^2)^{1/2}(x^2+y^2+z^2)} \\ (x^2+y^2+z^2)^{1/2}\sin\left[\arccos\left(\frac{z}{(x^2+y^2+z^2)^{1/2}}\right)\right]\left(\dfrac{-yv_x + xv_y}{x^2+y^2}\right) \end{bmatrix} \tag{5.73}$$

$$= \begin{bmatrix} \dfrac{xv_x + yv_y + zv_z}{r} \\ \dfrac{xzv_x + yzv_y - (x^2+y^2)v_z}{(x^2+y^2)^{1/2}r} \\ \dfrac{-yv_x + xv_y}{(x^2+y^2)^{1/2}} \end{bmatrix}. \tag{5.74}$$

The Jacobian for representing how vectors in a spherical coordinate system vary with respect to vectors in a Cartesian coordinate system is

$$\mathbf{J} = \begin{bmatrix} \dfrac{\partial \mathbf{r}_{\text{sph}}}{\partial \mathbf{r}_{\text{car}}} & \dfrac{\partial \mathbf{r}_{\text{sph}}}{\partial \mathbf{v}_{\text{car}}} \\ \dfrac{\partial \mathbf{v}_{\text{sph}}}{\partial \mathbf{r}_{\text{car}}} & \dfrac{\partial \mathbf{v}_{\text{sph}}}{\partial \mathbf{v}_{\text{car}}} \end{bmatrix}, \tag{5.75}$$

where

$$\frac{\partial \mathbf{r}_{\text{sph}}}{\partial \mathbf{r}_{\text{car}}} = \begin{bmatrix} \frac{\partial r_r}{\partial x} & \frac{\partial r_r}{\partial y} & \frac{\partial r_r}{\partial z} \\ \frac{\partial r_\theta}{\partial x} & \frac{\partial r_\theta}{\partial y} & \frac{\partial r_\theta}{\partial z} \\ \frac{\partial r_\phi}{\partial x} & \frac{\partial r_\phi}{\partial y} & \frac{\partial r_\phi}{\partial z} \end{bmatrix} = \begin{bmatrix} \frac{x}{r} & \frac{y}{r} & \frac{z}{r} \\ \frac{xz}{(x^2+y^2)^{1/2}r^2} & \frac{yz}{(x^2+y^2)^{1/2}r^2} & \frac{-x^2-y^2}{(x^2+y^2)^{1/2}r^2} \\ \frac{-y}{x^2+y^2} & \frac{x}{x^2+y^2} & 0 \end{bmatrix},$$

$$\frac{\partial \mathbf{r}_{\text{sph}}}{\partial \mathbf{v}_{\text{car}}} = \mathbf{0},$$

$$\frac{\partial \mathbf{v}_{\text{sph}}}{\partial \mathbf{r}_{\text{car}}} = \begin{bmatrix} \frac{\partial v_r}{\partial x} & \frac{\partial v_r}{\partial y} & \frac{\partial v_r}{\partial z} \\ \frac{\partial v_\theta}{\partial x} & \frac{\partial v_\theta}{\partial y} & \frac{\partial v_\theta}{\partial z} \\ \frac{\partial v_\phi}{\partial x} & \frac{\partial v_\phi}{\partial y} & \frac{\partial v_\phi}{\partial z} \end{bmatrix}$$

$$= \begin{bmatrix} \frac{(y^2+z^2)v_x - xyv_y - xzv_z}{r^3} & \frac{-xyv_x + (x^2+z^2)v_y - yzv_z}{r^3} & \frac{-xzv_x - yzv_y + (x^2+y^2)v_z}{r^3} \\ \frac{\alpha v_x + \beta v_y + \gamma v_z}{(x^2+y^2)^{3/2}r^3} & \frac{\beta v_x + \rho v_y + \eta v_z}{(x^2+y^2)^{3/2}r^3} & \frac{(x^2+y^2)^{1/2}(xv_x + yv_y + zv_z)}{r^3} \\ \frac{xyv_x + y^2 v_y}{(x^2+y^2)^{3/2}} & \frac{-x^2 v_x - xyv_y}{(x^2+y^2)^{3/2}} & 0 \end{bmatrix},$$

$$\frac{\partial \mathbf{v}_{\text{sph}}}{\partial \mathbf{v}_{\text{car}}} = \begin{bmatrix} \frac{\partial v_r}{\partial v_x} & \frac{\partial v_r}{\partial v_y} & \frac{\partial v_r}{\partial v_z} \\ \frac{\partial v_\theta}{\partial v_x} & \frac{\partial v_\theta}{\partial v_y} & \frac{\partial v_\theta}{\partial v_z} \\ \frac{\partial v_\phi}{\partial v_x} & \frac{\partial v_\phi}{\partial v_y} & \frac{\partial v_\phi}{\partial v_z} \end{bmatrix} = \begin{bmatrix} \frac{x}{r} & \frac{y}{r} & \frac{z}{r} \\ \frac{xz}{(x^2+y^2)^{1/2}r} & \frac{yz}{(x^2+y^2)^{1/2}r} & \frac{-(x^2+y^2)}{(x^2+y^2)^{1/2}r} \\ \frac{-y}{(x^2+y^2)^{1/2}} & \frac{x}{(x^2+y^2)^{1/2}} & 0 \end{bmatrix},$$

where $\alpha = -z(x^4 - y^4 - y^2z^2), \beta = -xyz(2x^2 + 2y^2 + z^2), \gamma = -xz^2(x^2 + y^2), \rho = z(x^4 + x^2z^2 - y^4)$, and $\eta = -yz^2(x^2 + y^2)$. We note that the determinant of $\mathbf{J}$ is $J = 1/r^2 \sin\theta$ and thus Eq. (5.55)

becomes

$$\nabla_{\mathbf{X}} \cdot \bar{\mathbf{F}} = \frac{1}{r^2 \sin\theta} \begin{bmatrix} \frac{\partial}{\partial r} \\ \frac{\partial}{\partial \theta} \\ \frac{\partial}{\partial \phi} \\ \frac{\partial}{\partial v_r} \\ \frac{\partial}{\partial v_\theta} \\ \frac{\partial}{\partial v_\phi} \end{bmatrix} \cdot \left\{ r^2 \sin\theta \, \mathbf{J} \begin{bmatrix} v_x f \\ v_y f \\ v_z f \\ a_x f \\ a_y f \\ a_z f \end{bmatrix} \right\}. \tag{5.76}$$

Computing the matrix-vector product defined in Eq. (5.76) and using Eq. (5.55), we have that the Vlasov equation in conservative form in spherical coordinates is

$$\begin{aligned} &\frac{\partial f}{\partial t} + \frac{1}{r^2 \sin\theta} \frac{\partial (r^2 \sin\theta v_r f)}{\partial r} + \frac{1}{r^2 \sin\theta} \frac{\partial (r^2 \sin\theta \frac{v_\theta}{r} f)}{\partial \theta} + \frac{1}{r^2 \sin\theta} \frac{\partial (r^2 \sin\theta \frac{v_\phi}{r \sin\theta} f)}{\partial \phi} \\ &\quad + \frac{1}{r^2 \sin\theta} \frac{\partial \left\{ r^2 \sin\theta \left[a_r + \frac{1}{r} \left(v_\theta^2 + v_\phi^2 \right) \right] f \right\}}{\partial v_r} + \frac{1}{r^2 \sin\theta} \frac{\partial \left\{ r^2 \sin\theta \left[a_\theta - \frac{1}{r} \left(v_r v_\theta - \cot\theta v_\phi^2 \right) \right] f \right\}}{\partial v_\theta} \\ &\quad + \frac{1}{r^2 \sin\theta} \frac{\partial \left\{ r^2 \sin\theta \left[a_\phi - \frac{1}{r} \left(v_r v_\phi + \cot\theta v_\theta v_\phi \right) \right] f \right\}}{\partial v_\phi} = 0. \end{aligned} \tag{5.77}$$

Simplifying the pre-factors yields

$$\begin{aligned} &\frac{\partial f}{\partial t} + \frac{1}{r^2} \frac{\partial (r^2 v_r f)}{\partial r} + \frac{1}{r \sin\theta} \frac{\partial (\sin\theta v_\theta f)}{\partial \theta} + \frac{1}{r \sin\theta} \frac{\partial (v_\phi f)}{\partial \phi} \\ &\quad + \frac{\partial \left\{ \left[a_r + \frac{1}{r} \left(v_\theta^2 + v_\phi^2 \right) \right] f \right\}}{\partial v_r} + \frac{\partial \left\{ \left[a_\theta - \frac{1}{r} \left(v_r v_\theta - \cot\theta v_\phi^2 \right) \right] f \right\}}{\partial v_\theta} \\ &\quad + \frac{\partial \left\{ \left[a_\phi - \frac{1}{r} \left(v_r v_\phi + \cot\theta v_\theta v_\phi \right) \right] f \right\}}{\partial v_\phi} = 0. \end{aligned} \tag{5.78}$$

The Vlasov equation in conservative form in spherical coordinates also include acceleration terms that are a result of the coordinate system transformation – just like in cylindrical coordinates. These acceleration terms correspond to acceleration due to the Coriolis effect that manifests itself

as a product of radial and angular velocities – the terms $v_r v_\theta$ and $v_r v_\phi$. Additional acceleration terms also appear due to centripetal acceleration which appear as squared velocities. We reiterate that only the a_r, a_θ, and a_ϕ terms in Eq. (5.78) that are due to the Lorentz force; the additional acceleration terms are purely a result of the coordinate transformation. In Sec. 5.3.3, we present the 1D-1V representation of the Vlasov equation in the Cartesian, cylindrical, and spherical coordinate system. These 1D-1V representations are the starting point for the numerical methods we use for solving kinetic equations as discussed in Sec. 5.5.1.

5.3.3 The 1D-1V Vlasov Equation in Cartesian, Cylindrical, and Spherical Coordinates

In this section we show the comparison of 1D-1V representations for Eqs. (5.47), (5.67), and (5.78). Equation (5.47) is the easiest to reduce to 1D-1V as the velocity and acceleration components do not depend on the differentiation variable. Thus, the 1D-1V conservative form of Eq. (5.47) is

$$\frac{\partial f}{\partial t} + \frac{\partial}{\partial x}(v_x f) + \frac{\partial}{\partial v_x}(a_x f) = 0. \tag{5.79}$$

Mathematically, by 1D-1V we are enforcing that $f(x, y, z, v_x, v_y, v_z, t) = f(x, v_x, t)$ and as a result, many of the partial derivatives equate to zero.

In cylindrical coordinates, we must explicitly carry out the product rule as some of the terms in the fluxes depend on the differentiation variable. Equation (5.67) becomes

$$\frac{\partial f}{\partial t} + \frac{v_\rho}{\rho}\left(\rho\frac{\partial}{\partial \rho}f + f\right) + \frac{v_\phi}{\rho}\frac{\partial}{\partial \phi}f + v_z\frac{\partial}{\partial z}f + \left(a_\rho + \frac{v_\phi^2}{\rho}\right)\frac{\partial}{\partial v_\rho}f \tag{5.80}$$

$$+ a_\phi\frac{\partial}{\partial v_\phi}f - \frac{v_\rho}{\rho}\left(v_\phi\frac{\partial}{\partial v_\phi}f + f\right) + a_z\frac{\partial}{\partial v_z}f = 0, \tag{5.81}$$

which in 1D-1V reduces to

$$\frac{\partial f}{\partial t} + v_\rho\frac{\partial}{\partial \rho}f + \left(a_\rho + \frac{v_\phi^2}{\rho}\right)\frac{\partial}{\partial v_\rho}f = 0, \tag{5.82}$$

which can also be readily expressed in conservative form:

$$\frac{\partial f}{\partial t} + \frac{\partial}{\partial \rho}(v_\rho f) + \frac{\partial}{\partial v_\rho}\left[\left(a_\rho + \frac{v_\phi^2}{\rho}\right)f\right] = 0. \tag{5.83}$$

We follow a similar procedure for spherical coordinates where Eq. (5.78) becomes

$$\frac{\partial f}{\partial t} + v_r \frac{\partial}{\partial r} f + \underline{\frac{2 v_r f}{r}} + \frac{v_\theta}{r} \frac{\partial}{\partial \theta} f + \underline{\underline{\frac{\cot\theta v_\theta f}{r}}} + \frac{v_\phi}{r \sin\theta} \frac{\partial}{\partial \phi} f + a_r \frac{\partial}{\partial v_r} f + \left(\frac{v_\theta^2 + v_\phi^2}{r} \right) \frac{\partial}{\partial v_r} f$$
$$+ a_\theta \frac{\partial}{\partial v_\theta} f + \frac{v_r v_\theta}{r} \frac{\partial}{\partial v_\theta} f - \underline{\frac{v_r f}{r}} + \frac{\cot\theta v_\phi^2}{r} \frac{\partial f}{\partial v_\theta} + a_\phi \frac{\partial}{\partial v_\phi} f - \frac{v_r v_\phi}{r} \frac{\partial}{\partial v_\phi} f$$
$$- \underline{\frac{v_r f}{r}} - \frac{\cot\theta v_\theta v_\phi}{r} \frac{\partial}{\partial v_\phi} f - \underline{\underline{\frac{\cot\theta v_\theta f}{r}}} = 0,$$

where the underlined terms cancel. In 1D-1V the above equation reduces to

$$\frac{\partial f}{\partial t} + v_r \frac{\partial}{\partial r} f + \left(a_r + \frac{v_\theta^2 + v_\phi^2}{r} \right) \frac{\partial}{\partial v_r} f = 0, \tag{5.84}$$

which can also be readily expressed in conservative form:

$$\frac{\partial f}{\partial t} + \frac{\partial}{\partial r} (v_r f) + \frac{\partial}{\partial v_r} \left[\left(a_r + \frac{v_\theta^2 + v_\phi^2}{r} \right) f \right] = 0. \tag{5.85}$$

The 1D-1V representations of the Vlasov equation in conservative form lend themselves nicely to numerical methods derived for hyperbolic conservation laws. Moreover, the assumed symmetries in 1D-1V result reduce the dimensionality of the problem from 6D to 2D decreasing the computational demands associated with numerically solving the Vlasov equation. In the case of the spherical coordinate system, radial symmetries are often observed in the expansion of UNPs into a vacuum when the UNP is initialized with a Gaussian density profile. In Sec. 5.4, we derive analytic models that approximate the radial expansion of a Gaussian plasma into a vacuum. our ultimate goal is to compare numerical simulations of the 1D-1V Vlasov equations to these analytic models to test their validity for single-species UNPs. Moreover, as no analytic models exist for describing the expansion of a multi-species UNP, these 1D-1V forms provide means of computing the evolution of UNP mixtures.

5.4 Plasma Expansion Into a Vacuum

The density profiles of UNPs in the absence of magnetic fields are often initialized as a spherically symmetric Gaussian profile. Additionally, UNPs are created in a vacuum in which they expand radially outward. One goal of this chapter is to compare analytic models to numerical

simulations of Gaussian UNPs. If the analytic models derived below are valid, we avoid the computation cost associated with the kinetic simulations for these plasmas. In what follows, we will derive expressions for the time evolution of the ion density and electron temperature in two cases: an isothermal case, and an adiabatic case. The derivations presented here have been originally presented in Ref. [273]; for completeness, we provide them here and provide our own insights.

To begin, we start with an expression for a Gaussian profile of the ion density

$$n_i(\mathbf{r}, t = 0) = n_{i0}\exp\left(-\frac{\mathbf{r}^2}{\sigma_0^2}\right), \tag{5.86}$$

where n_{i0} is the "peak" ion number density and σ_0 characterizes the initial width of the plasma. We now consider the conservation laws for the ion species where we assume that the plasma is isotropic such that we can describe the expansion in one-spatial dimension. The continuity and momentum equation for the ion species are

$$\frac{\partial n_i}{\partial t} + \frac{\partial}{\partial x}(n_i u_i) = 0, \tag{5.87}$$

$$\frac{\partial u_i}{\partial t} + u_i\frac{\partial}{\partial x}u_i + \frac{1}{m_i n_i}\frac{\partial}{\partial x}p = \frac{F}{m_i}, \tag{5.88}$$

where $n_i = n_i(x, t)$ and $u_i = u_i(x, t)$. Note that, $p = n_i T_i$ is the ideal gas pressure where $T_i = T_i(x, t)$ is the ion temperature in energy units and F is an internal or external force. For an initially cold plasma, we approximate $T_i = 0$ which also means that $p = 0$. We also assume that there are no external forces acting on the ions and that F describes the self-consistent electric field. That is

$$F = Z_i eE = -Z_i e\frac{\partial}{\partial x}\varphi, \tag{5.89}$$

where $\varphi = \varphi(x, t)$ is the electrostatic potential. The momentum equation with the above approximations becomes

$$\frac{\partial u_i}{\partial t} + u_i\frac{\partial}{\partial x}u_i = -\frac{Z_i e}{m_i}\frac{\partial}{\partial x}\varphi. \tag{5.90}$$

The momentum equation for the electrons is

$$\frac{\partial u_e}{\partial t} + u_e\frac{\partial}{\partial x}u_e + \frac{1}{m_e n_e}\frac{\partial}{\partial x}(n_e T_e) = \frac{e}{m_e}\frac{\partial}{\partial x}\varphi. \tag{5.91}$$

Now we assume that the electron temperature is independent of space so that $T_e = T_e(t)$. By quasineutrality we have $n_e = Z_i n_i$. From the continuity equation from the electrons and ions we find that $u_i = u_e$. With these assumptions, we have that Eq. (5.91) is

$$\frac{\partial u_i}{\partial t} + u_i \frac{\partial}{\partial x} u_i = \frac{e}{m_e} \frac{\partial}{\partial x} \varphi - \frac{T_e}{m_e n_e} \frac{\partial}{\partial x} n_e. \tag{5.92}$$

Subtracting Eqs. (5.92) and (5.90) re-arranging terms we get

$$\frac{\partial}{\partial x} n_e = n_e \left(1 + \frac{Z_i m_e}{m_i} \right) \frac{e}{T_e} \frac{\partial \varphi}{\partial x}. \tag{5.93}$$

The solution of the above equation is

$$n_e(x,t) = n_{e0} \exp \left[\left(1 + \frac{Z_i m_e}{m_i} \right) \frac{e\varphi}{T_e} \right], \tag{5.94}$$

where $n_{e0} = n_e(x, t = 0)$. Since $m_i \gg m_e$, we arrive at the familiar Boltzmann equilibrium distribution for the electron number density

$$n_e(x,t) = n_{e0} \exp \left(\frac{e\varphi}{T_e} \right). \tag{5.95}$$

We can once again make use of the quasineutral assumption that $n_e = Z_i n_i$ and Eq. (5.93) to write

$$\frac{\partial \varphi}{\partial x} = \frac{T_e}{n_i e} \frac{\partial}{\partial x} n_i. \tag{5.96}$$

Substituting the above equation into Eq. (5.90), we get

$$\frac{\partial u_i}{\partial t} + u_i \frac{\partial}{\partial x} u_i = -c_s^2 \frac{\partial}{\partial x} n_i, \tag{5.97}$$

where $c_s = (Z_i T_e / m_i)^{1/2}$ and is known as the ion acoustic velocity. Equation (5.97) admits a self-similar [274] solution of

$$n_i(x,t) = n_{i0} \frac{\sigma_0}{\sigma(t)} \exp \left[-\frac{x^2}{\sigma^2(t)} \right]. \tag{5.98}$$

From Eq. (5.98), the quasineutrality assumption, and Eq. (5.95) we get that

$$n_{e0} \exp \left(\frac{e\varphi}{T_e} \right) = n_{e0} \frac{\sigma_0}{\sigma(t)} \exp \left(-\frac{x^2}{\sigma^2(t)} \right). \tag{5.99}$$

By solving for φ we obtain

$$\varphi = -\frac{T_e x^2}{e\sigma^2(t)} + \frac{T_e}{e}\ln\left[\frac{\sigma_0}{\sigma^2(t)}\right]. \tag{5.100}$$

By substituting Eq. (5.98) into Eq. (5.87) we get

$$\frac{\partial}{\partial t}\left\{n_{i0}\frac{\sigma_0}{\sigma(t)}\exp\left[-\frac{x^2}{\sigma^2(t)}\right]\right\} + \frac{\partial}{\partial x}\left\{n_{i0}\frac{\sigma_0}{\sigma(t)}\exp\left[\frac{-x^2}{\sigma^2(t)}\right]u_i\right\} = 0. \tag{5.101}$$

Applying the product rule we get

$$n_{i0}\sigma_0\left\{\frac{1}{\sigma(t)}\exp\left[-\frac{x^2}{\sigma^2(t)}\right]\frac{2x^2}{\sigma^3(t)}\frac{d\sigma(t)}{dt} - \frac{1}{\sigma^2(t)}\exp\left[-\frac{x^2}{\sigma^2(t)}\right]\frac{d\sigma(t)}{dt}\right\}$$

$$+\frac{n_{i0}\sigma_0}{\sigma(t)}\left\{\exp\left[-\frac{x^2}{\sigma^2(t)}\right]\frac{\partial u_i}{\partial x} - \frac{2xu_i}{\sigma^2(t)}\exp\left[-\frac{x^2}{\sigma^2(t)}\right]\right\} = 0.$$

Dividing the exponential terms and using the fact that $\sigma^{-1}(t)d\sigma(t)/dt = d\ln\sigma(t)/dt$, we have

$$\frac{n_{i0}\sigma_0}{\sigma(t)}\left[\frac{2x^2}{\sigma^2(t)}\frac{d\ln\sigma(t)}{dt} - \frac{d\ln\sigma(t)}{dt}\right] + \frac{n_{i0}\sigma_0}{\sigma(t)}\left[\frac{\partial u_i}{\partial x} - \frac{2xu_i}{\sigma^2(t)}\right] = 0. \tag{5.102}$$

Note that from the above equation, $\frac{\partial u_i}{\partial x} = \frac{d\ln\sigma(t)}{dt}$ implies that

$$u_i = x\frac{d\ln\sigma(t)}{dt}. \tag{5.103}$$

Substituting Eq. (5.103) into Eq. (5.102) yields

$$\frac{n_{i0}\sigma_0}{\sigma(t)}\left[\frac{2x^2}{\sigma^2(t)}\frac{d\ln\sigma(t)}{dt} - \frac{d\ln\sigma(t)}{dt}\right] + \frac{n_{i0}\sigma_0}{\sigma(t)}\left[\frac{d\ln\sigma(t)}{dt} - \frac{2x^2}{\sigma^2(t)}\frac{d\ln\sigma(t)}{dt}\right] = 0, \tag{5.104}$$

which is a solution to the above equation. Substituting Eq. (5.103) into Eq. (5.90) gives

$$x\frac{d^2\ln\sigma(t)}{dt^2} + x\frac{d\ln\sigma(t)}{dt}\frac{\partial}{\partial x}x\frac{d\ln\sigma(t)}{dt} = -\frac{Z_i e}{m_i}\frac{\partial}{\partial x}\varphi, \tag{5.105}$$

which by using Eq. (5.100) reduces to

$$x\frac{d^2\ln\sigma(t)}{dt^2} + \left[\frac{d\ln\sigma(t)}{dt}\right]^2 = \frac{Z_i e}{m_i}\frac{T_e 2x}{e\sigma^2(t)}, \tag{5.106}$$

which is

$$x\frac{d}{dt}\left[\frac{\dot\sigma(t)}{\sigma(t)}\right] + \left[\frac{\dot\sigma(t)}{\sigma(t)}\right]^2 = \frac{Z_i e}{m_i}\frac{T_e 2x}{e\sigma^2(t)}. \tag{5.107}$$

where $\dot{\sigma(t)} \equiv d\sigma(t)/dt$. Taking another time derivative gives

$$x\frac{\sigma(t)\ddot{\sigma}(t) - \dot{\sigma}^2(t)}{\sigma^2(t)} + \frac{\dot{\sigma}^2(t)}{\sigma^2(t)} = \frac{Z_i e}{m_i}\frac{T_e 2x}{e\sigma^2(t)}, \tag{5.108}$$

which simplifies to

$$\frac{d^2\sigma(t)}{dt^2} = 2\frac{c_s^2}{\sigma(t)}, \tag{5.109}$$

or

$$\frac{d^2\sigma(t)}{dt^2} = 2\frac{Z_i T_e(t)}{m_i\sigma(t)}, \tag{5.110}$$

where the time dependence of the electron temperature has been made explicit. In the sections that follow, we solve Eq. (5.110) for two approximations: and isothermal approximation and an adiabatic approximation.

5.4.1 Isothermal Expansion

Isothermal expansion is one in which the temperature of a system remains constant during the expansion. This means that for a gas to expand and keep a constant temperature, an external energy source would need to provide energy to the expanding gas. Therefore, the statistical ensemble that this gas would occupy would be the canonical ensemble (NVT). In the context of the self-similar expansion model shown above, this would imply that the electron temperature T_e is independent of space and time. With this assumption, we can integrate Eq. (5.110) from 0 to t gives

$$\frac{1}{2}\left[\frac{d\sigma(t)}{dt}\right]^2 - \frac{1}{2}\left[\frac{d\sigma(0)}{dt}\right]^2 = 2c_s^2\ln\sigma(t) - 2c_s^2\ln\sigma(0). \tag{5.111}$$

Since the ions are initially at rest, $d\sigma(0)/dt = 0$ and Eq. (5.111) becomes

$$\frac{d\sigma(t)}{dt} = 2c_s\sqrt{\ln\left[\frac{\sigma(t)}{\sigma_0}\right]}. \tag{5.112}$$

Solving Eq. (5.112) for dt and integrating both sides gives

$$t = \frac{1}{2c_s}\int_{\sigma_0}^{\sigma(t)} \frac{1}{\sqrt{\ln\left[\frac{\sigma(t)}{\sigma_0}\right]}d\sigma(t)}. \tag{5.113}$$

Carrying out the integral in Eq. (5.113) results in

$$t = \frac{\sqrt{\pi}\sigma_0}{2c_s}\text{erfi}\left\{\sqrt{\ln\left[\frac{\sigma(t)}{\sigma_0}\right]}\right\}$$

$$= \frac{\sqrt{\pi}\sigma_0}{2c_s}\frac{1}{\sqrt{\pi}}\left(2\left\{\ln\left[\frac{\sigma(t)}{\sigma_0}\right]\right\}^{1/2} + \frac{2}{3}\left\{\ln\left[\frac{\sigma(t)}{\sigma_0}\right]\right\}^{3/2} + \cdots\right). \tag{5.114}$$

Retaining only the first term in the Taylor expansion of Eq. (5.114) gives

$$t = \frac{\sigma_0}{c_s}\left\{\ln\left[\frac{\sigma(t)}{\sigma_0}\right]\right\}^{1/2}. \tag{5.115}$$

Solving for $\sigma(t)$ in Eq. (5.115) yields

$$\sigma(t) = \sigma_0\exp\left(\frac{c_s^2t^2}{\sigma_0^2}\right). \tag{5.116}$$

For small t (i.e., $t \ll \sigma_0/c_s$), Taylor expansion of the exponential gives

$$\sigma(t) = \sigma_0\left(1 + \frac{c_s^2t^2}{\sigma_0^2}\right). \tag{5.117}$$

Using Eq. (5.117) in Eq. (5.98) gives an analytic expression for the self-similar evolution of ions in an isothermal system.

5.4.2 Adiabatic Expansion

In adiabatic expansion, the total energy in the system in conserved. During plasma expansion in a vacuum there is a transfer of energy between the electrons to the ions. To account for this in our determination of $\sigma(t)$, we begin with the temperature equation for the electrons in 1D

$$\frac{1}{2}\left[\frac{\partial(n_eT_e)}{\partial t} + \frac{\partial}{\partial x}(n_eT_eu_e)\right] + \frac{\partial}{\partial x}q_e + p_e\frac{\partial}{\partial x}u_e = 0. \tag{5.118}$$

where q_e and p_e denote the heat flux and pressure of the electrons respectively. If we assume that $q_e = 0$ and $p_e = n_eT_e$, Eq. (5.118) becomes

$$\frac{1}{2}\left[\frac{\partial(n_eT_e)}{\partial t} + \frac{\partial}{\partial x}(n_eT_eu_e)\right] + n_eT_e\frac{\partial}{\partial x}u_e = 0. \tag{5.119}$$

After selectively expanding out the derivative terms in the brackets and multiplying by 1/2, we get

$$n_e\frac{\partial T_e}{\partial t} + T_e\frac{\partial n_e}{\partial t} + T_e\frac{\partial}{\partial x}(n_eu_e) + n_eu_e\frac{\partial T_e}{\partial x} + 2n_eT_e\frac{\partial}{\partial x}u_e = 0. \tag{5.120}$$

The second and third term are zero from the continuity equation which reduces Eq. (5.120) to

$$n_e \frac{\partial T_e}{\partial t} + n_e u_e \frac{\partial T_e}{\partial x} + 2 n_e T_e \frac{\partial}{\partial x} u_e = 0. \tag{5.121}$$

Also note that by the continuity equation Eq. (5.121) becomes

$$n_e \frac{\partial T_e}{\partial t} + n_e u_e \frac{\partial T_e}{\partial x} - 2 T_e \frac{\partial n_e}{\partial t} - 2 T_e u_e \frac{n_e}{\partial x} = 0, \tag{5.122}$$

which can be written as

$$\frac{1}{T_e}\left(\frac{\partial T_e}{\partial t} + u_e \frac{\partial T_e}{\partial x}\right) = \frac{2}{n_e}\left(\frac{\partial n_e}{\partial t} + u_e \frac{\partial n_e}{\partial t}\right). \tag{5.123}$$

Equation (5.123) can be solved to obtain a spatio-temporal description of the electron temperature. If we assume that the electron temperature is constant in space, Eq. (5.123) reduces to

$$\frac{1}{T_e}\frac{dT_e}{dt} = -2\frac{\partial u_i}{\partial t}, \tag{5.124}$$

where we have yet again used the continuity equation along with the relation $u_e = u_i$. From Eq. (5.103), Eq. (5.124) becomes

$$\frac{1}{T_e}\frac{dT_e}{dt} = -\frac{2}{\sigma}\frac{d\sigma}{dt}. \tag{5.125}$$

Rearranging Eq. (5.125) and integrating from $\tau = 0$ to t yields

$$T_e(t) = \frac{T_e(0)\sigma^2(0)}{\sigma^2(t)}. \tag{5.126}$$

Substituting Eq. (5.126) into Eq. (5.110) yields

$$\frac{d\sigma(t)}{dt^2} = 2\frac{c_{s0}^2 \sigma_0^2}{\sigma^3(t)}, \tag{5.127}$$

where we have defined $c_{s0} \equiv (Z_i T_{e0}/m_i)^2$. Integrating Eq. (5.127) yields

$$\left[\frac{d\sigma(t)}{dt}\right]^2 = 2c_{s0}^2\left[1 - \frac{\sigma_0^2}{\sigma^2(t)}\right], \tag{5.128}$$

which has a solution of

$$\sigma(t) = (\sigma_0^2 + 2c_{s0}^2 t^2)^{1/2}. \tag{5.129}$$

Using Eq. (5.126) we get that

$$T_e(t) = T_{e0}\frac{\sigma_0^2}{\sigma_0^2 + 2c_{s0}^2 t^2}. \tag{5.130}$$

By substituting Eq. (5.129) into Eq. (5.98) we have an analytic model for the adiabatic expansion of a plasma along with an expression for the time evolution of the electron temperature.

In Sec. 5.6.2, we compare numerical solutions of 1D-1V kinetic equation and compare our numerical results with the analytic formulae given by Eq. (5.98) using Eq. (5.117) and (5.129). We show that the expansion of Gaussian single-species UNPs are well-described by the adiabatic model. The focus of Sec. 5.5 is on the presentation of the numerical methods we use to solve the 1D-1V equations.

5.5 Numerical Methods for Kinetic Equations

We numerically solve Eq. (5.1) in steps; the first step considers the advection terms on the left-hand side and the second step considers the collision operator on the right-hand side. We refer to the two steps as the “advection step" and the “collision step." We treat the advection step by using a second-order operator split method (Strang split) [275] to first advect the phase-space distribution function in physical space. Next, we advect the phase-space distribution function in velocity space and the advection step is complete[1]. After the advection step, we carry out the collision step which, for the BGK operator, consists of solving a time dependent ordinary differential equation. In the sections that follow, we detail the specifics of how we numerically treat each step.

In Sec. 5.5.1, we discuss how we treat the advection step using a high-order finite volume method [262, 272, 276] (FVM). The component of the advection step that advects the phase-space distribution function in velocity space requires the determination of a self-consistent electric field. In Sec. 5.5.2, we describe an approach for obtaining the electrostatic potential – and thus the self-consistent electric field – via Poisson’s equation. In most cases studied here, we do not explicitly model the electron species with a kinetic equation. Instead, we approximate the electron number density with a linear Poisson-Boltzmann or non-linear Poisson-Boltzmann approach. In the linear

[1]To be more precise, we advect in physical space with time step $\Delta t/2$, use the results to advect in velocity space for Δt, and then finally use that result and advect for $\Delta t/2$.

case, the system is solved exactly via matrix inversion; in the non-linear case, we employ a Newton iteration. In both cases, the Poisson equation is discretized to second-order using a simple second order central finite-difference. In practice, one could explicitly simulate the electrons as their own species but due to their small mass, a much smaller simulation time step is needed to retain numerical stability. Therefore, unless otherwise mentioned, the electron species is assumed to be treated with a non-linear Poisson solve. In this way, the interactions between the electrons and ions are implicitly accounted for in calculation of the self-consistent electric field through the total charge density.

The numerical treatment of the collision step varies in different stages of this work. For the 0D-1V simulations, the *method of lines* [277] is employed to allow the use of high-order implicit time integrators that are accessible in extant computational libraries. For the 0D-3V BGK simulations, we employ an explicit fourth-order Runge-Kutta time integrator. For the 1D-1V simulations, we employ a simple first order explicit time step for the BGK operator.

5.5.1 Finite Volume Methods

In contrast to finite difference methods (FDMs), FVMs are derived for numerically solving conservation laws – the governing equation of this chapter. We begin our discussion of FVMs by considering a conservation law in one space dimension that is in *differential form*

$$\frac{\partial q(x,t)}{\partial t} + \frac{\partial}{\partial x} f[q(x,t)] = 0, \tag{5.131}$$

where $q(x,t)$ is some conserved quantity (e.g., total number density of a system), and $f(q)$ is a flux. Finite difference methods numerically discretely approximate the derivatives in Eq. (5.131) using “stencils" – the choice of stencil distinguishes FDMs. In contrast, FVMs instead work with conservations laws in *integral form* where we integrate Eq. (5.131) over some volume $V_i = (x_{i-1/2}, x_{i+1/2})$ that yields

$$\frac{d}{dt}\int_{V_i} q(x,t)\, dV + \int_{V_i} \frac{\partial}{\partial x} f[q(x,t)]\, dV = 0, \tag{5.132}$$

which reduces to

$$\frac{d}{dt}\int_{V_i} q(x,t)\,dV + f[q(x_{i+1/2},t)] - f[q(x_{i-1/2},t)] = 0. \tag{5.133}$$

With the definition that

$$Q_i = \frac{1}{V_i}\int_{V_i} q(x,t)\,dV, \tag{5.134}$$

we have

$$\frac{d}{dt}Q_i = \frac{1}{V_i}\left\{f[q(x_{i-1/2},t)] - f[q(x_{i+1/2},t)]\right\} = 0. \tag{5.135}$$

Equation (5.135) represents the time evolution of average flux of q in some volume V_i. Integrating Eq. (5.135) over a time interval of t_n to t_{n+1} gives

$$Q_i^{n+1} = Q_i^n - \frac{\Delta t}{\Delta x}\left(F_{i+1/2} - F_{i-1/2}\right), \tag{5.136}$$

where we have assumed a simple Forward Euler time integration and have made the definition that

$$F_{i+1/2} = \int_{t_n}^{t_{n+1}} f[q(x_{i+1/2},t)]dt. \tag{5.137}$$

It is the choice of how we approximate the flux $F_{i+1/2}$, with an appropriate *numerical flux* that distinguishes FVMs from one another. Different choices of numerical fluxes usually result in methods of varying orders of accuracy or methods which attempt to control oscillations that occur in discontinuous solutions. A similar choice appears in FDMs where instead of choosing a numerical flux, we choose a *numerical derivative* (i.e., first-order forward, second-order central, etc.). Additionally, one could choose a different time integration for example, Backward Euler or a fourth-order Runge-Kutta method.

In this work, we implement three different choices for the numerical flux function. The first is the first-order upwinding flux [276], a second-order *superbee* flux limiter [276], and a fourth-order upwinding flux [262,272]. A convergence study for each of these choices is displayed in Figure 5.1 for the linear advection equation

$$\begin{cases} \dfrac{\partial u(x,t)}{\partial t} + v\dfrac{\partial u(x,t)}{\partial x} = 0 \quad x \in [0,1], \\ u(x,0) = \exp\left[-32(x-0.5)^2\right]\cos[16\pi(x-0.5)], \end{cases} \tag{5.138}$$

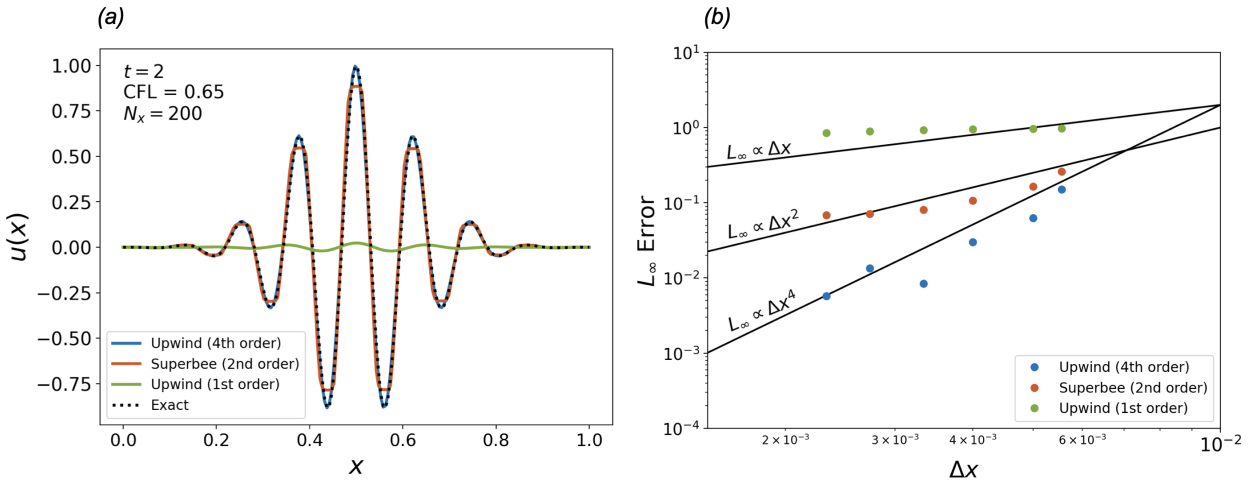

Figure 5.1: Comparison of different numerical flux functions for the linear advection equation. (a) numerical solution of the advection equation for a wave packet initial condition [Eq. (5.138)] with periodic boundary conditions. The wave passes two times through the domain and comparisons are shown with first, second, and fourth order methods; The first order method severely damps the numerical solution. (b) grid resolution convergence test. The first, second, and fourth order methods scale appropriately with grid resolution.

where we set $v = 1$ and we assume periodic boundary conditions. For the first and second-order method, a forward Euler time step was implemented, for the fourth-order upwinding flux a fourth-order Runge-Kutta time integrator was used as described in Ref. [262,272]. Figure 5.1(a) shows the numerical solution for each choice of numerical flux function with 2 passes through the domain. In contrast to the second- and fourth-order methods, we see that the first-order upwind method severely dampens the solution. Figure 5.1(b) shows a grid resolution convergence study using the L_∞-norm for each method; we have added three lines with slopes 1, 2, and 4, to guide the eye. We see that for smooth problems, each choice of numerical flux gives a reasonable approximation to the true solutions albeit in the first-order case, the numerical solution may be severely damped. For non-smooth problems, we cannot use the fourth order upwinding flux as it will introduce oscillations near the discontinuity. The appearance of oscillations from using the fourth-order upwinding flux

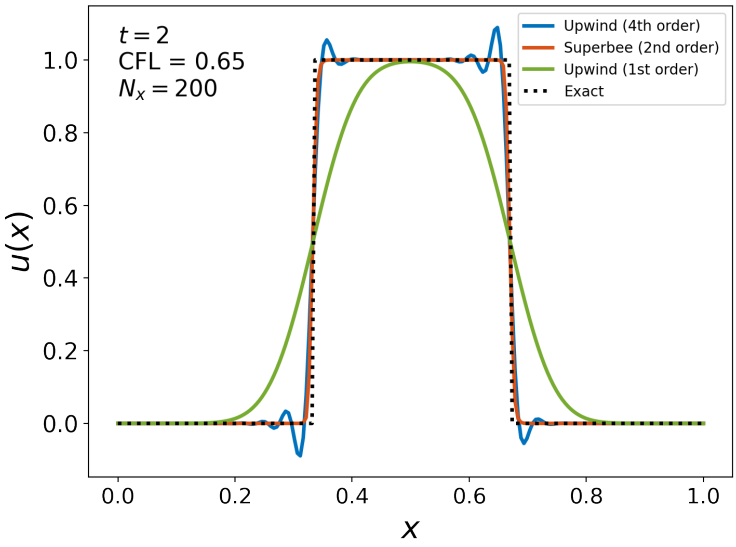

Figure 5.2: Comparison of numerical fluxes for a square pulse initial condition. Note that the fourth order upwinding scheme introduces oscillations in the numerical solution near the discontinuities; the first-order method does not introduce unphysical oscillations but smears the numerical solution.

is shown in Fig. 5.2 where we assume

$$\begin{cases} \dfrac{\partial u(x,t)}{\partial t} + v\dfrac{\partial u(x,t)}{\partial x} = 0 \quad x \in [0,1], \\ u(x,0) = 1 \quad |x| \leq 0.5, \\ u(x,0) = 0 \quad \text{otherwise}, \end{cases} \tag{5.139}$$

where again we let $v = 1$ and assume periodic boundary conditions. We observe that the first-order upwinding and second-order superbee numerical fluxes do not introduce oscillations near the discontinuity in contrast to the fourth-order upwinding flux. The comparison of the different numerical fluxes informs us on their appropriateness for solving kinetic equations. We conclude that if we expect the phase-space distribution function to be smooth for all time, a high-order upwinding method is appropriate for treating the advection terms on the left-hand side of Eq. (5.1). The smoothness of the phase-space distribution function is largely set by the initial condition but discontinuities may appear as a result of self-consistent forces or collisions in the plasma. For UNP simulations, the phase-space distribution function remains smooth for the problems studied in this chapter and we employ the fourth-order upwinding flux. However, if the problem of interest

includes a phase-space distribution with discontinuities, as is the case when there is an interface between two plasma species, a slope limiter methods, essentially non-oscillatory methods, or weighted essentially non-oscillatory, methods [278] are necessary to achieve higher than first-order accuracy.

5.5.2 Poisson's Equation in 1D Cartesian Coordinates

In 1D Cartesian coordinates Poisson's equation has the form

$$\frac{d^2}{dx^2}\varphi(x) = -4\pi\rho, \tag{5.140}$$

where $\rho = \sum_i^N Z_i e n_i$ is the total charge density of the system. We use a second order central difference approximation to Eq. (5.140) so that at some grid point $i = 0, 1, \cdots, N$, we have

$$\frac{\varphi_{i-1} - 2\varphi_i + \varphi_{i+1}}{\Delta x^2} = -4\pi\rho_i. \tag{5.141}$$

If we impose periodic boundary conditions at $i = 0$ and $i = N$, then we have that $\varphi_0 = \varphi_N$ and construct a linear system that is solved to obtain φ. Specifically, for a 6 cell system the linear system takes the following form:

$$\begin{bmatrix} -2 & 1 & 0 & 0 & 0 & 1 \\ 1 & -2 & 1 & 0 & 0 & 0 \\ 0 & 1 & -2 & 1 & 0 & 0 \\ 0 & 0 & 1 & -2 & 1 & 0 \\ 1 & 0 & 0 & 0 & 1 & -2 \end{bmatrix} \begin{bmatrix} \varphi_0 \\ \varphi_1 \\ \varphi_2 \\ \varphi_3 \\ \varphi_4 \\ \varphi_5 \end{bmatrix} = -4\pi\Delta x^2 \begin{bmatrix} \rho_0 \\ \rho_1 \\ \rho_2 \\ \rho_3 \\ \rho_4 \\ \rho_5 \end{bmatrix}. \tag{5.142}$$

Since the above system is singular, an additional constraint specifying that the average value of the potential is zero is introduced which results in the modified linear system

$$\begin{bmatrix} -2 & 1 & 0 & 0 & 0 & 1 \\ 1 & -2 & 1 & 0 & 0 & 0 \\ 0 & 1 & -2 & 1 & 0 & 0 \\ 0 & 0 & 1 & -2 & 1 & 0 \\ 1 & 0 & 0 & 0 & 1 & -2 \\ 1 & 1 & 1 & 1 & 1 & 1 \end{bmatrix} \begin{bmatrix} \varphi_0 \\ \varphi_1 \\ \varphi_2 \\ \varphi_3 \\ \varphi_4 \\ \varphi_5 \end{bmatrix} = -4\pi\Delta x^2 \begin{bmatrix} \rho_0 \\ \rho_1 \\ \rho_2 \\ \rho_3 \\ \rho_4 \\ \rho_5 \\ 0 \end{bmatrix}. \tag{5.143}$$

Equation (5.143) can be solved using various linear algebra techniques that exist in extant computational libraries. If using the electron density as defined in Eq. (5.94), a non-linear approach must be used since the total charge density will non-linearly depend on φ; in this work, a Newton iteration was implemented to determine φ. To avoid a non-linear solve, one can linearize Eq. (5.94) which results in a linear system that can be solve exactly; Figure 5.3 shows a comparison of a numerical solution from the linear case of Eq. (5.143) with a *manufactured* analytic solution. We note that the linearization holds in the high electron-temperature limit. Additional approaches for treating the electrons as quantum mechanical with Fermi-Dirac statistics can be found in Ref. [44]. The self-consistent electric field can be obtained via Eq. (5.6), where second-order central difference has been employed.

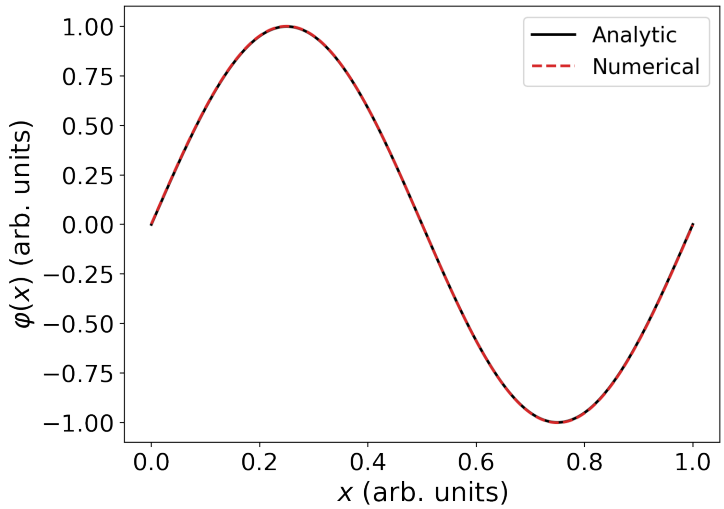

Figure 5.3: Electrostatic potential $\varphi(x)$ computed from Eq. (5.143) and compared against a manufactured analytic solution $\varphi(x) = \sin(2\pi x)$ with $\Delta x = 0.001$.

5.5.3 Poisson's Equation in 1D Spherical Coordinates

To convert Eq. (5.7) to spherical coordinates, we transform the gradient into spherical coordinates to obtain

$$\frac{1}{r^2}\frac{d}{dr}\left(r^2\frac{d}{dr}\varphi\right) = -4\pi\rho. \tag{5.144}$$

To discretize Eq. (5.144), we use a FVM framework. Importantly, the choice of FVM over FDM circumvents singularities at $r = 0$. Additional numerical implementations as well as extensions to higher dimensions can be found in Refs. [279,280]. Following the procedure outlined in Ref. [281], we obtain the discretization of Eq. (5.144)

$$\frac{(r^2\tilde{F}_r)_{i+\frac{1}{2}} - (r^2\tilde{F}_r)_{i-\frac{1}{2}}}{\Delta\mathcal{V}_{r,i}} = -4\pi\rho_i. \tag{5.145}$$

where we define the flux $\tilde{F}_r \equiv d\varphi/dr$ and $\Delta\mathcal{V}_{r,i} = (r^3_{i+1/2} - r^3_{i-1/2})/3$. Evaluating the fluxes at the cell interfaces we have

$$\frac{r^2_{i+\frac{1}{2}}}{r^3_{i+\frac{1}{2}} - r^3_{i-\frac{1}{2}}}\tilde{F}_{r,i+\frac{1}{2}} - \frac{r^2_{i-\frac{1}{2}}}{r^3_{i+\frac{1}{2}} - r^3_{i-\frac{1}{2}}}\tilde{F}_{r,i-\frac{1}{2}} = -\frac{4\pi\rho_i}{3}. \tag{5.146}$$

We approximate the fluxes with an upwinding numerical flux so that Eq. (5.146) becomes

$$\frac{r^2_{i+\frac{1}{2}}}{r^3_{i+\frac{1}{2}} - r^3_{i-\frac{1}{2}}}\left(\frac{\varphi_{i+1} - \varphi_i}{\Delta r}\right) - \frac{r^2_{i-\frac{1}{2}}}{r^3_{i+\frac{1}{2}} - r^3_{i-\frac{1}{2}}}\left(\frac{\varphi_i - \varphi_{i-1}}{\Delta r}\right) = -\frac{4\pi\rho_i}{3}. \tag{5.147}$$

Multiplying by Δr and grouping terms of φ with the same index we get

$$\frac{r_{i-\frac{1}{2}}^2}{r_{i+\frac{1}{2}}^3 - r_{i-\frac{1}{2}}^3}\varphi_{i-1} + \left(\frac{r_{i+\frac{1}{2}}^2 - r_{i-\frac{1}{2}}^2}{r_{i+\frac{1}{2}}^3 - r_{i-\frac{1}{2}}^3}\right)\varphi_i + \frac{r_{i+\frac{1}{2}}^2}{r_{i+\frac{1}{2}}^3 - r_{i-\frac{1}{2}}^3}\varphi_{i+1} = -\frac{4\pi\rho_i\Delta r}{3}. \tag{5.148}$$

The boundary conditions we use at the left, and right endpoints of the grid are chosen to be $\frac{d}{dr}\varphi\big|_{r=0} = 0$ at the left boundary and an outflow boundary at the right boundary. Together, Eq. (5.148) and these boundary conditions generate the matrix (for a 6 cell system)

$$\begin{bmatrix}
-\frac{r_{\frac{1}{2}}^2}{r_{\frac{1}{2}}^3 - r_{-\frac{1}{2}}^3} & \frac{r_{\frac{1}{2}}^2}{r_{\frac{1}{2}}^3 - r_{-\frac{1}{2}}^3} & 0 & 0 & 0 & 0 \\
\frac{r_{\frac{1}{2}}^2}{r_{\frac{3}{2}}^3 - r_{\frac{1}{2}}^3} & -\frac{r_{\frac{3}{2}}^2 + r_{\frac{1}{2}}^2}{r_{\frac{1}{2}}^3 - r_{-\frac{1}{2}}^3} & \frac{r_{\frac{3}{2}}^2}{r_{\frac{3}{2}}^3 - r_{\frac{1}{2}}^3} & 0 & 0 & 0 \\
0 & \frac{r_{\frac{3}{2}}^2}{r_{\frac{5}{2}}^3 - r_{\frac{3}{2}}^3} & -\frac{r_{\frac{5}{2}}^2 + r_{\frac{3}{2}}^2}{r_{\frac{3}{2}}^3 - r_{\frac{1}{2}}^3} & \frac{r_{\frac{5}{2}}^2}{r_{\frac{5}{2}}^3 - r_{\frac{3}{2}}^3} & 0 & 0 \\
0 & 0 & 0 & \frac{r_{\frac{5}{2}}^2}{r_{\frac{7}{2}}^3 - r_{\frac{5}{2}}^3} & -\frac{r_{\frac{7}{2}}^2 + r_{\frac{5}{2}}^2}{r_{\frac{7}{2}}^3 - r_{\frac{5}{2}}^3} & \frac{r_{\frac{7}{2}}^2}{r_{\frac{7}{2}}^3 - r_{\frac{5}{2}}^3} \\
0 & 0 & 0 & 0 & \frac{r_{\frac{9}{2}}^2 - r_{\frac{11}{2}}^2}{r_{\frac{11}{2}}^3 - r_{\frac{9}{2}}^3} & \frac{r_{\frac{11}{2}}^2 + r_{\frac{9}{2}}^2}{r_{\frac{11}{2}}^3 - r_{\frac{9}{2}}^3}
\end{bmatrix}
\begin{bmatrix} \varphi_0 \\ \varphi_1 \\ \varphi_2 \\ \varphi_3 \\ \varphi_4 \\ \varphi_5 \end{bmatrix}
= -\frac{4\pi\Delta r}{3}
\begin{bmatrix} \rho_0 \\ \rho_1 \\ \rho_2 \\ \rho_3 \\ \rho_4 \\ \rho_5 \end{bmatrix} \tag{5.149}$$

We validate our numerical method against the test case shown in Appenxdix A of constant charge density inside a sphere. In Fig. 5.4, we see a comparison of the analytic solution to our numerical solution for the electric field.

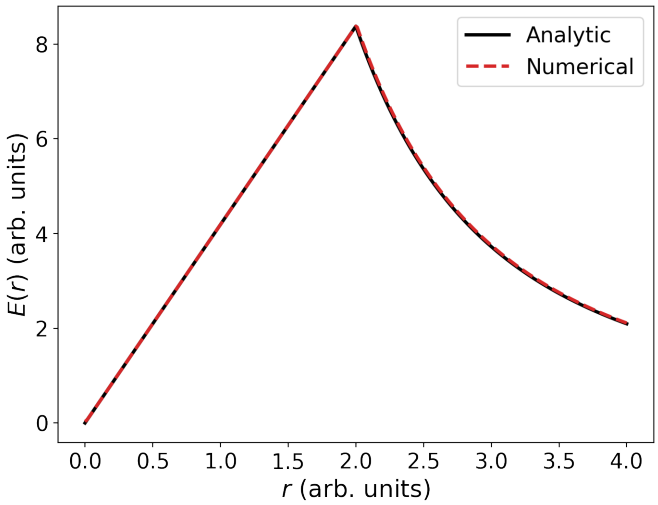

Figure 5.4: Electric field $E(r)$ computed the numerical method Eq. (5.5.3) and compared against the analytic solution Eq. (A.17). This case considers a sphere of size $R = 2$, with constant density of $\rho_0 = 1$, and $\Delta r = 0.01$, all with arbitrary units. We see that for $r \leq 2$, the numerical method correctly predicts the linear electric field and then transitions to the quadratic decay for $r > 2$.

5.6 Numerical Results

Using the numerical methods described in Sec. 5.5, we simulate a range of problems related to UNPs and HED plasmas.

We begin in Sec. 5.6.1 by simulating plasmas with zero spatial dimension where we focus on three distinct applications. The first application focuses on the verification of our numerical implementation in the context of temperature and momentum relaxation for HED plasmas. The second application focuses on the validation of our numerical implementation by simulating temperature relaxation in multi-species UNPs where we find that our kinetic model agrees well with experimental and MD simulation data. The third application is concerned with simulating the velocity distribution tail filling rate in an electron UNP where we compare two different collision operators.

In Sec. 5.6.2, we extend the scope of our numerical study to include one spatial dimension with two particular applications. Namely, the expansion of single- and multi-species UNPs into a vacuum, and the diffusion of materials across an interface in HED mixtures. First, we find that the single-species UNP expansion is adiabatic and that the plasma is so quickly driven to

equilibrium by collisions, that the expansion is well described by the Vlasov equation. Because of this, our simulations suggest that the expansion of a single-species UNP is time-reversible. Next, we compare results from our numerical simulations to results from the analytic models derived in Sec. 5.4 and find that although the assumption that the electron temperature is spatially independent is invalid for the cases studied here, the overall dynamics of the UNP do not appear to be significantly impacted by this choice. Then, for the case of multi-species UNPs, we find that our multi-species BGK simulations disagree with multi-species Vlasov simulations which implies that thermodynamic forces such as heat flux, viscous flux, and diffusive fluxes generate entropy in the plasma. Lastly, we carry out numerical simulations of diffusive mixing in HED experiments. We find that the dominant drivers of diffusion in our simulations are caused by electrodiffusion: diffusion driven by electric fields.

The kinetic calculations in all sections of this chapter *except* for those reported in Sec. 5.6.2.3 were numerically implemented in the “Python" programming language; the specific version used here is Python 3.7. To increase the performance of our Python code, which is an interpreted language, we (i) utilized numerically efficient pre-compiled libraries like NumPy [282] and SciPy [283] and (ii) compiled non-compiled portions of the code separately using the Numba just-in-time complier [284]. For the latter, we saw drastic performance gains; in many cases the computation cost was reduced by orders of magnitude. All simulations, except for those reported in Sec. 5.6.2.3, were carried out on a single core of a 2.7 GHz Core i7-8559U CPU. In Sec. 5.6.2.3, a variant of the multi-component BGK code[2] – which is written in the “C" programming language – was used.

5.6.1 0D Kinetic Simulations

Kinetic equations are composed of advection terms – the left-hand side of Eq. (5.1) – and a collision operator – the right hand-side of (5.1). We begin our presentation of numerical results by first verifying the multi-species BGK collision operator is conservative and also validate it against experimental data. By reducing Eq. (5.1) to 0D-3V, i.e., retaining only the velocity degrees of freedom, we carry out a direct numerical study of the collision operator. For the multi-species

[2]See: https://github.com/lanl/Multi-BGK.

BGK collision operator, Eq. (5.1) becomes

$$\frac{df_i}{dt} = \sum_{i=1}^{N} \nu_{ij}[\mathcal{M}_{ij}(\mathbf{v}; n_i, \mathbf{u}_{ij}, T_{ij}) - f_i], \quad j = 1, 2, \cdots, N. \tag{5.150}$$

5.6.1.1 Verification of the Multi-Species BGK Operator

To verify the multi-species BGK collision operator, Eq. (5.150), we compare our implementation to one reported in Ref. [267]. We compare our numerical results to a test case of a C^{6+}-H^{+} mixture where $n_C = n_H = 1 \times 10^{23}$ cm^{-3}, the initial temperatures of each species are $T_C = 10$ eV, and $T_H = 12$ eV, and their initial velocity vectors are $\mathbf{u}_C = (1.26 \times 10^5, 0, 0)$ cm s^{-1}, and $\mathbf{u}_H = (0, 0, 0)$ cm s^{-1}. For the electron species, we set $n_e = 2 \times 10^{23}$ cm^{-3} and $T_e = 11$ eV. The equilibrium temperature and momentum can be calculated by via the conservation of energy and momentum. The equilibrium velocity of the mixture is

$$u_{eq}^2 = \frac{m_1 n_1 u_1^2 + m_2 n_2 u_2^2}{\rho}, \tag{5.151}$$

which for the above conditions is $u_{eq}^2 \approx 1.162 \times 10^5$ cm s^{-1}. Similarly, for the temperature of the system, conservation of energy yields

$$T_{eq} = \frac{n_1 T_1 + n_2 T_2 + m_1 n_1 u_1^2 + m_2 n_2 u_2^2 - \rho u_{eq}^2}{n}, \tag{5.152}$$

which for the conditions above is $T_{eq} \approx 11.0$ eV.

In our implementation, Eq. (5.150) is numerically solved using a fourth-order explicit Runge-Kutta time integrator with a time step of $\Delta t = 1 \times 10^{-16}$s. The 3D velocity grid is initialized with an upper (and lower) bound of magnitude $|v_{max}| = 4 \times \sqrt{T/m}$ cm/s with a grid resolution of $\Delta v = 0.2$ cm/s in each velocity direction. The simulations took approximately 40 minutes to complete. We note that these particular simulations are highly resolved in time in order to compare our results to data in the literature; a time step that is a factor of 10 larger appears to be sufficient for obtaining data and a simulation using this time step takes roughly 4 minutes to complete. We compare our results with those reported in Ref. [267]. Our comparison is displayed in Figure 5.5 where we compare our calculations with the results provided in Figure 2 of Ref. [267]; we denote their data

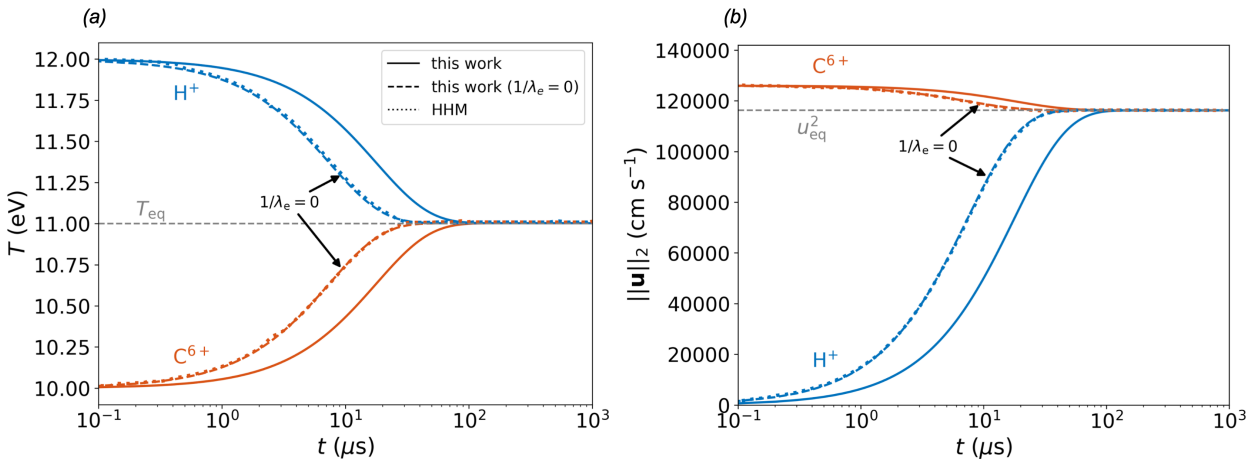

Figure 5.5: 0D-3V multi-species BGK simulations of a C^{6+}-H^+ mixture with plasma conditions described in Sec. 5.6.1.1. The collision rate model used here is given by Eq. (5.16). (a) temperature relaxation and (b) shows momentum relaxation between the species. Note that in the absence of electron screening ($1/\lambda_e = 0$), the system equilibrates more quickly because the collision rate is larger. Our numerical results *without* electron screening match data provided in Ref. [267]. The equilibrium velocity and temperature values are computed from Eq. (5.151) and (5.152) respectively; our results show that the multi-species BGK operator approaches the correct result; this is not the case for some multi-species BGK operators [267].

by “HHM." We find that by setting the inverse electron screening length to zero in Eq. (5.19), we recover their results. By including a non-zero inverse electron screening length (solid lines), we see that in Figure 5.5(a) and Figure 5.5(b), the relaxation time is longer because the collision rate *decreases* due to the presence of electron screening. Electron screening plays an important role in many HED and UNP experiments and we include it by using Eq. (5.20) in Eq. (5.19) for all results shown in this chapter.

5.6.1.2 Validation of the Multi-Species BGK Operator

Now that we have verified our numerical scheme, we validate it with data of temperature relaxation in UNP mixtures. In Figure 5.6, we compare results from our multi-species BGK model to experimental and simulation data for a UNP Ca^+-Yb^+ mixture at two different conditions (see Refs. [260] and [24]). In both simulations, the 3D velocity grid is initialized with an upper (and lower) bound of magnitude $|v_{\max}| = 4 \times \sqrt{T/m}$ cm/s with a grid resolution of $\Delta v = 0.2$ cm/s in each velocity direction; an explicit fourth-order Runge-Kutta time integrator was employed with

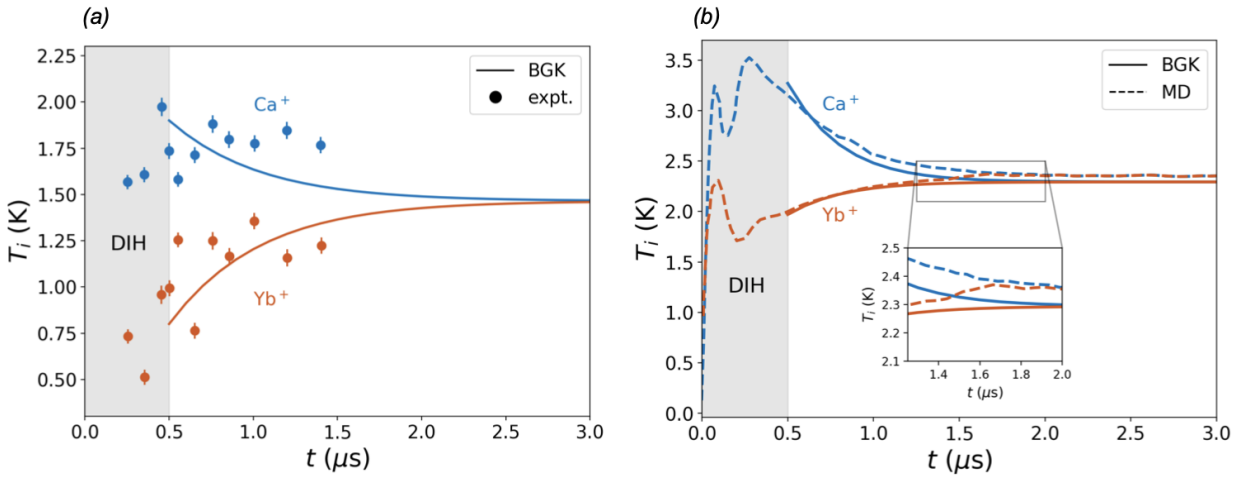

Figure 5.6: 0D-3V multi-species BGK simulations of a Ca^+-Yb^+ UNP mixture with plasma conditions described in Sec. 5.6.1.2. The collision rate model used here is the *temperature relaxation* rate given in Eq. (5.16). We show the temperature relaxation predicted by the BGK model compared to (*a*) experimental data from Ref. [260] and (*b*) MD data obtained from Ref. [24]. We find that the BGK model accurately predicts the temperature relaxation rate compared to both experimental and MD data. These results provide confidence in the use of the BGK model for modeling UNP mixtures beyond the disorder-induced heating region which is labeled as "DIH" and denoted with a grey shaded rectangle in (*a*) and (*b*).

time step of $\Delta t = 1 \times 10^{-7}$ s. In Fig. 5.6(a) we set the ion densities to be $n_{Ca^+} = 2.9 \times 10^9$ cm^{-3} and $n_{Yb^+} = 1.9 \times 10^9$ cm^{-3}. The initial ion temperatures are computed from the average of the experimental data from $t = 0.4$ to 0.5 μs which results in $T_{Ca^+} = 1.9$ K, and $T_{Yb^+} = 0.8$ K. The electrons have a temperature of $T_e = 96$ K and we assume the electron temperature decreases according to a modified form of the adiabatic model Eq. (5.130) which is

$$T_e(t) = \frac{T_{e0}}{1 + t^2/\bar{\tau}^2}, \tag{5.153}$$

where $T_{e0} = T_e(0)$ and $\bar{\tau} \equiv \bar{\sigma}_0/\bar{c}_{s0}$. We define the mixture width and sound speed parameters

$$\bar{\sigma}_0 = \frac{\sigma_{i,0} n_i + \sigma_{j,0} n_j}{n}, \tag{5.154}$$

$$\bar{c}_{s0}^2 = T_{e0} \frac{\langle Z_i^2/m_i \rangle}{\langle Z_i \rangle}, \tag{5.155}$$

where $n = n_i + n_j$, $\langle A_i^\alpha \rangle \equiv x_i A_i^\alpha + x_j A_j^\alpha$, and $x_i = n_i/n$ denotes the number concentration of species i. Lastly, we assume that the drift velocities are $\mathbf{u}_{Ca^+} = \mathbf{u}_{Yb^+} = \mathbf{0}$. We see that our numerical results well approximate experimental data for temperature relaxation and can be used to extrapolate past

the disorder induced heating region denoted as "DIH." In Fig. 5.6(b) we compare our multi-species BGK results against temperature relaxation data from an MD simulation. For this case, the ion densities are $n_{Ca^+} = 4.3 \times 10^9$ cm^{-3} and $n_{Yb^+} = 1.3 \times 10^{10}$ cm^{-3}. The initial ion temperatures are determined from the average of the MD data from $t = 0.4$ to 0.5 μs which results in $T_{Ca^+} = 3.27$ K, and $T_{Yb^+} = 1.97$ K. The initial electron temperature is $T_{e0} = 100$ K and its time dependence is given by Eq. (5.153). Additionally, we set $\mathbf{u}_{Ca^+} = \mathbf{u}_{Yb^+} = \mathbf{0}$. For this case, we see that our multi-species BGK model accurately predicts the equilibrium temperature to within 4%; this discrepancy is due to uncertainties from the approach used to compute the initial ion temperatures. To account for these uncertainties, an ensemble of simulations could be carried out with different initial ion temperatures. These temperatures could be generated by sampling from a normal distribution of temperatures with mean and variance determined by experimental or MD data. Additionally, we can measure the rate at which equilibration of these simulation occurs by computing the entropy source term in Eq. (5.37). Figure 5.7 shows the entropy source term for both cases in Fig. 5.6.

It is important to note that by using a kinetic simulation in place of MD, we drastically reduce the dimensionality of the problem – from 6N dimensional to 3 dimensional – which decreases the computation time by a factor of roughly 3000. Specifically, the MD results reported above state an MD run – using the Sarkas MD code [285] – took approximately 20 hours to complete on a single core of an Intel Core i7-8700K CPU for a total simulation length of approximately 4 μs. In contrast, our 0D-3V kinetic simulations took approximately 3 minutes and 51 seconds for a total simulation time length of 100 μs.

5.6.1.3 Tail Filling in UNPs

The previous sections were concerned with multi-species ion plasmas. In this section, we change our focus to simulating the equilibration of a velocity distribution of a single-species electron plasma with conditions relevant to UNPs. Specifically, we consider an electron plasma with a truncated distribution function that is nearly zero over some range of velocities: a depleted tail. An example of physical systems in which this type of distribution function occurs is in situations where evaporation occurs. In this scenario, the highest energy particles escape and leave

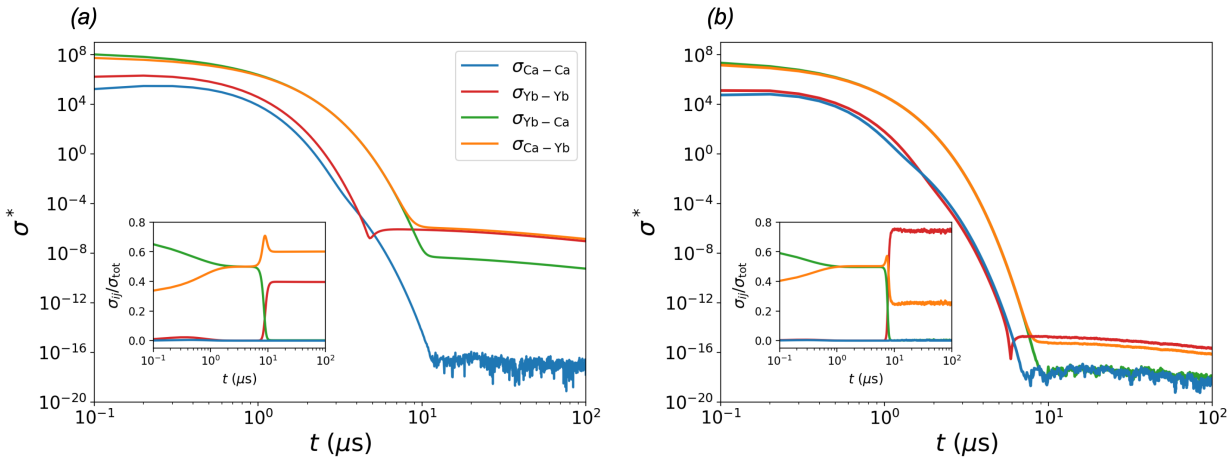

Figure 5.7: Entropy source term calculated from Eq. (5.37) from the simulations displayed in Fig. 5.6. (a) corresponds to the plasma conditions in Fig. 5.6(a) and (b) corresponds to the plasma conditions in Fig. 5.6(b). We see that certain terms correspond to a larger amount of entropy than others, specifically, the Yb^+-Yb^+ and cross-species collisions. Since entropy is being generated, the system is irreversible. The source of irreversibility is associated with transport coefficients like the interdiffusion, thermal conductivity, and viscosity of the plasma.

behind particles with a missing high-energy tail. Thermonuclear fusion also results in a distribution function with a depleted tail by converting the fast tail particles into different species through a nuclear reaction. The question we aim to answer with kinetic theory is: how long does it take for these distribution functions to become Maxwellian?

Ultracold neutral plasmas provide a unique laboratory for studying the rate at which the tails of the velocity distribution repopulate because their low densities effectively slow physical processes to a measurable time scale. To examine just the physics of the forms of the collision operators, we consider a kinetic model with zero spatial dimensions and one velocity dimension (0D-1V). Numerical results are obtained for spatially homogeneous tail filling. In 0D-1V, Eq. (5.1) has the form

$$\frac{\partial f_e}{\partial t} = Q(f_e, f_e), \tag{5.156}$$

where $f_e \equiv f_e(v,t)$ is the distribution function of an electron species. We will consider two forms for the collision operator in this section: the BGK and LBD operators which in 0D-1V have the

form

$$Q^{\text{BGK}} = \nu_{ee}\left[\mathcal{M}_e(v; n_e, u_e, T_e) - f_e\right], \tag{5.157}$$

$$Q^{\text{LBD}} = \nu_{ee}\frac{\partial}{\partial v}\left[(v - u_e)f_e + v_{th}^2\frac{\partial}{\partial v}f_e\right]. \tag{5.158}$$

We discretize each of the collision operators using the *method of lines* approach allowing us to use high-order time integrators[3] in extant software libraries [283]. The initial Maxwellian distribution function is shown in Fig. 5.8 and is given by

$$\mathcal{M}_e(v) = n_e\left(\frac{m_e}{2\pi T_e}\right)^{1/2}\exp\left[\frac{-m_e}{2T_e}(v - u_e)^2\right]. \tag{5.159}$$

Here, we set $n_e = 3 \times 10^7$ cm^{-3}, $u_e = 0$ cms^{-1}, and $T_e = 3.5$ K which are conditions relevant to UNPs. We "truncate" the tails of the equilibrium distribution to remove the fastest 1% of electrons on either side as shown in Fig. 5.8; this reduces the electron temperature to roughly $T_e = 3.1$ K. Using the truncated distribution function as our initial condition, we carry out simulations using the BGK and LBD operator to measure to rate at which the tails of the truncated distribution replenish/fill. For these simulations, the distribution function was first truncated, and the collision rate ν_{ee} is calculated using eight distinct models – see Table 5.2. We simulate the expansion of the electron distribution function for a total simulation length of 0.2 μs with a time step of $\Delta t = 0.002$ μs. The 1D velocity grid is initialized with an upper (and lower) bound of magnitude $|v_{\text{max}}| = 4 \times \sqrt{T/m}$ cm/s with a grid resolution of $\Delta v = 0.026$ cm/s.

Figure 5.8 shows the initial condition at $t = 0$ and at the final time $t = 0.2\mu$s. We see that the BGK and LBD operators equilibrate to the same equilibrium distribution to within 1% at the peak. The distribution does not return to its initial condition prior to truncation because of evaporation: the high-energy tails have been removed; this results in an equilibrium distribution function that has a larger magnitude at $v/v_{th} = 0$. In Fig. 5.9(a), we compare the time evolution of the distribution function using the BGK and LBD collision operators with the HHM collision rate given in Table 5.2. By plotting the difference of the distribution functions, we highlight the impact each collision operator has on the tail-filling rate. Because the LBD operator incorporates

[3] We used the "Radau" time integrator for this work.

Model	$\ln\Lambda$	ν_{ee} (Hz$\times 10^{-7}$)	Description	Ref.
LS	1.41	3.96	Straight-line trajectories	[270]
GMS-1	1.41	3.96	Straight-line trajectories	[269]
GMS-2	1.71	4.80	Straight-line trajectories	[269]
GMS-3	2.00	5.62	Straight-line trajectories	[269]
GMS-4	1.44	4.04	Hyperbolic trajectories	[269]
GMS-5	1.72	4.84	Hyperbolic trajectories	[269]
GMS-6	1.72	4.84	Hyperbolic trajectories	[269]
HHM	–	3.41	Correlations beyond binary interactions	[267]

Table 5.2: A comparison of the numerical values of the electron-electron collision rate ν_{ee}. All values of ν_{ee} were obtained via Eqs. (5.25) and (5.26) with values of $n_e = 2.9 \times 10^7$ gcm^{-3} and $T_e = 3.1$ K; these values of n_e and T_e correspond to the electron density and temperature of the *truncated* distribution shown in Fig. 5.8.

velocity gradients in its functional form, the tails fill more quickly than the BGK operator. We see that after $t \approx 0.12$ μs, the difference between the LBD and BGK operator is small and the truncated distribution function has equilibrated.

To measure the rate of tail filling, we compute the ratio of the number of electrons in the truncated regions to the number of electrons in the tail of the full distribution N_0 given by Eq. (5.159); results using both the BGK and LBD operator using all eight of the collision frequencies given in Table 5.2 are shown in Fig. 5.9(b). Because the initial condition of the distribution function contained essentially infinite gradients at the truncated regions, we expect the LBD operator to drive the distribution function to equilibrium more quickly than the BGK operator which relaxes the the distribution function to equilibrium by the difference of M_e and f_e. At a high level, we have found that two models result in two different tail-filling rates which is not surprising. However, one model – the LBD operator – predicts a four times quicker tail filling rate than the BGK operator. The difference in the tail-filling rate predicted by the BGK and LBD models is non-negligible and should be compared to experimental data in order to appropriately simulate these processes using kinetic models. Additionally, by increasing the electron temperature, we find that the collision frequencies begin to converge to the same results in contrast to the results shown in Fig. 5.9(b). To

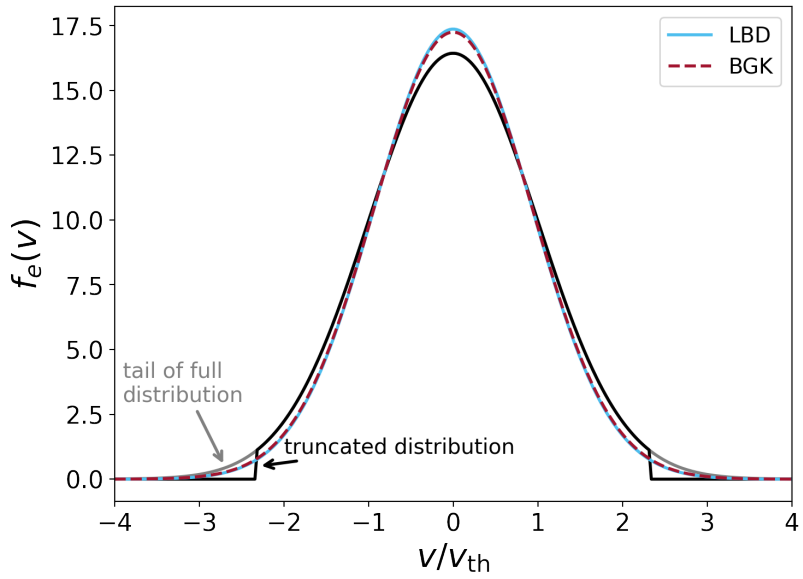

Figure 5.8: Initial velocity distribution of electrons with $n_e = 3 \times 10^7 \text{cm}^{-3}$, and $T_e = 3.5$ K. The "full" and "truncated" distributions overlap until $|v/v_{th}| \approx 2.3$, where the tails of the full distribution have been truncated beyond this amount; this removes the fastest 1% of the electrons on either side of the distribution. We show the equilibrated velocity distribution function using the BGK and LBD collision operators with the HHM collision rate; both collision operators results in the same equilibrated distribution function. Note that the distribution function does not return to its original shape because of evaporation.

maximize the benefit of this analysis, an ensemble of experiments should be carried out at different temperatures to assess the validity of different collision operators and collision rate models.

5.6.2 1D Kinetic Simulations

We now extend our kinetic simulations to include one spatial dimension where we focus our simulations on quantifying (i) the expansion of single-species UNPs, (ii) the expansion of multi-species UNP, and (iii) the diffusive mixing in HED plasma mixtures.

5.6.2.1 Expansion of Single-species UNPs

In this section, we answer the following three distinct questions: (1) can we approximate the electron species with analytic formulae avoiding the need for explicit calculations [See Eqs. (5.130) and (5.94)] (2) what is the role of a collision operator for single-species UNPs and (3) are single-species UNPs time-reversible? For the simulations carried out here, the initial ion density is

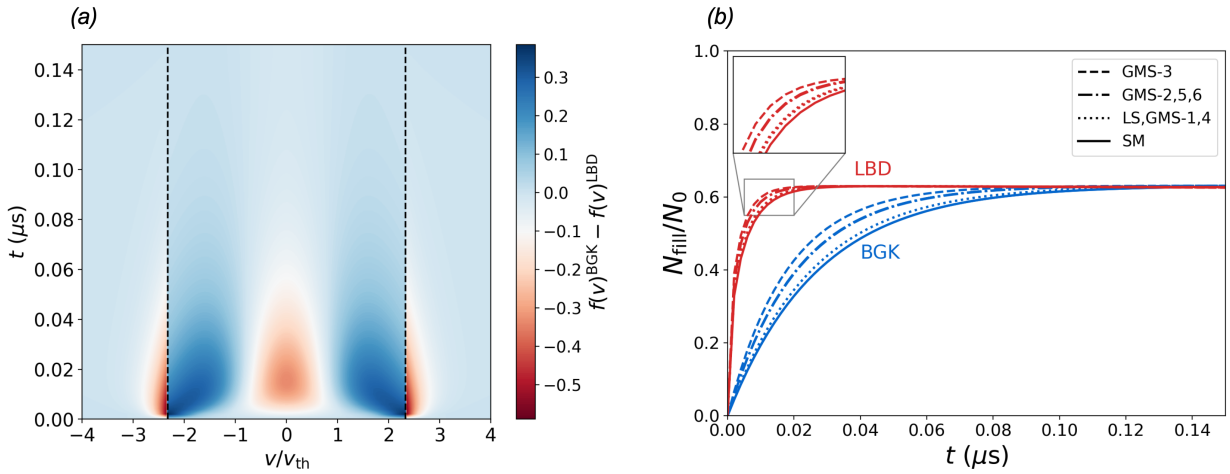

Figure 5.9: (a) Difference of distribution functions using the BGK and LBD operator with HHM collision rate versus velocity and time. The dashed vertical lines mark that locations where the full distribution was truncated (see Fig. 5.8). The negative values show where the distribution function evolved using the LBD operator is smaller than the corresponding BGK operator opinion. Large gradients at the truncation locations cause the LBD operator to quickly fill the tail regions in contrast to the BGK operator which does not use information of velocity gradients. (b) tail filling rate using the BGK and LBD collision operators in 0D-1V dimensions (spatially homogeneous) with the collision rates given in Table 5.2. N_0 denotes the number of electrons originally in the tails of the *full* distribution before truncation (see Fig. 5.8). Approximately 60% of the original number of electrons replenish the tail after equilibration which occurs at $t \approx 0.12$ μs.

assumed to be Gaussian and given by

$$n_i(x, t = 0) = n_{i,0}\exp\left(-\frac{x^2}{2\sigma_{i,0}^2}\right), \tag{5.160}$$

where $n_{i,0}$ is the initial "peak" ion density and $\sigma_{i,0}$ is the initial width of the plasma.

We begin by answering the question: can we approximate the electron species with analytic formulae and avoid the need for explicit calculations? The main assumptions we will check in deriving the analytic formulae given by Eqs. (5.130) and (5.94) is the spatial independence of the electron temperature and that the electron density can be well-approximated by Eq. (5.94). To do this, we carry out a multi-species Vlasov simulation of a UNP mixture of Ca^+ ions and an electron species where we approximate the electron's mass to be $m_e = m_{Ca^+}/183$. While this is not the true proton-electron mass ratio, it should be a good approximation for the electron species in that the electrons respond relatively quickly to the dynamics of the ion species. Additionally, since the electrons in an UNP are classical – see Table 5.1 – we can directly use Eq. (5.1) without introducing

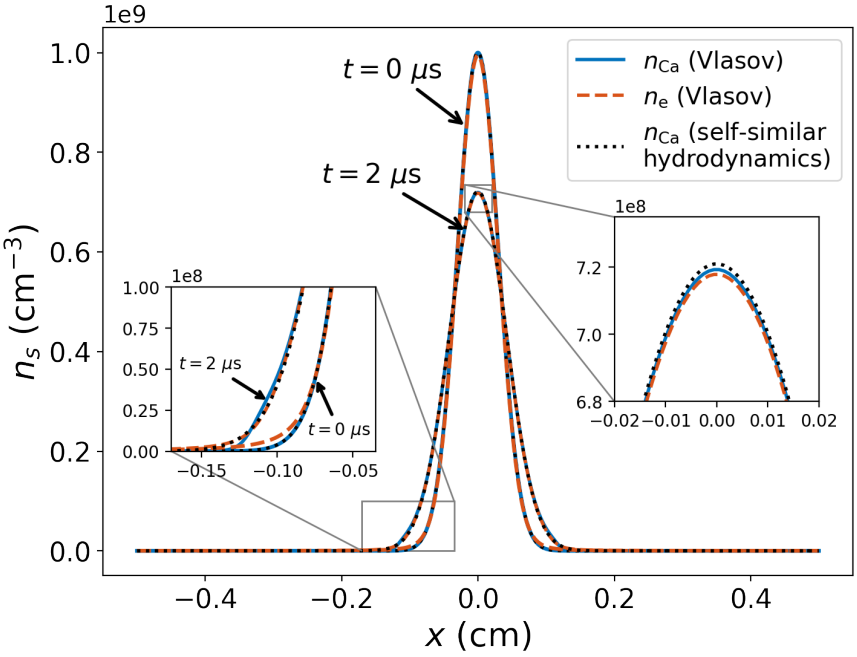

Figure 5.10: Density profiles for a Ca^+-e UNP computed from a multi-species Vlasov simulation. Two simulation snapshots are shown: one at $t = 0$ μs and another at $t = 2$ μs. The density profile obtained from the adiabatic self-similar hydrodynamics model [Eq. (5.129)] is also shown. The density evolution of the Ca^+ species agrees with the self-similar hydrodynamics model to sub-percent accuracy.

quantum statistics in the distribution function. We initialize our Ca^+-e mixture with conditions relevant to ongoing UNP experiments. For the case shown here, we initialize the peak ion density to be $n_{Ca^+,0} = 1 \times 10^9$ cm^{-3} with a width of $\sigma_{Ca^+,0} = 3$ mm and an ion temperature of $T_{Ca^+} = 1$ K. The initial density of the electron species is calculated self-consistently from the ion density with an initial temperature of $T_e = 100$ K. We then solve the multi-species Vlasov equation [Eq. (5.5)] where the self-consistent electric field is obtained with a fast-Fourier transform [262]. The total simulation length time was 2μs with a Courant–Friedrichs–Lewy (CFL) value of 0.4. The 1D spatial grid is initialized with an upper (and lower) bound of magnitude $|x_{max}| = 0.5$ cm with a grid resolution of $\Delta x = 0.001$ cm. The 1D velocity grid is initialized with an upper (and lower) bound of magnitude $|v_{max}| = 40 \times \sqrt{T/m}$ cm/s with a grid resolution of $\Delta v = 0.02$ cm/s. For the advection terms, we use a fourth-order upwinding FVM reconstruction. The simulation took approximately 60 hours to complete.

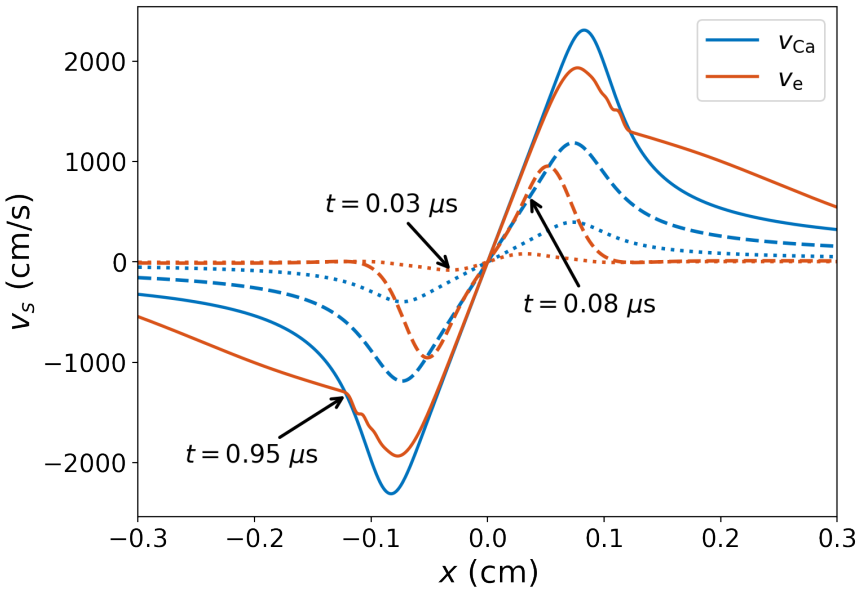

Figure 5.11: Velocity profiles of a Ca^+-e UNP computed from a multi-species Vlasov simulation at various time steps. The dotted lines denote $T = 0.03\ \mu$s, the dashed lines denote $t = 0.08\ \mu$s, and the solid lines denote $t = 0.95\ \mu$s. After roughly $t = 0.1\ \mu$s, the velocity profiles of Ca^+ and the electrons "lock" together i.e., the process of momentum relaxation. Since the momentum relaxation occurs on a timescale much quicker than the ion dynamics, the assumption of instantaneous momentum relaxation – the basis for the derivation of the self-similar hydrodynamics models – is valid.

The simulation results of the Ca^+-e expansion are shown in Fig. 5.10. Initially, the electrons and ions differ the most in the tails as shown by the insert of Fig. 5.10. At $t = 2\mu$s, the ions agree with the adiabatic expansion model to within 0.5% at the peak density ($x = 0$ cm). Moreover, the electron density retains the form of Eq. (5.94) from $t = 0$ to 2 μs suggesting that the Poisson-Boltzmann form [Eq. (5.94)] is sufficient in describing the electron density in an expanding UNP. Figure 5.11 shows the velocity profiles for different times throughout the simulation. We see that momentum relaxation between the ions and electrons occurs roughly on the order of 0.1 μs which is much faster than the dynamics of the ion species. We note that the Poisson-Boltzmann approximation essentially enforces instantaneous momentum relaxation which appears to be a valid assumption for the case of the Ca^+-e UNP mixture.

Lastly, we assess the temperature evolution of the electron species – the input to the Poisson-Boltzmann expression Eq. (5.94) – and compare our simulation results to the adiabatic model Eq. (5.130). The comparison of the simulation and the adiabatic expansion model Eq. (5.130) is

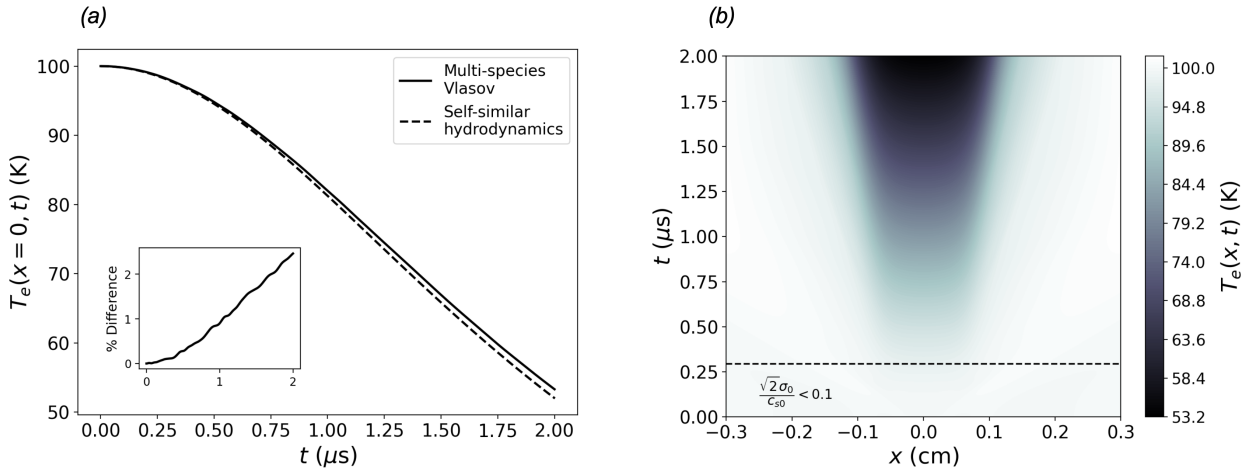

Figure 5.12: Electron temperature of a Ca^+-e UNP computed from a multi-species Vlasov simulation. (a) the electron temperature at the center of the plasma compared to the self-similar hydrodynamics model Eq. (5.130). The electron temperature is within ∼2% for all time as shown by the insert. (b) the electron temperature versus space and time. The adiabatic self-similar hydrodynamics model Eq. (5.130) agrees well with an isothermal model for $\sqrt{2}\sigma_0/c_{s0} \ll 1$. Although there is a spatial dependence of the electron temperature, 90% of the plasma is within a region of space for which the electron temperature is within 10% of the self-similar hydrodynamics model Eq. (5.130). This substantiates the approximation of a spatially independent electron temperature in the derivation of the self-similar hydrodynamics models.

displayed in Fig. 5.12. Figure 5.12(a) shows that that the electron temperature from the Ca^+-e simulation results agree to within ∼2% of the adiabatic model at the peak region ($x = 0$ cm). In Fig. 5.12, we see that there is indeed a spatial dependence of the electron temperature however, the adiabatic model for the electron temperature holds to within ∼10% for all time between the range of $x \in [-0.07, 0.07]$ cm. We note that only ∼10% of the ion and electron density occupy the region outside of this range of x. Therefore, although the electron temperature differs from the adiabatic model, the majority of the plasma occupies the range where Eq. (5.130) is accurate. We also note that the isothermal and adiabatic models are approximately equivalent when the parameter $\sqrt{2}\sigma_0/c_{s0} \ll 1$. We plot a horizontal line in Fig. 5.12(b) that validates this approximation. That is, below the horizontal line, the electrons are essentially at a constant temperature. The Ca^+-e simulations verify that for a single species UNP, the adiabatic expansion model is accurate for approximating the expansion of an UNP modeled by the Vlasov equation. However, the analytic formulae were derived under the assumption of a *collisionless* plasma. Since UNPs are highly

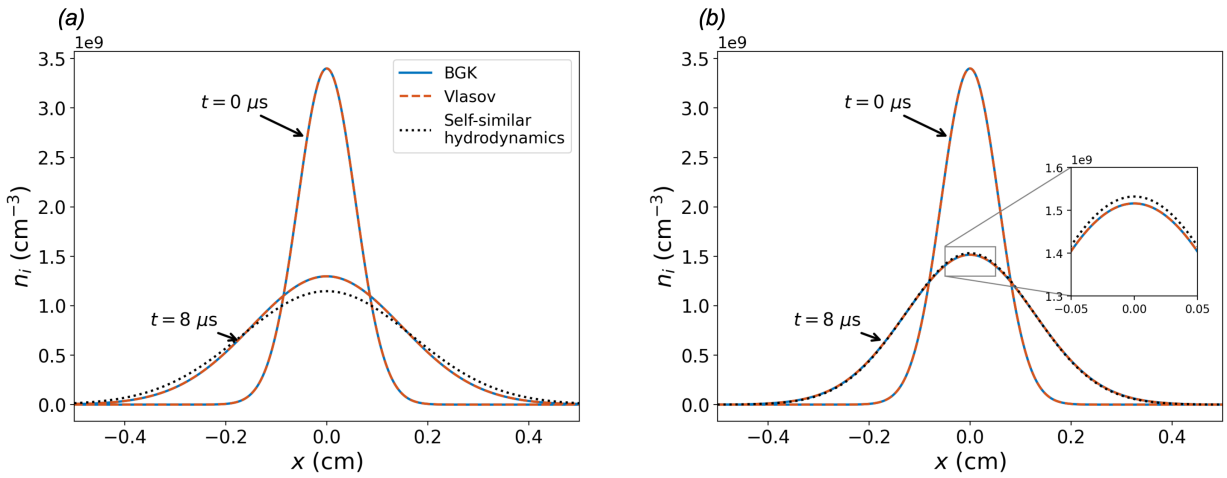

Figure 5.13: Comparison of the (a) isothermal electrons (b) adiabatic electrons. The relative error at the peak between the BGK simulations and the self-similar hydrodynamics model is $\sim 1\%$. Note that the density profiles from the BGK and Vlasov simulations agree nearly exactly for all time.

collisional – see Table 5.1 – we extend the numerical study of single-species UNPs to include collisions by introducing a BGK collision operator with collision rates given by Eq. (5.16). We carry out single-species BGK simulations of Ca^+ and treat the electrons in two ways: isothermally with density given by Eq. (5.94) and adiabatically with density given by Eq. (5.94) and temperature given by Eq. (5.130). For these simulations, we pick plasma conditions relevant to ongoing UNP experiments. Specifically, we set $n_{Ca^+,0} = 3.4 \times 10^9$ cm^{-3} with width $\sigma_{Ca^+,0} = 0.57$ mm and $T_{Ca^+} = 1.9$ K. For the isothermal case we set $T_e = 96$ K for all time and for the adiabatic case, we set $T_{e0} = 96$ K and calculate the temperature profile from Eq. (5.130). The total simulation time is 8μs with a CFL of 0.7. The 1D spatial grid is initialized with an upper (and lower) bound of magnitude $|x_{max}| = 0.5$ cm with a grid resolution of $\Delta x = 0.00125$ cm. The 1D velocity grid is initialized with an upper (and lower) bound of magnitude $|v_{max}| = 50 \times \sqrt{T/m}$ cm/s with a grid resolution of $\Delta v = 0.2$ cm/s. We carry out two simulation for both the isothermal and adiabatic cases. One simulation is collisionless (i.e., the Vlasov equation) and another is with the BGK collision operator. Each of the four simulations took approximately 1 hour to complete. In contrast to the explicit Ca^+-e simulations, the Ca^+ simulations with an *implicit* electron species decreased computation time by roughly a factor of 240.

The density profiles of the simulation results are displayed in Fig. 5.13. In Fig. 5.13(a) we show results from assuming the electrons are isothermal, and in Fig. 5.13(b) we show results from assuming the electrons are adiabatic. In the isothermal case, we see that both the Vlasov and BGK data disagree with the isothermal self-similar expansion model Eq. (5.117). In the adiabatic case, we see that the Vlasov, BGK, and adiabatic self-similar model [Eq. (5.129)] all agree implying that the plasma expansion is adiabatic. Moreover, in both cases, the Vlasov and BGK models agree almost exactly – to within a few percent for the first three moments of the distribution function – implying that the dynamics of the single-species UNP are *time-reversible* since the Vlasov equation does not generate entropy.

The above simulations showcase interesting features of single-species UNPs. Namely, we have verified that the electron and ion species are well-approximated by a self-similar hydrodynamic model. While other work has been done to validate this point Ref. cite, we have quantified the validity of various approximations in the derivation of the self-similar hydrodynamics models with kinetic simulations. Specifically, we have shown that although the electron temperature is not spatially independent, the errors associated with that approximation are on the order of a few percent. Additionally, we have assessed the role that collisions have in the expansion of UNPs. We have found that the Vlasov and BGK simulations agree to sub-percent accuracy in the first three moments and within 1% of the self-similar expansion model Eq. (5.129). Therefore, the UNP expansion is adiabatic and little to no entropy is being generated by collisions. Because of this, single-species UNPs should be *time-reversible* which perhaps can be verified experimentally. We note that the self-similar model is based around a Gaussian UNP which may not be the case in the presence of magnetic fields. Thus, if the initial condition is not carefully controlled, the UNPs may no longer be time-reversible. We will show in the next section, that UNP mixtures do not follow the same self-similar expansion properties of single-species UNPs and that the amount of entropy generated in them can be mitigated by the initial plasma conditions.

5.6.2.2 Expansion of Multi-species UNPs

In this section, we extend our numerical study to plasmas UNP mixtures where we answer the question: can the UNP mixture conditions be chosen to minimize the amount of entropy being generated? Recently the capability to create UNP mixtures has provided the ability to validate models for plasma mixtures and allowed for measurements of process otherwise unattainable such as temperature relaxation. We begin this section by studying the impact that changing the plasma conditions has on entropy generation.

We compare the numerical results of four different plasma conditions. The first case we will analyze is a Ca^+-Yb^+ mixture with plasma conditions relevant to ongoing UNP mixture experiments [24]. Specifically, the plasma conditions here are $n_{Ca^+,0} = 1.4 \times 10^{10}$ cm^{-3}, and $n_{Yb^+,0} = 2.7 \times 10^{10}$ cm^{-3} with widths $\sigma_{Ca^+,0} = 0.76$ mm and $\sigma_{Yb^+,0} = 0.44$ mm. The initial ion temperatures are taken to be $T_{Ca^+} = 2$ K and $T_{Yb^+} = 1$ K. The second case we study is the same as the first case but instead with $\sigma_{Ca^+,0} = \sigma_{Yb^+,0} = 0.5$ mm. For the third case we now assume that both species share the same peak density and width. Specifically, $n_{Ca^+,0} = n_{Yb^+,0} = 2 \times 10^{10}$ cm^{-3} with widths $\sigma_{Ca^+,0} = \sigma_{Yb^+,0} = 0.5$ mm. The initial ion temperatures are taken to be $T_{Ca^+} = 2$ K and $T_{Yb^+} = 2$ K with the initial electron temperature is $T_{e0} = 96$ K. The fourth and final case is instead a UNP mixture of Ca^+-K^+ with $n_{Ca^+,0} = n_{K^+,0} = 2 \times 10^{10}$ cm^{-3} with widths $\sigma_{Ca^+,0} = \sigma_{K^+,0} = 0.5$ mm. The initial ion temperatures are taken to be $T_{Ca^+} = 1$ K and $T_{K^+} = 1$ K. For all cases the initial electron temperature is $T_{e0} = 96$ K and we assume that the electron temperature profile follows Eq. (5.130). The plasma conditions for all four cases are summarized in Table 5.3; each simulation took approximately 2.5 hours to complete.

For all simulations, the following conditions are the same: (i) the total simulation time is 8 μs with a CFL of 0.6, (ii) the 1D spatial grid is initialized with an upper (and lower) bound of magnitude $|x_{\max}| = 0.5$ cm with a grid resolution of $\Delta x = 0.001$ cm, (iii) the 1D velocity grid is initialized with an upper (and lower) bound of magnitude $|v_{\max}| = 40 \times \sqrt{T/m}$ cm/s with a grid resolution of $\Delta v = 0.1$ cm/s, and (iv) a fourth-order upwinding FVM reconstruction is used with a Newton iteration to obtain the electron density. To assess the timer-reversibility of each case given

Case	Species 1	Species 2	n_1 (cm^{-3})	n_2 (cm^{-3})	$\sigma_{1,0}$ (mm)	$\sigma_{2,0}$ (mm)	T_1 (k)	T_2 (K)
(a)	Ca^+	Yb^+	1.4×10^{10}	2.7×10^{10}	0.76	0.44	2	1
(b)	Ca^+	Yb^+	1.4×10^{10}	2.7×10^{10}	0.5	0.5	2	1
(c)	Ca^+	Yb^+	2×10^{10}	2×10^{10}	0.5	0.5	2	2
(d)	Ca^+	K^+	2×10^{10}	2×10^{10}	0.5	0.5	1	1

Table 5.3: Plasma conditions of four UNP mixtures. By varying the initial conditions of the plasma mixture, we aim to minimize the amount of entropy generated in the system. Numerical results for cases (a) - (d) are displayed in the corresponding panels of Fig. 5.14. We see that by selecting certain plasma parameters, the Vlasov and BGK numerical results agree suggesting that specific UNP mixtures are time-reversible.

in Table 5.3, both a Vlasov and BGK simulation were carried out. The initial condition and final density profiles are for each case in Table 5.3 are displayed in Fig. 5.14. In Fig. 5.14(a), we see that the Vlasov and BGK results differ greatly. The role of collisions in this case prevent the Ca^+ species from being forced away from the more massive Yb^+ species. In an attempt to control the spread of the Ca^+ species in the Vlasov simulations, we make the initial width of Ca^+ and Yb^+ the same which is shown in Fig. 5.14(b). The Vlasov results show that the Ca^+ ions still spread away from the Yb^+ species but the Ca^+ species retains an overall Gaussian profile. Next, we make the densities and temperatures of the Ca^+ and Yb^+ the same and the numerical results are shown in Fig. 5.14(c). We observe that for the Ca^+ species, the Vlasov results are in better agreement to the BGK results. Lastly, we change the second species to K^+ so that both species have similar mass. These results are shown in Fig. 5.14(d). We see that the Vlasov and BGK results agree to within sub-percent accuracy and retain an overall Gaussian shape. Our numerical results suggests that of all the cases given in Table 5.3 case (d) is the most likely multi-species UNP to be time-reversible.

It is worth summarizing the results of comparing the Vlasov and BGK results for the different cases of UNP mixtures. From our numerical results, we see that enforcing the same width parameter results in Gaussian profiles for both species; this suggests that the expansion of the UNP mixture may be self-similar although there is currently no self-similar expansion models for plasma mixtures. Next, by enforcing that the number densities of both species are the same, we find that the expansion of the Ca^+ species is less than the case where both species only have the same width parameters.

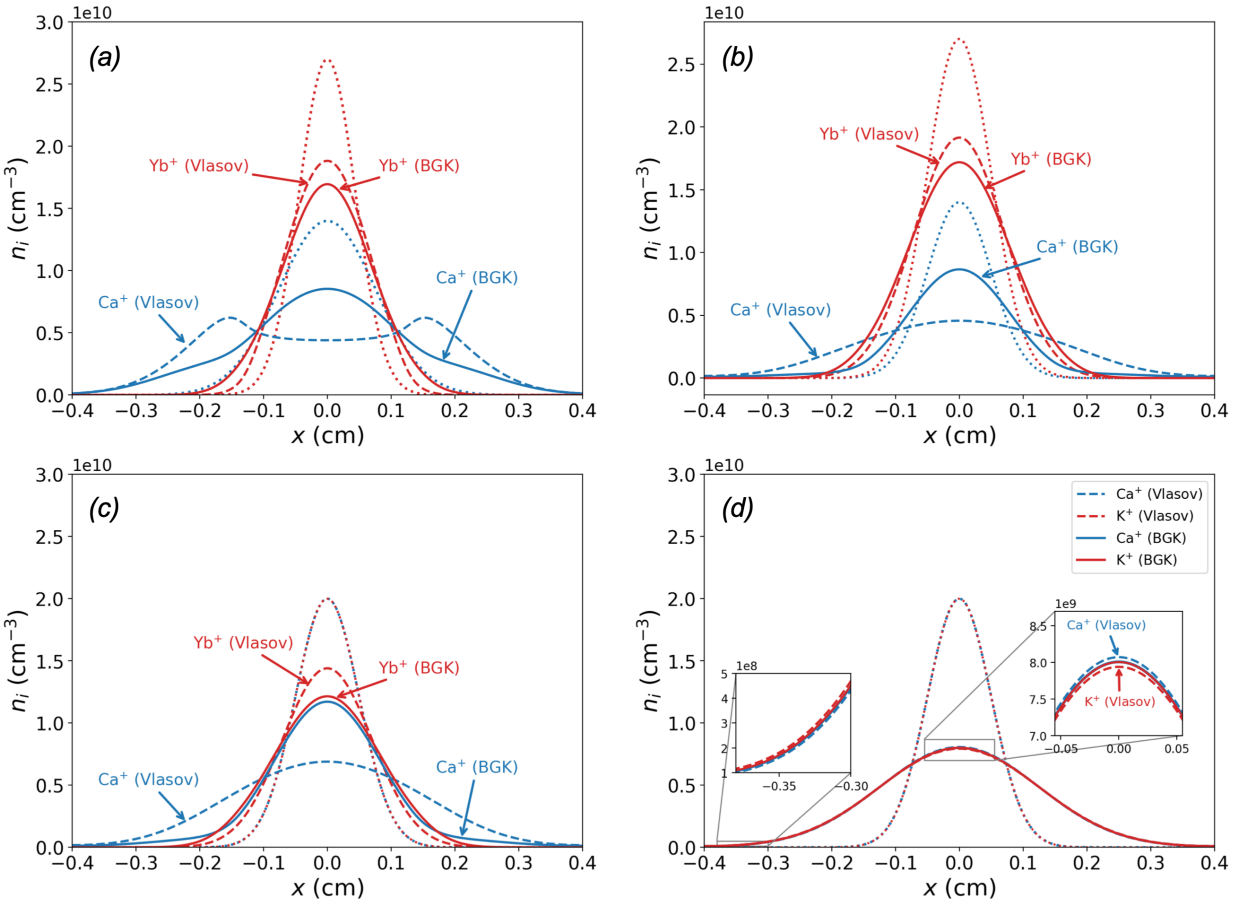

Figure 5.14: Number density profiles for UNP mixtures for the plasma conditions given by cases (a)-(d) in Table 5.3.

Lastly, we see that by picking both species to have roughly the same mass, number density, and temperature, the Vlasov and BGK agree nearly exactly. Unfortunately, no experimental data exist to validate these numerical simulations. As was the case of the time-reversible single-species UNP, it may be possible to "reverse" the dynamics of UNP mixture experiments; our numerical results suggest that the highest probability of success for time-reversible UNP mixtures is case (d) of Table 5.3. The claim of time-reversibility of the UNP mixture with conditions given by case (d) of Table 5.3 is substantiated by calculating the total entropy that is generated during these simulations. Figure 5.15 displays the total entropy source term given by Eq. (5.37) for each of the four cases in Table 5.3. Noting the scale of the colorbar for each panel, we see that the cases (a) and (b) generate roughly the same amount of entropy. In contrast, cases (c) and (d) generate considerably

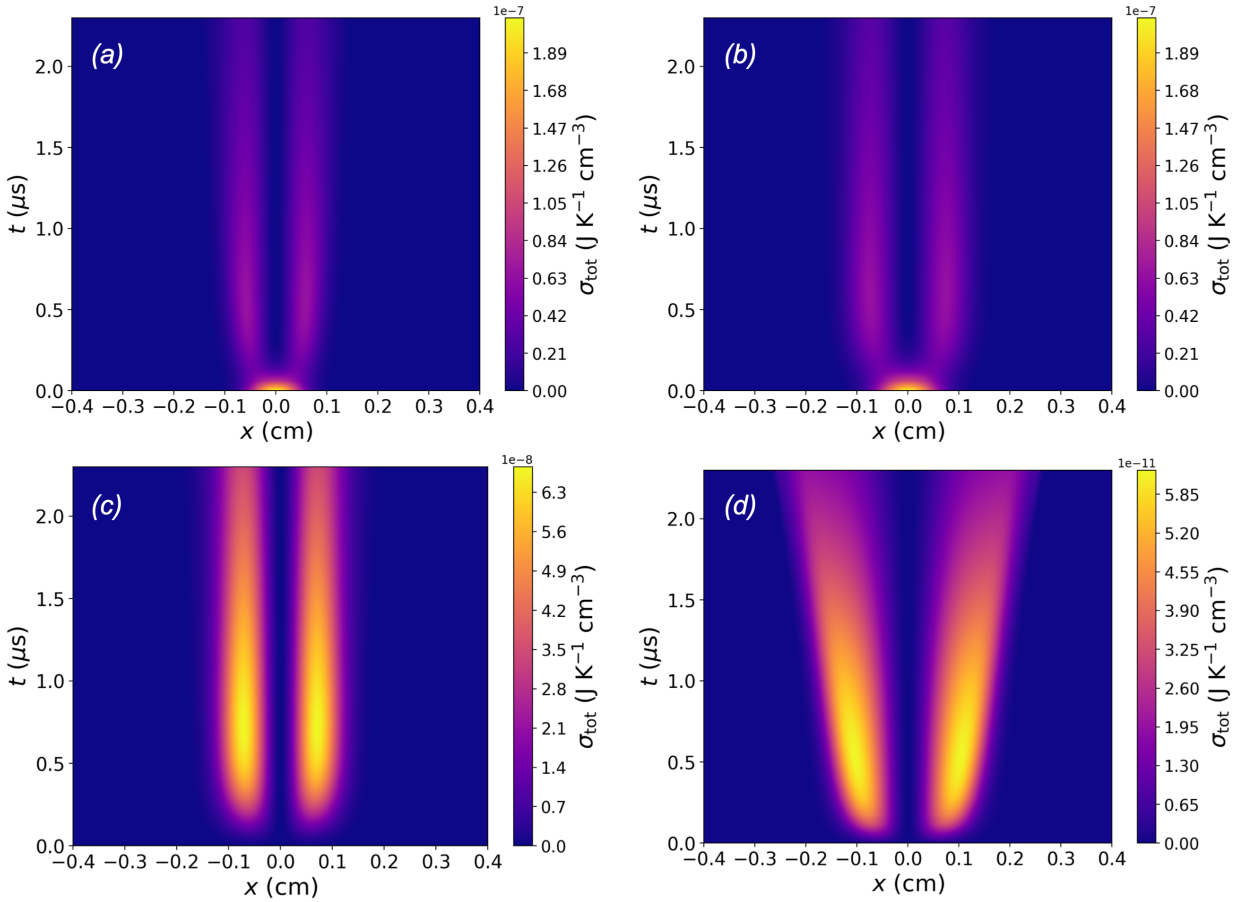

Figure 5.15: Total entropy source [Eq. (5.37)] for cases (a)-(d) in Table 5.3. Note the scale on the colorbar for each case. Cases (a) and (b) generate roughly the same amount of entropy, whereas (c) and (d) generate considerably less entropy. The amount of entropy being generated in case (d) suggests that the dynamics of the UNP mixture are time-reversible. This is further confirmed by the agreement of the Vlasov and BGK results in Fig. 5.14.

less entropy with the latter case generating roughly 4 orders of magnitude less that cases (a) and (b).

5.6.2.3 Diffusive Mixing in HED Plasmas

As illustrated by Fig. 1.1, HED plasmas are much higher in density and temperature than UNPs. However as previously mentioned there is a crossover regime at which UNPs and HED plasmas roughly share the same dimensionless parameters. Using the multi-species BGK model[4], we simulate a system that is pertinent to ongoing experiments on the Z machine at Sandia National

[4]For this section, the 1D-3V code used to simulate this work can be found at: https://github.com/lanl/Multi-BGK.

Laboratory[5]. The main goal of the experiment and the simulations of the experiments is to quantify atomic-scale mixing across an interface of between a material with high nuclear charge and a material with low nuclear charge. The initial condition is displayed in Fig. 5.16. We assume the system is periodic and is comprised of a region made up of the elements V and Al in the center that is 50 μm wide. The VAl region is surrounded on either side by a 50 μm plastic region made up of the elements C,H, and O.

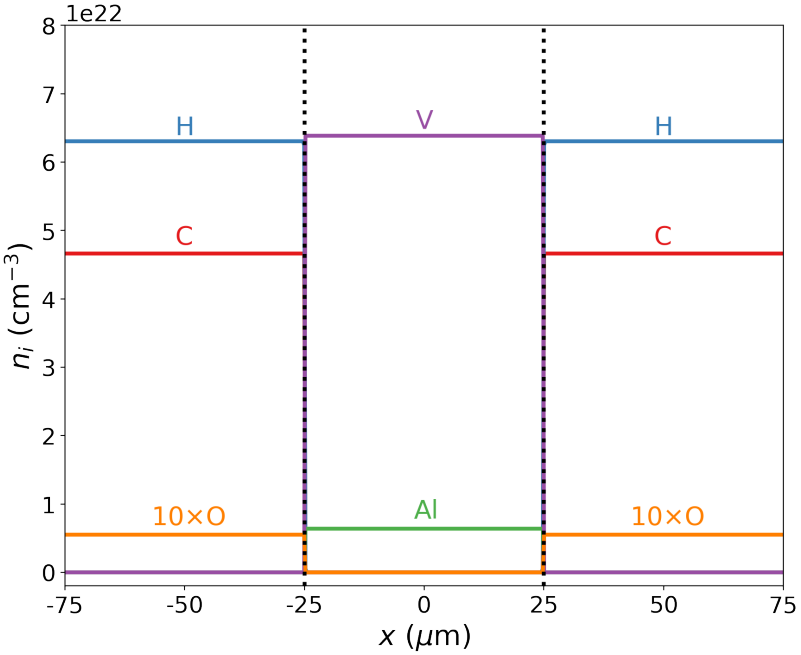

Figure 5.16: Initial condition for the 1D-3V multi-species BGK simulation. The dotted vertical lines denote the VAl/CHO interface and the number density of O has been multiplied by 10 for visual clarity.

To account for partially-degenerate electrons, we employ a linear Thomas-Fermi model [44] instead of the classical Possion-Boltzmann formula Eq. (5.94). As previously mentioned a main benefit of kinetic models is that they return an infinite number of macroscopic variables via moments of the distribution function. Additionally, in contrast to many hydrodynamic models,

[5]Sandia National Laboratories is a multimission laboratory managed and operated by National Technology & Engineering Solutions of Sandia, LLC, a wholly owned subsidiary of Honeywell International Inc., for the U.S. Department of Energy's National Nuclear Security Administration under contract DE-NA0003525. This section describes objective technical results and analysis. Any subjective views or opinions that might be expressed in this section do not necessarily represent the views of the U.S. Department of Energy or the United States Government: SAND2022-16353 T.

kinetic models allow for each species to have distinct moments which results in density, velocity and temperature fields for each species in the system. In interface mixing in particular, the need for multiple continuity, momentum, and temperature fields is crucial as the velocity fields of each species become uncoupled [44, 88].

The work done in this section is part of a much larger simulation effort at Sandia National Laboratories that also consists of radiation-hydrodynamic simulations[6]. The radiation-hydrodynamics simulations include models of radiation that ultimately turns the initial condition shown in Fig. 5.16 into a plasma. Since the current kinetic models do not directly treat radiation, we use data from the radiation-hydrodynamics simulations to estimate an electron temperature ramp that acts as an external (radiation) energy source in the kinetic simulations. The electron temperature ramps are determined from the *ion* temperature of the radiation-hydrodynamics simulations and are shown in Fig. 5.17. To obtain a functional form for the electron temperature that can be evaluated at any time, we fit ion temperature data of the VAl portion of two radiation-hydrodynamics simulations. The data follow linear trends (see Fig. 5.17) and a linear best-fit function is used as the electron temperature ramp for the electron temperature model.

[6]The radiation-hydrodynamics simulations were carried out using the ALEGRA code [286].

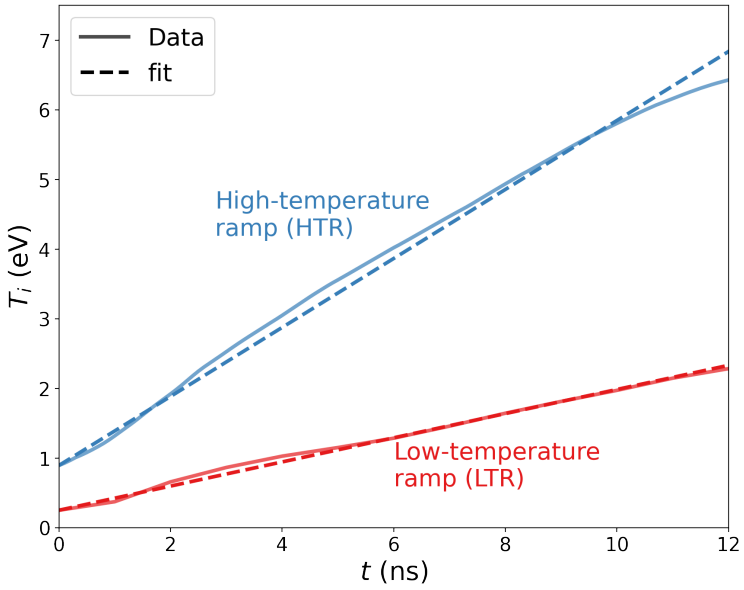

Figure 5.17: Temperature of ion species calculated from two radiation-hydrodynamics simulations. The data are shown as solid lines with linear fits denoted by dashed lines. We assume that the temperature of the electrons follows the linear trend and the linear fits are used as the electron temperature ramp in the multi-species BGK simulations.

For brevity, we denote the temperature ramp with the larger magnitude as the “high-temperature ramp" (HTR), and the temperature ramp with the lower magnitude as the “low-temperature ramp" (LTR).

The kinetic simulations have simulation length of $12ns$ and use a first-order upwinding flux; a CFL number is chosen to ensure stability. A Newton iteration was employed for determining the self-consistent electric field. For the BGK operator, we employ a collision rate given by Eq. (5.16). The density profiles at $t = 12$ ns using both the LTR and HTR are displayed in Figs. 5.18(a) and 5.18(b). We see qualitative differences between the density profiles computed with the low- and high-temperature ramps but the overall number density of each species appears to be the same in each region of both cases. For example, the amount of V in the region from $x \in [25, 75]\mu$m appears to be roughly equivalent in Figs. 5.18(a) and 5.18(b).

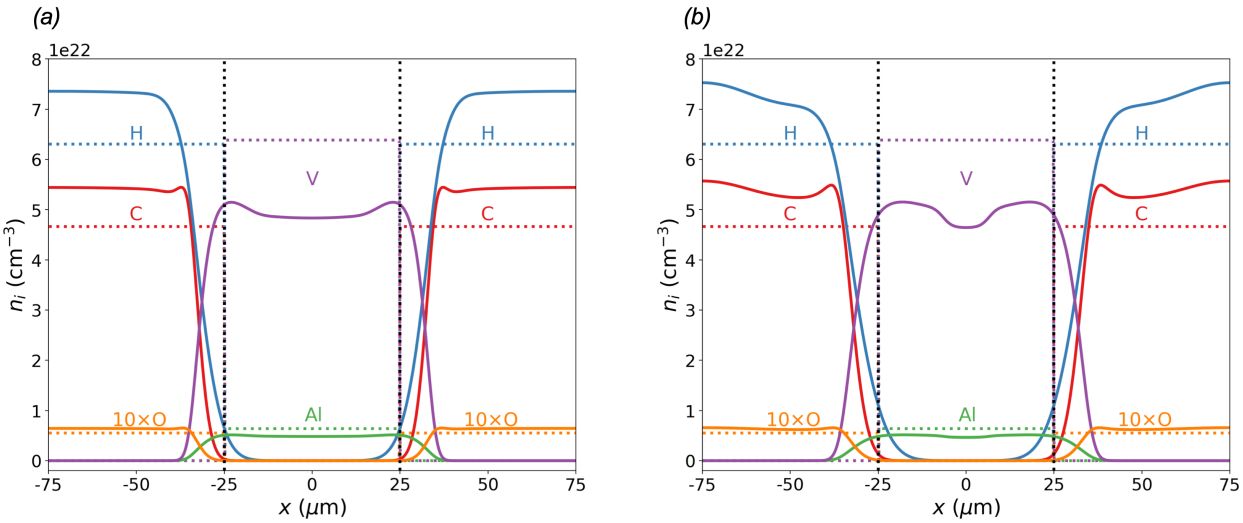

Figure 5.18: Simulation snapshot at $t = 12$ ns of the density profile with the (a) the LTR shown in Fig. 5.17 and (b) the HTR shown in Fig. 5.17. The initial condition is denoted by horizontal dotted lines and the location of the interface is shown as vertical black dotted lines.

To quantify the amount of diffusion that occurs throughout the simulation time, we introduce a metric for computing the amount of diffusion across the interfaces at $x = -25$ μm and $x = 25$ μm. The total number density of N ion species in the region of x_1 and x_2 is computed via

$$A(t) = \sum_i^N \int_{x_1}^{x_2} n_i(x,t)\, dx. \tag{5.161}$$

Using Eq. (5.161) we compute the total amount of V and Al in the region of $x \in [25, 75]\mu$m; the initial density of V and Al in this region is zero. We see that for the case of the HTR, the amount of V and Al diffuses in to the CHO region more quickly than does the case where we use the LTR. This is consistent with the fact that for higher temperatures, the diffusion will be greater. Between the time range of $t =\sim 9$ to 12 ns, we see that the amount of V and Al in the CHO region decreases and is approximately the same as the amount of diffusion using the LTR. This phenomenon is due to the periodic nature of the system; the V and Al expand outwards into the CHO region and then return to the VAl region more quickly in the HTR case.

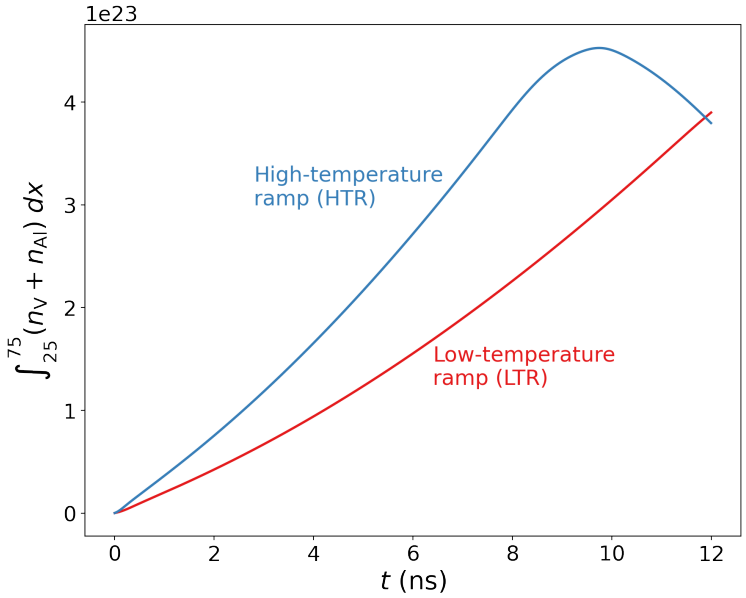

Figure 5.19: Total density of V and Al in the CHO region using the HTR and LTR. We see that the HTR results in more diffusion of the VAl species than the LTR. Due to the periodic nature of the system, the total density of VAl decreases between $t =\sim 9$ to 12 ns.

While Fig. 5.19 provides some insight into the *amount* of diffusion that has occurred during the simulation, it does not provide any insight as to what factors *caused* the diffusion to occur. To answer the question of what factors are driving the diffusion in the simulations, we consider the diffusion driving forces defined by [44]

$$\mathbf{d}_i = \nabla x_i + (x_i - y_i)\nabla \ln p + \frac{\rho_i}{p}\left(\frac{Z_i e}{m_i} - \sum_j y_j \frac{Z_j e}{m_j}\right)\mathbf{E}, \tag{5.162}$$

where $p = nT$, $\mathbf{E}$ is the electric field, and $\rho_i = m_i/n_i$ is the mass density. The atom fraction and mass fraction are given by $x_i = n_i/n$ and $y_i = \rho_i, /\rho$, respectively, with $n = \sum_i^{N_i} n_i$ and $\rho = \sum_i^{N_i} \rho_i$. The first term on the right-hand side of Eq. (5.162) corresponds to *Fickian diffusion* (diffusion due to concentration gradients), the second term corresponds to *barodiffusion* (diffusion due to pressure gradients) and the last term corresponds to *electrodiffusion* (diffusion due to electric fields).

We display the spatio-temporal evolution of the diffusion driving forces with the LTR and HTR for C [panels (a) – (c)] and V [panels (d) - (f)] in Figs. 5.20 and 5.21. A comparison of Fig. 5.20(c) and Fig. 5.21(c) highlight the periodic boundary conditions and show how the HTR causes faster diffusion than does the LTR. In both for both the HTR and LTR cases, the dominant diffusive flux

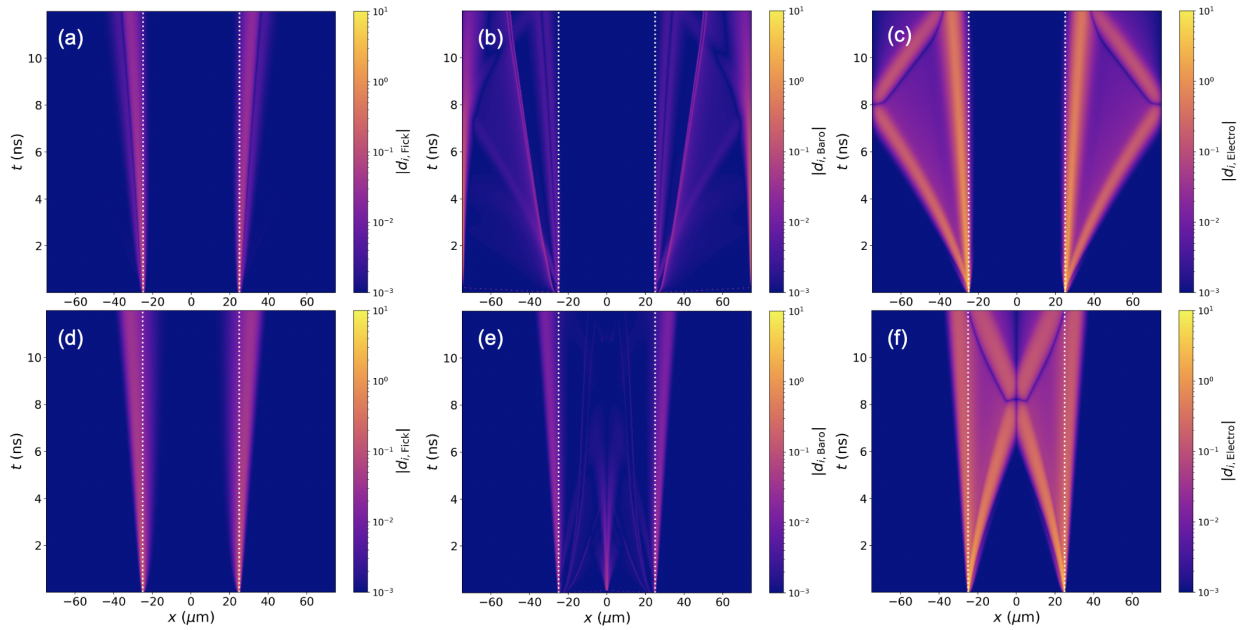

Figure 5.20: Space-time diagrams of Fickian, electro-, and barodiffusion fluxes with the LTR. (a) − (c) show the diffusive fluxes for C where (a) is the Fickian diffusion flux, (b) is the barodiffusion flux, and (c) is the electrodiffusion flux. (d) − (f) show the diffusive fluxes for V where (d) is the Fickian diffusion flux, (e) is the barodiffusion flux, and (f) is the electrodiffusion flux.

is electrodiffusion. The charge imbalance at the interface results in stron electric fields. The role that these electric fields play is that the C species in the CHO region moves away from the interface and the V species in the VAl region move toward the center of the VAl region.

5.7 Conclusions and Outlook

The focus of this chapter has been on the development and numerical implementation of kinetic models for simulating strongly coupled plasmas. We have validated our numerical scheme against data for multi-species UNP temperature data and have used our simulations to elucidate various processes in UNPs and HED plasmas. Specifically, we have been able to simulate the tail filling rate in UNPs showing that the tail filling rate is sensitive to the choice of collision operator and collision frequency. The next steps are to validate our models with experimental data.

We have also analyzed the role that collisions play in the expansion of single-species UNPs with a Gaussian initial condition. We find that the collisions rapidly drive the system to equilibrium as evidenced by the agreement of the Vlasov and BGK simulations. By carrying out explicit

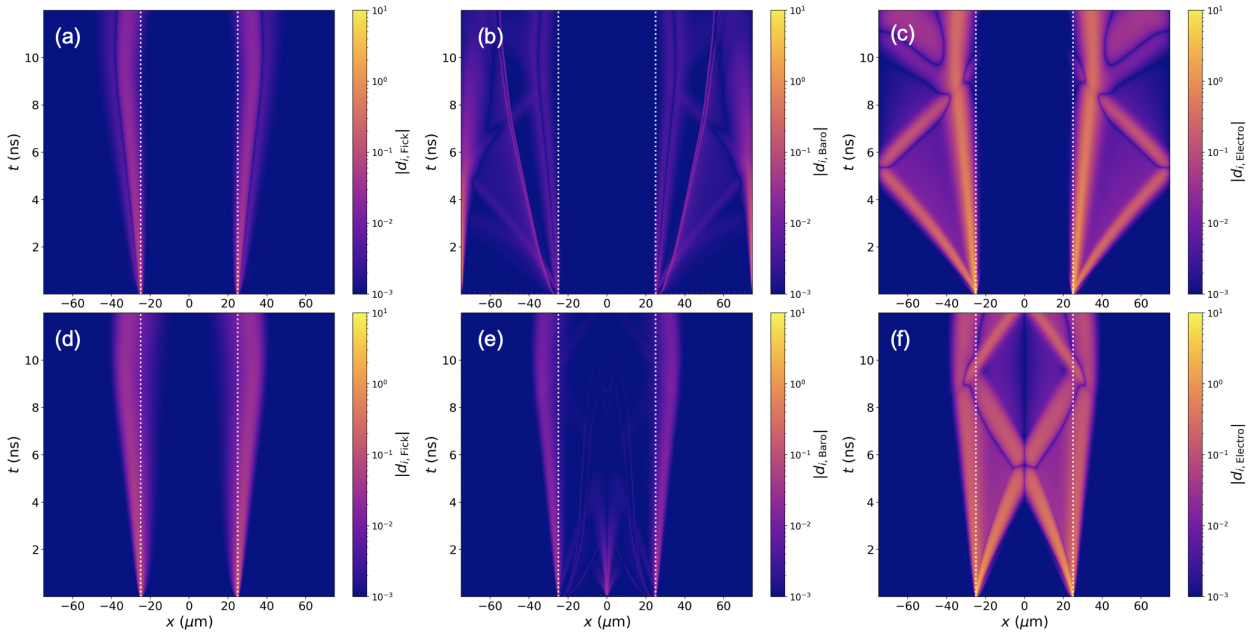

Figure 5.21: Space-time diagrams of Fickian, electro-, and barodiffusion fluxes with the HTR. (a) – (c) show the diffusive fluxes for C where (a) is the Fickian diffusion flux, (b) is the barodiffusion flux, and (c) is the electrodiffusion flux. (d) – (f) show the diffusive fluxes for V where (d) is the Fickian diffusion flux, (e) is the barodiffusion flux, and (f) is the electrodiffusion flux.

Ca^+-e simulations, we test various assumptions of analytic models for the electron temperature in a single-species UNP. We find that the spatial independence assumption is quite accurate and that the electrons can be treated adiabatically eliminating the need to explicitly simulate them.

For UNP mixtures initialized with a Gaussian profile, we find that certain plasma conditions result in self-similar expansion. Specifically, by picking two ion species with similar mass, we find that Vlasov and BGK simulations agree to within a percent. Our numerical results suggests that for this choice of plasma conditions, the UNP mixture is time-reversible like the case of single species UNPs with a Gaussian initial condition. These results can be used to guide future experimental calculations to verify our models.

Lastly, for HED plasmas relevant to experiments on the Z machine at Sandia National Laboratories, we find that the main source of diffusive mixing is due to strong electric fields that occur in regions of a sharp interface. To mitigate the diffusive mixing, specific choices of elements can be chosen to avoid a disparate charge imbalance reducing the strength of the electric field.

The results in this chapter can be expanded upon in a variety of ways. First, UNPs are often spherically symmetric which lends itself to simulations in a spherical coordinate system. As such, we have provided a derivation of the Vlasov equation in spherical coordinates, showing that there are additional terms that appear due to fictitious forces. Additionally, we have developed a second-order spherical FVM stencil (see Appendix C) in r space which still needs to be implemented numerically. In general, the numerical method provided here relies on the operator splitting technique and one improvement could be to solve the “two-dimensional" FVM directly allowing for the implementation of high-order time integrators. Moreover, an implicit time integrator could be used for the multi-species BGK collision operator allowing for larger time steps when needed.

CHAPTER 6

CONCLUSIONS AND FUTURE WORK

In this dissertation, we have presented four projects all with applications to non-ideal plasmas. The first project focused on an exhaustive benchmarking study which validated the use of simple force laws for molecular dynamics simulation of dense plasmas. The results of this work have allowed us to dismiss force laws that lack the non-parametric nature of the force-matched potentials we employed here. By using multiple metrics for comparison, we found that an agreement of time-independent properties like the radial distribution function is not sufficient for estimating the validity of force laws as compared to a Kohn-Sham MD calculation. We have also illustrated that although Kohn-Sham MD includes important physics that simpler models, results from Kohn-Sham MD can be heavily plagued by finite-size effects, introducing large amounts of statistical errors. Extensions of this work include simulations of additional elements at different densities and temperatures. This will allow for a greater understanding of the functional form of pair potentials in the warm dense matter regime. Additionally, the natural extension of this work is to apply this data-driven discovery of force laws from high-fidelity data to plasma mixtures. By obtaining pair potentials for plasma mixtures, we gain access to Kohn-Sham MD accurate pair potentials for simulating systems that are pertinent to nuclear fusion experiments.

The second project focused on deriving theoretical models for interdiffusion of binary plasma mixtures. For multiple plasma conditions, our models eliminate the need to perform costly MD simulations altogether while only incurring an error on the order of a few percent. Our closed form formulae provide accurate approximations for values that are typically ignored altogether in the MD community. Additionally, we were able to dismiss and highlight the inadequacies of the so-called “Darken formula" for the interdiffusion coefficient by highlighting its inability to converge to the true result. The culmination of the work results in a simple-to-use closed form expression for the interdiffusion in a binary ionic mixture, which is reasonably accurate in the strongly coupled regime. Extensions of this work include a more comprehensive study of the efficacy of these models for the thermodynamic factor which relies on the generation of datasets that span temperature, density,

and atomic number.

The third project focused on employing machine learning techniques for combining datasets of multiple fidelities. By applying this general machine learning framework to plasma transport coefficient data, we showed that interpolating data from multiple models ranging in fidelity results in a more accurate, confident prediction in regions absent of high-fidelity data. We highlighted the use of this framework in multiple dimensions and developed a sampling approach for high-fidelity data to reduce prediction errors. We could further extend the work done in this project by developing models which allow for more accurate extrapolation beyond the range of data based on a low-fidelity trend. Additionally, while Gaussian-process regression was the primary method used for interpolation in this project, we could explore the use of other methods such as neural networks for multi-fidelity modeling.

Lastly, the fourth project focused on developing kinetic models to simulate strongly coupled plasma mixtures. We simulated UNPs and HED plasmas using 0D and 1D kinetic simulations. Our kinetic model included the LBD collision operator, the BGK collision operator and multi-species BGK operator. We used our kinetic models to study the time evolution of single-species UNPs and UNP mixtures and also the rate of entropy production in these plasmas. By varying the initial plasma conditions, we determined plasma conditions that minimize the amount of entropy being produced suggesting that the specific UNP mixture is time-reversible. In addition, we used experimental data to validate collision rate models for the BGK operator adding confidence to their use for non-ideal plasmas. We found that in our 0D simulations that we can accurately reproduce data from MD simulation for UNP mixtures decreasing the computation cost by approximately 3000 times. By carrying out an explicit ion-electron UNP simulation, we quantified the errors associated with various approximations in analytic formulae used to approximate electrons in a UNP. We found that the temperature of the electrons in a UNP well-treated by an adiabatic mode that assumes no spatial dependence. For the HED plasmas, we simulated a plasma mixture that is relevant to ongoing interface mixing experiments on the Z machine at Sandia National Laboratory. We found that the diffusive mixing in these experiments is dominated by strong electric fields that

originate due to charge imbalances between the species on either side of the interface. Although much of this work in this project is numerical, we have used our results to suggest experimental cases to further validate our models. Extensions of this work could be to include the electrons as an explicit species in the BGK model to examine their contribution to the amount of entropy being generated. Moreover, we can connect the rate of entropy production to the various thermodynamic forces driving the system to equilibrium in order to determine the dominant transport processes in UNPs.

BIBLIOGRAPHY

[1] I Adamovich, S Agarwal, E Ahedo, LL Alves, S Baalrud, N Babaeva, A Bogaerts, A Bourdon, PJ Bruggeman, C Canal, et al. The 2022 plasma roadmap: low temperature plasma science and technology. *Journal of Physics D: Applied Physics*, 55(37):373001, 2022.

[2] Peter LG Ventzek, Timothy J Sommerer, Robert J Hoekstra, and Mark J Kushner. Two-dimensional hybrid model of inductively coupled plasma sources for etching. *Applied physics letters*, 63(5):605–607, 1993.

[3] Thomas C. Killian. Ultracold neutral plasmas. *Science*, 316(5825):705–708, 2007.

[4] AB Zylstra, OA Hurricane, DA Callahan, AL Kritcher, JE Ralph, HF Robey, JS Ross, CV Young, KL Baker, DT Casey, et al. Burning plasma achieved in inertial fusion. *Nature*, 601(7894):542–548, 2022.

[5] H. F. Robey, L. Berzak Hopkins, J. L. Milovich, and N. B. Meezan. The I-Raum: A new shaped hohlraum for improved inner beam propagation in indirectly-driven ICF implosions on the National Ignition Facility. *Physics of Plasmas*, 25(1):012711, 2018.

[6] Abu-Shawareb et al. Lawson criterion for ignition exceeded in an inertial fusion experiment. *Phys. Rev. Lett.*, 129:075001, Aug 2022.

[7] Setsuo Ichimaru. Strongly coupled plasmas: high-density classical plasmas and degenerate electron liquids. *Reviews of Modern Physics*, 54(4):1017, 1982.

[8] Setsuo Ichimaru. *Statistical plasma physics: basic principles*. CRC Press, 2018.

[9] Michael S Murillo. Strongly coupled plasma physics and high energy-density matter. *Physics of Plasmas*, 11(5):2964–2971, 2004.

[10] S Hamaguchi, RT Farouki, and DHE Dubin. Triple point of Yukawa systems. *Physical Review E*, 56(4):4671, 1997.

[11] Michael S Murillo and Jon C Weisheit. Dense plasmas, screened interactions, and atomic ionization. *Physics Reports*, 302(1):1–65, 1998.

[12] Michael S Murillo, Jon Weisheit, Stephanie B Hansen, and MWC Dharma-Wardana. Partial ionization in dense plasmas: Comparisons among average-atom density functional models. *Physical Review E*, 87(6):063113, 2013.

[13] Li Dan, Li-Xin Guo, and Jiang-Ting Li. Propagation characteristics of electromagnetic waves in dusty plasma with full ionization. *Physics of Plasmas*, 25(1):013707, 2018.

[14] István Donkó, Peter Hartmann, and Zoltán Donkó. Molecular dynamics simulation of a two-dimensional dusty plasma. *American Journal of Physics*, 87(12):986–993, 2019.

[15] Scott D Bergeson, Scott D Baalrud, C Leland Ellison, Edward Grant, Frank R Graziani, Thomas C Killian, Michael S Murillo, Jacob L Roberts, and Liam G Stanton. Exploring the crossover between high-energy-density plasma and ultracold neutral plasma physics. *Physics of Plasmas*, 26(10):100501, 2019.

[16] T Ott, M Bonitz, LG Stanton, and MS Murillo. Coupling strength in Coulomb and Yukawa one-component plasmas. *Physics of Plasmas*, 21(11):113704, 2014.

[17] T Saigo and S Hamaguchi. Shear viscosity of strongly coupled Yukawa systems. *Physics of Plasmas*, 9(4):1210–1216, 2002.

[18] RT Farouki and S Hamaguchi. Thermodynamics of strongly-coupled yukawa systems near the one-component-plasma limit. ii. molecular dynamics simulations. *The Journal of chemical physics*, 101(11):9885–9893, 1994.

[19] P Seuferling, J Vogel, and C Toepffer. Correlations in a two-temperature plasma. *Physical Review A*, 40(1):323, 1989.

[20] Setsuo Ichimaru. *Statistical Plasma Physics: Volume II: Condensed Plasmas*. CRC Press, 2018.

[21] Manuel Torrilhon. Modeling nonequilibrium gas flow based on moment equations. *Annual review of fluid mechanics*, 48:429–458, 2016.

[22] Enrico Fermi, P Pasta, Stanislaw Ulam, and Mary Tsingou. Studies of the nonlinear problems. Technical report, Los Alamos National Lab.(LANL), Los Alamos, NM (United States), 1955.

[23] Daan Frenkel and Berend Smit. *Understanding molecular simulation: from algorithms to applications*, volume 1. Elsevier, 2001.

[24] R Tucker Sprenkle, LG Silvestri, MS Murillo, and SD Bergeson. Temperature relaxation in strongly-coupled binary ionic mixtures. *Nature communications*, 13(1):1–9, 2022.

[25] Luís FM Franco, Marcelo Castier, and Ioannis G Economou. Anisotropic parallel self-diffusion coefficients near the calcite surface: A molecular dynamics study. *The Journal of Chemical Physics*, 145(8):084702, 2016.

[26] Rajdeep Singh Payal and Sundaram Balasubramanian. Homogenous mixing of ionic liquids: molecular dynamics simulations. *Physical Chemistry Chemical Physics*, 15(48):21077–21083, 2013.

[27] F El-Hajjaji, M Messali, A Aljuhani, MR Aouad, B Hammouti, ME Belghiti, DS Chauhan, and MA Quraishi. Pyridazinium-based ionic liquids as novel and green corrosion inhibitors of carbon steel in acid medium: electrochemical and molecular dynamics simulation studies. *Journal of Molecular Liquids*, 249:997–1008, 2018.

[28] Vikram S Dharodi and Michael S Murillo. Sculpted ultracold neutral plasmas. *Physical Review E*, 101(2):023207, 2020.

[29] R Ayllon, H Terças, and JT Mendonça. Electron trapping in freely expanding ultracold neutral plasmas. *Physics of Plasmas*, 26(3):033501, 2019.

[30] D Murphy and BM Sparkes. Disorder-induced heating of ultracold neutral plasmas created from atoms in partially filled optical lattices. *Physical Review E*, 94(2):021201, 2016.

[31] BB Zelener, BV Zelener, EA Manykin, S Ya Bronin, AA Bobrov, and DR Khikhlukha. Self-diffusion and conductivity in an ultracold strongly coupled plasma: Calculation by the method of molecular dynamics. In *Journal of Physics: Conference Series*, volume 946, page 012126. IOP Publishing, 2018.

[32] HY Sun, Dongdong Kang, Yong Hou, and JY Dai. Transport properties of warm and hot dense iron from orbital free and corrected Yukawa potential molecular dynamics. *Matter and radiation at extremes*, 2(6):287, 2018.

[33] Alexander V Sidorenkov, Sergey V Kolesnikov, and Alexander M Saletsky. Molecular dynamics simulation of graphene on Cu (111) with different Lennard-Jones parameters. *The European Physical Journal B*, 89(10):1–7, 2016.

[34] A Ansari Dezfoli, MA Mehrabian, and H Hashemipour. Molecular dynamics simulation of heavy metal ions in aqueous solution using Lennard-Jones 12-6 potential. *Chemical Engineering Communications*, 202(12):1685–1692, 2015.

[35] Chengping Wu and Leonid V Zhigilei. Microscopic mechanisms of laser spallation and ablation of metal targets from large-scale molecular dynamics simulations. *Applied Physics A*, 114(1):11–32, 2014.

[36] R Ravelo, TC Germann, O Guerrero, Q An, and BL Holian. Shock-induced plasticity in tantalum single crystals: Interatomic potentials and large-scale molecular-dynamics simulations. *Physical Review B*, 88(13):134101, 2013.

[37] Joseph E Basconi and Michael R Shirts. Effects of temperature control algorithms on transport properties and kinetics in molecular dynamics simulations. *Journal of chemical theory and computation*, 9(7):2887–2899, 2013.

[38] Donatas Surblys, Frédéric Leroy, Yasutaka Yamaguchi, and Florian Müller-Plathe. Molecular dynamics analysis of the influence of Coulomb and van der Waals interactions on the work of adhesion at the solid-liquid interface. *The Journal of chemical physics*, 148(13):134707, 2018.

[39] Oscar Buneman. Dissipation of currents in ionized media. *Physical Review*, 115(3):503, 1959.

[40] John Dawson. One-dimensional plasma model. *The Physics of Fluids*, 5(4):445–459, 1962.

[41] John M Dawson. Particle simulation of plasmas. *Reviews of modern physics*, 55(2):403, 1983.

[42] Francis H Harlow. PIC and its progeny. *Computer Physics Communications*, 48(1):1–10, 1988.

[43] Charles K Birdsall and A Bruce Langdon. *Plasma physics via computer simulation*. CRC press, 2018.

[44] Jeffrey R Haack, Cory D Hauck, and Michael S Murillo. Interfacial mixing in high-energy-density matter with a multiphysics kinetic model. *Physical Review E*, 96(6):063310, 2017.

[45] Atul Kumar and Juan F Caneses Marin. Kinetic simulations of collision-less plasmas in open magnetic geometries. *Plasma Physics and Controlled Fusion*, 64(3):035012, 2022.

[46] Janez Krek, Yangyang Fu, Guy M. Parsey, and John P. Verboncoeur. Benchmark of the KGMf with a coupled Boltzmann equation solver. *Computer Physics Communications*, 260:107748, 2021.

[47] Vladimir Kolobov, Robert Arslanbekov, and Dmitry Levko. Boltzmann-Fokker-Planck kinetic solver with adaptive mesh in phase space. In *AIP Conference Proceedings*, volume 2132, page 060011. AIP Publishing LLC, 2019.

[48] Kentaro Hara, Iain D Boyd, and Vladimir I Kolobov. One-dimensional hybrid-direct kinetic simulation of the discharge plasma in a hall thruster. *Physics of Plasmas*, 19(11):113508, 2012.

[49] N Moschuering, KV Lotov, K Bamberg, F Deutschmann, and H Ruhl. First fully kinetic three-dimensional simulation of the AWAKE baseline scenario. *Plasma Physics and Controlled Fusion*, 61(10):104004, 2019.

[50] SN Razavinia and M Ghorbanalilu. Semi-Lagrangian Vlasov simulation of the interaction between femtosecond chirped and double laser pulses with a thin plasma slab. *Plasma Physics and Controlled Fusion*, 62(4):045007, 2020.

[51] A Schmidt, V Tang, and D Welch. Fully kinetic simulations of dense plasma focus z-pinch devices. *Physical review letters*, 109(20):205003, 2012.

[52] Alex Friedman, Ronald H Cohen, David P Grote, Steven M Lund, William M Sharp, Jean-Luc Vay, Irving Haber, and Rami A Kishek. Computational methods in the warp code framework for kinetic simulations of particle beams and plasmas. *IEEE Transactions on Plasma Science*, 42(5):1321–1334, 2014.

[53] Ari Le, Thomas JT Kwan, Mark J Schmitt, Hans W Herrmann, and Steven H Batha. Simulation and assessment of ion kinetic effects in a direct-drive capsule implosion experiment. *Physics of Plasmas*, 23(10):102705, 2016.

[54] C Bellei, H Rinderknecht, A Zylstra, M Rosenberg, H Sio, CK Li, R Petrasso, SC Wilks, and PA Amendt. Species separation and kinetic effects in collisional plasma shocks. *Physics of Plasmas*, 21(5):056310, 2014.

[55] DW Hill and RJ Kingham. Enhancement of pressure perturbations in ablation due to kinetic magnetized transport effects under direct-drive inertial confinement fusion relevant conditions. *Physical Review E*, 98(2):021201, 2018.

[56] M Sherlock and JJ Bissell. Suppression of the Biermann battery and stabilization of the thermomagnetic instability in laser fusion conditions. *Physical Review Letters*, 124(5):055001, 2020.

[57] A Schmidt, A Link, D Welch, J Ellsworth, S Falabella, and V Tang. Comparisons of dense-plasma-focus kinetic simulations with experimental measurements. *Physical Review E*, 89(6):061101, 2014.

[58] Linchun Wu, Mike Phillips, Sarah Messer, Andrew Case, and F Douglas Witherspoon. Numerical simulation of merging plasma jets using high-z gases. *IEEE Transactions on Plasma Science*, 41(4):1011–1017, 2013.

[59] F Douglas Witherspoon, Dale R Welch, John R Thompson, Joeseph J MacFarlane, Michael W Phillips, Nicki Bruner, Chris Mostrom, Carsten Thoma, RE Clark, Nick Bogatu, et al. Development and benchmarking of a hybrid pic code for dense plasmas and fast ignition. Technical report, HyperV Technologies Corp., 2014.

[60] Carsten Thoma, RE Clark, DR Welch, and SC Hsu. Numerical simulations of collisionless shock formation in merging plasma jet experiments. In *2013 19th IEEE Pulsed Power Conference (PPC)*, pages 1–6. IEEE, 2013.

[61] Katerina Falk, Milan Holec, Christopher John Fontes, Christopher Lee Fryer, Carl William Greeff, Heather Marie Johns, DS Montgomery, Derek William Schmidt, and M Šmíd.

Measurement of preheat due to nonlocal electron transport in warm dense matter. *Physical Review Letters*, 120(2):025002, 2018.

[62] A Skoulakis, G Koundourakis, A Ciardi, E Kaselouris, I Fitilis, J Chatzakis, M Bakarezos, N Vlahakis, NA Papadogiannis, M Tatarakis, et al. High performance simulations of a single X-pinch. *Plasma Physics and Controlled Fusion*, 64(2):025003, 2021.

[63] Ryan D McBride, Stephen A Slutz, Christopher A Jennings, DB Sinars, Michael Edward Cuneo, MC Herrmann, Raymond William Lemke, MR Martin, Roger A Vesey, KJ Peterson, et al. Penetrating radiography of imploding and stagnating beryllium liners on the Z accelerator. *Physical review letters*, 109(13):135004, 2012.

[64] Paul T Campbell, Christopher A Walsh, Brandon K Russell, Jeremy P Chittenden, Aidan Crilly, Gennady Fiksel, Philip M Nilson, Alexander GR Thomas, Karl Krushelnick, and Louise Willingale. Magnetic signatures of radiation-driven double ablation fronts. *Physical Review Letters*, 125(14):145001, 2020.

[65] B Jones, Christopher Deeney, John Lee McKenney, Christopher Joseph Garasi, Thomas Alan Mehlhorn, Allen Conrad Robinson, Scott Edward Wunsch, Simon Nicholas Bland, Sergey V Lebedev, Jeremy Paul Chittenden, et al. Study of three-dimensional structure in wire-array z pinches by controlled seeding of axial modulations in wire radius. *Physical review letters*, 95(22):225001, 2005.

[66] RJ Shalloo, C Arran, L Corner, J Holloway, J Jonnerby, R Walczak, HM Milchberg, and SM Hooker. Hydrodynamic optical-field-ionized plasma channels. *Physical Review E*, 97(5):053203, 2018.

[67] Dae-Won Cho, Woo-Hyun Song, Min-Hyun Cho, and Suck-Joo Na. Analysis of submerged arc welding process by three-dimensional computational fluid dynamics simulations. *Journal of Materials Processing Technology*, 213(12):2278–2291, 2013.

[68] Hang Zhao, Zhichao Li, Dong Yang, Xin Li, Yaohua Chen, Xiaohua Jiang, Yonggang Liu, Tao Gong, Liang Guo, Sanwei Li, et al. Progress in optical Thomson scattering diagnostics for ICF gas-filled hohlraums. *Matter and Radiation at Extremes*, 4(5):055201, 2019.

[69] TR Dittrich, OA Hurricane, DA Callahan, EL Dewald, T Döppner, DE Hinkel, LF Berzak Hopkins, S Le Pape, T Ma, JL Milovich, et al. Design of a high-foot high-adiabat ICF capsule for the National Ignition Facility. *Physical review letters*, 112(5):055002, 2014.

[70] E. Vold, R. Rauenzahn, and A. N. Simakov. Multi-species plasma transport in 1D direct-drive ICF simulations. *Physics of Plasmas*, 26(3):032706, 2019.

[71] AJ Harvey-Thompson, M Geissel, CA Jennings, MR Weis, MR Gomez, JR Fein, DJ Ampleford, GA Chandler, ME Glinsky, KD Hahn, et al. Constraining preheat energy deposition in

MagLIF experiments with multi-frame shadowgraphy. *Physics of Plasmas*, 26(3):032707, 2019.

[72] M Meziane, Olivier Eichwald, JP Sarrette, Olivier Ducasse, Mohammed Yousfi, and Frédéric Marchal. Electro-hydrodynamics and kinetic modelling of polluted air flow activated by multi-tip-to-plane corona discharge. *Journal of Applied Physics*, 113(15):153302, 2013.

[73] Chanchal Loha, Himadri Chattopadhyay, and Pradip K Chatterjee. Euler-Euler CFD modeling of fluidized bed: Influence of specularity coefficient on hydrodynamic behavior. *Particuology*, 11(6):673–680, 2013.

[74] Manuel Krauß and Roland Rzehak. Reactive absorption of CO2 in NaOH: An Euler-Euler simulation study. *Chemical Engineering Science*, 181:199–214, 2018.

[75] A Sahai, NN Mansour, B Lopez, and M Panesi. Modeling of high pressure arc-discharge with a fully-implicit Navier–Stokes stabilized finite element flow solver. *Plasma Sources Science and Technology*, 26(5):055012, 2017.

[76] C. R. Weber, D. S. Clark, A. W. Cook, D. C. Eder, S. W. Haan, B. A. Hammel, D. E. Hinkel, O. S. Jones, M. M. Marinak, J. L. Milovich, P. K. Patel, H. F. Robey, J. D. Salmonson, S. M. Sepke, and C. A. Thomas. Three-dimensional hydrodynamics of the deceleration stage in inertial confinement fusion. *Physics of Plasmas*, 22(3):032702, 2015.

[77] Chris Orban, Milad Fatenejad, Sugreev Chawla, Scott C Wilks, and Donald Q Lamb. A radiation-hydrodynamics code comparison for laser-produced plasmas: FLASH versus HYDRA and the results of validation experiments. *arXiv preprint arXiv:1306.1584*, 2013.

[78] David J Strozzi, LJ Perkins, MM Marinak, DJ Larson, JM Koning, and BG Logan. Imposed magnetic field and hot electron propagation in inertial fusion hohlraums. *Journal of Plasma Physics*, 81(6), 2015.

[79] Kelly Machado, Didier Zanghi, Vincent Sarou-Kanian, Sylvian Cadars, Mario Burbano, Mathieu Salanne, and Catherine Bessada. Study of NaF–AlF3 Melts by Coupling Molecular Dynamics, Density Functional Theory, and NMR Measurements. *The Journal of Physical Chemistry C*, 121(19):10289–10297, 2017.

[80] Mandy Bethkenhagen, Abhiraj Sharma, Phanish Suryanarayana, John E Pask, Babak Sadigh, and Sebastien Hamel. Thermodynamic, structural, and transport properties of dense carbon up to 10 million Kelvin from Kohn-Sham density functional theory calculations. *arXiv preprint arXiv:2110.01034*, 2021.

[81] Martin French, Gerd Röpke, Maximilian Schörner, Mandy Bethkenhagen, Michael P Desjarlais, and Ronald Redmer. Electronic transport coefficients from density functional theory across the plasma plane. *Physical Review E*, 105(6):065204, 2022.

[82] Jeremy Rabone, Eddie Lopez-Honorato, and Paul Van Uffelen. Silver and cesium diffusion dynamics at the β-SiC Σ5 grain boundary investigated with density functional theory molecular dynamics and metadynamics. *The Journal of Physical Chemistry A*, 118(5):915–926, 2014.

[83] Travis Sjostrom and Jérôme Daligault. Ionic and electronic transport properties in dense plasmas by orbital-free density functional theory. *Physical Review E*, 92(6):063304, 2015.

[84] Noel Jakse and Alain Pasturel. Liquid aluminum: Atomic diffusion and viscosity from ab initio molecular dynamics. *Scientific Reports*, 3(1):1–8, 2013.

[85] Martin French and Thomas R Mattsson. Thermoelectric transport properties of molybdenum from ab initio simulations. *Physical Review B*, 90(16):165113, 2014.

[86] Justin B Haskins, Charles W Bauschlicher Jr, and John W Lawson. Ab initio simulations and electronic structure of lithium-doped ionic liquids: structure, transport, and electrochemical stability. *The Journal of Physical Chemistry B*, 119(46):14705–14719, 2015.

[87] Lucas J Stanek, Raymond C Clay III, MWC Dharma-Wardana, Mitchell A Wood, Kristian RC Beckwith, and Michael S Murillo. Efficacy of the radial pair potential approximation for molecular dynamics simulations of dense plasmas. *Physics of Plasmas*, 28(3):032706, 2021.

[88] LG Stanton, JN Glosli, and MS Murillo. Multiscale molecular dynamics model for heterogeneous charged systems. *Physical Review X*, 8(2):021044, 2018.

[89] TG White, S Richardson, BJB Crowley, LK Pattison, JWO Harris, and G Gregori. Orbital-free density-functional theory simulations of the dynamic structure factor of warm dense aluminum. *Physical review letters*, 111(17):175002, 2013.

[90] Mohan Chen, Xiang-Wei Jiang, Houlong Zhuang, Lin-Wang Wang, and Emily A Carter. Petascale orbital-free density functional theory enabled by small-box algorithms. *Journal of chemical theory and computation*, 12(6):2950–2963, 2016.

[91] C Ticknor, SD Herring, F Lambert, LA Collins, and JD Kress. First principles nonequilibrium plasma mixing. *Physical Review E*, 89(1):013108, 2014.

[92] Jean Clérouin, Philippe Arnault, Benoit-Joseph Gréa, Sébastien Guisset, Marc Vandenboomgaerde, Alexander J White, Lee A Collins, Joel D Kress, and Christopher Ticknor. Static and dynamic properties of multi-ionic plasma mixtures. *Physical Review E*, 101(3):033207, 2020.

[93] Haoyu S Yu, Shaohong L Li, and Donald G Truhlar. Perspective: Kohn-Sham density functional theory descending a staircase. *The Journal of chemical physics*, 145(13):130901, 2016.

[94] William C Witt, G Beatriz, Johannes M Dieterich, and Emily A Carter. Orbital-free density functional theory for materials research. *Journal of Materials Research*, 33(7):777–795, 2018.

[95] Jouko Lehtomäki, Ilja Makkonen, Miguel A Caro, Ari Harju, and Olga Lopez-Acevedo. Orbital-free density functional theory implementation with the projector augmented-wave method. *The Journal of Chemical Physics*, 141(23):234102, 2014.

[96] Valentin V Karasiev, Debajit Chakraborty, Olga A Shukruto, and SB Trickey. Nonempirical generalized gradient approximation free-energy functional for orbital-free simulations. *Physical Review B*, 88(16):161108, 2013.

[97] Qianrui Liu, Denghui Lu, and Mohan Chen. Structure and dynamics of warm dense aluminum: a molecular dynamics study with density functional theory and deep potential. *Journal of Physics: Condensed Matter*, 32(14):144002, 2020.

[98] Joseph J Williams, Gautham Dharuman, Mathieu Marciante, James Hamilton Cooley, and Michael S Murillo. Bump-on-tail instability across coupling and interaction-range regimes. *Physical Review Research*, 1(3):033166, 2019.

[99] C. E. Starrett, J. Clérouin, V. Recoules, J. D. Kress, L. A. Collins, and D. E. Hanson. Average atom transport properties for pure and mixed species in the hot and warm dense matter regimes. *Physics of Plasmas*, 19(10):102709, 2012.

[100] David E. Hanson, Lee A. Collins, Joel D. Kress, and Michael P. Desjarlais. Calculations of the thermal conductivity of National Ignition Facility target materials at temperatures near 10 eV and densities near 10 g/cc using finite-temperature quantum molecular dynamics. *Physics of Plasmas*, 18(8):082704, 2011.

[101] J Vorberger and DO Gericke. Effective ion–ion potentials in warm dense matter. *High Energy Density Physics*, 9(1):178–186, 2013.

[102] Yong Hou, Jiayu Dai, Dongdong Kang, Wen Ma, and Jianmin Yuan. Equations of state and transport properties of mixtures in the warm dense regime. *Physics of Plasmas*, 22(2):022711, 2015.

[103] K Wünsch, J Vorberger, and DO Gericke. Ion structure in warm dense matter: Benchmarking solutions of hypernetted-chain equations by first-principle simulations. *Physical Review E*, 79(1):010201, 2009.

[104] LG Stanton and MS Murillo. Unified description of linear screening in dense plasmas. *Physical Review E*, 91(3):033104, 2015.

[105] WD Wilson, LG Haggmark, and JP Biersack. Calculations of nuclear stopping, ranges, and straggling in the low-energy region. *Physical Review B*, 15(5):2458, 1977.

[106] Louis Harbour, MWC Dharma-Wardana, Dennis D Klug, and Laurent J Lewis. Pair potentials for warm dense matter and their application to x-ray thomson scattering in aluminum and beryllium. *Physical Review E*, 94(5):053211, 2016.

[107] MWC Dharma-Wardana. Electron-ion and ion-ion potentials for modeling warm dense matter: Applications to laser-heated or shock-compressed Al and Si. *Physical Review E*, 86(3):036407, 2012.

[108] François Perrot and MWC Dharma-Wardana. Equation of state and transport properties of an interacting multispecies plasma: Application to a multiply ionized al plasma. *Physical Review E*, 52(5):5352, 1995.

[109] L Harbour, GD Förster, MWC Dharma-Wardana, and Laurent J Lewis. Ion-ion dynamic structure factor, acoustic modes, and equation of state of two-temperature warm dense aluminum. *Physical review E*, 97(4):043210, 2018.

[110] Timothy C Germann and Kai Kadau. Trillion-atom molecular dynamics becomes a reality. *International Journal of Modern Physics C*, 19(09):1315–1319, 2008.

[111] Wolfgang Eckhardt, Alexander Heinecke, Reinhold Bader, Matthias Brehm, Nicolay Hammer, Herbert Huber, Hans-Georg Kleinhenz, Jadran Vrabec, Hans Hasse, Martin Horsch, Martin Bernreuther, Colin W. Glass, Christoph Niethammer, Arndt Bode, and Hans-Joachim Bungartz. 591 TFLOPS multi-trillion particles simulation on SuperMUC, 2013.

[112] Alexander Heinecke, Wolfgang Eckhardt, Martin Horsch, and Hans-Joachim Bungartz. Supercomputing for molecular dynamics simulations: Handling multi-trillion particles in nanofluidics, 2015.

[113] Aldo Glielmo, Claudio Zeni, and Alessandro De Vita. Efficient nonparametric n-body force fields from machine learning. *Physical Review B*, 97(18):184307, 2018.

[114] Stefan Chmiela, Huziel E Sauceda, Klaus-Robert Müller, and Alexandre Tkatchenko. Towards exact molecular dynamics simulations with machine-learned force fields. *Nature communications*, 9(1):1–10, 2018.

[115] Jonathan Schmidt, Mário RG Marques, Silvana Botti, and Miguel AL Marques. Recent advances and applications of machine learning in solid-state materials science. *npj Computational Materials*, 5(1):1–36, 2019.

[116] G. Kresse and J. Hafner. Ab initio molecular dynamics for liquid metals. *Phys. Rev. B*, 47:558–561, Jan 1993.

[117] G. Kresse and J. Furthmüller. Efficiency of ab initio total energy calculations for metals and semiconductors using a plane-wave basis set. *Computational Materials Science*, 6(1):15 – 50, 1996.

[118] G. Kresse and J. Furthmüller. Efficient iterative schemes for ab initio total-energy calculations using a plane-wave basis set. *Phys. Rev. B*, 54:11169–11186, Oct 1996.

[119] G. Kresse and D. Joubert. From ultrasoft pseudopotentials to the projector augmented-wave method. *Phys. Rev. B*, 59:1758–1775, Jan 1999.

[120] John P. Perdew, Kieron Burke, and Matthias Ernzerhof. Generalized gradient approximation made simple. *Phys. Rev. Lett.*, 77:3865–3868, Oct 1996.

[121] P. E. Blöchl. Projector augmented-wave method. *Phys. Rev. B*, 50:17953–17979, Dec 1994.

[122] Lars Hedin. New method for calculating the one-particle green's function with application to the electron-gas problem. *Physical Review*, 139(3A):A796, 1965.

[123] A. Baldereschi. Mean-value point in the brillouin zone. *Phys. Rev. B*, 7:5212–5215, Jun 1973.

[124] Furio Ercolessi and James B Adams. Interatomic potentials from first-principles calculations: the force-matching method. *EPL (Europhysics Letters)*, 26(8):583, 1994.

[125] Michael P Allen and Dominic J Tildesley. Computer simulation of liquids, 2017.

[126] Sergei Izvekov, Michele Parrinello, Christian J Burnham, and Gregory A Voth. Effective force fields for condensed phase systems from ab initio molecular dynamics simulation: A new method for force-matching. *The Journal of chemical physics*, 120(23):10896–10913, 2004.

[127] P. Brommer and F. Gähler. Effective potentials for quasicrystals from ab-initio data. *Philosophical Magazine*, 86(6-8):753–758, 2006.

[128] Peter Brommer and Franz Gähler. Potfit: effective potentials from ab initio data. *Modelling and Simulation in Materials Science and Engineering*, 15(3):295, 2007.

[129] Peter Brommer, Alexander Kiselev, Daniel Schopf, Philipp Beck, Johannes Roth, and Hans-Rainer Trebin. Classical interaction potentials for diverse materials from ab initio data: a review of potfit. *Modelling and Simulation in Materials Science and Engineering*, 23(7):074002, sep 2015.

[130] D Wolff and WG Rudd. Tabulated potentials in molecular dynamics simulations. *Computer physics communications*, 120(1):20–32, 1999.

[131] A.P. Thompson, L.P. Swiler, C.R. Trott, S.M. Foiles, and G.J. Tucker. Spectral neighbor analysis method for automated generation of quantum-accurate interatomic potentials. *Journal of Computational Physics*, 285:316 – 330, 2015.

[132] Mitchell A Wood and Aidan P Thompson. Extending the accuracy of the SNAP interatomic potential form. *The Journal of Chemical Physics*, 148(24):241721, 2018.

[133] Ralf Drautz. Atomic cluster expansion for accurate and transferable interatomic potentials. *Physical Review B*, 99(1):014104, 2019.

[134] JA Porter, NW Ashcroft, and GV Chester. Pair potentials for simple metallic systems: Beyond linear response. *Physical Review B*, 81(22):224113, 2010.

[135] Gérald Faussurier and Christophe Blancard. Relativistic quantum average-atom model with relativistic exchange potential. *Physics of Plasmas*, 26(4):042705, 2019.

[136] PA Sterne, SB Hansen, BG Wilson, and WA Isaacs. Equation of state, occupation probabilities and conductivities in the average atom purgatorio code. *High Energy Density Physics*, 3(1-2):278–282, 2007.

[137] MS Murillo. Viscosity estimates for strongly coupled Yukawa systems. *Physical Review E*, 62(3):4115, 2000.

[138] H. M. Antia. Rational Function Approximations for Fermi-Dirac Integrals. *apjs*, 84:101, January 1993.

[139] Toshio Fukushima. Precise and fast computation of Fermi–Dirac integral of integer and half integer order by piecewise minimax rational approximation. *Applied Mathematics and Computation*, 259:708–729, 2015.

[140] Michael S. Murillo. Viscosity estimates of liquid metals and warm dense matter using the yukawa reference system. *High Energy Density Physics*, 4(1):49 – 57, 2008.

[141] L. B. Fletcher, H. J. Lee, T. Döppner, E. Galtier, B. Nagler, P. Heimann, C. Fortmann, S. LePape, T. Ma, M. Millot, A. Pak, D. Turnbull, D. A. Chapman, D. O. Gericke, J. Vorberger, T. White, G. Gregori, M. Wei, B. Barbrel, R. W. Falcone, C. C. Kao, H. Nuhn, J. Welch, U. Zastrau, P. Neumayer, J. B. Hastings, and S. H. Glenzer. Ultrabright x-ray laser scattering for dynamic warm dense matter physics. *Nature Photonics*, 9(4):274–279, 2015.

[142] T. Ma, T. Döppner, R. W. Falcone, L. Fletcher, C. Fortmann, D. O. Gericke, O. L. Landen, H. J. Lee, A. Pak, J. Vorberger, K. Wünsch, and S. H. Glenzer. X-ray scattering measurements of strong ion-ion correlations in shock-compressed aluminum. *Phys. Rev. Lett.*, 110:065001, Feb 2013.

[143] S. H. Glenzer, L. B. Fletcher, E. Galtier, B. Nagler, R. Alonso-Mori, B. Barbrel, S. B. Brown, D. A. Chapman, Z. Chen, C. B. Curry, F. Fiuza, E. Gamboa, M. Gauthier, D. O. Gericke, A. Gleason, S. Goede, E. Granados, P. Heimann, J. Kim, D. Kraus, M. J. MacDonald, A. J. Mackinnon, R. Mishra, A. Ravasio, C. Roedel, P. Sperling, W. Schumaker, Y. Y. Tsui, J. Vorberger, U. Zastrau, A. Fry, W. E. White, J. B. Hasting, and H. J. Lee. Matter under extreme conditions experiments at the linac coherent light source. *Journal of Physics B: Atomic, Molecular and Optical Physics*, 49(9):092001, apr 2016.

[144] Hannes R Rüter and Ronald Redmer. Ab initio simulations for the ion-ion structure factor of warm dense aluminum. *Physical review letters*, 112(14):145007, 2014.

[145] A. L. Kritcher, P. Neumayer, C. R. D. Brown, P. Davis, T. Döppner, R. W. Falcone, D. O. Gericke, G. Gregori, B. Holst, O. L. Landen, H. J. Lee, E. C. Morse, A. Pelka, R. Redmer, M. Roth, J. Vorberger, K. Wünsch, and S. H. Glenzer. Measurements of ionic structure in shock compressed lithium hydride from ultrafast x-ray thomson scattering. *Phys. Rev. Lett.*, 103:245004, Dec 2009.

[146] Steve Plimpton. Fast parallel algorithms for short-range molecular dynamics. *Journal of Computational Physics*, 117(1):1 – 19, 1995.

[147] Junzo Chihara. Unified description of metallic and neutral liquids and plasmas. *Journal of Physics: Condensed Matter*, 3(44):8715, 1991.

[148] J.P. Hansen and I.R. McDonald. *Theory of simple liquids*. Elsevier, 1990.

[149] Changho Kim, Oleg Borodin, and George Em Karniadakis. Quantification of sampling uncertainty for molecular dynamics simulation: Time-dependent diffusion coefficient in simple fluids. *Journal of Computational Physics*, 302:485–508, 2015.

[150] In-Chul Yeh and Gerhard Hummer. System-size dependence of diffusion coefficients and viscosities from molecular dynamics simulations with periodic boundary conditions. *The Journal of Physical Chemistry B*, 108(40):15873–15879, 10 2004.

[151] Liam G Stanton and Michael S Murillo. Ionic transport in high-energy-density matter. *Physical Review E*, 93(4):043203, 2016.

[152] Richard C Remsing, Michael L Klein, and Jianwei Sun. Dependence of the structure and dynamics of liquid silicon on the choice of density functional approximation. *Physical Review B*, 96(2):024203, 2017.

[153] Michael S Murillo, Mathieu Marciante, and Liam G Stanton. Machine learning discovery of computational model efficacy boundaries. *Physical Review Letters*, 125(8):085503, 2020.

[154] AK Soper. Empirical potential Monte Carlo simulation of fluid structure. *Chemical Physics*, 202(2-3):295–306, 1996.

[155] E. M. Apfelbaum. The reconstruction of the effective interaction potential on the base of pair correlation function measurements in dusty plasma. *Physics of Plasmas*, 14(12):123703, 2007.

[156] Lucas J. Stanek and Michael S. Murillo. Analytic models for interdiffusion in dense plasma mixtures. *Physics of Plasmas*, 28(7):072302, 2021.

[157] Ernest Kirkendall. Rates of diffusion of copper and zinc in alpha brass. *Trans. AIME*, 133:186–203, 1939.

[158] EO Kirkendall. Diffusion of zinc in alpha brass. *Trans. Aime*, 147:104–110, 1942.

[159] AD Smigelskas. Zinc diffusion in alpha brass. *Trans. Aime*, 171:130–142, 1947.

[160] L So Darken. Diffusion, mobility and their interrelation through free energy in binary metallic systems. *Trans. Aime*, 175:184–201, 1948.

[161] M. Schoen and C. Hoheisel. The mutual diffusion coefficient D 12 in binary liquid model mixtures. Molecular dynamics calculations based on Lennard-Jones (12-6) potentials. *Molecular Physics*, 52(1):33–56, 1984.

[162] GA Fernandez, J Vrabec, and H Hasse. A molecular simulation study of shear and bulk viscosity and thermal conductivity of simple real fluids. *Fluid phase equilibria*, 221(1-2):157–163, 2004.

[163] John Cahoon, Yuning Jiao, Kedar Tandon, and Mahesh Chaturvedi. Interdiffusion in liquid tin. *Journal of phase equilibria and diffusion*, 27(4):325–332, 2006.

[164] H Weis, F Kargl, M Kolbe, M M Koza, T Unruh, and A Meyer. Self- and interdiffusion in dilute liquid germanium-based alloys. *Journal of Physics: Condensed Matter*, 31(45):455101, aug 2019.

[165] E. García-Berro, L. G. Althaus, A. H. Córsico, and J. Isern. Gravitational Settling of 22Ne and White Dwarf Evolution. *The Astrophysical Journal*, 677(1):473–482, apr 2008.

[166] M Salaris and A Weiss. Atomic diffusion in stellar interiors and field halo subdwarfs ages. In *Astrophysical Ages and Times Scales*, volume 245, page 367, 2001.

[167] Lars Bildsten and David M Hall. Gravitational settling of 22Ne in liquid white dwarf interiors. *The Astrophysical Journal Letters*, 549(2):L219, 2001.

[168] D. Arnett. The role of mixing in astrophysics. *The Astrophysical Journal Supplement Series*, 127(2):213–217, apr 2000.

[169] Brian M Haines, RC Shah, Joseph Michael Smidt, Brian James Albright, Tana Cardenas, Melissa Rae Douglas, C Forrest, V Yu Glebov, Mark A Gunderson, C Hamilton, et al. The rate of development of atomic mixing and temperature equilibration in inertial confinement fusion implosions. *Physics of Plasmas*, 27(10):102701, 2020.

[170] V Rana, H Lim, J Melvin, J Glimm, B Cheng, and DH Sharp. Mixing with applications to inertial-confinement-fusion implosions. *Physical Review E*, 95(1):013203, 2017.

[171] C. R. Weber, D. S. Clark, A. Pak, N. Alfonso, B. Bachmann, L. F. Berzak Hopkins, T. Bunn, J. Crippen, L. Divol, T. Dittrich, A. L. Kritcher, O. L. Landen, S. Le Pape, A. G. MacPhee, E. Marley, L. P. Masse, J. L. Milovich, A. Nikroo, P. K. Patel, L. A. Pickworth, N. Rice, V. A. Smalyuk, and M. Stadermann. Mixing in ICF implosions on the National Ignition Facility caused by the fill-tube. *Physics of Plasmas*, 27(3):032703, 2020.

[172] John Lindl. Development of the indirect-drive approach to inertial confinement fusion and the target physics basis for ignition and gain. *Physics of Plasmas*, 2(11):3933–4024, 1995.

[173] A. Pak, L. Divol, C. R. Weber, L. F. Berzak Hopkins, D. S. Clark, E. L. Dewald, D. N. Fittinghoff, V. Geppert-Kleinrath, M. Hohenberger, S. Le Pape, T. Ma, A. G. MacPhee, D. A. Mariscal, E. Marley, A. S. Moore, L. A. Pickworth, P. L. Volegov, C. Wilde, O. A. Hurricane, and P. K. Patel. Impact of localized radiative loss on inertial confinement fusion implosions. *Phys. Rev. Lett.*, 124:145001, Apr 2020.

[174] O. Larroche, H. G. Rinderknecht, and M. J. Rosenberg. Nuclear yield reduction in inertial confinement fusion exploding-pusher targets explained by fuel-pusher mixing through hybrid kinetic-fluid modeling. *Phys. Rev. E*, 98:031201, Sep 2018.

[175] Melissa Rae Douglas. Marble brief overview. Technical report, Los Alamos National Lab.(LANL), Los Alamos, NM (United States), 2014.

[176] Patrick Knapp, Kristian Beckwith, Kyle Cochrane, Raymond C Clay III, and Thomas Mattsson. Experimental validation of dense plasma transport models using the z-machine. Technical report, Sandia National Lab.(SNL-NM), Albuquerque, NM (United States), 2019.

[177] Cameron Allen, Matthew Oliver, Thomas White, Wolfgang Theobald, Alison Saunders, Yuan Ping, Otto Landen, Laurent Divol, and Tilo Doeppner. Developing x-ray Fresnel Diffractive-Refractive Radiography for Measuring Mutual Diffusion in Warm Dense Matter. *Bulletin of the American Physical Society*, 2020.

[178] RE Olson, TJ Murphy, BM Haines, MR Douglas, BJ Albright, MA Gunderson, Y Kim, T Cardenas, CE Hamilton, and RB Randolph. Development of the Marble experimental platform at the National Ignition Facility. *Physics of Plasmas*, 27(10):102703, 2020.

[179] Tomorr Haxhimali, Robert Rudd, James Glosli, Catherine Burcklen, Tommaso Pardini, and Stefan Hau-Riege. Modelling of diffusive interface broadening between materials at warm dense conditions in support of XFEL experiments. *Bulletin of the American Physical Society*, 2020.

[180] P.E. Grabowski, S.B. Hansen, M.S. Murillo, L.G. Stanton, F.R. Graziani, A.B. Zylstra, S.D. Baalrud, P. Arnault, A.D. Baczewski, L.X. Benedict, C. Blancard, O. Čertík, J. Clérouin, L.A. Collins, S. Copeland, A.A. Correa, J. Dai, J. Daligault, M.P. Desjarlais, M.W.C. Dharma-wardana, G. Faussurier, J. Haack, T. Haxhimali, A. Hayes-Sterbenz, Y. Hou, S.X. Hu, D. Jensen, G. Jungman, G. Kagan, D. Kang, J.D. Kress, Q. Ma, M. Marciante, E. Meyer, R.E. Rudd, D. Saumon, L. Shulenburger, R.L. Singleton, T. Sjostrom, L.J. Stanek, C.E. Starrett, C. Ticknor, S. Valaitis, J. Venzke, and A. White. Review of the first charged-particle transport coefficient comparison workshop. *High Energy Density Physics*, 37:100905, 2020.

[181] JP Hansen, F Joly, and IR McDonald. Self-diffusion, interdiffusion and long wavelength plasma oscillations in binary ionic mixtures. *Physica A: Statistical Mechanics and its Applications*, 132(2-3):472–488, 1985.

[182] A. J. White, C. Ticknor, E. R. Meyer, J. D. Kress, and L. A. Collins. Multicomponent mutual diffusion in the warm, dense matter regime. *Phys. Rev. E*, 100:033213, Sep 2019.

[183] David Rosenberger, Nicholas Lubbers, and Timothy C. Germann. Evaluating diffusion and the thermodynamic factor for binary ionic mixtures. *Physics of Plasmas*, 27(10):102705, 2020.

[184] Calen J Leverant, Jacob A Harvey, and Todd M Alam. Machine learning-based upscaling of finite-size molecular dynamics diffusion simulations for binary fluids. *The Journal of Physical Chemistry Letters*, 11(24):10375–10381, 2020.

[185] C. Paquette, C. Pelletier, G. Fontaine, and G. Michaud. Diffusion Coefficients for Stellar Plasmas. *apjs*, 61:177, may 1986.

[186] MV Beznogov and DG Yakovlev. Effective potential and interdiffusion in binary ionic mixtures. *Physical Review E*, 90(3):033102, 2014.

[187] Yanhua Zhou and Gregory H Miller. Green-Kubo formulas for mutual diffusion coefficients in multicomponent systems. *The Journal of Physical Chemistry*, 100(13):5516–5524, 1996.

[188] Yanhua Zhou and Gregory H Miller. Mutual diffusion in binary Ar-Kr mixtures and empirical diffusion models. *Physical Review E*, 53(2):1587, 1996.

[189] Sybren Ruurds De Groot and Peter Mazur. *Non-equilibrium thermodynamics*. Courier Corporation, 2013.

[190] Rajamani Krishna and Jasper M. van Baten. Describing diffusion in fluid mixtures at elevated pressures by combining the Maxwell–Stefan formulation with an equation of state. *Chemical Engineering Science*, 153:174–187, 2016.

[191] David B. Boercker and E. L. Pollock. Interdiffusion in binary ionic mixtures. *Phys. Rev. A*, 36:1779–1785, Aug 1987.

[192] Peter Amendt, O. L. Landen, H. F. Robey, C. K. Li, and R. D. Petrasso. Plasma barodiffusion in inertial-confinement-fusion implosions: Application to observed yield anomalies in thermonuclear fuel mixtures. *Phys. Rev. Lett.*, 105:115005, Sep 2010.

[193] Grigory Kagan and Xian-Zhu Tang. Thermo-diffusion in inertially confined plasmas. *Physics Letters A*, 378(21):1531–1535, 2014.

[194] Tomorr Haxhimali, Robert E Rudd, William H Cabot, and Frank R Graziani. Diffusivity in asymmetric Yukawa ionic mixtures in dense plasmas. *Physical Review E*, 90(2):023104, 2014.

[195] Juliusz Dąbrowa and Marek Danielewski. State-of-the-art diffusion studies in the high entropy alloys. *Metals*, 10(3), 2020.

[196] Dieter Bothe and Pierre-Etienne Druet. On the structure of continuum thermodynamical diffusion fluxes–a novel closure scheme and its relation to the maxwell-stefan and the fick-onsager approach. *arXiv preprint arXiv:2008.05327*, 2020.

[197] Yiming Duan, Weiguang Zhang, Weidu Wang, and Liqun Shi. Studies on mutual diffusion between Mo and α-Ti during thermal evaporation. *Vacuum*, 187:110115, 2021.

[198] TR Paul, Irina V Belova, EV Levchenko, AV Evteev, and GE Murch. Determining a tracer diffusivity by way of the Darken-Manning equation for interdiffusion in binary alloy systems. In *Diffusion Foundations*, volume 4, pages 25–54. Trans Tech Publ, 2015.

[199] David W McCall and Dean C Douglass. Diffusion in binary solutions. *The Journal of Physical Chemistry*, 71(4):987–997, 1967.

[200] Donn L. Jolly and Richard J. Bearman. Molecular dynamics simulation of the mutual and self diffusion coefficients in Lennard-Jones liquid mixtures. *Molecular Physics*, 41(1):137–147, 1980.

[201] Lei Liu, Zhi-Guo Li, Jia-Yu Dai, Qi-Feng Chen, and Xiang-Rong Chen. Quantum molecular dynamics study on the proton exchange, ionic structures, and transport properties of warm dense hydrogen-deuterium mixtures. *Physical Review E*, 97(6):063204, 2018.

[202] JD Kress, James S Cohen, DA Horner, F Lambert, and LA Collins. Viscosity and mutual diffusion of deuterium-tritium mixtures in the warm-dense-matter regime. *Physical Review E*, 82(3):036404, 2010.

[203] A. Diaw and M. S. Murillo. A dynamic density functional theory approach to diffusion in white dwarfs and neutron star envelopes. *The Astrophysical Journal*, 829(1):16, sep 2016.

[204] N.W. Ashcroft and D. Stroud. Theory of the thermodynamics of simple liquid metals. volume 33 of *Solid State Physics*, pages 1–81. Academic Press, 1978.

[205] K Hoshino and W H Young. The ordering potential and concentration-concentration structure factor of a liquid Li-Na alloy. *Journal of Physics F: Metal Physics*, 16(11):1671–1680, nov 1986.

[206] Philippe Arnault. Modeling viscosity and diffusion of plasma for pure elements and multi-component mixtures from weakly to strongly coupled regimes. *High Energy Density Physics*, 9(4):711–721, 2013.

[207] François Perrot and M. W. C. Dharma-wardana. Exchange and correlation potentials for electron-ion systems at finite temperatures. *Phys. Rev. A*, 30:2619–2626, Nov 1984.

[208] John G Kirkwood and Frank P Buff. The statistical mechanical theory of solutions. I. *The Journal of chemical physics*, 19(6):774–777, 1951.

[209] Noura Dawass, Peter Krüger, Sondre K Schnell, Jean-Marc Simon, and Thijs JH Vlugt. Kirkwood-Buff integrals from molecular simulation. *Fluid Phase Equilibria*, 486:21–36, 2019.

[210] Peter Krüger, Sondre K. Schnell, Dick Bedeaux, Signe Kjelstrup, Thijs J. H. Vlugt, and Jean-Marc Simon. Kirkwood–Buff integrals for finite volumes. *The Journal of Physical Chemistry Letters*, 4(2):235–238, 2013. PMID: 26283427.

[211] K Wünsch, P Hilse, M Schlanges, and DO Gericke. Structure of strongly coupled multicomponent plasmas. *Physical Review E*, 77(5):056404, 2008.

[212] Bruce J Berne and GD Harp. On the calculation of time correlation functions. *Adv. Chem. Phys*, 17:63–227, 1970.

[213] Jean Pierre Boon and Sidney Yip. *Molecular hydrodynamics*. Courier Corporation, 1991.

[214] Nathaniel R. Shaffer, Scott D. Baalrud, and Jérôme Daligault. Effective potential theory for diffusion in binary ionic mixtures. *Phys. Rev. E*, 95:013206, Jan 2017.

[215] Lucas J. Stanek, Shaunak D. Bopardikar, and Michael S. Murillo. Multifidelity regression of sparse plasma transport data available in disparate physical regimes. *Phys. Rev. E*, 104:065303, Dec 2021.

[216] Agnes Dewaele, Mohamed Mezouar, Nicolas Guignot, and Paul Loubeyre. High melting points of tantalum in a laser-heated diamond anvil cell. *Physical review letters*, 104(25):255701, 2010.

[217] Youhong Li, Donald J Siegel, James B Adams, and Xiang-Yang Liu. Embedded-atom-method tantalum potential developed by the force-matching method. *Physical Review B*, 67(12):125101, 2003.

[218] J.A. Gaffney, S.X. Hu, P. Arnault, A. Becker, L.X. Benedict, T.R. Boehly, P.M. Celliers, D.M. Ceperley, O. Čertík, J. Clérouin, G.W. Collins, L.A. Collins, J.-F. Danel, N. Desbiens, M.W.C. Dharma-wardana, Y.H. Ding, A. Fernandez-Pañella, M.C. Gregor, P.E. Grabowski, S. Hamel, S.B. Hansen, L. Harbour, X.T. He, D.D. Johnson, W. Kang, V.V. Karasiev, L. Kazandjian, M.D. Knudson, T. Ogitsu, C. Pierleoni, R. Piron, R. Redmer, G. Robert, D. Saumon, A. Shamp, T. Sjostrom, A.V. Smirnov, C.E. Starrett, P.A. Sterne, A. Wardlow, H.D. Whitley, B. Wilson, P. Zhang, and E. Zurek. A review of equation-of-state models for inertial confinement fusion materials. *High Energy Density Physics*, 28:7 – 24, 2018.

[219] Eve Bélisle, Zi Huang, Sébastien Le Digabel, and Aïmen E Gheribi. Evaluation of machine learning interpolation techniques for prediction of physical properties. *Computational Materials Science*, 98:170–177, 2015.

[220] M Attarian Shandiz and R Gauvin. Application of machine learning methods for the prediction of crystal system of cathode materials in lithium-ion batteries. *Computational Materials Science*, 117:270–278, 2016.

[221] Carl Edward Rasmussen. Gaussian processes in machine learning. In *Summer School on Machine Learning*, pages 63–71. Springer, 2003.

[222] M. C. Kennedy and A. O'Hagan. Predicting the output from a complex computer code when fast approximations are available. *Biometrika*, 87(1):1–13, 2000.

[223] Maziar Raissi and George Karniadakis. Deep multi-fidelity Gaussian processes. *arXiv preprint arXiv:1604.07484*, 2016.

[224] P. Perdikaris, M. Raissi, A. Damianou, N. D. Lawrence, and G. E. Karniadakis. Nonlinear information fusion algorithms for data-efficient multi-fidelity modelling. *Proceedings of the*

Royal Society A: Mathematical, Physical and Engineering Sciences, 473(2198):20160751, 2017.

[225] Kurt Cutajar, Mark Pullin, Andreas Damianou, Neil Lawrence, and Javier González. Deep Gaussian Processes for Multi-fidelity Modeling, 2019.

[226] M. Giselle Fernández-Godino, Chanyoung Park, Nam-Ho Kim, and Raphael T. Haftka. Review of multi-fidelity models, 2017.

[227] Alexander I. J. Forrester, András Sóbester, and Andy J. Keane. Multi-fidelity optimization via surrogate modelling. *Proceedings: Mathematical, Physical and Engineering Sciences*, 463(2088):3251–3269, 2007.

[228] Abhirup Patra, Rohit Batra, Anand Chandrasekaran, Chiho Kim, Tran Doan Huan, and Rampi Ramprasad. A multi-fidelity information-fusion approach to machine learn and predict polymer bandgap. *Computational Materials Science*, 172:109286, 2020.

[229] Jiaqing Kou and Weiwei Zhang. Multi-fidelity modeling framework for nonlinear unsteady aerodynamics of airfoils. *Applied Mathematical Modelling*, 76:832–855, 2019.

[230] Xuhui Meng and George Em Karniadakis. A composite neural network that learns from multi-fidelity data: Application to function approximation and inverse PDE problems. *Journal of Computational Physics*, 401:109020, 2020.

[231] Naoki Seryo, Takeshi Sato, John J. Molina, and Takashi Taniguchi. Learning the constitutive relation of polymeric flows with memory. *Phys. Rev. Research*, 2:033107, Jul 2020.

[232] Taeksang Lee, Ilias Bilionis, and Adrian Buganza Tepole. Propagation of uncertainty in the mechanical and biological response of growing tissues using multi-fidelity Gaussian process regression. *Computer Methods in Applied Mechanics and Engineering*, 359:112724, 2020.

[233] Soumalya Sarkar, Sudeepta Mondal, Michael Joly, Matthew E Lynch, Shaunak D Bopardikar, Ranadip Acharya, and Paris Perdikaris. Multifidelity and multiscale bayesian framework for high-dimensional engineering design and calibration. *Journal of Mechanical Design*, 141(12), 2019.

[234] Haitao Liu, Yew-Soon Ong, Jianfei Cai, and Yi Wang. Cope with diverse data structures in multi-fidelity modeling: A gaussian process method. *Engineering Applications of Artificial Intelligence*, 67:211–225, 2018.

[235] Zhendong Guo, Liming Song, Chanyoung Park, Jun Li, and Raphael T. Haftka. Analysis of dataset selection for multi-fidelity surrogates for a turbine problem. *Structural and Multidisciplinary Optimization*, 57(6):2127–2142, 2018.

[236] Zhi-Guo Li, Yan Cheng, Qi-Feng Chen, and Xiang-Rong Chen. Equation of state and transport properties of warm dense helium via quantum molecular dynamics simulations. *Physics of Plasmas*, 23(5):052701, 2016.

[237] Cong Wang, Yao Long, Ming-Feng Tian, Xian-Tu He, and Ping Zhang. Equations of state and transport properties of warm dense beryllium: A quantum molecular dynamics study. *Physical Review E*, 87(4):043105, 2013.

[238] Cong Wang, Zhe-Bin Wang, Qi-Feng Chen, and Ping Zhang. Quantum molecular dynamics study of warm dense iron. *Physical Review E*, 89(2):023101, 2014.

[239] J. P. Hansen, I. R. McDonald, and E. L. Pollock. Statistical mechanics of dense ionized matter. iii. dynamical properties of the classical one-component plasma. *Phys. Rev. A*, 11:1025–1039, Mar 1975.

[240] GPy. GPy: A Gaussian process framework in python.

[241] F. Pedregosa, G. Varoquaux, A. Gramfort, V. Michel, B. Thirion, O. Grisel, M. Blondel, P. Prettenhofer, R. Weiss, V. Dubourg, J. Vanderplas, A. Passos, D. Cournapeau, M. Brucher, M. Perrot, and E. Duchesnay. Scikit-learn: Machine learning in Python. *Journal of Machine Learning Research*, 12:2825–2830, 2011.

[242] Richard H Byrd, Peihuang Lu, Jorge Nocedal, and Ciyou Zhu. A limited memory algorithm for bound constrained optimization. *SIAM Journal on scientific computing*, 16(5):1190–1208, 1995.

[243] Anthony O'Hagan. A Markov property for covariance structures. *Statistics Research Report*, 98(13):1, 1998.

[244] Andrei Paleyes, Mark Pullin, Maren Mahsereci, Neil Lawrence, and Javier González. Emulation of physical processes with Emukit. In *Second Workshop on Machine Learning and the Physical Sciences, NeurIPS*, 2019.

[245] H. Nyquist. Certain topics in telegraph transmission theory. *Transactions of the American Institute of Electrical Engineers*, 47(2):617–644, 1928.

[246] Claude Elwood Shannon. Communication in the presence of noise. *Proceedings of the IRE*, 37(1):10–21, 1949.

[247] Loic Le Gratiet and Josselin Garnier. Recursive co-kriging model for design of computer experiments with multiple levels of fidelity. *International Journal for Uncertainty Quantification*, 4(5), 2014.

[248] Andreas Damianou and Neil D Lawrence. Deep gaussian processes. In *Artificial intelligence and statistics*, pages 207–215. PMLR, 2013.

[249] Andreas Damianou. *Deep Gaussian processes and variational propagation of uncertainty*. PhD thesis, University of Sheffield, 2015.

[250] Joseph A Hevesi, Jonathan D Istok, and Alan L Flint. Precipitation estimation in mountainous terrain using multivariate geostatistics. part i: structural analysis. *Journal of applied meteorology*, 31(7):661–676, 1992.

[251] Joseph A Hevesi, Alan L Flint, and Jonathan D Istok. Precipitation estimation in mountainous terrain using multivariate geostatistics. part ii: Isohyetal maps. *Journal of applied meteorology*, 31(7):677–688, 1992.

[252] J. H. Halton. Algorithm 247: Radical-inverse quasi-random point sequence. *Commun. ACM*, 7(12):701–702, December 1964.

[253] C Caruso and F Quarta. Interpolation methods comparison. *Computers & Mathematics with Applications*, 35(12):109–126, 1998.

[254] Andrew Pensoneaulta, Xiu Yangb, and Xueyu Zhua. Nonnegativity-enforced gaussian process regression. *arXiv preprint arXiv:2004.04632*, 2020.

[255] F Douglas Swesty. Thermodynamically consistent interpolation for equation of state tables. *Journal of Computational Physics*, 127(1):118–127, 1996.

[256] Frank X Timmes and F Douglas Swesty. The accuracy, consistency, and speed of an electron-positron equation of state based on table interpolation of the Helmholtz free energy. *The Astrophysical Journal Supplement Series*, 126(2):501, 2000.

[257] Anna M Michalak. A Gibbs sampler for inequality-constrained geostatistical interpolation and inverse modeling. *Water Resources Research*, 44(9), 2008.

[258] CE Simien, YC Chen, P Gupta, S Laha, YN Martinez, PG Mickelson, SB Nagel, and TC Killian. Using absorption imaging to study ion dynamics in an ultracold neutral plasma. *Physical review letters*, 92(14):143001, 2004.

[259] Jose Castro, Patrick McQuillen, and TC Killian. Ion acoustic waves in ultracold neutral plasmas. *Physical Review Letters*, 105(6):065004, 2010.

[260] Luciano G Silvestri, R Tucker Sprenkle, Scott D Bergeson, and Michael S Murillo. Relaxation of strongly coupled binary ionic mixtures in the coupled mode regime. *Physics of Plasmas*, 28(6):062302, 2021.

[261] TC Killian, VS Ashoka, P Gupta, S Laha, SB Nagel, CE Simien, S Kulin, SL Rolston, and SD Bergeson. Ultracold neutral plasmas: recent experiments and new prospects. *Journal of Physics A: Mathematical and General*, 36(22):6077, 2003.

[262] Genia Vogman. *Fourth-order conservative Vlasov-Maxwell solver for Cartesian and cylindrical phase space coordinates*. University of California, Berkeley, 2016.

[263] Richard L Liboff. *Kinetic theory: classical, quantum, and relativistic descriptions*. Springer Science & Business Media, 2003.

[264] Rodrigo Soto. *Kinetic theory and transport phenomena*, volume 25. Oxford University Press, 2016.

[265] Prabhu Lal Bhatnagar, Eugene P Gross, and Max Krook. A model for collision processes in gases. i. small amplitude processes in charged and neutral one-component systems. *Physical review*, 94(3):511, 1954.

[266] Andrew Lenard and Ira B Bernstein. Plasma oscillations with diffusion in velocity space. *Physical Review*, 112(5):1456, 1958.

[267] Jeffrey R Haack, Cory D Hauck, and Michael S Murillo. A conservative, entropic multispecies BGK model. *Journal of Statistical Physics*, 168(4):826–856, 2017.

[268] Joseph Donald Huba. *NRL plasma formulary*, volume 6790. Naval Research Laboratory, 1998.

[269] DO Gericke, MS Murillo, and M Schlanges. Dense plasma temperature equilibration in the binary collision approximation. *Physical Review E*, 65(3):036418, 2002.

[270] Lyman Spitzer. *Physics of fully ionized gases*. Courier Corporation, 2006.

[271] Liam G Stanton and Michael S Murillo. Efficient model for electronic transport in high energy-density matter. *Physics of Plasmas*, 28(8):082301, 2021.

[272] GV Vogman, U Shumlak, and P Colella. Conservative fourth-order finite-volume Vlasov-Poisson solver in cylindrical coordinates. Technical report, Lawrence Livermore National Lab.(LLNL), Livermore, CA (United States), 2018.

[273] P Mora. Collisionless expansion of a Gaussian plasma into a vacuum. *Physics of plasmas*, 12(11):112102, 2005.

[274] MS Murillo and E Timmermans. Self-similar wavepackets for describing warm dense matter. *Contributions to Plasma Physics*, 43(5-6):333–337, 2003.

[275] Gilbert Strang. On the construction and comparison of difference schemes. *SIAM journal on numerical analysis*, 5(3):506–517, 1968.

[276] Randall J LeVeque et al. *Finite volume methods for hyperbolic problems*, volume 31. Cambridge university press, 2002.

[277] William E Schiesser. *The numerical method of lines: integration of partial differential equations*. Elsevier, 2012.

[278] Chi-Wang Shu. Essentially non-oscillatory and weighted essentially non-oscillatory schemes for hyperbolic conservation laws. *Advanced numerical approximation of nonlinear hyperbolic equations*, pages 325–432, 1998.

[279] Adilson Costa da Silva, José Abdalla Helayël Neto, and Vladimir Santos da Costa. A numerical procedure to solve Poisson's equation in spherical coordinates. *Revista Brasileira de Ensino de Física*, 43, 2021.

[280] Ramiar Sadegh-Vaziri, Helen Winberg-Wang, and Matthaus U Babler. 1d finite volume scheme for simulating gas–solid reactions in porous spherical particles with application to biomass pyrolysis. *Industrial & Engineering Chemistry Research*, 60(29):10603–10614, 2021.

[281] A. Mignone. High-order conservative reconstruction schemes for finite volume methods in cylindrical and spherical coordinates. *Journal of Computational Physics*, 270:784–814, 2014.

[282] Stefan Van Der Walt, S Chris Colbert, and Gael Varoquaux. The NumPy array: a structure for efficient numerical computation. *Computing in science & engineering*, 13(2):22–30, 2011.

[283] Pauli Virtanen, Ralf Gommers, Travis E Oliphant, Matt Haberland, Tyler Reddy, David Cournapeau, Evgeni Burovski, Pearu Peterson, Warren Weckesser, Jonathan Bright, et al. SciPy 1.0: fundamental algorithms for scientific computing in Python. *Nature methods*, 17(3):261–272, 2020.

[284] Siu Kwan Lam, Antoine Pitrou, and Stanley Seibert. Numba: A llvm-based python jit compiler. In *Proceedings of the Second Workshop on the LLVM Compiler Infrastructure in HPC*, pages 1–6, 2015.

[285] Luciano G Silvestri, Lucas J Stanek, Gautham Dharuman, Yongjun Choi, and Michael S Murillo. Sarkas: a fast pure-python molecular dynamics suite for plasma physics. *Computer Physics Communications*, 272:108245, 2022.

[286] Allen Robinson, Thomas Brunner, Susan Carroll, Richard Drake, Christopher Garasi, Thomas Gardiner, Thomas Haill, Heath Hanshaw, David Hensinger, Duane Labreche, et al. ALEGRA: An arbitrary Lagrangian-Eulerian multimaterial, multiphysics code. In *46th aiaa aerospace sciences meeting and exhibit*, page 1235, 2008.

APPENDIX A

ANALYTIC SOLUTION TO POISSON'S EQUATION IN SPHERICAL COORDINATES

For simple test cases, we can obtain an analytic solution to Poisson's equation which will be used to test the accuracy of our numerical method described in Sec. 5.5.3. Consider a uniform charge density ρ_0 inside a sphere of radius R. The charge density is assumed to be zero for $r > R$. Therefore, Poisson's equation for these two cases is

$$\begin{cases} \frac{1}{r^2}\frac{d}{dr}\left(r^2\frac{d}{dr}\varphi\right) = -4\pi\rho_0, & \text{for } r \leq R, \\ \\ \frac{1}{r^2}\frac{d}{dr}\left(r^2\frac{d}{dr}\varphi\right) = 0, & \text{for } r > R. \end{cases} \tag{A.1}$$

We solve the first equation by first expanding out the derivative using the product rule which yields

$$\frac{d^2}{dr^2}\varphi + \frac{2}{r}\frac{d}{dr}\varphi = -4\pi\rho_0. \tag{A.2}$$

Multiplying by r^2 we get

$$r^2\frac{d^2}{dr^2}\varphi + 2r\frac{d}{dr}\varphi = -4r^2\pi\rho_0. \tag{A.3}$$

We now assume a solution of the form a $\varphi = r^\lambda$ and determine the complementary solution from

$$r^2\left[\lambda(\lambda-1)r^{\lambda-2}\right] + 2r\lambda r^{\lambda-1} = 0. \tag{A.4}$$

The above equation yields the auxiliary equation

$$\lambda(\lambda+1) = 0, \tag{A.5}$$

which implies a complementary solution of the form

$$\varphi_c(r) = c_1 + \frac{c_2}{r}. \tag{A.6}$$

We note that the complementary solution is also the solution to the $r > R$ case in Eq. (A.1). For the particular solution, we use variation of parameters. The particular solution has the form

$$\varphi_p(r) = u_1\varphi_1 + u_2\varphi_2 = u_1 + u_2\frac{1}{r}. \tag{A.7}$$

We have the following Wronskians:

$$W = \begin{vmatrix} 1 & \frac{1}{r} \\ 0 & -\frac{1}{r^2} \end{vmatrix}, \quad W_1 = \begin{vmatrix} 0 & \frac{1}{r} \\ -4\pi\rho_0 & -\frac{1}{r^2} \end{vmatrix}, \quad W_2 = \begin{vmatrix} 1 & 0 \\ 0 & -4\pi\rho_0 \end{vmatrix}. \tag{A.8}$$

Using the fact that $u_1' = W_1/W$ and $u_2' = W_2/W$, we have

$$u_1 = -2\pi\rho_0 r^2, \quad u_2 = \frac{4}{3}\pi\rho_0 r^3, \tag{A.9}$$

which gives

$$\varphi_p = -\frac{2\pi r^2 \rho_0}{3}. \tag{A.10}$$

Thus, the solution to Eq. (A.1) is

$$\begin{cases} \varphi_{\text{in}} = c_1 + \frac{c_2}{r} - \frac{2\pi r^2 \rho_0}{3}, & \text{for } r \le R, \\ \varphi_{\text{out}} = c_3 + \frac{c_4}{r}, & \text{for } r > R. \end{cases} \tag{A.11}$$

Where the subscripts “in" and “out" denote the solution inside and outside the sphere of uniform charge density respectively. To determine the unknown constants c_1, c_2, c_3 and c_4, we employ the boundary conditions

$$\frac{d}{dr}\varphi_{\text{in}}\bigg|_{r=0} = 0, \tag{A.12}$$

$$\frac{d}{dr}\varphi_{\text{in}}\bigg|_{r=R} = \frac{d}{dr}\varphi_{\text{out}}\bigg|_{r=R}, \tag{A.13}$$

$$\varphi_{\text{in}}(R) = \varphi_{\text{out}}(R), \tag{A.14}$$

$$\lim_{r\to\infty} \varphi_{\text{out}} = 0. \tag{A.15}$$

Applying these conditions result in $c_1 = 6\pi R^2\rho_0/3, c_2 = 0, c_3 = 0$, and $c_4 = 4\pi R^3\rho_0/3$. Eq. (A.11) becomes

$$\begin{cases} \varphi_{\text{in}} = 2\pi\rho_0 \left(R^2 - \frac{r^2}{3}\right), & \text{for } r \le R, \\ \varphi_{\text{out}} = \frac{4\pi R^3 \rho_0}{3r}, & \text{for } r > R. \end{cases} \tag{A.16}$$

From Eq. (A.16) we can obtain the electric field via $E = -\frac{d}{dx}\varphi$ which gives

$$\begin{cases} E_{\text{in}} = \frac{4\pi\rho_0 r}{3}, & \text{for } r \leq R, \\ E_{\text{out}} = \frac{4\pi R^3 \rho_0}{3r^2}, & \text{for } r > R. \end{cases} \tag{A.17}$$

We use Eq. (A.17) to verify that our numerical scheme for solving Eq. (5.144) in Sec. 5.5.3.

APPENDIX B

DYNAMIC STRUCTURE FACTOR IN THE RANDOM PHASE APPROXIMATION

The dynamic structure factor for a Coulomb potential (OCP) can be computed by

$$S(\mathbf{k},\omega) = -\frac{T}{\pi u_C(k)\omega}\mathrm{Im}\left[\frac{1}{\varepsilon(\mathbf{k},\omega)}\right], \tag{B.1}$$

where $u_C(k) = 4\pi(Ze)^2/k^2$ is the Coulomb potential and

$$\varepsilon(\mathbf{k},\omega) = 1 + \left(\frac{k_D}{k}\right)^2 W\left(\frac{\omega}{k\sqrt{T/m}}\right), \tag{B.2}$$

$$W(Z) = \frac{1}{\sqrt{2\pi}}\int_{-\infty}^{\infty} dx \frac{x}{x - Z - i\eta}\exp\left(\frac{-x^2}{2}\right), \tag{B.3}$$

where $k_D^2 = 4\pi n Z^2 e^2/T$. For a generic potential $u(k)$, we re-write the dynamic structure factor using the density response function

$$\chi(\mathbf{k},\omega) = -\frac{1}{u_C(k)}\left[1 - \frac{1}{\varepsilon(\mathbf{k},\omega)}\right], \tag{B.4}$$

which can be rearranged so that

$$u_C(k)\chi(\mathbf{k},\omega) + 1 = \frac{1}{\varepsilon(\mathbf{k},\omega)}. \tag{B.5}$$

Substituting Eq. (B.5) into Eq. (B.1) gives

$$S(\mathbf{k},\omega) = -\frac{T}{\pi\omega}\mathrm{Im}\left[\chi(\mathbf{k},\omega)\right]. \tag{B.6}$$

With the ideal gas density response function, we have for some arbitrary potential $u(k)$ that

$$\chi(\mathbf{k},\omega) = \frac{\chi_0(\mathbf{k},\omega)}{1 - u(k)[1 - G(\mathbf{k},\omega)]\chi_0(\mathbf{k},\omega)}. \tag{B.7}$$

Setting the dynamic local-field correction $G(\mathbf{k},\omega) = 0$, we have the random phase approximation (RPA)

$$\chi^{\mathrm{RPA}}(\mathbf{k},\omega) = \frac{\chi_0(\mathbf{k},\omega)}{1 - u(k)\chi_0(\mathbf{k},\omega)}. \tag{B.8}$$

By plugging Eq. (B.8) into Eq. (B.6), we have

$$S^{\mathrm{RPA}}(\mathbf{k},\omega) = -\frac{T}{\pi\omega}\mathrm{Im}\left[\chi^{\mathrm{RPA}}(\mathbf{k},\omega)\right], \tag{B.9}$$

where the imaginary part of $\chi^{\mathrm{RPA}}(\mathbf{k},\omega)$ is obtained from solving

$$1 - u_C(k)\chi_0(\mathbf{k},\omega) = 1 + \left(\frac{k_D}{k}\right)^2 W\left(\frac{\omega}{k\sqrt{T/m}}\right), \tag{B.10}$$

which simplifies to

$$\chi_0(\mathbf{k},\omega) = -\frac{1}{u_C(k)}\left(\frac{k_D}{k}\right)^2 W\left(\frac{\omega}{k\sqrt{T/m}}\right). \tag{B.11}$$

Note that when $\omega = 0$, the ideal gas response function is simply

$$\chi_0 = -\frac{n}{T}. \tag{B.12}$$

B.1 Fourier Transform of Interaction Potentials

We begin with

$$v(\mathbf{k}) = \int d^3r v(\mathbf{r}) e^{i\mathbf{k}\cdot\mathbf{r}}. \tag{B.13}$$

Writing the above equation in spherical coordinates (assuming that the potential is radially symmetric), we have

$$\begin{aligned} u(k) &= \int_0^{2\pi} d\phi \int_0^{\infty} dr \int_0^{\pi} d\theta\ v(r) e^{ikr\cos\theta} r^2 \sin\theta \\ &= 2\pi \int_0^{\infty} dr \int_0^{\pi} d\theta\ v(r) e^{ikr\cos\theta} r^2 \sin\theta \\ &= 2\pi \int_0^{\infty} dr v(r) \int_0^{\pi} d\theta\ e^{ikr\cos\theta} r^2 \sin\theta. \end{aligned} \tag{B.14}$$

Letting $u = \cos\theta$ means that $du = -\sin\theta d\theta$ and the new limits of the θ integral are $u = -1$ and 1 . Thus,

$$\begin{aligned} u(k) &= 2\pi \int_0^{\infty} dr v(r) r^2 \int_{-1}^{1} du\ e^{ikru} \\ &= 2\pi \int_0^{\infty} dr v(r) r^2 \frac{1}{ikr}\left[e^{ikru}\right]_{-1}^{1} \\ &= 2\pi \int_0^{\infty} dr v(r) r^2 \frac{2}{kr}\sin(kr) \\ &= 4\pi \int_0^{\infty} dr v(r) r \frac{1}{k}\sin(kr). \end{aligned} \tag{B.15}$$

Which yields

$$u(k) = \frac{4\pi}{k}\int_0^{\infty} dr\ r v(r)\sin(kr). \tag{B.16}$$

B.2 Computing $u(k)$ Using a Discrete Sine Transform

We make use of Python's discrete sine transform (DST-I) function to compute $u(k)$. We begin by making the following definitions

$$x_i = a + i\Delta x, \quad k_j = b + j\Delta k. \tag{B.17}$$

The DST-I algorithm assumes the form

$$F(k_j) = 2\sum_{i=0}^{N-1} f(x_i)\sin\left[\frac{\pi(i+1)(j+1)}{N+1}\right]. \tag{B.18}$$

To map our problem into the above convention, we begin by defining, for some maximum distance $r_{\max}$, the real space grid and the Fourier grid

$$x_i = \frac{r_{\max}(i+1)}{N+1}, \quad k_j = \frac{\pi(j+1)}{r_{\max}}. \tag{B.19}$$

With a Riemann sum, we have

$$I(k_j) = \frac{\pi}{k_j}\Delta x \sum_{i=0}^{N-1} x_i u(x_i)\sin(k_j x_i). \tag{B.20}$$

B.3 Computing the $W(Z)$ function

To compute the $W(Z)$ function we have from Ref. [8] that

$$\begin{aligned} W(Z) &= 1 - Z\exp\left(-\frac{Z^2}{2}\right)\int_0^Z dy\, \exp\left(\frac{y^2}{2}\right) + i\sqrt{\frac{\pi}{2}}Z\exp\left(-\frac{Z^2}{2}\right) \\ &= 1 - Z\exp\left(-\frac{Z^2}{2}\right)\left[\int_0^Z dy\, \exp\left(\frac{y^2}{2}\right) - i\sqrt{\frac{\pi}{2}}\right] \\ &= 1 - Z\sqrt{\frac{\pi}{2}}\exp\left(-\frac{Z^2}{2}\right)\left[\sqrt{\frac{2}{\pi}}\int_0^Z dy\, \exp\left(\frac{y^2}{2}\right) - i\right] \\ &= 1 - iZ\sqrt{\frac{\pi}{2}}\exp\left(-\frac{Z^2}{2}\right)\left[\frac{1}{i}\sqrt{\frac{2}{\pi}}\int_0^Z dy\, \exp\left(\frac{y^2}{2}\right) - 1\right]. \end{aligned} \tag{B.21}$$

The above expression reduces further

$$
\begin{aligned}
W(Z) &= 1 + iZ\sqrt{\frac{\pi}{2}}\exp\left(-\frac{Z^2}{2}\right)\left[1 - \frac{1}{i}\sqrt{\frac{2}{\pi}}\int_0^Z dy\, \exp\left(\frac{y^2}{2}\right)\right] \\
&= 1 + iZ\sqrt{\frac{\pi}{2}}\exp\left(-\frac{Z^2}{2}\right)\left[1 - \frac{1}{i}\sqrt{\frac{2}{\pi}}\sqrt{2}i\int_0^{-ix} dt\, \exp\left(-t^2\right)\right] \\
&= 1 + iZ\sqrt{\frac{\pi}{2}}\exp\left(-\frac{Z^2}{2}\right)\left[1 - \frac{2}{\sqrt{\pi}}\int_0^{-ix} dt\, \exp\left(-t^2\right)\right] \\
&= 1 + iZ\sqrt{\frac{\pi}{2}}\exp\left(-x^2\right)\mathrm{erfc}(-ix). \qquad \text{(B.22)}
\end{aligned}
$$

We can use Python's "wofz" function to obtain

$$
W(Z) = 1 + iZ\sqrt{\frac{\pi}{2}}\mathrm{wofz}(Z/\sqrt{2}). \qquad \text{(B.23)}
$$

APPENDIX C

SECOND-ORDER UPWINDING STENCIL IN SPHERICAL COORDINATES

The procedure shown here has been detailed in Ref. [262] for Cartesian and cylindrical coordinates; we extend the approach to spherical coordinates. Our goal is to construct a second-order upwinding stencil for the Vlasov equation in Spherical coordinates. We use a one-dimensional polynomial reconstruction with a second-order polynomial

$$P(r) = p_2 r^2 + p_1 r + p_0 . d \tag{C.1}$$

We can derive a second-order FVM stencil by solving a linear system for the unknown coefficients $\{p_2, p_1, p_0\}$ in terms of the cell averaged distribution function which we denote here as $\langle f \rangle_i$. Once we have the coefficients of the polynomial $P(r)$, we evaluate it at the cell interfaces to obtain a numerical flux function at the interface. For a second-order upwinding stencil, we require three values of our cell averaged distribution function. Specifically, we have that the linear system is given by the relations

$$\langle f \rangle_{i-2} = \int_{r_{i-5/2}}^{r_{i-3/2}} P(r) 4\pi r^2 \, dr, \tag{C.2}$$

$$\langle f \rangle_{i-1} = \int_{r_{i-3/2}}^{r_{i-1/2}} P(r) 4\pi r^2 \, dr, \tag{C.3}$$

$$\langle f \rangle_{i} = \int_{r_{i-1/2}}^{r_{i+1/2}} P(r) 4\pi r^2 \, dr, \tag{C.4}$$

$$\langle f \rangle_{i+1} = \int_{r_{i+1/2}}^{r_{i+3/2}} P(r) 4\pi r^2 \, dr. \tag{C.5}$$

From the above relations, we solve the linear system to obtain the coefficients $\{p_2, p_1, p_0\}$. For the case where the advection speed $v > 0$, we construct a linear system from $\langle f \rangle_{i-1}$, $\langle f \rangle_i$, and $\langle f \rangle_{i+1}$. When $v < 0$ we construct a linear system from $\langle f \rangle_{i-2}$, $\langle f \rangle_{i-1}$, and $\langle f \rangle_i$. Assuming that $v > 0$ and

solving the linear system for the coefficients of $P(r)$ and then evaulating $P(r)$ at $r_{i+1/2}$ yields

$$\begin{aligned}\langle f\rangle_{i+1/2} = \frac{1}{24\pi\Delta r^3(4+6\ell-9\ell^2-20\ell^3+15\ell^4+30\ell^5+10\ell^6)}\Big\{ \\ +(24+96\ell+144\ell^2+90\ell^3+20\ell^4)\langle f\rangle_{i-1} \\ +(69-96\ell-63\ell^2+90\ell^3+50\ell^4)\langle f\rangle_i \\ +(-3+9\ell^2-10\ell^4)\langle f\rangle_{i+1}\Big\},\end{aligned} \tag{C.6}$$

where $\ell = r_{i+1/2}/\Delta_r$. For $v < 0$

$$\begin{aligned}\langle f\rangle_{i+1/2} = \frac{1}{24\pi\Delta r^3(4-6\ell-9\ell^2+20\ell^3+15\ell^4-30\ell^5+10\ell^6)}\Big\{ \\ +(-3+9\ell^2-10\ell^4)\langle f\rangle_{i-2} \\ +(69+96\ell-63\ell^2-90\ell^3+50\ell^4)\langle f\rangle_{i-1} \\ +(24-96\ell+144\ell^2-90\ell^3+20\ell^4)\langle f\rangle_i\Big\}.\end{aligned} \tag{C.7}$$